Spectroscopy of exotic nuclei across the nuclide chart : from ^{11}LI,^{13}Li to $^{1\ 2}$Sn

Paul André

▶ **To cite this version:**

Paul André. Spectroscopy of exotic nuclei across the nuclide chart : from ^{11}LI,^{13}Li to $^{1\ 2}$Sn. Nuclear Experiment [nucl-ex]. Université Paris-Saclay, 2022. English. NNT : 2022UPASP109 . tel-03948368

HAL Id: tel-03948368

https://theses.hal.science/tel-03948368

Submitted on 20 Jan 2023

HAL is a multi-disciplinary open access archive for the deposit and dissemination of scientific research documents, whether they are published or not. The documents may come from teaching and research institutions in France or abroad, or from public or private research centers.

L'archive ouverte pluridisciplinaire **HAL**, est destinée au dépôt et à la diffusion de documents scientifiques de niveau recherche, publiés ou non, émanant des établissements d'enseignement et de recherche français ou étrangers, des laboratoires publics ou privés.

université
PARIS-SACLAY

Spectroscopy of exotic nuclei across the nuclide chart: from ^{11,13}Li to ^{102}Sn

Spectroscopie des noyaux exotiques à travers la carte des nucléides : de ^{11,13}Li à ^{102}Sn

Thèse de doctorat de l'université Paris-Saclay

École doctorale n° 576 : Particules, hadrons, énergies et noyau : instrumentation, imagerie et simulation (PHENIICS)
Spécialité de doctorat: Structure et réactions nucléaires
Graduate School : Physique, Référent : Faculté des Sciences d'Orsay

Thèse préparée dans l'unité de recherche Département de Physique Nucléaire (Université Paris-Saclay, CEA)
sous la direction de Anna CORSI, ingénieure de recherche,
le co-encadrement de Aldric REVEL, ingénieur de recherche

Thèse soutenue à Paris-Saclay, le 21 octobre 2022, par

Paul ANDRÉ

Composition du jury

Élias KHAN Professeur, IJCLab, Université Paris-Saclay	Président du jury
Miguel MARQUÉS Directeur de recherche, LPC Caen, Université Caen Normandie	Rapporteur & Examinateur
Kathrin WIMMER Chargée de recherche, GSI Helmholtzzentrum für Schwerionenforschung	Rapporteur & Examinatrice
Marlène ASSIÉ Chargée de recherche, IJCLab, Université Paris-Saclay	Examinatrice
Olivier SORLIN Directeur de recherche, GANIL, Université Caen Normandie	Examinateur
Anna CORSI Ingénieure de recherche, IRFU, CEA, Université Paris-Saclay	Directrice de thèse

THESE DE DOCTORAT
NNT : 2022UPASP109

Acknowledgments

I would like first to thank my two supervisors, Anna Corsi and Aldric Revel. They have always worked hard to provide me with the best working environment possible, and pushed me towards excellence. They always kept their door and their mind open to answer my scientific or personal questions. I would like to express my deep gratitude for accompanying me throughout these three years, even in the middle of cold French and German winters, even in the middle of world-shaking events.

I would then like to thank Elias Khan, Miguel Marqués, Kathrin Wimmer, Marlène Assié and Olivier Sorlin for accepting to be part of my PhD jury. Their careful reading of my work, and the resulting contructive criticisms and comments, have helped giving additional clarity and depth to this manuscript. The discussion during the defense has also given me lots of new insights about nuclear spectroscopy.

I have had the chance to meet very warm and welcoming people during my stay at DPhN. I would like to thank Alain, Valérie and Lolly, who have contributed to make my time in Saclay easy and enjoyable by providing me with friendly discussions, and chocolate. I would also like to thank Vittorio, Thomas, Lorenzo, Francesco, Benjamin and Gianluca for helping me navigate the sea of nuclear structure theories.

I also met a group of very nice fellow PhD students who shared my doubts when I had some, but also shared good laughs. I would like to thank Christopher, Brian, Mikael, Zoé, Aude, Rudolphe, Rémi, Aurore, and Hervé, and I would like to wish them all the best for what is coming next for them. I would like to give my warmest support and encouragements to Borana, Pierre, Desi, Michael, Andrii, Emmanuel, Matteo, Élie, Kevin and Alberto, who , I hope, are enjoying the journey that is a PhD. I would like to give special thanks to Sébastien, who shared with me a taste for weird and niche internet humor. I would also like to especially thank the Andreas (Andrea P. and Andrea L.) for their ability to meet me in the lab despite the rain, the wind, the snow or the blazing July sun, for spending eternities in traffic jams on board the CEA bus with me, and overall, for their friendship.

Carrying out this work made me meet people from other scientific institutions, who were kind enough to share their knowledge with me. I would like to thank Pieter, Liliana, Chen, Sophie and Marc who helped me with the analysis of our results on ^{102}Sn, and Uesaka-san, Kubota-san, Yelei, Zaihong ,Yutian and Jesús who helped me with the intricacy of neutron-rich Li isotopes. I would also like to thank Valerii, Ryo and Antoine, who I had the pleasure to meet during my trips at GSI. I would also like to credit Makiko Andro-Ueda for her time and her help with the translation of the two haikus presented in this manuscript.

I was lucky enough to receive tremendous support outside of the lab. I would like to thank the notorious CDB for putting up with me during all these years, and laughing at my stupid jokes when we were stuck at home. I would like to thank Baptiste and Justin for their long-lasting friendship. I would also like to thank Hugo, Maud and Marianne. Their kind words always made me see the glass half full, glass that we then usually drank and refilled at the bar. I would like to thank Erik for his strange jokes and his misleading movie descriptions. I would like to thank Robin for constantly beating me at chess and being my best provider of life hacks.

Eventually, I would like to thank my family for their never-ending support, my dad, Valou. The last lines of this section are devoted to thanking my mother and Maitane. They were not only vital throughout my PhD, but are, and will always be, vital to my life.

Contents

List of Figures

List of Tables

Introduction

Mankind has been discovering elements as early as the Neolithic, as the discovery of Copper (Cu) happened around 9000 BC. The first modern discovery of an element is considered to be the discovery of Phosphorus (Ph) in 1669 by H. Brand. The first classification of these elements is attributed to A. Lavoisier in 1789, before the first periodic table of D. Mendeleev in 1869. Since this era, the periodic table has been completed from element number 1, Hydrogen (H), to element number 118, Oganesson (Og), first synthesized in 2002 [1]. In 1911, E. Rutherford provides the experimental proof of the existence of the atomic nucleus, as a dense core of positively charged matter at the heart of the atom. The current simplest description of the nucleus is that of a many-body system composed of Z protons and of N neutrons, making up together A nucleons. Whereas the protons repel each other as they are positively charged, all the nucleons are tied together thanks to the strong interaction. Two years after this founding experiment, the existence of isotopes is proposed by F. Soddy. A nucleus is defined as an isotope of an element when it has the same number of protons but a different number of neutrons. This opened the gates to the discovery and the study of stable nuclei and their isotopic variations. There are approximately 300 known stable nuclei and almost 3300 isotopes in total have already been discovered [2]. They are represented on the nuclide chart, first proposed by K. Guggenheimer in 1934, with N as the x-axis of the chart, and Z as its y-axis. It is shown in figure 1. Unifying the behavior of these 3300 systems with universal and fundamental properties is an immensely difficult task and is the endeavor of the nuclear physicists. Having such a range of different systems also has the perk of providing that many testing grounds for theoreticians and experimentalists.

Since the high energy experiments providing evidences for the Standard model of particle physics, it is known that protons and neutrons are not elementary particles and are themselves composed of quarks. One way of studying the atomic nucleus would be to explain the nuclear properties from the study of quarks directly. Quantum chromodynamics (QCD) provide the tools to study the interaction between quarks, but such computations are not feasible beyond few-body systems. An attempt has been performed by N. Ishii, S. Aoki and T. Hatsuda [4]. T. Hatsuda discusses the limitations of such a method [5]. One could then treat protons and neutrons as elementary particles and apply quantum perturbation theory (QPT) on a system of A nucleons. However, the shape of the strong interaction between nucleons is not well defined and would be a too intense perturbation to apply QPT. One could then try to rely on macroscopic techniques and consider the atomic nucleus like a fluid. Such a development was first performed with the liquid drop model, in which the atomic nucleus is represented by a liquid drop. This representation lead to the semi-empirical Bethe-Weizsäcker mass formula, which provides the binding energy of a nucleus as a function of N and Z, and also enabled a first representation of

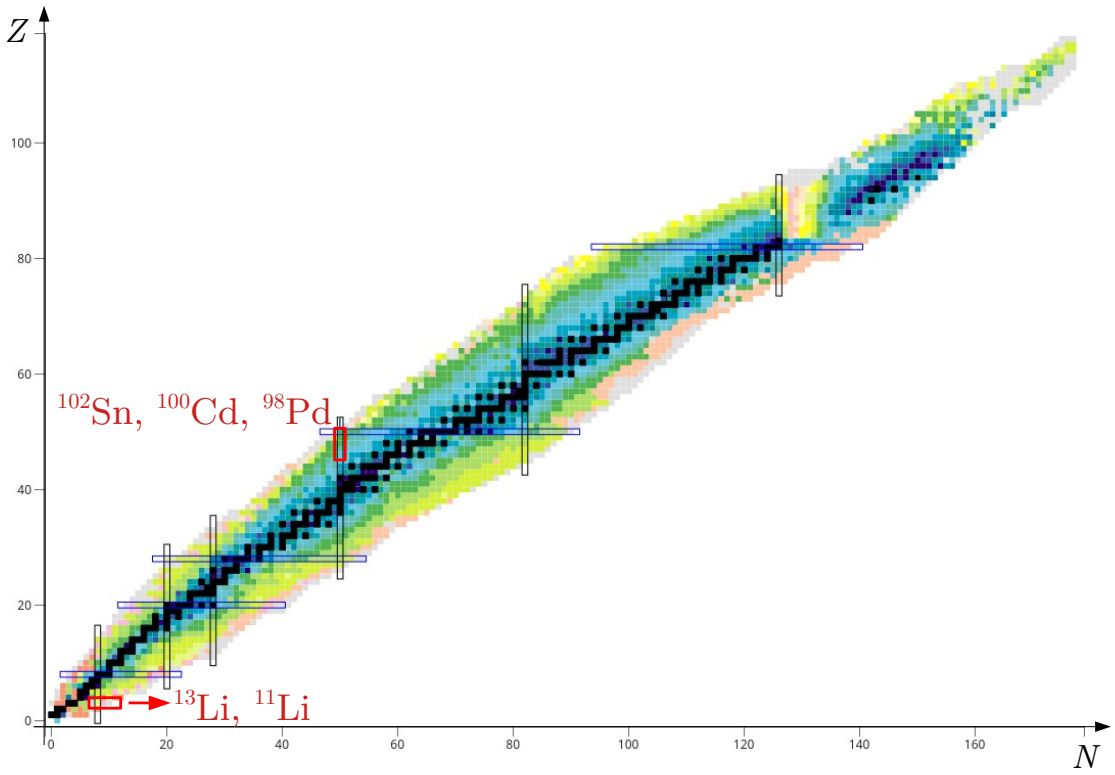

Figure 1: The nuclide chart. The two areas of interest for this thesis are indicated. Image from [3].

the nuclear deformations. However, this model does not reproduce quantum effects, such as shell effects (detailed in chapter 1). As a consequence, the need for new theoretical tools has been identified rapidly, with the two main goals of providing a realistic nuclear potential and a method to solve the Schrödinger equation, with the nuclear Hamiltonian. Historically, the most widely used model is the Shell Model. The fundamental premise of the shell model is that nucleons behave in first approximation as independent particles in a common potential generated by the net effect of all the other particles. Different implementations have been provided in different regions of the nuclide chart and managed to successfully reproduce experimental observations [6].

One can try to find nuclear potentials from first principles, using *ab initio* methods, considering the nucleons as the degrees of freedom. A method inherited from QCD named nuclear Effective Field Theory (EFT) is widely studied for the determination of nuclear forces [7]. One can mention the No Core Shell Model (NCSM) [8], the Coupled-Cluster (CC) method [9], the self-consistent Green's functions method [9], the In-Medium Similarity Renormalization Group (IMSRG) [10], as methods solving the resulting nuclear Hamiltonian. Progresses made in the implementation of these methods made it possible to compute the structure of light and medium-mass nuclei from first principles, as it is shown in [11], from which figure 2 is taken.

To be able to describe heavier systems, mean-field approaches are also considered, where the potential is averaged over all nucleons. One can mention mean-field potentials such as the Woods-Saxon potential [12], the Skyrme [13], Migdal [14] or the Gogny interaction [15]. Coupled with self-consistent methods, such as the Hartree-Fock (HF) method [16]

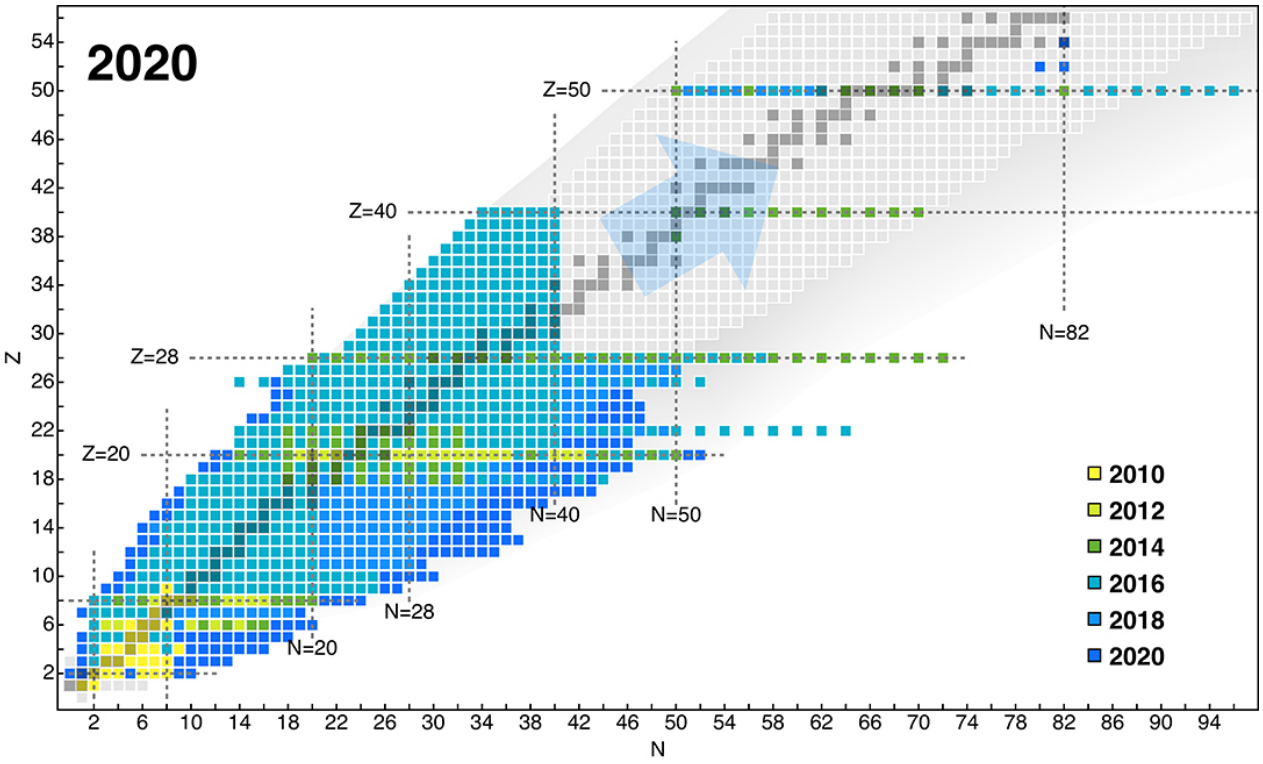

Figure 2: The nuclide chart with accessible nuclei via *ab initio* methods per year. Figure from [11].

and its further development, the Time-Dependent Hartree-Fock method (TDHF) or the Hartree-Fock-Bogoliubov (HFB) method, based on a variational principle and a density-dependent potential, mean-field calculations are able to provide structure calculations for medium-weight and heavy nuclei. Density Functional Theory (DFT) [17], based on the Kohn-Hohenberg theorem and on an adaptation of the self-consistent Kohn-Sham algorithm to the nuclear case, is also a widely used self-consistent method providing mean-field potentials. One can note that efforts have been made recently to link DFT with *ab initio* methods [18]. Overall, theoreticians progress towards an implementation of all the aforementioned methods and models to the whole nuclide chart, starting with small, experimentally well-known systems, reaching heavier and more exotic nuclei. Some studies have recently started exploring the opposite dynamic, performing calculations for nuclear matter, an ideal system of nucleons of infinite size, and applying the results to the structure calculations of medium-weight nuclei, namely Ca isotopes in the case of [19,20]. From all these considerations, the goal of nuclear structure theories is ultimately to find a comprehensive representation for the whole nuclide chart, that is computationally affordable.

From the experimental point of view, the challenge resides in the measurement of observables in as many nuclides as possible, getting closer and even beyond the drip lines, which are the limits in terms of Z and N for which a nucleus starts decaying via the emission of one or several nucleons. Thanks to technical breakthroughs, beams of exotic nuclei have become more and more intense. High intensity primary beams are now produced at the Radioactive Isotope Beam Factory (RIBF,Japan), at the Gesellschaft für SchwerIonenforschung (GSI, Germany), at the Grand Accélérateur National d'Ions Lourds (GANIL, France), and at the brand new Facility for Rare Isotopes Beams (FRIB, United States).

After undergoing fragmentation, these beams provide secondary beams that are intense enough to allow the study of more and more exotic systems. The Facility for Antiproton and Ion Research (FAIR, Germany) is expected to provide beams of high energy and high intensity from 2025 on. RIBF, GSI and FRIB provide beams of high energy, from 100 MeV/nucleon to few GeV/nucleon. However, not only beams of various masses, but beams of various energies are required to probe specific nuclear properties, with applications in nuclear structure or in nuclear astrophysics. The Isotope Separator Online DEvice facility (ISOLDE, CERN, Switzerland), the SPES (Selective Production of Exotic Species, Legnaro, Italy) project, or the TRIUMF accelerators (Vancouver, Canada), aim at providing low energy beams of all masses. The Optimized Energy Degrading Optics project (OEDO, [21]) at the RIBF facility has recently been designed with the purpose of producing low energy beams of heavy radioactive ions.

One of the issues in nuclear physics is the immense variety of existing complex systems. As a consequence, both theoreticians and experimentalists of the nuclear community have to design an immense variety of versatile methods. In this context, this thesis provides the results for two experimental studies of the structure of exotic nuclei, with modern setups. One will focus on nuclei close to the proton drip line, with the inelastic excitation of ^{102}Sn, ^{100}Cd and ^{98}Pd. The other will focus on the neutron drip line, with the two-neutron decay of ^{13}Li and ^{11}Li.

Part I

Inelastic excitation of ^{102}Sn, ^{100}Cd and ^{98}Pd

つね憎き　烏も雪の　朝哉

Usually hateful,

Even the crow is appealing —

The snowy morning.

Bashō, 1691

Chapter 1

Tin isotopes and nuclear structure

Contents

The wide variety of existing nuclei, usually represented in the nuclide chart, provides a large number of systems enabling the benchmark of the current knowledge on nuclear structure. The Sn isotopes constitute the longest isotopic chain between two doubly magic nuclei, namely ^{100}Sn ($N = Z = 50$) and ^{132}Sn ($Z = 50$ and $N = 82$). As a consequence, this isotopic chain provides a large panel of structures enabling the study of different systematics. In the following paragraphs, the concept of magicity will be briefly introduced as well as how it relates to the study of Sn isotopes. The efforts to understand the unexpected collectivity of light Sn isotopes will be presented, providing the context of the study described in the first part of this thesis.

1.1 Magic numbers and their evolution

The concept of magic numbers is inherently linked to the nuclear shell model. To understand better the concept of shells in atomic nuclei, one can start from the time-dependent Schrödinger equation for the atomic nucleus:

$$\hat{H}\psi(\overrightarrow{r},t) = i\hbar\frac{\partial\psi(\overrightarrow{r},t)}{\partial t}, \tag{1.1}$$

with $\hat{H}$ the Hamiltonian of the system, and $\psi(\overrightarrow{r},t)$ the wave-function of the system. The Hamiltonian can be written in the following way:

$$\hat{H} = \hat{T} + \hat{U} \tag{1.2}$$

with $\hat{T}$ the kinetic energy, and $\hat{U}$ the potential of the system. These two quantities can themselves be written the following way:

$$\begin{aligned} \hat{T} &= \sum_{i=1}^{A} \hat{T}_i \\ \hat{U} &= \sum_{i \neq j} \hat{V}_{2B,ij} + \sum_{i \neq j \neq k} \hat{V}_{3B,ijk} + \sum_{i \neq j \neq k \neq m} \hat{V}_{4B,ijkm} + ..., \end{aligned} \tag{1.3}$$

with A the mass number, $\hat{T}_i$ the kinetic energy for each nucleon, $\hat{V}_{2B,ij}$ the interaction between each pair of nucleons, $\hat{V}_{3B,ijk}$ the interaction between each group of three nucleons, $\hat{V}_{4B,ijkm}$ the interaction between each group of four nucleons. The sum goes on until the interaction between the whole group of A nucleons. This Hamiltonian has the general form of the Hamiltonian for many-body problems. Solving many-body problems is still an ongoing challenge in various fields of physics, including nuclear physics, as no analytical solution of the Schrödinger equation with such an operator has been found yet in the general case. A simplified way of viewing these operators is to consider, as a first approximation, the two-body interaction only, to consider each nucleon individually and to use a mean-field approach for the potential. This way, the wave function ψ can be written as:

$$\psi = \prod_{i=1}^{A} \phi_i, \tag{1.4}$$

with ϕ_i the single-particle wave function. One can also rewrite the potential:

$$V_i = \sum_{j \neq i} \langle \phi_j | \, V_{ij} \, | \phi_j \rangle \, . \tag{1.5}$$

The nucleons are affected by the nuclear interaction. One can now write the single-particle Hamiltonian:

$$H_{sp} = T_i + V_n, \tag{1.6}$$

with

$$T_i = -\frac{\hbar^2}{2M} \Delta, \tag{1.7}$$

and V_n the nuclear potential, M the average nucleon mass and Δ the Laplacian operator. The challenge is then to find a suitable nuclear potential to model the strong interaction. The first choice has been intuitively to use the harmonic oscillator, with a potential of the shape:

$$V_n(r) = \frac{M\omega_0^2}{2} r^2, \tag{1.8}$$

with ω_0 the angular frequency of the oscillator. For this potential, an analytical solution exists, with a level scheme of degenerate orbitals, equally spaced of $\hbar\omega_0$. Counting the number of nucleons necessary to fill each level yields a first set of the so-called magic numbers: 2, 8, 20, 40, 70, 112. Considering a more realistic nuclear potential yields other magic numbers. A rather straightforward modification is the modified oscillator potential proposed by S.G. Nilsson in 1955 [22]:

$$V_{MO} = \frac{1}{2} M\omega_0 r^2 - \kappa\hbar\omega_0 \left[2\mathbf{l} \cdot \mathbf{s} + \mu \left(l^2 - \langle l^2 \rangle_N \right) \right], \tag{1.9}$$

with $\mathbf{l}$ the angular momentum operator, $\mathbf{s}$ the spin operator, κ the spin-orbit coupling strength, and μ (also sometimes written as $\mu' = \kappa\mu$) the surface diffuseness depth. The resulting shells for the harmonic oscillator and modified oscillator are shown in figure 1.1.

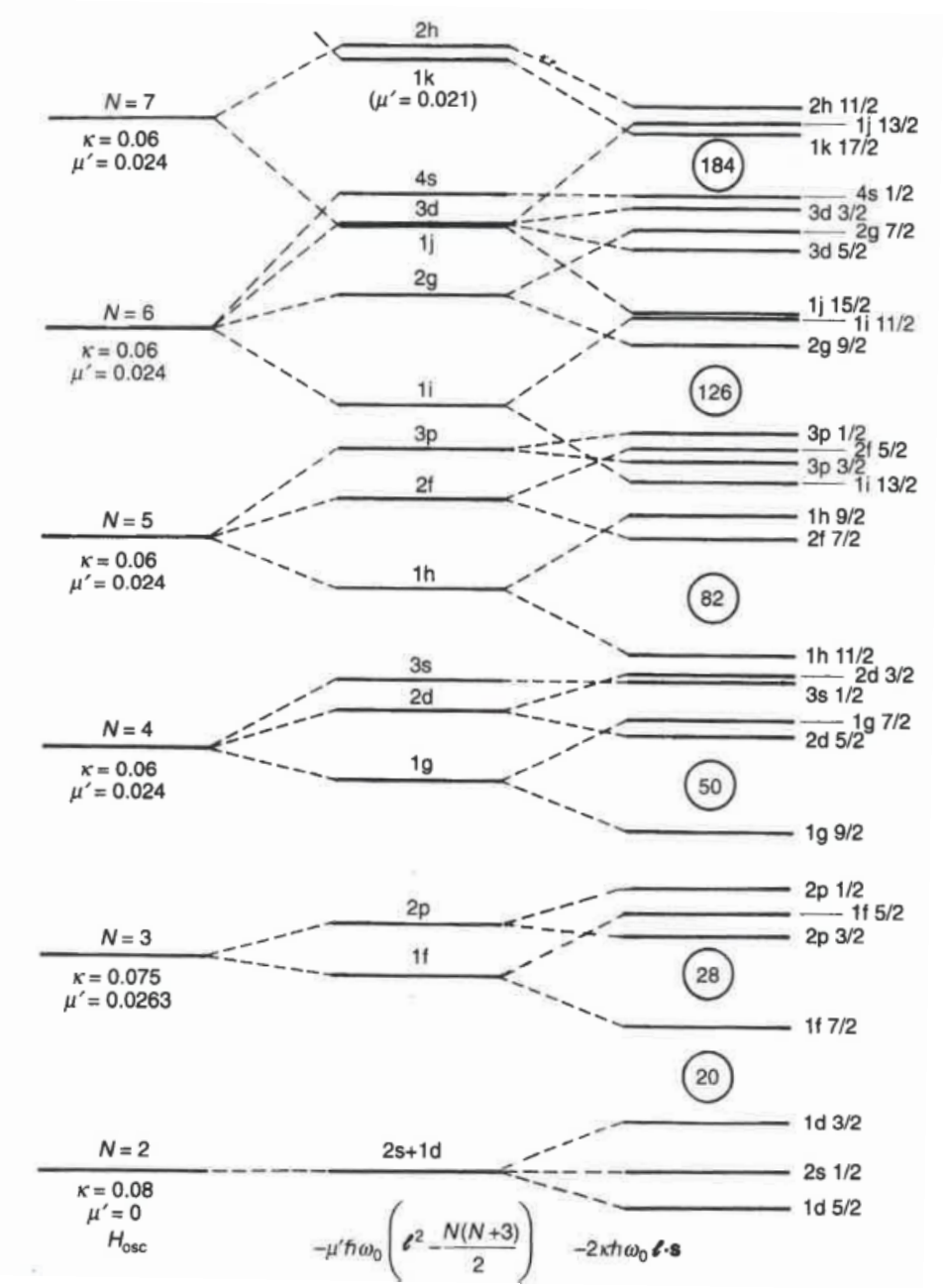

Figure 1.1: Shells for different nuclear interaction models. H_{osc} indicates the level for the harmonic oscillator, the level scheme in the middle shows the result for the harmonic oscillator with the l^2 term, and the level scheme on the right is the result for the whole modified harmonic oscillator. Figure 6.3 from [23].

This potential takes as a starting point the harmonic oscillator described previously, adding a spin-orbit term, proposed already in 1949 by O. Haxel, J. H. D. Jensen and H. E. Suess [24], and an l^2 term interpolating the harmonic oscillator with the square well potential. The values for κ and μ are chosen to reproduce the structure for the neutrons in ^{208}Pb [23]. The perk of this model is to be solvable analytically and to effectively

reproduce a Woods-Saxon shape thanks to the l^2 term. A review by M. Goeppert-Mayer in 1948 [25] of experimental results on the isotopic abundance and the absorption cross-section, among other quantities, reveal the exceptional stability of nuclei with 20, 50, 82 and 126 protons or neutrons, thus providing experimental evidences for the magic numbers.

Figure 1.1 shows the change in expected magic numbers when adding terms from an intuitive potential, the harmonic oscillator, in order to get closer to a realistic nuclear potential. As a consequence, it shows the link between the concept of magic numbers and their actual value, and the interpretation of the nuclear structure as being organized in shells, as well as the model chosen for this representation. This interpretation is supported from the experimental point of view, as shown by Goeppert-Mayer's seminal study. In addition to the quantities presented in the original article [25], one can consider the energy of the 2^+ state $E(2^+)$ and the reduced transition probability $B(E2, 0^+ \rightarrow 2^+)$ for the observation and determination of shell closure, and as a consequence magicity. In even-even nuclei (N and Z even), the 2^+ state is often the first excited state, and $B(E2, 0^+ \rightarrow 2^+)$ translates as the collectivity of the first excited state, which is related to the number of holes involved in the excitation of the nucleus. As one gets closer to shell closure, and as the nuclei are expected to become more stable, $E(2^+)$ is expected to increase, and $B(E2, 0^+ \rightarrow 2^+)$ is expected to decrease. Representing $E(2^+)$ as a function of N in the case of an isotopic chain would yield a parabola-shaped curve with a maximum at the shell closure and the minimum at mid-shell. Similarly $B(E2, 0^+ \rightarrow 2^+)$ is expected to reach its maximum at mid-shell, and to decrease as one reaches shell closure. An example of that is given in figure 1.2.

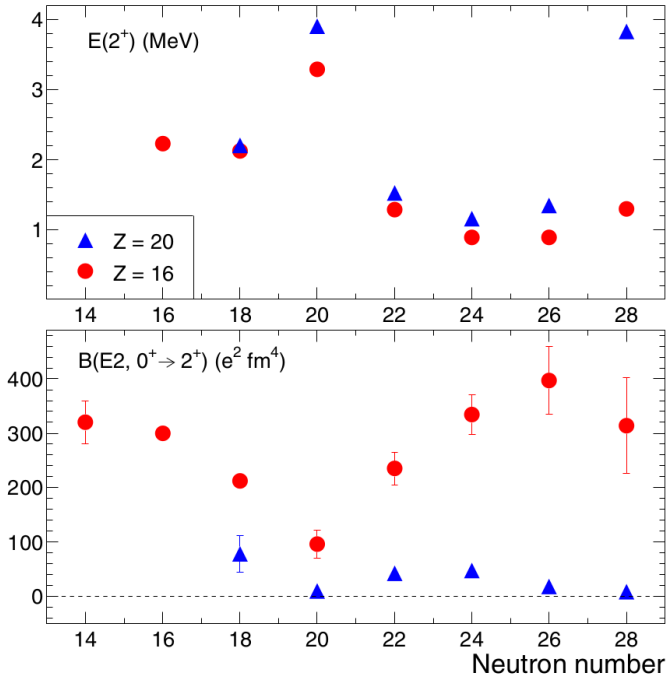

Figure 1.2: Evolution of $E(2^+)$ and $B(E2, 0^+ \rightarrow 2^+)$ for the first 2^+ excited state for Sulfur ($Z = 16$, red dots) and Calcium ($Z = 20$, blue triangles) isotopes. Figure 13 from [26].

This shows the evolution of $E(2^+)$ and $B(E2, 0^+ \rightarrow 2^+)$ with the neutron number N. The Ca isotopes exhibit a sharp increase in $E(2^+)$ and a dip in $B(E2, 0^+ \rightarrow 2^+)$ for the doubly

magic ^{40}Ca and ^{48}Ca. The values of $E(2^+)$ and $B(E2, 0^+ \rightarrow 2^+)$ for the Ca isotopes are constantly higher and lower respectively than the ones for the S isotopes, in agreement with the fact that Ca isotopes are all magic due to their 20 protons.

The disappearance of known magic numbers and the appearance of new ones in exotic nuclei has been studied both experimentally and theoretically [6, 27]. Figure 1.2 shows signs of this phenomenon. One can note that ^{44}S exhibits a low $E(2^+)$ and a relatively high $B(E2, 0^+ \rightarrow 2^+)$, hinting at a quenched $N = 28$ shell closure [28]. More cases have been found thanks to the development of exotic beams in the recent years. For example, the study of the one-neutron removal and the neutron decay on ^{24}O [29–31] provides evidences of shell closure for $N = 16$ via a measurement of its $E(2^+)$. The unbound nature of ^{28}O is a first hint of reduction of the $N = 20$ gap in O isotopes [32]. Invariant mass data on ^{28}O are currently under analysis and should give information concerning the magnitude of this shell closure. In-beam studies of exotic nuclei have also been used to measure the $E(2^+)$ of ^{52,54}Ca, providing evidences for an $N = 32, 34$ sub-shell closure [33,34]. Neutron-rich Ni isotopes have also challenged the known magic numbers. Coulomb excitation has been first used to measure the value of $B(E2, 0^+ \rightarrow 2^+)$ [35] showing shell closure for $N = 40$. Measurement of $E(2^+)$ closer to the drip line for these isotopes via in-beam γ ray spectroscopy has then recently shown that the $Z = 28$ and $N = 50$ shell closure are still holding that far from stability [36].

Besides 2^+ energies, the reduced transition probability $B(E2, 0^+ \rightarrow 2^+)$ has been used to track down shell evolution. The $B(E2, 0^+ \rightarrow 2^+)$ is usually extracted in Coulomb excitation or lifetime measurements, and is related to the proton transition matrix element of the electromagnetic operator. The information about the stability given by this matrix element can be completed by the value of the neutron transition matrix element, often measured by inelastic excitation measurements. Details about these matrix elements are given in the following paragraph.

Several explanations have been put forward to explain shell evolution. In the framework of the shell model, the appearance of a sub-shell gap for $N = 32, 34$ in Ca isotopes is driven by the tensor term of the nuclear interaction [34]. The tensor force was also used to explain the shell evolution in the Ni isotopes, with a new shell closure at $N = 40$, and possibility of quenching of the one at $N = 50$ [37]. As mentioned above, the interpretation of recent results on ^{78}Ni shows the persistence of this shell closure but suggests its quenching above ^{78}Ni [36]. In the case of ^{28}O, its unbound nature was correctly predicted for the first time thanks to the use of three-body forces [38].

1.2 Multipole operators and their matrix elements

Among the various methods to link experiment to theory, this paragraph proposes one way to establish this connection, foreshadowing the topic of this thesis, namely hadron inelastic scattering.

The previous Hamiltonian given in equation (1.2) provides a description of the interaction of the nucleons in the nucleus. But one can also consider the nucleus in an external electromagnetic field. The resulting Hamiltonian can be written as (Appendix B in [39]):

$$\hat{H} = \hat{H}_{nucl} + \hat{H}_{field} + \hat{H}_{int}, \tag{1.10}$$

with $\hat{H}_{nucl}$ the nuclear Hamiltonian (written considering the desired model), $\hat{H}_{field}$ the Hamiltonian of the external electromagnetic field, and $\hat{H}_{int}$ the Hamiltonian of the interaction between the nucleus and the field. The latter can be written in the following way [40]:

$$\hat{H}_{int} = \sum_{\lambda\mu} a_{\lambda\mu}\hat{O}^{\lambda\mu} + \sum_{\lambda\mu} b_{\lambda\mu}\hat{B}^{\lambda\mu} \tag{1.11}$$

with $\hat{O}^{\lambda\mu}$ and $\hat{B}^{\lambda\mu}$ the electric and magnetic multipole operators. $a_{\lambda\mu}$ and $b_{\lambda\mu}$ are the coefficients of the multipolar expansions for the electric and magnetic multipole operators respectively. $\hat{B}^{\lambda\mu}$ can be written as the following integral [39]:

$$\hat{B}^{\lambda\mu} = \int \mu(r)\nabla\left(r^{\lambda}Y_{\lambda\mu}(\theta,\phi)\right)\mathrm{d}^3r, \tag{1.12}$$

with $Y_{\lambda\mu}$ the spherical harmonics and $\mu(r)$ the density of the magnetic moment. This paragraph will focus more on the electric multipole operator, written as:

$$\hat{O}^{\lambda\mu} = b_p^F\hat{O}_p^{\lambda\mu} + b_n^F\hat{O}_n^{\lambda\mu}, \tag{1.13}$$

with

$$\begin{aligned}\hat{O}_p^{\lambda\mu} &= \sum_p r_i^{\lambda}Y_{\lambda\mu}(\mathbf{r}_i),\\ \hat{O}_n^{\lambda\mu} &= \sum_n r_i^{\lambda}Y_{\lambda\mu}(\mathbf{r}_i).\end{aligned} \tag{1.14}$$

$\hat{O}_p^{\lambda\mu}$ and $\hat{O}_n^{\lambda\mu}$ are the proton and neutron part of the electric multipole operator respectively. b_p^F and b_n^F are respectively the proton and neutron multipole field strength. These two quantities depend on the field F that is applied on the protons and neutrons. For instance, in the case of an electromagnetic transition, $b_p^F = 1$ and $b_n^F = 0$, and in the case of inelastic proton scattering at 1 GeV, $b_n^F/b_p^F = 0.95$ [40]. In a similar way, one can write the reduced matrix elements for the electric multipole operator:

$$\begin{aligned}M &= \langle J_fTT_z\|\hat{O}^{\lambda\mu}\|J_iTT_z\rangle,\\ &= b_p^F M_p + b_n^F M_n,\end{aligned} \tag{1.15}$$

with the final and initial states in isospin representation respectively. As shown in the previous equation, it is also possible to split M into a proton, M_p, and a neutron part, M_n. Another definition of M_p (and M_n) can be written with the proton (and neutron) transition density $\rho_{fi}^{p(n)}$ [40]:

$$M_{p(n)} = \int_0^{\infty} \rho_{fi}^{p(n)}(r)r^{\lambda+2}\mathrm{d}r, \tag{1.16}$$

giving a direct link with the transition rate $B(E\lambda)$ between the initial state J_i and the final state J_f [41]:

$$B(E\lambda, J_i \to J_f) = \frac{M_p^2}{2J_i+1}, \tag{1.17}$$

with λ the multipolarity. As there is a direct link between $B(E\lambda)$ and the cross-section for electric excitation [42], Coulomb excitation experiments are a way to experimentally

access the value of M_p. Bernstein, Brown and Madsen in [41] also provide a way to link the inelastic scattering cross-section and the proton and neutron matrix elements:

$$\sigma_{inel} \propto \left(b_p^F M_p + b_n^F M_n\right)^2 = \left(b_p^F\right)^2 \left(M_p + \frac{b_n^F}{b_p^F} M_n\right)^2 . \tag{1.18}$$

On practice, for a given probe and a given range in energy, experimental and calculated values have been found for the ratio b_n/b_p. For a purely electromagnetic external field, this ratio is 0, and the measured cross-section provides M_p directly. For reactions with a proton between 10 and 50 MeV, $b_n/b_p \simeq 3$, while it is equal to 0.95 at 1 GeV [40]. It now appears that one needs (at least) two different probes F to obtain a value for M_p and M_n, and the measurement of the reaction cross-section provides access to these quantities.

1.3 The case of Tin isotopes

As stated earlier, the Sn isotopic chain is the longest one between two doubly magic nuclei in the nuclide chart. It is as a result a good testing ground for shell evolution. Towards the neutron drip line, the doubly magic character of ^{132}Sn has been confirmed as the measured $E(2^+)$ is relatively high, and as the spin-parity assignment of the first excited state follows the systematics of other double magic nuclei [43]. Going towards the neutron-deficient side of the chart, an increase in $B(E2, 0^+ \rightarrow 2^+)$, and so in collectivity, is visible around $N = 60$, which was not reproduced for a long time by theoretical calculations, as it is displayed in figure 1.3. When one gets closer to the proton drip line, the information becomes very scarce. The value for the $B(E2, 0^+ \rightarrow 2^+)$ from Coulomb excitation cross-section was first measured for ^{104}Sn in 2013 by G. Guastalla *et al.* at GSI with a value of 0.10(4) e^2b^2 [44]. This value is in agreement with advanced shell model calculations, predicting shell closure for $N = 50$. The same year, V.M. Bader *et al.* perform another measurement at the National Superconducting Cyclotron Laboratory (NSCL, United States) with a higher statistics, which yields a value of 0.180(37)e^2b^2 [45]. This new value however is not in agreement with the aforementioned calculations and appears to be higher, indicating a softer shell closure in this region. In 2014, P. Doornenbal *et al.* performs another measurement at RIBF with high statistics, providing a value of 0.173(28)e^2b^2 for the $B(E2, 0^+ \rightarrow 2^+)$ of ^{104}Sn, in agreement with Bader's value, giving more credit to the soft shell closure hypothesis [46]. This is summed up in figure 1.3.

Proton inelastic scattering on ^{104}Sn has been first performed in 2015 by A. Corsi *et al.* [47] providing the first value of 1.4 for M_n/M_p. The experimental values of M_p in the Sn isotopic chain is shown in figure 1.4. Theoretical values for M_n and M_p calculated using the Quasi-particle Random Phase Approximation (QRPA) are also displayed. This figure shows a dip in the theoretical values for M_n and M_p for ^{102}Sn before the doubly magic ^{100}Sn, giving hints of shell closure at $N = Z = 50$. This has not yet been measured experimentally, as no such experimental information is available for ^{102}Sn.

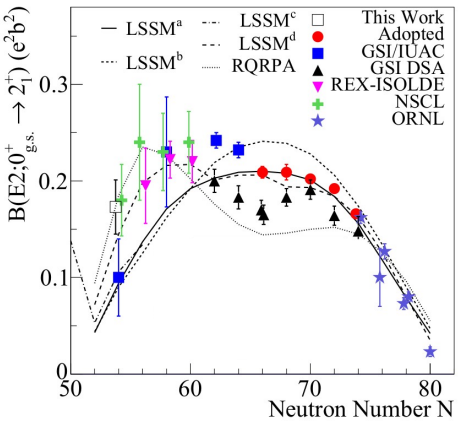

Figure 1.3: Evolution of the value for $B(E2, 0^+ \rightarrow 2^+)$ for the Sn isotopic chain as a function of N. Figure 4 from [46].

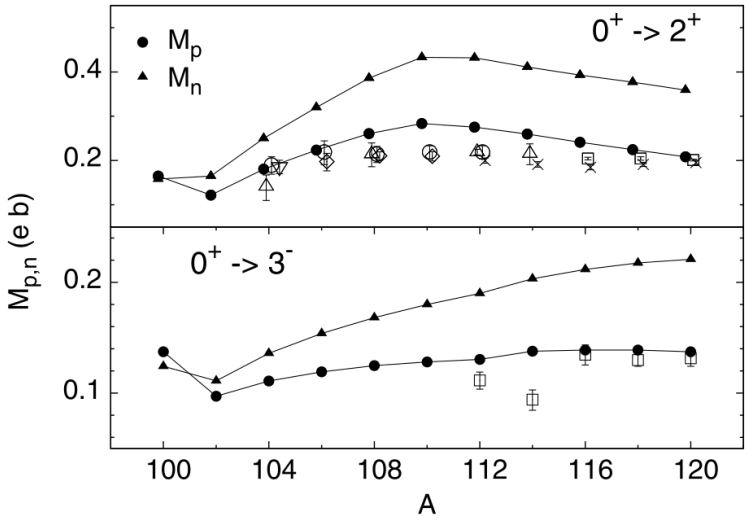

Figure 1.4: Evolution of the value for M_p and M_n for the Sn isotopic chain as a function of N. The black symbols are the results of QRPA calculations, while the white symbols are experimental values for M_p only. Figure 4 from [47].

In 1995, R. Schneider *et al.* have measured the half-life of ^{102}Sn, along with the first production and identification of ^{100}Sn [48]. One year later, M. Lipoglavšek *et al.* provide the first spectroscopy of the excited states of ^{102}Sn [49], as well as the first measurement of the half-life of the isomer of ^{102}Sn [50]. The level scheme of ^{102}Sn is then precised and completed by A. Corsi *et al.* [51] using in-beam γ ray spectroscopy and populating ^{102}Sn via two-neutron knockout. The half-life of the isomer has also been measured by H. Grawe *et al.* [52]. The level scheme of ^{102}Sn will be discussed in more details later, in section 3.2.4 and in chapter 4. As stated earlier, the first production and identification of ^{100}Sn was made by R. Schneider *et al.* [48]. The first measurement of the β decay of this isotope has then been performed in 1997 by K. Sümmerer *et al.* [53] using implantation. In 2012, C.B. Hinke *et al.* [54] studied the β decay of ^{100}Sn, with the highest statistics ever acquired for this isotope, providing indirect evidences for the persistence of shell closure at $N = Z = 50$.

The theoretical models shown in figure 1.3 do not manage to reproduce the evolution of the $B(E2, 0^+ \rightarrow 2^+)$ for the whole experimentally studied portion of the isotopic chain. In 2018, T. Togashi *et al.* used Monte Carlo shell model (MCSM) calculations capable of reproducing quite well the experimental $B(E2, 0^+ \rightarrow 2^+)$, as well as the experimental $E(2^+)$ [55]. This is shown in figures 1.5 and 1.6. One of the novelty of this approach is activating the $1g_{9/2}$ orbital instead of constraining it to remain full. This change enabled the aforementioned increase in $B(E2, 0^+ \rightarrow 2^+)$ at $N = 60$ to be reproduced by theoretical calculations.

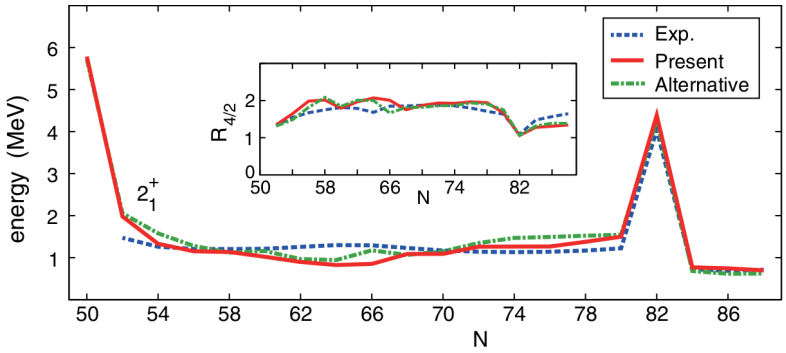

Figure 1.5: Comparison between the calculations of Togashi *et al.* [55] and the experimental values for $E(2^+)$ as a function of the neutron number N for the Sn isotopes. The solid red line is the model proposed by Togashi *et al.*, and the blue dashed line represents the experimental values. The inset is the ratio between $E(2^+)$ and $E(4^+)$.

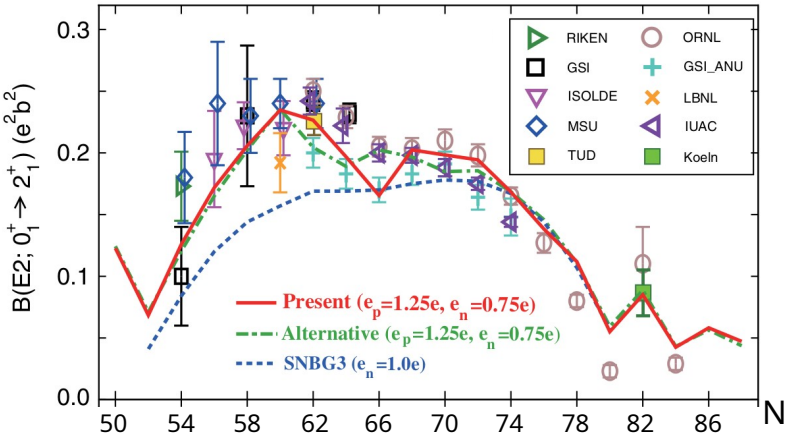

Figure 1.6: Comparison between the calculations of Togashi *et al.* [55] and the experimental values for $B(E2, 0^+ \rightarrow 2^+)$ as a function of the neutron number N for the Sn isotopes. The solid red line is the model proposed by Togashi *et al.*, and the markers are the experimental values.

In 2018, T.D. Morris *et al.* investigated through In-Medium Similarity Renormalization Group (IMSRG) and Coupled Cluster (CC) calculations the structure of ^{100}Sn [56]. This study also hints at the double magicity of ^{100}Sn and proposes several calculated values depending on the considered interaction for its $E(2^+)$, ranging from 4.19 to 5.51 MeV,

and $B(E2, 0^+ \rightarrow 2^+)$, ranging from approximately 0.05 to 0.12 e^2b^2. This is shown in figure 1.7.

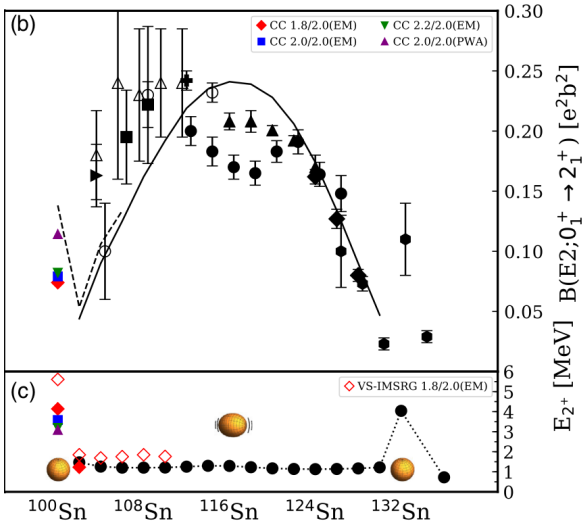

Figure 1.7: $E(2^+)$ (bottom) and $B(E2, 0^+ \rightarrow 2^+)$ (top) for the Sn isotopic chain. The black markers are the experimental data. The colored markers are the calculated values for ^{100}Sn and other light Sn isotopes proposed by Morris *et al.*. Figure from [56].

The ensemble of results presented here shows that uncertainties remain regarding the strength of the shell closure approaching ^{100}Sn. No measurements of the $B(E2, 0^+ \rightarrow 2^+)$ for ^{102}Sn and ^{100}Sn have been performed yet, for the beam intensities available worldwide for this type of experiment are at the limit. No spectroscopic information is available at all for ^{100}Sn. As highlighted by the two aforementioned studies, these data are the missing piece to confirm whether the shell closure in this area of the nuclide chart is softer than expected, as suggested by the data on ^{104}Sn.

This study presents the inelastic excitation of ^{102}Sn and the measurement of its cross-section. This quantity has also been measured for two other isotones of ^{102}Sn, namely ^{100}Cd and ^{98}Pd. This way the evolution of M_n/M_p will be accessible as a function of N, with the data provided in figure 1.4, but also as a function of Z. During the experimental campaign, Coulomb excitation of ^{102}Sn has also been performed, providing the first measurement $B(E2, 0^+ \rightarrow 2^+)$ for ^{102}Sn, and its analysis is assigned to another team in the collaboration. The following chapters will introduce the experimental setup as well as the data analysis. Eventually, the results will be exposed and discussed.

Chapter 2

Experimental setup

Contents

The experiment described in this work have been conducted at the Radioactive Isotope Beam Factory (RIBF) at the RIKEN Nishina Center for Accelerator-Based Science, Wakō, Japan. It consists in shooting a beam of ^{124}Xe on a primary target made of ^{9}Be. This collision creates a secondary beam composed of several isotopes, that will then hit either a plastic (CH_2) target or a ^{12}C target. The channel of interest for this study is the inelastic excitation of ^{102}Sn. The data from this reaction will then be compared to the inelastic excitation of two others $N = 52$ isotones: ^{100}Cd and ^{98}Pd.

One can divide the experimental apparatus in three parts. The beam is produced in the source and is accelerated towards the primary target. The resulting secondary beam then enters the BigRIPS separator, which role is to separate, select and identify the different fragments. This cocktail of isotopes then hits the secondary target, populating excited states via inelastic excitation, before entering the ZeroDegree spectrometer. The γ rays emitted with the deexcitation are detected by the DALI2 array surrounding the target. These elements can be seen in figure 2.1.

The experimental setup used for this experiment is described in this chapter, that will be divided in three parts. First, an overview of the beam production as well as the beam fragmentation will be proposed, followed by a description of the different detectors installed on the beam-line. Then, details will be given about the γ ray detector DALI2.

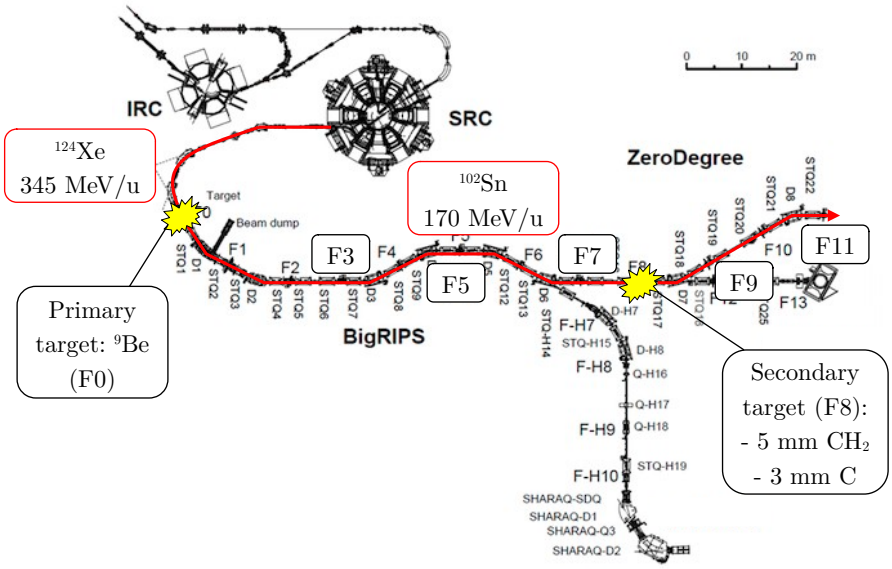

Figure 2.1: Schematic view of the BigRIPS-ZeroDegree beam-line at RIBF. IRC stands for Intermediate stage Ring Cyclotron, and SRC for Superconducting Ring Cyclotron. These are parts of the accelerators used before BigRIPS. The primary and secondary targets are indicated, as well as the primary and secondary beam energies. The position of the focal planes mentioned later in the present work are also indicated. Image from [57].

2.1 BigRIPS

The Radioactive Isotopic Projectile Separator (BigRIPS) is an in-flight beam separator used for the identification of the nuclei in the cocktail beam produced at the primary target, also called production target. Figure 2.2 shows a schematic view of the BigRIPS separator. It is composed of superconducting quadrupole triplets (STQ) and of room-temperature dipoles (RTD, simply abbreviated by D in figure 2.2). These magnets and their wide apertures offer a large acceptance to the beam-line, and as a result a great intensity. The beam is focused in foci noted F in figure 2.2.

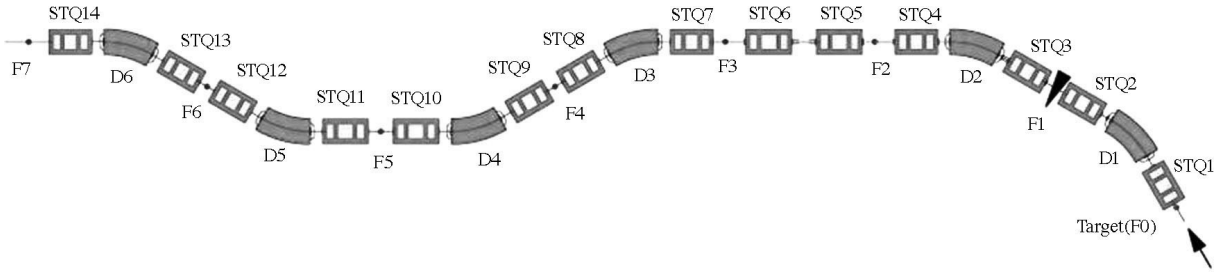

Figure 2.2: Schematic view of the BigRIPS separator. Image from [58].

The $B\rho$-ΔE-TOF method for fragment selection is used in BigRIPS. This method relies on the measurement of β, via the measurement of the time of flight (TOF) of each nucleus, combined with the measurement of the magnetic rigidity $B\rho$ and the energy loss ΔE. The measurement of these three quantities provides the value for the atomic number and the

mass of the nuclei in the beam through two equations. The first one is,

$$B\rho = \frac{A}{Q} \times \frac{u\gamma\beta}{c}, \tag{2.1}$$

with B the magnetic field, ρ the bending radius, β the relative velocity of the isotope, c the speed of light, $\gamma = \frac{1}{\sqrt{1-\beta^2}}$ the relativistic Lorentz factor, and u the atomic mass unit. The other one is the Bethe-Bloch formula [59],

$$-\frac{dE}{dx} = \frac{4\pi e^4 z^2}{m_0 v^2} nZ \left(\ln\left(\frac{2m_0 v^2}{I}\right) - \ln(1-\beta^2) - \beta^2 \right), \tag{2.2}$$

with $\frac{dE}{dx}$ the specific energy loss along the x-axis (also called linear stopping power), e the elementary charge, m_0 the electron mass, v the velocity of the isotope, n the atomic density, z the charge of the isotope, and I the average excitation and ionization potential of the absorber.

2.2 Beam-line detectors

2.2.1 PPAC detectors

Parallel Plate Avalanche Counter (PPAC) detectors [60] are used to measure the position of the beam on the XY-plane. This device is composed of two parallel plates, an anode and a cathode, connected to delay lines, with gas in between. Each plate measures 240x150 mm^2. When a particle crosses the detector, the gas is ionized and charges are released. They then drift to the plates where they are collected. The time difference between each end of the delay line multiplied by the velocity of the signal yields the position of the beam on the plate. One plate provides the horizontal coordinate, while the other provides the vertical one.

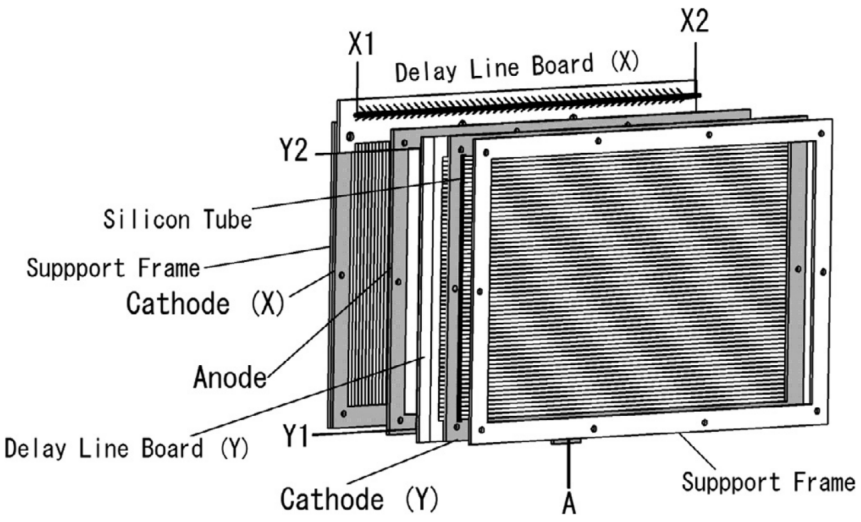

Figure 2.3: Schematic view of the PPAC detectors. Figure from [60].

2.2.2 Plastic scintillators

Plastic scintillators are used along the beam-line to measure the time-of-flight of the beam particles at various locations. The dimensions of those detectors can vary: 100x100 mm^2, 120x100 mm^2 or 240x100 mm^2 for their surfaces, 0.1, 0.2, 1.0 or 3.0 mm in thickness. For this application, polymers (polyvinyltoluene in the present case) are particularly interesting materials for scintillators. The output pulses of these devices are usually of the order of 2 ns in duration, which is ideal for time measurements. It is also rather easy to build molds that will give plastic scintillators any desired shape, and it makes it possible to have detectors with a large surface. These scintillators are mounted with photomultiplier tubes (PMT) to raise the output tension to hundreds of mV.

The plastic scintillators used at RIKEN are the EJ-212 and EJ-230, manufactured by ELJEN Technology. The PMTs are the H1949-50MOD manufactured by Hamamatsu Photonics.

2.2.3 MUSIC detectors

Two ionization chambers are used in the beam-line at focal planes 7 and 11, namely before and after the secondary target. These are MUltiple Sampling Ionization Chamber (MUSIC) [61]. The one at F7 is 586×300×364 mm^3, while the one at F11 is slightly larger with a size of 670×300×396 mm^3. These detectors are made of 12 anodes and 13 cathodes, tilted by 30°, each separated by 17 mm for the one at F7 and 20 mm for the one at F11, in a chamber filled with a mix of 90% of Ar and 10% of CH_4. A schematic view of the MUSIC detector is given in figure 2.4.

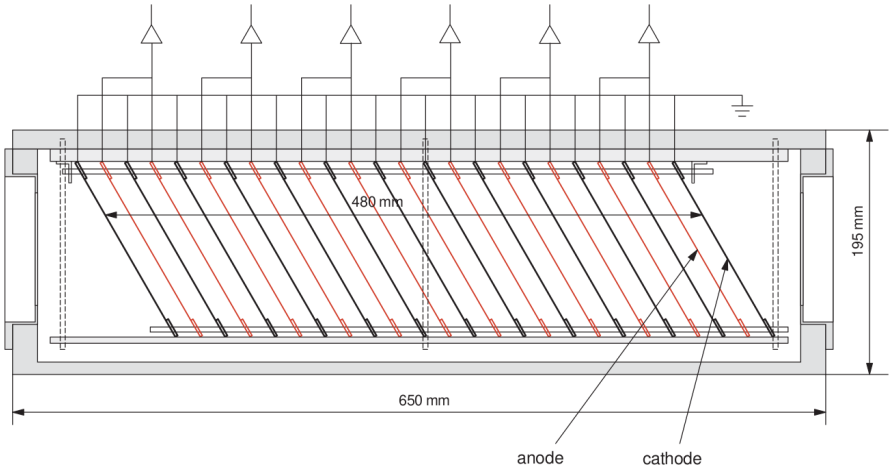

Figure 2.4: Schematic view of the MUSIC detector. Figure from [61].

When a nucleus from the beam goes through the chamber, the gas is ionized and the charges thus created drift towards the electrodes. Thanks to their angular tilt, the charges drift away from the beam to the closest electrode. The number of charges collected that way is proportional to the energy loss in the chamber. Using the Bethe-Bloch formula (equation (2.2)) together with an independent measurement of the velocity of the ions, the measurement of the energy loss yields the charge Z of the incident nucleus.

2.3 DALI2

DALI2 is the array of NaI(Tl) crystal scintillators used for γ ray detection at the secondary target [62]. It is composed of 226 NaI(Tl) crystals arranged in a flower pattern. This constitutes an upgrade from the original DALI2, composed of 186 crystals.

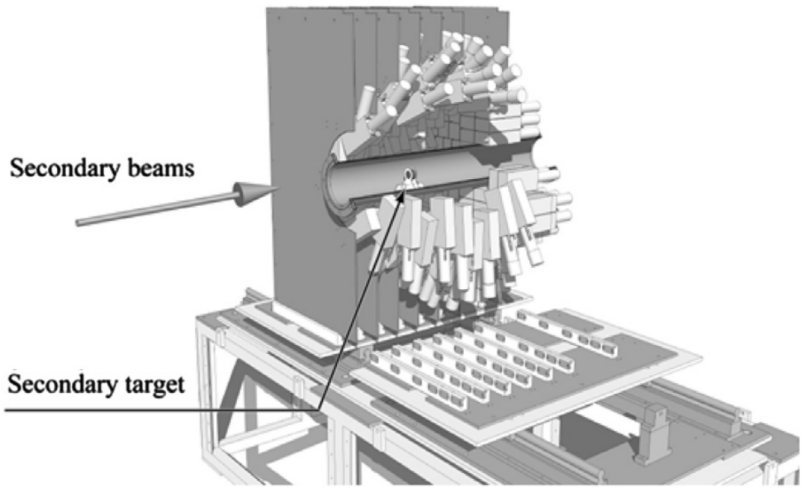

Figure 2.5: Schematic 3D view of the DALI2 array. The version of the DALI2 array shown here is only composed of 186 crystals. Figure taken from [62].

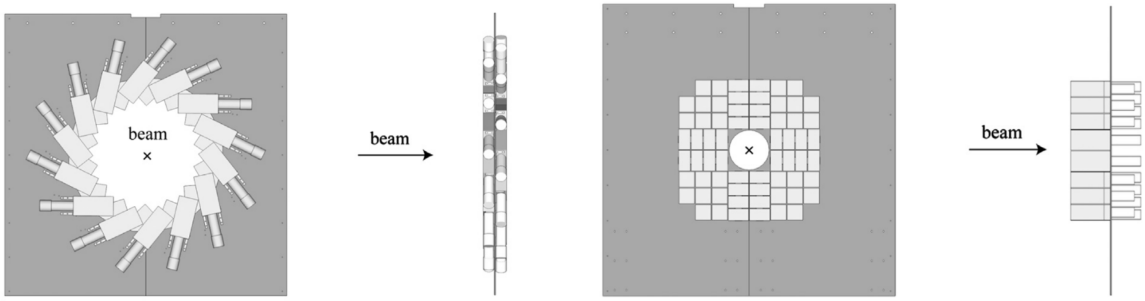

(a) (b)

Figure 2.6: Different sectional view of the DALI2 array. Both pictures are taken from [62]. (a) Schematic view of the DALI2 array for the layers before the target, at backward angles. (b) Schematic view of the DALI2 array for the layers after the target, at forward angles.

The position of each crystal is given in cartesian coordinates, with $\vec{z}$ being the axis with the same direction as the beam. Figure 2.6 shows that the crystals are organized in different layers going along $\vec{z}$. The crystals are also numbered along $\vec{z}$, the first ones being at the entrance of the detector, and the last ones at the end. The secondary target is placed in the cavity of the DALI2 array at $z = 0$.

Chapter 3

Data Analysis

Contents

In order to extract the inelastic excitation cross-sections of interest, the data acquired during the experiment have been processed. This analysis is presented in the following sections. The data have been first cleaned and calibrated, in order to reconstruct the γ energy spectra with maximized resolution and statistics, as shown in section 3.1. The cross-section is derived from the number of γ rays from the $2^+ \rightarrow 0^+$ transition detected in the DALI2 array. This number is estimated via a fit of the γ energy spectra using simulated response functions. This procedure is explained in section 3.2.

3.1 Calibrations

3.1.1 Particle identification

Particle identifications (PID) plots are essential to select the events of interest in the data, and hence the reaction channel of interest. PID plots are 2D histograms where Z,

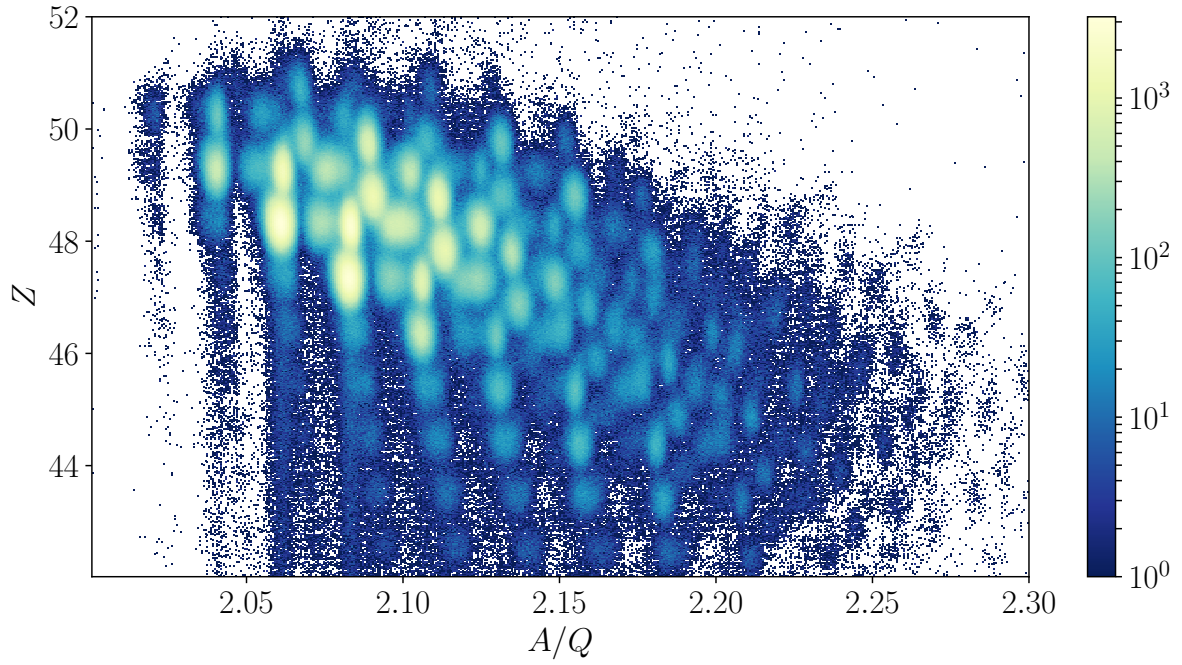

Figure 3.1: PID in the ZeroDegree spectrometer. The different quantities used for the x and y-axis are measured between focal planes 8 and 11, located right after the secondary target. This figure is made using a physics run on CH_2 target.

the atomic number of the isotope, is chosen as the y-axis and $\frac{A}{Q}$ as the x-axis, with A the mass of the isotope and Q the effective charge of the isotope. The choice of these physical quantities for the axis is linked to the $B\rho-\Delta E-$TOF identification method. This quantity is measured by the plastic scintillators in the beam line (see section 2.2.2) and yields the velocity of the isotopes,

$$v = \frac{L}{t_{\text{TOF}}} \quad \text{and} \quad \beta = \frac{v}{c} \tag{3.1}$$

with L the length between two plastic scintillators, t_{TOF} the time of flight. One can then plug β into equation (2.1) to obtain $\frac{A}{Q}$, and into equation (2.2) to obtain Z. The resulting plot can be seen in figure 3.1.

Charge state changes

The acceleration of the nuclei is such that the electrons surrounding those nuclei are removed, or stripped, from their orbitals. The energies at play in this experiment are high enough to leave the isotopes without any electron around them. In this case, one talks about fully stripped isotopes, and these constitute most of the radioactive beam. As a consequence, the accelerated nuclei are positively charged and the value of this charge is referred to as their charge state. However, the accelerated particles encounter various materials on their way such as the different targets or the different detectors. The interaction between an isotope and a given material can change this charge state, and thus have an impact on the various quantities measured along the beam line. Figure 3.2 shows the different changes in charge state that can occur in the beam line after the secondary target, considering the example of Sn for clarity. The 50^+ charge state corresponds to the fully stripped case when considering Sn, and 49^+ is when an electron is added to the

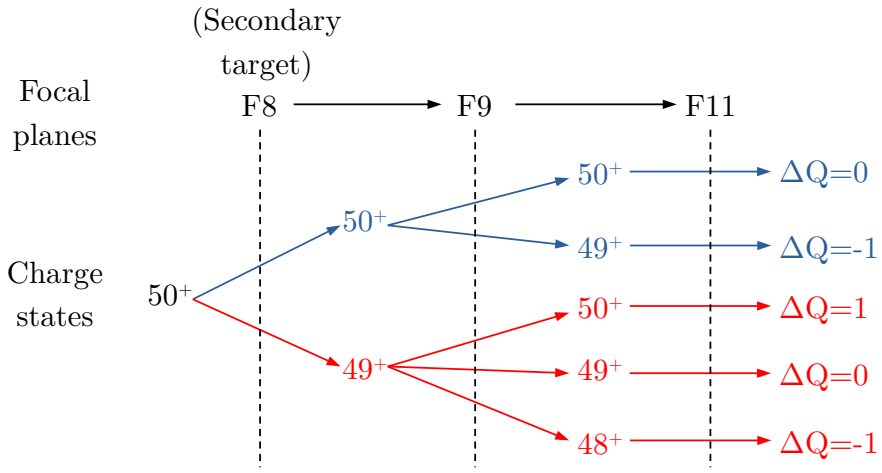

Figure 3.2: Schematic view of the different changes in charge state that can occur after the secondary target, in the case of Sn. ΔQ is the change in charge state after the ZeroDegree spectrometer.

system. The quantity ΔQ is the change in charge state. The different focal planes are visible in figure 2.1.

The different charge state changes are visible in the data, and are displayed in figure 3.3. Three different charge state changes can be seen there. The boxed area on the plot corresponds to an unchanged charge state in ZeroDegree, so $\Delta Q = 0$, as $B\rho_{F8-F9}/B\rho_{F9-F11} = 1$ for those events. As the isotopes are supposed to arrive fully stripped (without any electrons) to the secondary target, and assuming most of them remain fully stripped after the target, one can assume those events remain fully stripped in ZeroDegree. The spot that is more on the left has $B\rho_{F8-F9}/B\rho_{F9-F11} < 1$, which means that the isotopes have gone from charge Q to $Q+1$. With this same logic, the right spot is where the isotopes have gone from charge $Q+1$ to Q (or Q to $Q-1$).

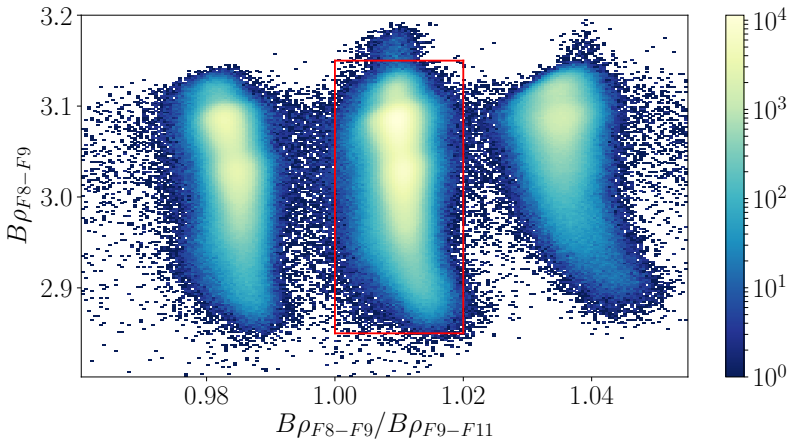

Figure 3.3: Histograms of the different charge states changes in the ZeroDegree spectrometer. The x-axis is the ratio between the magnetic rigidity between focal planes 8 and 9, and between focal planes 9 and 11. The y-axis is the magnetic rigidity between focal planes 8 and 9. The boxed area corresponds to an unchanged charge states through ZeroDegree. This figure is made using a physics run on CH_2 target for all nuclei in the secondary beam.

This change of charge state means that $Q \neq Z$. It also causes issues in the velocity measurement, as the magnetic rigidity changes in the middle of the spectrometer, which has an impact on the determination of Z. It leads to PID plots with blurry spots that are shifted in the $(\frac{A}{Q}, Z)$ plane with respect to the fully stripped isotopes. This can be seen in figure 3.4.

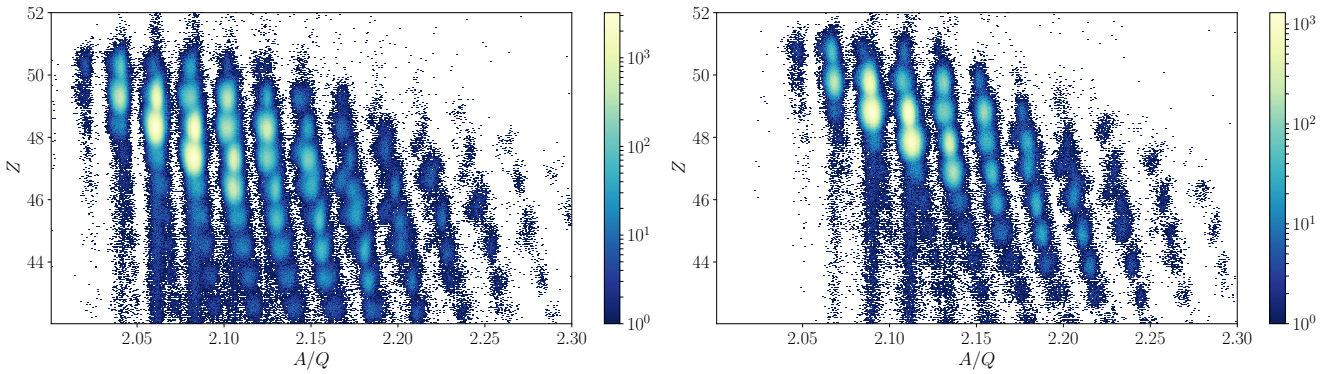

(a) (b)

Figure 3.4: PID in the ZeroDegree spectrometer, with different event selection on the charge states of the isotopes. One can note the improvement with respect to figure 3.1. The different quantities used for the x and y-axis are measured between focal planes 8 and 11, so right after the secondary target.This figure is made using a physics run on CH_2 target. (a) With a selection on the fully stripped isotopes (boxed area in figure 3.3). (b) With a selection on the left spot, corresponding to $\Delta Q = 1$.

This is why fully stripped events with no charge state changes are preferred. However, this selection is slightly detrimental to the statistics of the considered reaction channels, as a substantial part of the events are omitted. However, one can identify the desired isotopes on the PID drawn using only fully stripped isotopes, and then, as the PIDs for other charge states display the same pattern, identify the desired isotopes with other charge states. This way, with adjusted selections for the different PIDs, one can use the statistics of other charge states as well.

3.1.2 Further PID corrections

To select the events corresponding to the reaction channels of interest, a selection is applied based on the different spots displayed on the PID plot, as each of them corresponds to an isotope in the cocktail beam. To ensure the good quality of the final γ ray spectrum, it is necessary to make this selection as accurate as possible. To do so, one needs to make sure that each spot is not smeared out, and at its correct $(\frac{A}{Q},Z)$ coordinate. The following paragraphs describe the various corrections applied to the PID plot in order to optimize the isotope selection.

Correcting the energy loss measurement

The position in Z (a quantity which is determined from energy loss measurements) of the events on the PID plot shifts as the experiment progresses. A correctly calibrated Z at the beginning of the experiment may deteriorate at the end of it, and a time-dependent correction needs to be applied. This feature is suspected to come from gain drifts in

gaseous detectors used in the measurement of Z. The relationship between Z and the run number can be seen in figure 3.5.

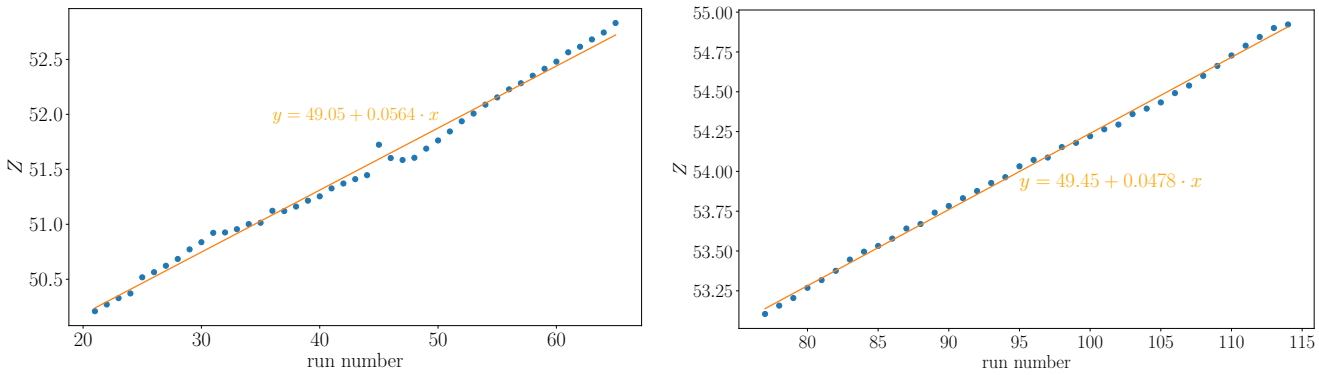

(a) (b)

Figure 3.5: Shift in Z as a function of the run number for CH_2 target and C target. The orange line is a linear fit of the shift. (a) For CH_2 target. The inelastic excitation run were numbered from 21 to 65 with this target. (b) For C target. The inelastic excitation run were numbered from 77 to 114 with this target.

For each inelastic excitation run file, the PID plot has been projected over Z, and a gaussian curve has been fitted over the resulting projection. Figure 3.5 displays the centroid given by this fit as a function of the run number. This trend is observed for all the nuclei in the secondary beam. This correction has been optimized for the ^{102}Sn channel, and therefore the projection shown in figure 3.5 is performed for this nucleus, which is on the $Z = 50$ line. A linear regression has then been performed (represented by the orange line). Using these regression coefficients, one can then correct and align the events at $Z = 50$.

Removing background events from the plastic scintillators

The plastic scintillators are used in the beam-line to measure the time of flight of the particles in the beam (see subsection 2.2.2). Each detector is mounted with one PMT at each side of it, in which the charge resulting from the scintillation is collected. It is then possible to link the charge collected in these tubes to the position of the incident isotope on the plastic scintillator. This relationship can be written as

$$\begin{aligned} q_1 &= q_0 \exp\left(-\frac{L+x}{\lambda}\right), \\ q_2 &= q_0 \exp\left(-\frac{L-x}{\lambda}\right), \end{aligned} \tag{3.2}$$

with q_1 and q_2 the signals from both PMTs, q_0 the charge left by the isotope in the plastic scintillator, L is the length of the scintillator, x the horizontal coordinate of the hit of the isotope on the scintillator, and λ the attenuation length of light in the scintillator (equation 8 in [63]). These expressions translate the attenuation that the signal undergoes while traveling through the scintillator. Combining these formulas, one can deduce x as

$$x = -\frac{\lambda}{2} \ln\left(\frac{q_1}{q_2}\right). \tag{3.3}$$

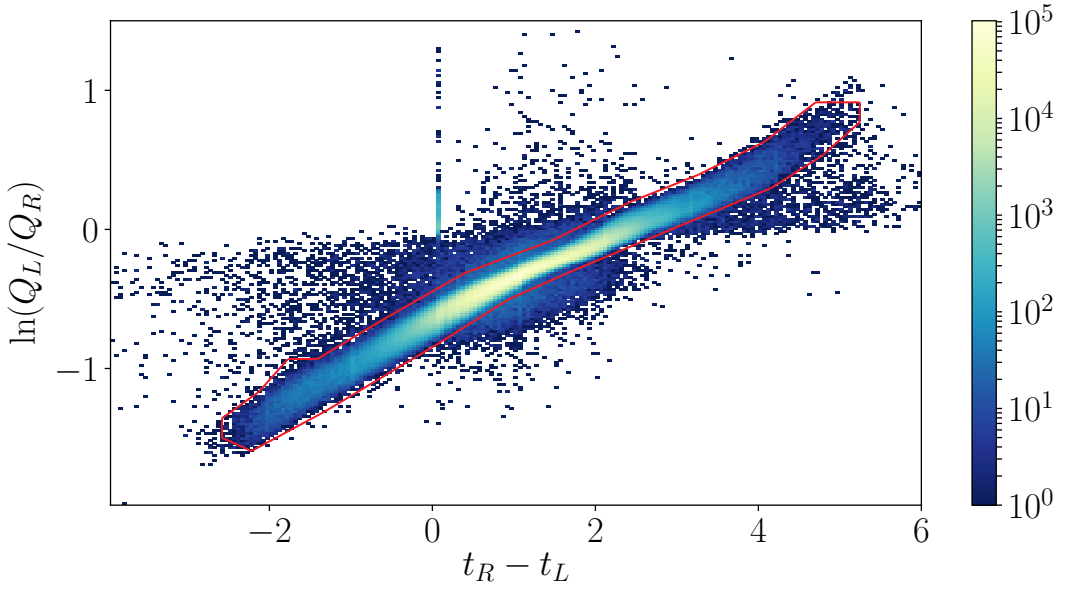

Figure 3.6: Correlation between $\ln\left(\frac{q_1}{q_2}\right)$ and $(t_2 - t_1)$ for the plastic scintillator at focal plane F8. The red line shows the selection of correlated events that has been made. The data are from an inelastic excitation run on CH_2 target.

It is possible to compute x in another way, considering the timing of the two signals detected in the PMTs, with the equation:

$$x = -\frac{V}{2}(t_2 - t_1), \tag{3.4}$$

with t_1 and t_2 the times when q_1 and q_2 respectively were detected by the PMTs, and V the velocity of the signal in the scintillator (equation 9 in [63]). Combining both expressions for x yields the following equality (equation 10 in [63]):

$$\lambda \ln\left(\frac{q_1}{q_2}\right) = V(t_2 - t_1). \tag{3.5}$$

After plotting $\ln\left(\frac{q_1}{q_2}\right)$ versus $(t_2 - t_1)$, all events must follow the correlation between these two quantities. The events outside of the correlation can then be discarded. Such a selection is done for focal planes F3, F7 (both before the secondary target), F8 (at the secondary target) and F11 (after the secondary target). An example of such a selection is shown for focal plane F8 in figure 3.6.

Improving $\frac{A}{Q}$ resolution

A critical quantity involved in the accurate selection of the isotopes of interest is the resolution of $\frac{A}{Q}$ for the PID plot. The good resolution of $\frac{A}{Q}$ in BigRIPS comes from the trajectory reconstruction, performed thanks to the various PPAC detectors (see subsection 2.2.1) used to measure the position of the beam around the focal planes. This resolution can then be enhanced using the ion-optical transformation between two focal planes [63]. The first-order terms of this transformation are corrected during the experiment by the accelerator team. Once this is done, the higher-order terms of the ion-optical transformation can be determined empirically using experimental data after the experiment, as

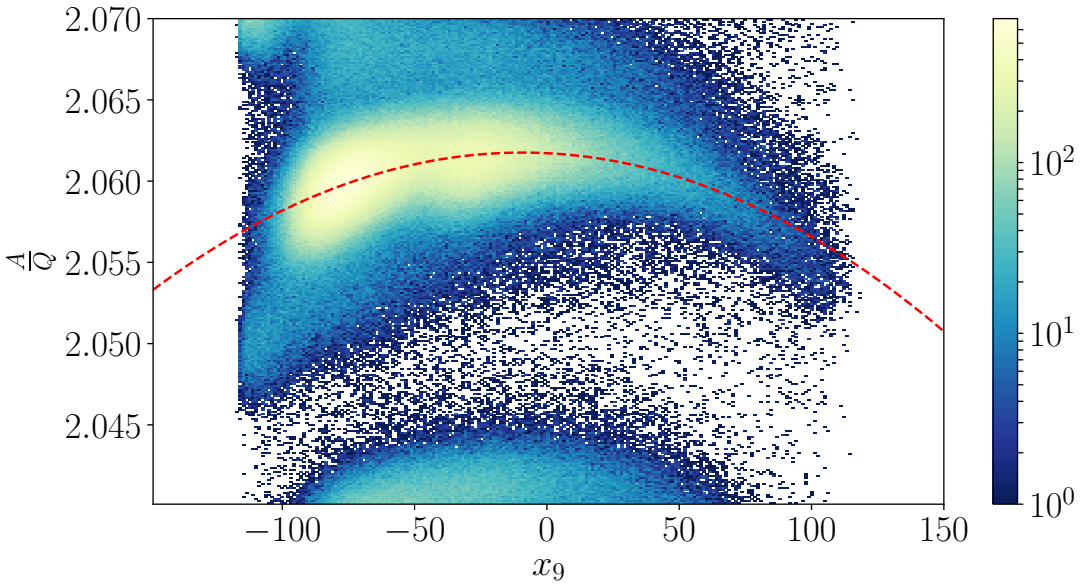

Figure 3.7: $\frac{A}{Q}$ as a function of x_9. The red dashed line shows the polynomial fit performed on the plot. The data corresponds to an inelastic excitation run on CH_2 target.

stated in [63]. Taking as an example the transformation between focal planes F9 and F11, one can write $\frac{A}{Q}$ as

$$\begin{aligned}\frac{A}{Q} =&\alpha_0 + \alpha_1 x_9 + \alpha_2 x_9^2 + \alpha_3 x_9^3 + \alpha_4 a_9 + \alpha_5 a_9^2 + \alpha_6 a_9^3 \\ &+\alpha_7 x_{11} + \alpha_8 x_{11}^2 + \alpha_9 x_{11}^3 + \alpha_{10} a_{11} + \alpha_{11} a_{11}^2 + \alpha_{12} a_{11}^3,\end{aligned} \tag{3.6}$$

with x_9 and x_{11} being respectively the x coordinate of the beam at F9 and F11, a_9 and a_{11} the angle of the beam projected on the x-axis at F9 and F11 and α_i being scalars. To determine the α coefficients, $\frac{A}{Q}$ is plotted as a function of the different terms of equation (3.6). A fit using a third-degree polynomial is then performed as illustrated in figure 3.7 with the example of x_9. This procedure needs to be repeated for each contribution, here x_9, x_{11}, a_9 and a_{11}. Once the polynomial coefficients have been obtained, it is possible to correct $\frac{A}{Q}$. The result of this correction can be seen in figure 3.8.

Removing pile-up events

The charge Z in BigRIPS is determined using the ionization chamber. This detector is subject to pile-up, which occurs when two charges arrive simultaneously at the detector. This yields a signal with a reconstructed charge equal to the sum of the impinging charges. These events end up creating noise in the PID plot, and as a result in the γ ray spectra. To remove these events, one can determine Z in a way that is not subject to pile-up. This is done using the velocity and magnetic rigidity measured in the focal plane 3, 5 and 7. The energy of a given nucleus in BigRIPS is given by:

$$E = (\gamma - 1)uA, \tag{3.7}$$

with u the atomic mass unit, A the number of nucleons and γ the Lorentz factor. The velocity is given between two focal planes. As a result, one can define the two velocities β_{35} and β_{57}, the velocity between focal plane 3 and 5, and between focal plane 5 and 7

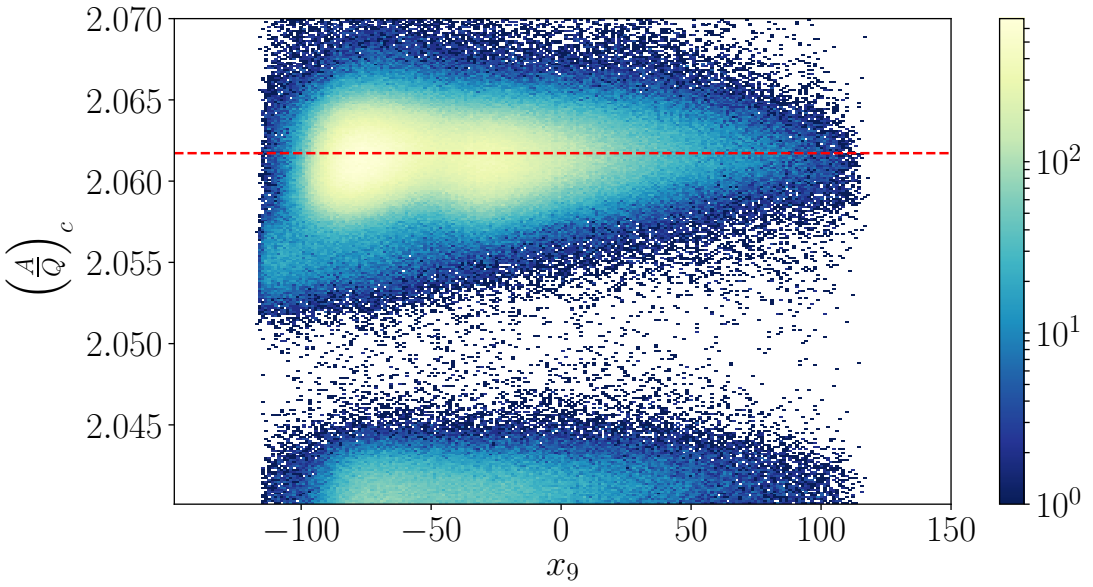

Figure 3.8: $\left(\frac{A}{Q}\right)_c$ as a function of x_9. The subscript c stands for "corrected". The red dashed line shows the remaining offset α_0 once the higher order contributions have been eliminated. The data used is the same as in figure 3.7.

respectively. From there, one can also define γ_{35} and γ_{57}. One can now write the energy difference ΔE between these two segments of BigRIPS:

$$\Delta E = (\gamma_{35} - \gamma_{57})uA. \tag{3.8}$$

Plugging this quantity in equation (2.1) and in the Bethe-Bloch formula (equation (2.2)) yields:

$$Z_{B\rho} \propto \left(\frac{B\rho_{35}}{\beta_{35}} - \frac{B\rho_{57}}{\beta_{57}}\right)\left(\frac{\beta_{35} + \beta_{57}}{2}\right)^2. \tag{3.9}$$

This charge measured using the magnetic rigidity, noted $Z_{B\rho}$, is not affected by pile-up. If, for a given event, the charge measured with the ionization chamber, simply denoted Z, matches the value of $Z_{B\rho}$, the event is not affected by pile-up. Representing the (Z,$Z_{B\rho}$) provides an event selection removing pile-up events. This can be seen in figure 3.9.

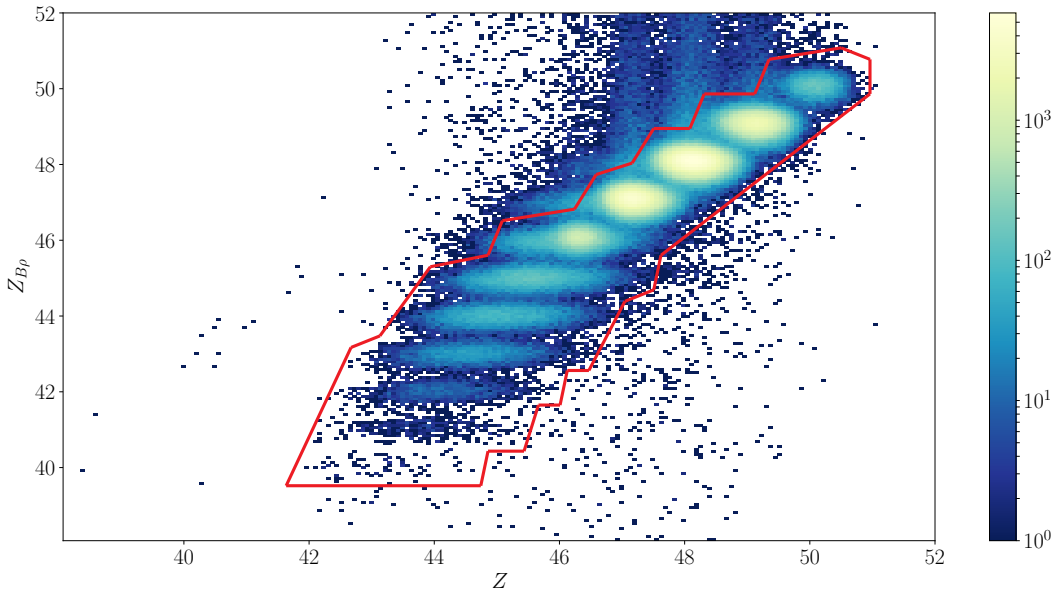

Figure 3.9: $Z_{B\rho}$ as a function of Z. The events outside the area delimited by the red solid line are considered pile-up events.

Final PID and channel selection

All these aforementioned corrections are applied to the A/Q and Z of each event. As a result, the spots corresponding to each nucleus in the PID plot are better separated, making the reaction channel selection easier and more precise. The fully corrected PID plot for the incoming beam can be seen in figure 3.10a. The PID plot for outgoing fragments are also shown in figure 3.10b, 3.10c and 3.10d with a selection on the incoming beam isotones of interest. The outgoing events corresponding to the inelastic excitation channels are also shown. As each nucleus is well separated, the selectivity on the data is increased.

3.1.3 Energy calibration

In order to extract the energy of the γ rays emitted during the deexcitation, each crystal of the DALI2 array has been calibrated in energy. The calibration runs have been performed before the runs for inelastic excitation, at the target change, and after the runs for inelastic excitation. To compute the calibration coefficients, the γ peaks of the raw ADC emission spectra of known sources are fitted using a Gaussian function with a second-degree polynomial background. The spectra are built for each crystal and as a consequence, the calibration coefficients are computed for each crystal. The radioactive sources that have been used are:

- ^{137}Cs, with a γ peak at 661.66 keV.
- ^{60}Co, with two γ peaks at 1173.24 keV and 1332.50 keV.
- ^{88}Y, with a γ peak at 1836.06 keV.

The centroid of each fitted Gaussian peak is then extracted and plotted as a function of the aforementioned γ peaks energy. The relation between raw ADC channels and energies

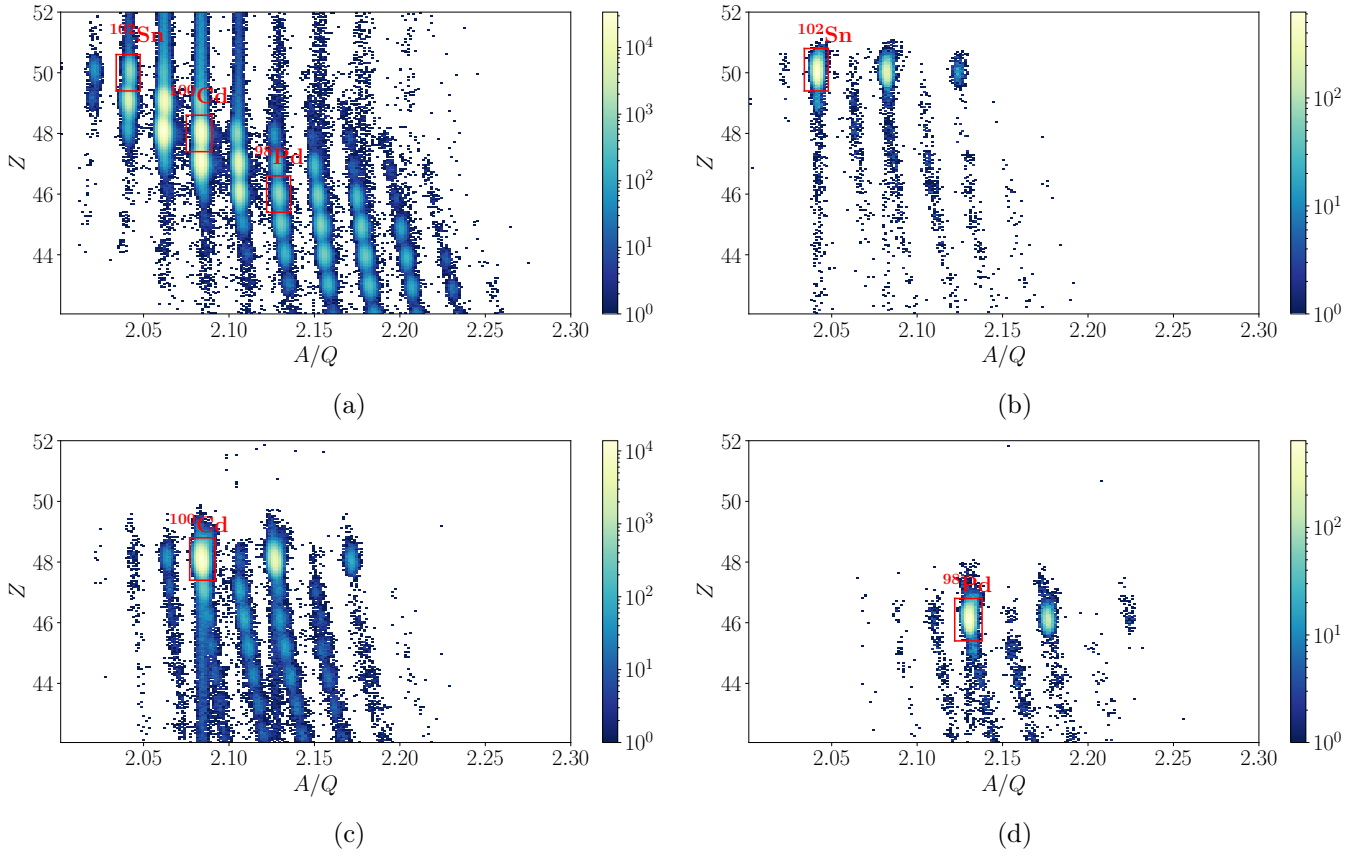

Figure 3.10: Fully corrected PID plots. The isotones of interest are indicated to show the possible channel selection. The data of this plot are for one run on CH_2 target. (a) PID plot with A/Q and Z for the beam nuclei. The three isotones of interest are indicated. (b) PID plot with A/Q and Z for the fragments, with ^{102}Sn impinging on the target. The outgoing ^{102}Sn events are indicated. (c) PID plot with A/Q and Z for the fragments, with ^{100}Cd impinging on the target. The outgoing ^{100}Cd events are indicated. (d) PID plot with A/Q and Z for the fragments, with ^{98}Pd impinging on the target. The outgoing ^{98}Pd events are indicated.

is linear, which yields two calibration coefficients for each NaI crystal. An example of such a calibration is given in figure 3.11.

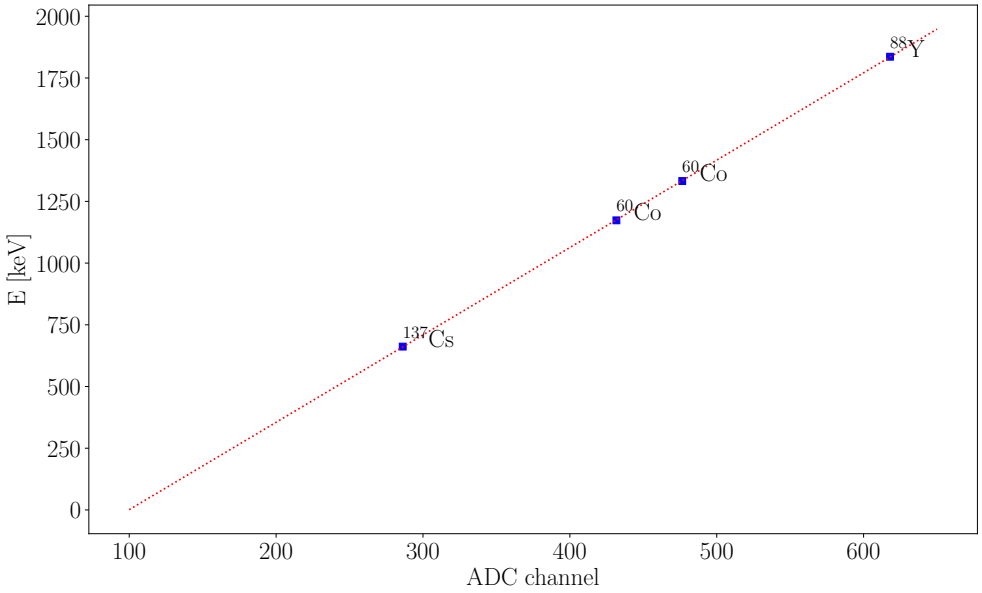

Figure 3.11: Example of energy calibration of DALI2 for crystal 56.

The calibration during target change is the only one that used the ^{137}Cs. In addition, as the detectors are exposed to the beam, the calibration coefficients slightly vary. The advantage of using the calibration at the target change is that the coefficients will be correct for both sets of inelastic excitation runs, which is why this calibration run has been used for the determination of the calibration coefficients of all the physics runs. The difference in calibrated energies yielded by the various calibration runs falls within a range of 10 keV, which guarantees that all calibration runs provide similar calibrations anyway.

After applying the calibration to the raw ADC spectra of the sources, one can compare the newly obtained experimental energies with the tabulated values of the γ peaks, to check the quality of the calibration. This is done through the quantity,

$$\Delta E = E_{cal} - E_{tab} \tag{3.10}$$

with E_{cal} the calibrated experimental energy and E_{tab} the tabulated energy. Figure 3.12 shows ΔE as a function of the detector id for each radioactive source.

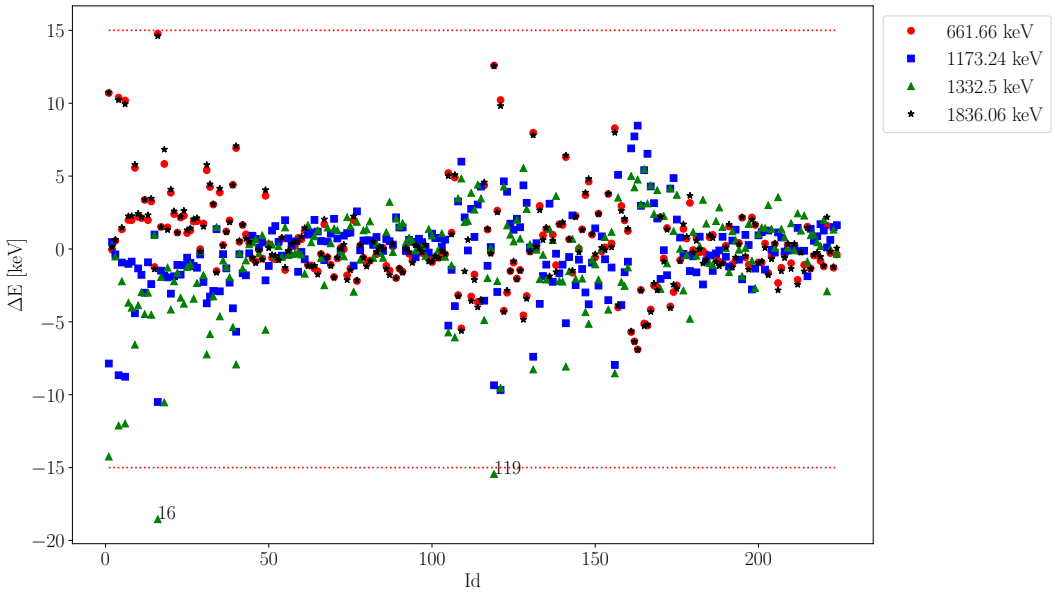

Figure 3.12: ΔE in keV as a function of the detector id for each radioactive source used in the calibration. The two red dotted line show the interval [-15keV;15keV].

In figure 3.12, one can remark that all crystals except crystal 16, 119 and 111 (that has a ΔE outside the figure for ^{137}Cs) have their ΔE between -15 keV and 15 keV. This is rather satisfactory as 15 keV is smaller than the typical size of the bins used in the experimental γ spectra. One can also notice a block structure in this plot. Detectors 1 to 50 have on average a larger ΔE than detectors 50 to 100. The same disparities can be seen with detectors 100 to 185 and with detectors 185 to 226. This repartition is not accidental and is linked to the organization of the NaI in the array, as described in section 2.3. The target is at $z = 0$, which corresponds to the crystals 33 to 66. Therefore, the newer and more accurate crystals were put around the secondary target, which is where most of the γ rays will be detected. The NaIs at the end of DALI2 are also more accurate on average because they are the new crystals added to upgrade the array from 186 crystals to 226 crystals.

3.1.4 Determination of the resolution

The resolution of the DALI2 detector is determined crystal by crystal, as it is complicated to define a resolution for the overall array. From the previously mentioned fit of the photopeaks yielded by the calibration sources (see subsection 3.1.3), the width of the said photopeaks is extracted and plotted against the energy. It is then fitted by a function with the following shape:

$$r(E) = a \cdot E^b, \tag{3.11}$$

with r the resolution for a given crystal, E the energy, and a and b the free fit parameters. An example of such a fit is given in figure 3.13.

3.1.5 Doppler correction

In the case of inelastic excitation in inverse kinematics, the beam is composed of the studied exotic nucleus, which is then excited at the target, and deexcites itself via the

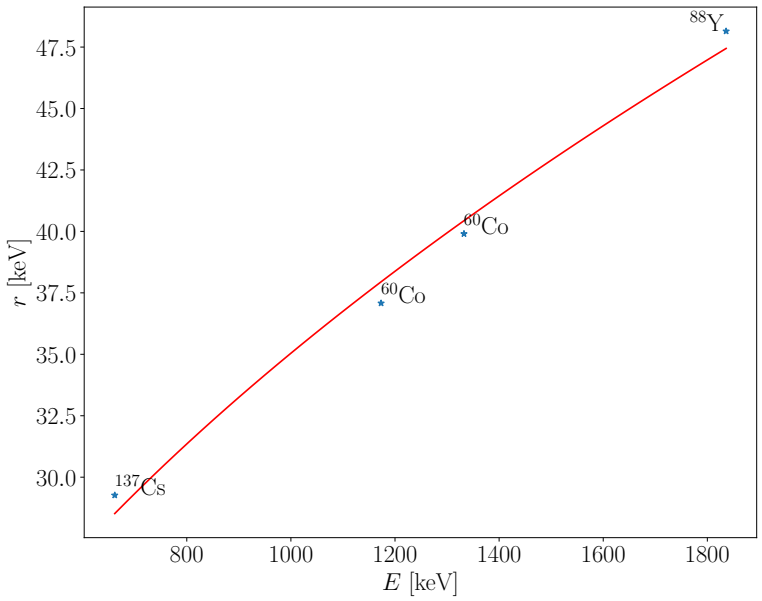

Figure 3.13: r in keV as a function of the γ energy in keV. The red line is the fit with the function of equation (3.11).

emission of a photon. The considered nucleus then becomes a moving source of radiations, and is as a result affected by the Doppler effect, which changes the frequency, hence the energy, of the detected γ ray. The magnitude of the effect depends on the velocity of the source, which in this case is relativistic, and on the position of the receiver, which in this case is the hit crystal of the DALI2 array. The formula relating the detected and the actual γ ray energies is:

$$E_{CM} = \frac{1 - \beta \cos(\theta)}{\sqrt{1 - \beta^2}} E_{lab}, \tag{3.12}$$

with E_{CM} the energy in the center of mass, which is the desired energy of the emitted photon, E_{lab} the energy in the frame of the laboratory, which is the detected energy, β the reduced velocity of the nucleus, and θ the angle between the γ ray and the ejectile. Some targets are built with a tracking system to precisely reconstruct the position of the reaction vertex. This is the case of the MINOS target, introduced in details in section 7.2. No such system was installed in this experiment. The position of the emission vertex was then assumed to be in the middle of the target, and the angles for the DALI2 crystals were then computed from this position to the barycenter of the interaction in the crystal (simulated with the SHOGUN package, detailed in subsection 3.2.1).

The velocity of the impinging nucleus has been measured before and after the target. The beamline detectors and their positions, as well as the velocity before the target, have been set as inputs in the LISE++ software [64], which has then been used to compute the velocity via the energy loss in the middle of the target. The same was performed with the velocity after the target as an input for consistency. This energy loss was then applied to each event, providing the velocity of the impinging nucleus in the middle of the target. In the end, the average of the velocities reconstructed with this procedure, using the measurement before the target and after the target, has been used for the Doppler correction of each event.

The reaction vertex and the γ emission vertex are considered the same in this study,

which is true (or at least a good approximation) for short-lived excited states. If the half-life of the excited state is long enough, both vertices are then in different positions, which will cause an imperfect Doppler correction. The exotic nuclei hitting the reaction target travel in the beam-line at approximately half the speed of light. At this velocity, a half-life of 300ps is equivalent to half of the γ rays emitted 5 cm after the target. This will cause broader photopeaks that are shifted towards low E_γ. This phenomenon is taken into account and is exemplified in subsection 3.2.5.

3.1.6 Addback procedure

In addition to the Doppler correction, an addback procedure is applied to the data. A γ ray hitting a DALI2 crystal can be affected by several effects. It can be absorbed by the photoelectric effect, which yields one signal with the full γ energy in the hit crystal. It can produce a positron-electron pair. The annihilation of the created positron can then produce two γ rays of 511 keV each. One or both of these photons can be absorbed, via photoelectric effect, or exit the crystal. But the dominant effect for the considered range of γ energy ($\sim$1MeV) is the Compton effect, as shown in figure 3.14.

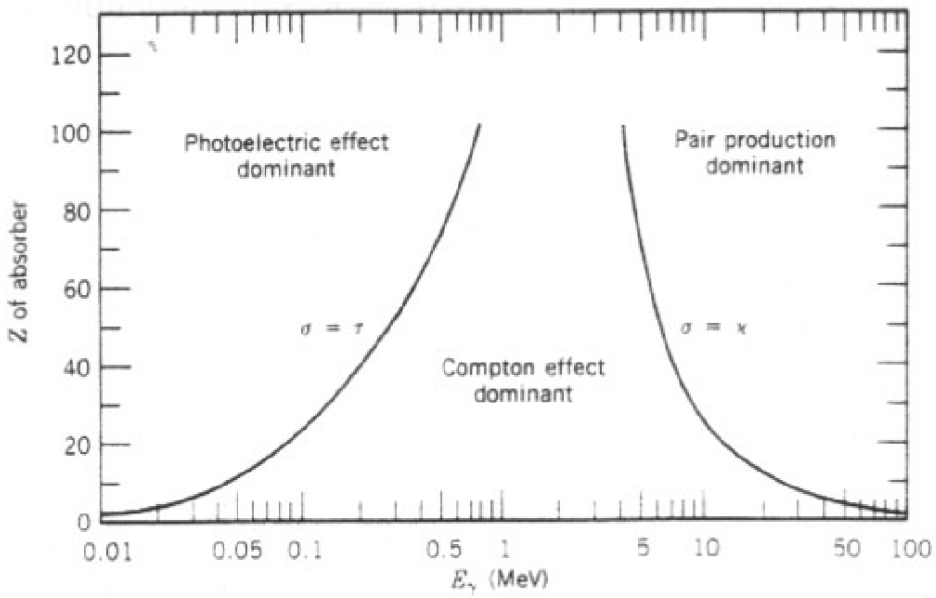

Figure 3.14: Atomic number of the nucleus used to detect the γ rays as a function of γ ray energy. Areas are delimited to indicate the dominant interaction between a γ ray and an NaI crystal. Figure from [65].

Compton scattering is the scattering of the emitted γ ray on an electron of the crystal. The energy transferred to the electron is then detected, and the scattered photon can either be absorbed or leave the crystal, yielding an incomplete energy reconstruction in the crystal. But as the DALI2 detector is an array of detectors, this scattered photon can hit a neighboring crystal and undergo the same interactions as the one previously described. This situation is represented in figure 3.15.

One can then look for simultaneous signals in neighboring crystals in a given radius, noted R_{ab} in figure 3.15. Summing up the energy deposited in these crystals will reconstruct

the total energy of the emitted γ ray. This procedure is called the addback procedure, and for this work, R_{ab}=20 cm.

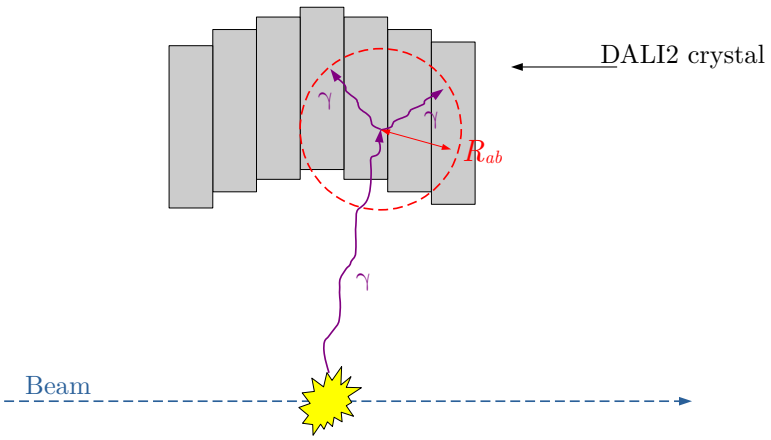

Figure 3.15: Schematic view of the Compton diffusion, yielding signals in neighboring DALI2 crystals. R_{ab} is the addback radius.

3.2 Cross-sections

3.2.1 Fitting principles

As explained in the previous paragraph, fitting the γ energy spectra is necessary to access the number of γ rays emitted as a result of inelastic excitation. Equation (3.38) shows the shape of the response function used to reproduce the γ energy spectrum, and from it two aspects of this procedure can be distinguished.

First, the response functions g_i must be as close to the real energy spectrum produced in the experimental conditions of this study as possible. This then requires to simulate accurately the interaction of the γ rays produced by the excitation of isotopes on a target with DALI2. This has been done using a GEANT4-based [66] simulation package developed by P. Doornenbal at the RIKEN Nishina Center called SHOGUN. An example of simulation of inelastic excitation reactions on ^{72,74}Ni and ^{76,80}Zn can be found in [67].Then, one needs to adjust each coefficients p_i, as well as the parameters of $B(E)$, to match as precisely as possible the experimental data points. A χ^2 minimization code is used to fit these coefficients. The different steps of both the simulation and the minimization are described in the following subsections.

Another way of computing the number of γ rays emitted as a result of inelastic excitation would be by integrating the gaussian photopeaks and adjusting with detection efficiency and acceptance effects. However, choosing the integration boundaries in such a procedure is rather arbitrary, and counting more or less γ rays corresponding to a given transition changes the final value of the desired cross-section. With the different steps briefly described in the previous paragraph, and detailed hereafter, no quantities are arbitrarily fixed. Transition contributions depends on the value of χ^2, and other contributions, like carbon excitation or isomer deexcitation, are fixed by physical constraints. Those constraints are also explained in the following subsections.

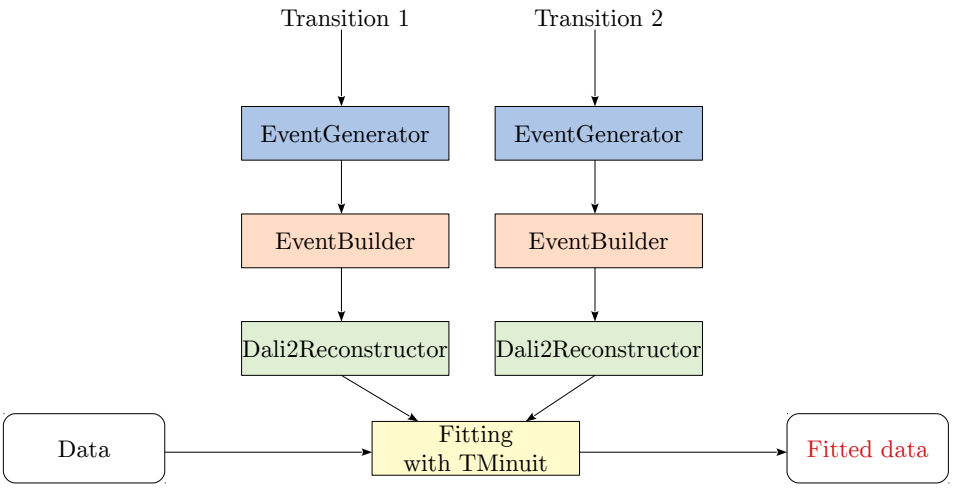

Figure 3.16: Schematic view of the workflow used in the SHOGUN simulation package.

Simulating with SHOGUN is a process divided in three parts: generating events, building events and reconstructing events. A flowchart summarizing the interaction between these three parts and the minimization procedure can be seen in figure 3.16. Each considered transitions are first generated. Physical observables, such as the velocity and energy distributions, are created according to the input level scheme for the considered isotope, the considered reaction, the beam parameters, and the target parameters. The interaction between the emitted γ rays and the crystals from the DALI2 spectrometer is simulated in the event builder. The resolution in energy for each crystal, the resolution of β and the precision on the position of each NaI crystal are taken as input parameters by the builder. It provides as an output the interaction vertex and the emission vertex (that are different in case of a transition with a non-zero half-life), as well as the time spectrum, and the energy deposited for each simulated crystal. With this information, the reconstructor reproduces the treatment that is done on the experimental data. Taking as an input the velocity used for the Doppler correction, the different options regarding the addback procedure, and the energy threshold of the DALI2 crystals, it yields as an output the response function for the considered transition, and concludes the simulation stage. Once the response function for all transitions, and additional contributions (such as carbon excitation and isomer contribution, detailed in subsections 3.2.3 and 3.2.4), have been simulated, they are fitted to the experimental energy spectrum via the TMinuit package included in ROOT. TMinuit is the transcription in C++ of the MINUIT program [68], initially written in FORTRAN. Fitting the γ energy spectra is done by minimizing the value of a χ^2 function defined as [69]:

$$\chi^2 = \sum_{i=1}^{N} \left(\frac{d_i - f(E_i)}{\sigma_i} \right)^2 = \sum_{i=1}^{N} \frac{(d_i - f(E_i))^2}{d_i}, \tag{3.13}$$

with N the number of bins on which the fit is performed, $f(E_i)$ the expected value of the data point d_i, and σ_i the uncertainty on d_i. In the case of counting events measured by

a NaI crystal, $\sigma_i = \sqrt{d_i}$. Combining equation (3.13) with equation (3.38), one gets

$$\chi^2 = \sum_{i=1}^{N} \frac{\left(d_i - B(E_i) - \sum_j p_j g_j(E_i)\right)^2}{d_i}. \tag{3.14}$$

χ^2 is then minimized through the free parameters p_j using the MIGRAD from the TMinuit package.

The previous paragraphs propose an overview of the fitting principles used to extract the desired cross-sections. The simulation of the transitions in the level scheme of the considered isotopes have been explained. Other contributions, namely the excitation of carbon and the deexcitation of isomer states, have been mentioned several times without further details. These contributions are presented in the two following subsections.

3.2.2 Background contribution

The background contribution for inelastic excitation γ energy spectra is the consequence of several phenomena. The main cause is bremsstrahlung: the high-Z isotopes of the beam knock out some electrons in the target, that are then slowed down in the material. This phenomenon causes the emission of mostly low-energy photons. The high-energy background is due to the excitation of high-energy states, that are below the proton separation energy, in a given isotope. These contributions are taken into account in an effective way, and the following shape has been used for the background function:

$$B(E) = \exp(b_1 + b_2 E) + \exp(b_3 + b_4 E). \tag{3.15}$$

This B function is the same as in equation (3.38), and the b_i parameters are fitted to the spectra. These background effects are very hard to take into account analytically, which is why the double exponential function is preferred. However, it is possible to apply the background fitted for a given isotope to another isotope, using some normalization coefficients for the low energy bremsstrahlung contribution. The b_1 and b_2 coefficients have then been fitted on the channel with the highest statistics, ^{100}Cd in that case, and applied to the two other nuclei of interest. Since the cross-section for bremsstrahlung depends mainly on the squared atomic number Z^2 of the incident particle and target, and the statistics of the studied reaction channels being different, the normalization coefficient used for the low energy background is:

$$B_b(E,^{102}\,\mathrm{Sn}) = \frac{Z(^{100}\mathrm{Cd})^2}{Z(^{102}\mathrm{Sn})^2} \cdot \frac{N(^{102}\mathrm{Sn})}{N(^{100}\mathrm{Cd})} B_b(E,^{100}\,\mathrm{Cd}), \tag{3.16}$$

when applying ^{100}Cd background to ^{102}Sn, in the case of a given target [70]. $Z(^{100}\mathrm{Cd})$ (respectively $Z(^{102}\mathrm{Sn})$) is the atomic number of ^{100}Cd (^{102}Sn), $N(^{100}\mathrm{Cd})$ ($N(^{102}\mathrm{Sn})$) is the number of events with incoming and outgoing ^{100}Cd (^{102}Sn), and $B_b(E,^{100}\,\mathrm{Cd})$ ($B_b(E,^{102}\,\mathrm{Sn})$) is the bremsstrahlung background obtained for ^{100}Cd (^{102}Sn), namely one of the two exponential in $B(E)$. Using the same normalization, it is also possible to apply the background for ^{100}Cd to ^{98}Pd. Transposing the high energy background from one isotone to another is however not possible in such a simple manner. This is due to the fact that the proton separation energy S_p for the three considered nuclei are quite different: 6.01(4) MeV for ^{98}Pd, 4.771(6) MeV for ^{100}Cd, and 3.68(10) MeV for ^{102}Sn [71].

Thus, the energy levels below S_p are due to structural properties that are different from one nucleus to the other. The amplitude for the high energy background, given by b_3 with the notations of equation (3.15), is as a result left free, and is fitted for every considered reaction channel.

3.2.3 Carbon excitation

As the beam of radioactive isotopes passes through the CH_2 or carbon target, it is possible to excite the carbon nuclei in both targets. The first excited state of ^{12}C is a 2^+ state at 4439.82(21)keV [72]. It is then possible to populate this state and the γ peak resulting from the $2^+ \rightarrow 0^+$ transition. This peak is visible in figure 3.17.

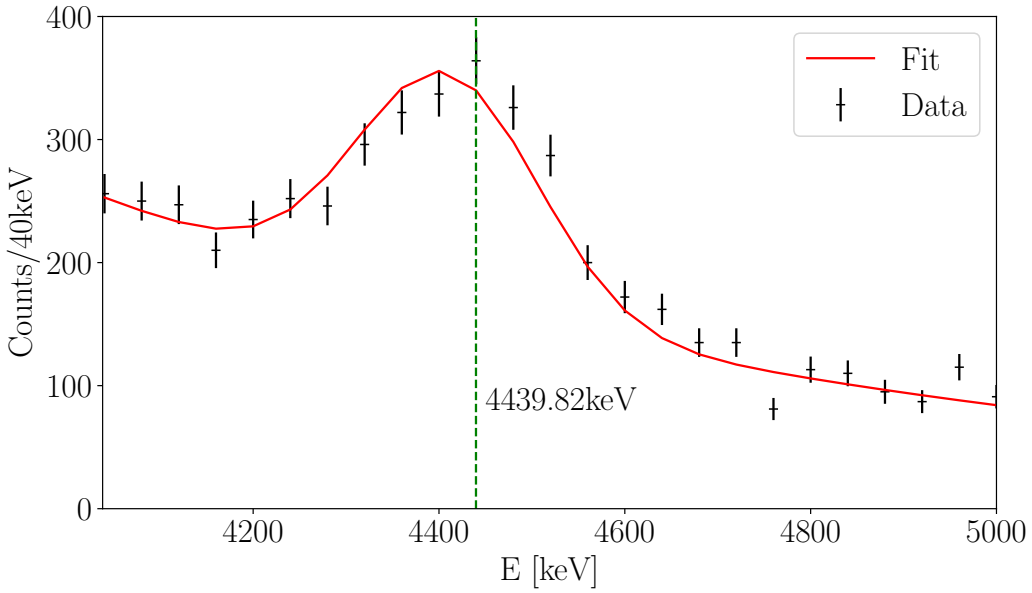

Figure 3.17: Energy Spectrum of ^{100}Cd. This spectrum is computed without Doppler correction. The fit is performed using a Gaussian curve superimposed to an exponential background.

Unlike ^{102}Sn, ^{100}Cd or ^{98}Pd, that are moving sources of γ rays in this experiment, ^{12}C is immobile in the laboratory reference frame. The peak mentioned previously is then only visible on the spectrum if no Doppler correction is applied. After Doppler correction, the γ peak will be smeared out and add a background contribution to the Doppler-corrected spectra of the isotopes of interest. As a consequence, the simulation of the excitation of ^{12}C needs to apply Doppler correction to this peak and reproduce this smearing effect. The simulated response function for carbon excitation is displayed in figure 3.18.

3.2.4 Isomer contribution

Both ^{100}Cd and ^{102}Sn have isomer states. The isomer of ^{100}Cd is an 8^+ state with an energy of 2548.2(18) keV and a half-life of 62(6) ns [73]. The one of ^{102}Sn is a 6^+ state of 2057 keV with a half-life of 367(11) ns [52]. The deexcitation of these states provides a background contribution that needs to be taken into account in the fit of the spectra. Indeed, after the primary target, the produced isotopes can either be in their ground state or in an excited state, one of them being the isomer state. As the half-life of isomer states is rather long (the distance between the primary and the secondary targets is 89.5

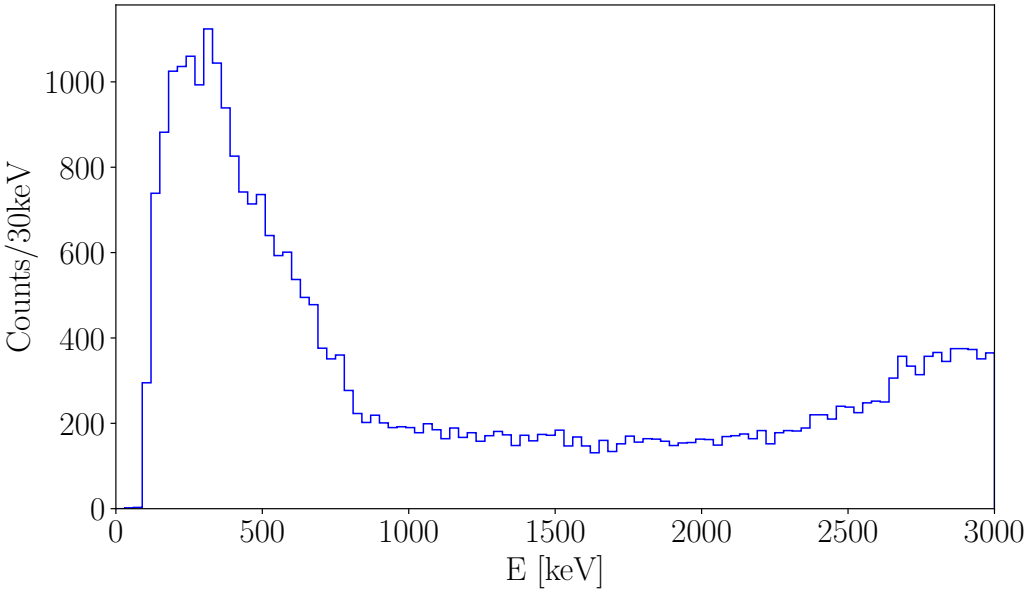

Figure 3.18: Response function for ^{12}C excitation due to a beam of ^{100}Cd.

m and one can keep as a rule of thumb that the isotopes travel at roughly 0.15 m/ns), the decay happens randomly between the primary target and the end of the beamline following an exponential distribution. However, knowing the half-life of the isomer states, it is possible to estimate the number of deexcitation occurring in a given range of the beamline. The crucial quantity to perform this computation and the simulation of this effect is the isomeric ratio, which is the ratio between the number of isomers in the beam and the number of isotopes in their ground state.

It is possible to extract this quantity for this experiment as two specific runs with that intent have been performed. Instead of the C and CH_2 target, a thick (between 3 and 4 cm) plastic wall was inserted at the position of the secondary target. The isotopes impinging this wall are stopped by it. Once in the wall, the isomer will deexcite and emit γ rays. Measuring and counting these, and dividing it by the total number of isotopes hitting the plastic wall, yields the isomeric ratio at the position of the plastic wall.

Once this ratio has been determined, it can be used to constrain the contribution of the isomer deexcitation in the fit of each spectra. For clarity, one can write the following equations in the case of the estimation of the isomeric ratio of ^{102}Sn in the experiment. The definition of the isomeric ratio can be written in the following way:

$$R = \frac{N_{Sn*}}{N_{Sn,tot}}, \tag{3.17}$$

with N_{Sn*} the number of Sn nuclei in their isomer state in the beam, and $N_{Sn,tot} = N_{Sn*} + N_{Sn}$ the total number of ^{102}Sn isotopes in the beam. As explained previously, the plastic wall stops the beam and all the isomers trapped in it deexcite. As a result, one can write

$$N_{Sn*} = N_{\gamma,Sn*}, \tag{3.18}$$

with $N_{\gamma,Sn*}$ the number of γ rays emitted by the isomer nuclei. However, $N_{\gamma,Sn*}$ is different from the number of measured γ rays because of the efficiency of the DALI2 array, noted

ϵ_{DALI}. So

$$N_{\gamma,Sn*} = \frac{N_{\gamma,Sn*,\text{measured}}}{\epsilon_{DALI}}. \tag{3.19}$$

$N_{Sn,tot}$ is determined by counting the triggers for ^{102}Sn. Plugging equations (3.18) and (3.19) into equation (3.17) yields

$$R = \frac{N_{\gamma,Sn*,\text{measured}}/\epsilon_{DALI}}{N_{Sn,tot}}. \tag{3.20}$$

The fit of the γ spectra from the implantation runs yields the amplitude p_t for the response function of the photopeaks. As a result, one can write

$$N_{\gamma,Sn*,\text{measured}}/\epsilon_{DALI} = p_t \cdot N_{\gamma,sim,imp}, \tag{3.21}$$

with $N_{\gamma,sim,imp}$ the input number of simulated γ rays for the implantation runs. One can note that, because all transitions in the implantation runs come from the cascade from the isomer state, p_t is the same for all observed transitions, normalized to the relative intensity of each transition. Adding equation (3.21) in equation (3.20), R is written as

$$R = \frac{p_t \cdot N_{\gamma,sim,imp}}{N_{Sn,tot}}. \tag{3.22}$$

Equation (3.17) provides a rather general and physical definition of the isomeric ratio, while equation (3.21) links quantities that consider the isomer deexcitation from the point of view of the experimental setup and of the data analysis. Equation (3.22) mixes both types of quantities, namely $N_{Sn,tot}$ and $N_{\gamma,sim,imp}$. To eventually define R from both the physical and the experimental point of view, one can note that, in the case of this experiment, $N_{Sn,tot}$ is the number of ^{102}Sn isotopes detected in the beam in BigRIPS during the implantation runs, and could also be noted $N_{Sn,BR,imp}$. One can now define R using quantities relevant to the physics of the problem only, or using quantities relevant to the data analysis only:

$$R = \frac{N_{Sn*}}{N_{Sn,tot}} = \frac{p_t \cdot N_{\gamma,sim,imp}}{N_{Sn,BR,imp}}. \tag{3.23}$$

As explained previously, the plastic wall stops the beam and forces all the isomers still present in the beam to emit their γ rays into the DALI2 array. This is not the case in the physics run, as the beam is not stopped. The fact that the DALI2 array only detects part of the γ rays from the isomer then needs to be taken into account. One can suppose that DALI2 detects γ rays emitted in a range $[z_1\ ;\ z_2]$, with $z_1 < z_2$ (recalling that the center of the target is at the origin of the z-axis). The isomeric ratio can then be extrapolated in z_1 and z_2, called respectively R_{z_1} and R_{z_2}:

$$\begin{aligned} R_{z_1} &= R\exp(-\lambda\frac{z_1}{\beta c}), \\ R_{z_2} &= R\exp(-\lambda\frac{z_2}{\beta c}), \end{aligned} \tag{3.24}$$

with βc the velocity of the isotope, $\lambda = \frac{\ln(2)}{\tau_{1/2}}$ the decay constant of the isomer and $\tau_{1/2}$ the half-life of the isomer. The proportion of isomer deexciting between $[z_1\ ;\ z_2]$ is then given by

$$\Delta R = R_{z_1} - R_{z_2}. \tag{3.25}$$

The contribution of the isomer deexcitation in the inelastic excitation spectrum is then given by:

$$C_i = \Delta R \cdot \frac{N_{Sn,BR,ZD,inex}}{N_{\gamma,sim,inex}}, \tag{3.26}$$

with $N_{\gamma,sim,inex}$ the input number of simulated γ rays for the inelastic excitation runs (also referred to in this study as the physics runs), and $N_{Sn,BR,ZD,inex}$ the number of ^{102}Sn isotopes detected in both the beam and the fragment during the physics runs. Even though these notations make the previous equations slightly more complicated, it is necessary to differentiate between $N_{\gamma,sim,imp}$ and $N_{\gamma,sim,inex}$ to keep track of the data used for the determination of each quantity. R is determined using the implantation runs, and is then used to compute ΔR and C_i in order to constrain the inelastic excitation γ spectra. Therefore, the ratio $N_{Sn,BR,ZD,inex}/N_{\gamma,sim,inex}$ in equation (3.26) acts as a normalization for ΔR, taking into account the number of nuclei impinging on the target and the number of simulated γ rays.

Using these elements, the two following paragraphs will exhibit the isomeric ratio for ^{102}Sn and ^{100}Cd, and the corresponding simulated contribution of the isomer deexcitation in the inelastic excitation spectra.

The isomer of ^{102}Sn

The lifetime of the isomer state for the considered tin isotope is 367(11) ns [52]. This state, with a spin-parity $J^{\Pi} = 6^+$, is located at an excitation energy of 2057 keV, as shown on the level scheme of ^{102}Sn given in figure 3.19.

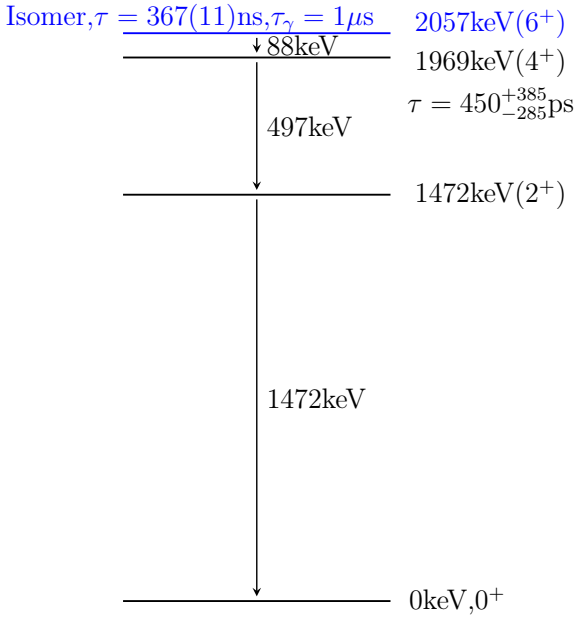

Figure 3.19: The level scheme of ^{102}Sn [74]. The spin and parity assignments in parentheses are suggested in [74].

However, there is a competition between gamma emission and internal conversion. This influences the lifetime of the isomer as described by equation 10.19 in [65]:

$$\lambda_t = \lambda_\gamma + \lambda_e, \tag{3.27}$$

with λ_t the total decay constant for the isomer state, λ_γ the decay constant arising from γ emission, and λ_e the decay constant arising from internal conversion. λ is defined as

$$\lambda_i = \frac{1}{\tau_i}, \tag{3.28}$$

with i being t, γ or e, and τ being the corresponding lifetime. To compute the contribution of γ emission and internal conversion, one can use the BRICC program [75]. To do so, one considers the internal conversion coefficient α defined as [65]

$$\alpha = \frac{\lambda_e}{\lambda_\gamma}. \tag{3.29}$$

Considering only the E2 multipolarity, and the K electron shell, BRICC yields $\alpha = 1.75$. Combining equations (3.27), (3.28) and (3.29), one can write

$$\tau_\gamma = (1 + 1.75)\tau_t = 1.009\mu\text{s}. \tag{3.30}$$

Additionally, the nuclei in the beam travel at a velocity of approximately $c/2$. At such speed, relativistic effects need to be taken into account, such as time dilation. The γ lifetime for the isomer becomes,

$$\tau_{\gamma,r} = \tau_\gamma \cdot \gamma, \tag{3.31}$$

with $\tau_{\gamma,r}$ the relativistic γ lifetime, γ the Lorentz factor defined as $\gamma = \frac{1}{\sqrt{1-\beta^2}}$. As explained with equation (3.24), the isomeric ratio found at F8 then needs to be extrapolated at other positions in the beamline, namely between 50 cm before the target and 50 cm after, as γ rays emitted in this range can be detected by the DALI2 array, and as a consequence the isomer response function is simulated in that range. One then considers four different β in this range:

- between -50 cm and the beginning of the target, at -0.25 cm,
- in the first half of the target (between -0.25 cm and 0 cm),
- in the second half of the target (between 0 cm and 0.25 cm),
- between the end of the target and 50 cm.

The Lorentz factor for each considered section is then used to extrapolate the isomeric ratio at the production target, and compute ΔR.

The spectrum for the measurement of the isomeric ratio of ^{102}Sn is displayed in figure 3.20. The result of this fit provides the parameter previously referred to as p_t for both transitions. As an additional verification, one can check that this coefficient is the same for both transition. This yields, for the $2^+ \rightarrow 0^+$ and $4^+ \rightarrow 2^+$ transitions respectively, an isomeric ratio of 33.2(7)% and 33.0(8)% at focal plane F8. Finding two consistent isomeric ratios increases the confidence in the procedure. If one extrapolates these ratios at the primary target, one gets 45.1(9)% and 44.8(9)% of isomer, respectively. The simulation of the isomer deexcitation for ^{102}Sn is performed by generating a distribution of events spanning range from 50 cm before the target to 50 cm after the target, as stated previously. This distribution is considered flat as the γ lifetime of the isomer state is rather long, and the exponential decay can be approximated by a flat distribution in this small window compared to the size of the beamline. The γ rays from the deexcitation of the whole

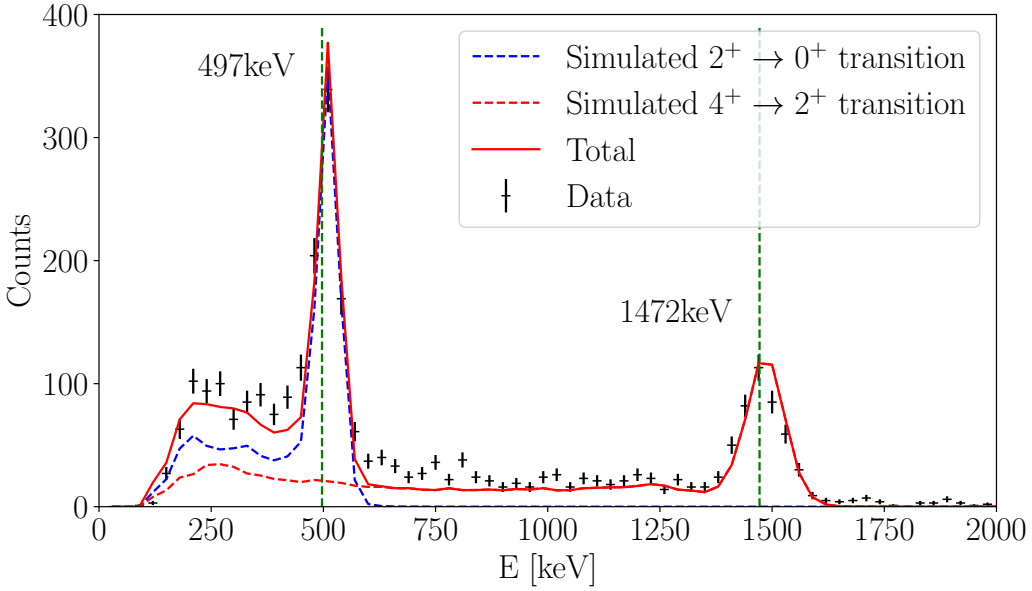

Figure 3.20: Data and fit for the γ spectrum of the plastic wall runs for ^{102}Sn. This spectrum has been performed without addback, selecting events with multiplicity ≤ 3.

cascade starting at the isomer state is considered and simulated. Due to the emission in a large spatial range (around 200 times the size of the target), the energy of most γ rays will be poorly reconstructed after the Doppler correction. The resulting response functions are displayed in figure 3.21.

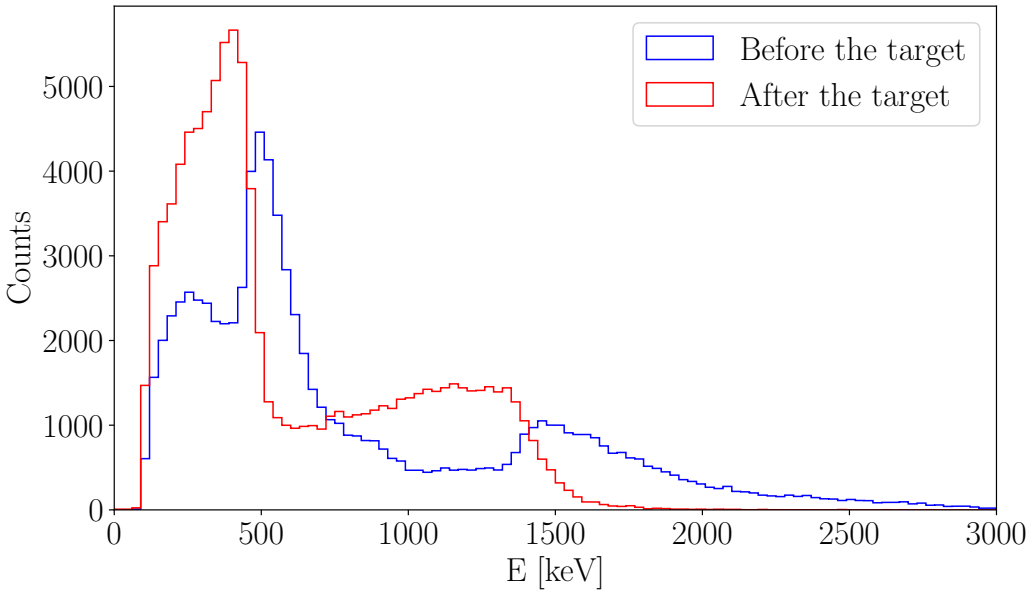

Figure 3.21: Doppler corrected response functions for isomer deexcitation of ^{102}Sn, to be used in the fit of the inelastic excitation γ ray spectra. In blue, the events have been generated in the 50 cm before the target, in red, in the 50 cm after the target.

Knowing the isomeric ratio at F8 and the γ lifetime τ_γ, one can then compute the percentage of isotopes in the beam that are isomers and decaying between $z = -50$ cm and $z = 50$ cm, through equations (3.24) and (3.25) with the correct relativistic γ half-

life. This percentage is 0.137(3)% for ^{102}Sn. It is now possible to apply this number to the statistics of the CH_2 and C target runs to constraint the contribution of the isomer deexcitation in the fit of the γ spectrum.

The isomer of ^{100}Cd

There also exists an isomer state in ^{100}Cd, at $E = 2548.19(18)$ keV and with a half-life of $\tau = 62(6)$ ns, as stated previously in subsection 3.2.4. It is represented on the level scheme of ^{100}Cd given in figure 3.22. For this transition, BRICC yields an internal conversion coefficient of the order of 10^{-3}. It is then reasonable to consider the approximation $\tau_t = \tau_\gamma = 62(6)$ ns.

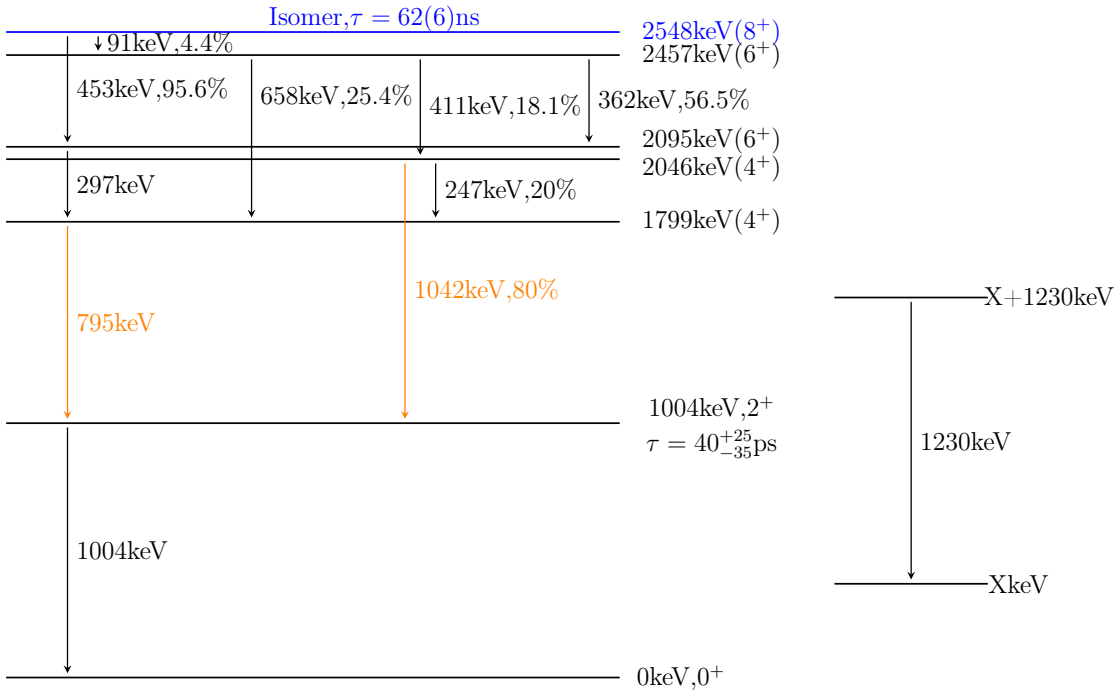

Figure 3.22: The level scheme of ^{100}Cd [71]. The selected levels are the one decaying from the isomer state in blue, and the detected ones as well as the rest of their cascade (if they are part of one). The yrast band is the cascade aligned on the left of the spectrum. The orange arrows point at the direct feeders of the first 2^+ state. A 1230keV-transition is measured and placed on the side since it corresponds to no known transitions. The spin and parity assignments in parentheses are suggested in [71].

Figure 3.23 shows the various gates used for background subtraction on the isomeric γ spectrum and on the time spectrum. One can note that the absolute value of the time t on this figure has an arbitrary offset. The γ spectrum is obtained by projecting the events between the green dashed lines on the y-axis of figure 3.23. The projection on the y-axis of the events between the pink dashed lines yields the background γ spectrum, normalized and subtracted from the isomeric γ spectrum in order to improve the resolution. The result of this subtraction as well as its fit can be seen in figure 3.24. All four transitions have the same intensity, and therefore should yield the same minimization parameter. From the previous number, one can note that this is the case for all transitions except the one at 296 keV ($6^+ \rightarrow 4^+$). This can be explained by the fact that its energy is low enough to be heavily impacted by the threshold of the detectors, and the higher contribution of the background noise at low energy.

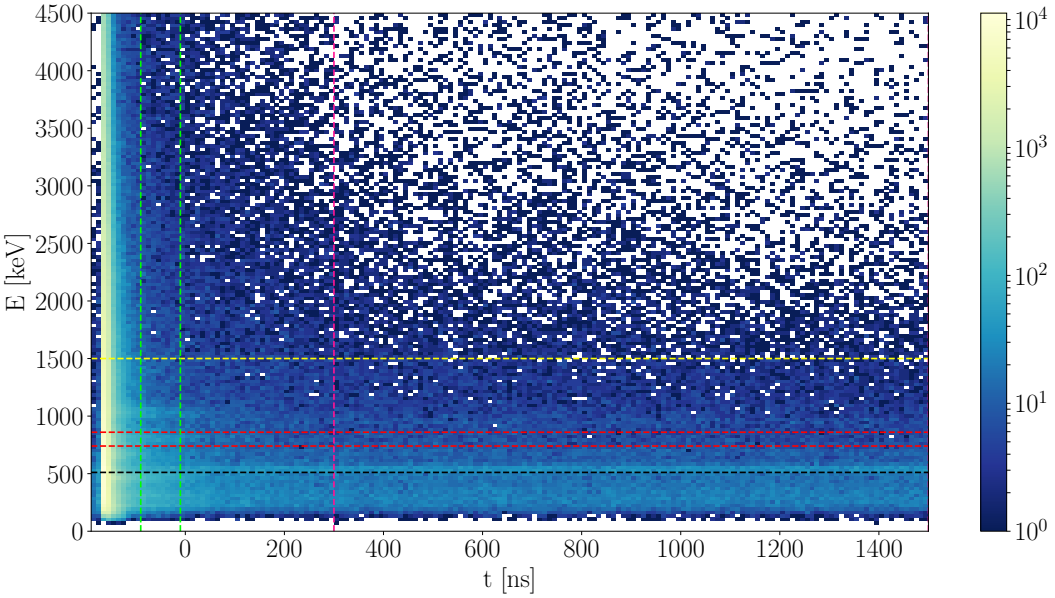

Figure 3.23: Histogram displaying the energy of the detected γ rays versus the time of their emission for the plastic wall runs. A cut on the events' multiplicity has been performed to draw this histogram. Only events with a multiplicity ≤ 5 have been kept. The black dashed line shows the background peak at 511 keV. The green dashed lines show the time range used for the projection on E to compute the γ spectrum for the ^{100}Cd isomer. The purple dashed lines (at 300 ns and 1500 ns) show the range used for the background γ rays selection. The red dashed lines show the gate on the $4^+ \rightarrow 2^+$ (795 keV) chosen for the projection on t. The yellow dashed lines (at 1500 keV and 4500 keV) show the range used for the selection of background for t.

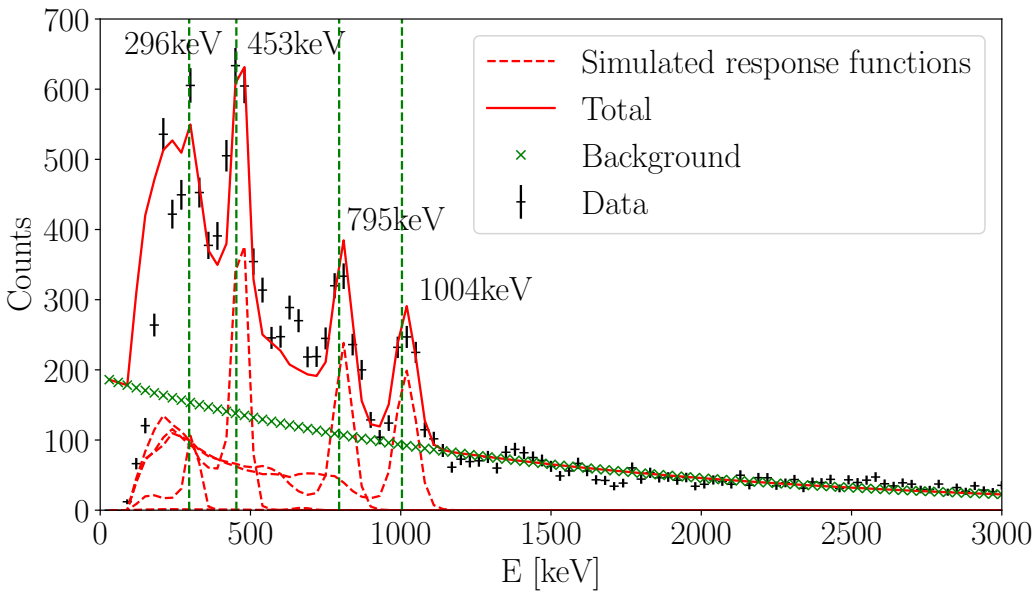

Figure 3.24: Energy spectrum of the isomer deexcitation for ^{100}Cd for the implantation runs.

As explained in the beginning of subsection 3.2.4, the fitted amplitudes are used to determine the number of γ rays measured during the implantation runs. However, as explained earlier, a selection has been used to improve the signal-to-noise ratio of the photopeaks. Therefore, the statistics presented in the spectrum is not the complete statistics, and a

correction needs to be applied. Equation (3.20) shows that the isomeric ratio depends on the number of measured γ rays and on the total number of ^{100}Cd nuclei impinging on the plastic wall. The aforementioned correction will then either reduce the number of impinging nuclei to match the fraction of the statistics used in the γ spectrum, either increase the number of measured γ rays to match the total number of impinging nuclei. In this study, the latter option has been chosen.

To do so, one considers the time spectrum for a given photopeak. This is obtained by projecting the events between the two red dashed lines on the x-axis, corresponding to the 795keV-photopeak. The background, corresponding to the projection on the x-axis of the events above the yellow dashed lines, has been subtracted. The result can be seen in figure 3.25. Once this spectrum is built, the exponential decay of the isomer is visible. This decay is then fitted and the resulting equation is integrated between the two boundaries of the time cut used to produce the isomer γ spectrum, and from the start to the end of the decay. The two integrals are compared, which yields the normalization factor. To fit

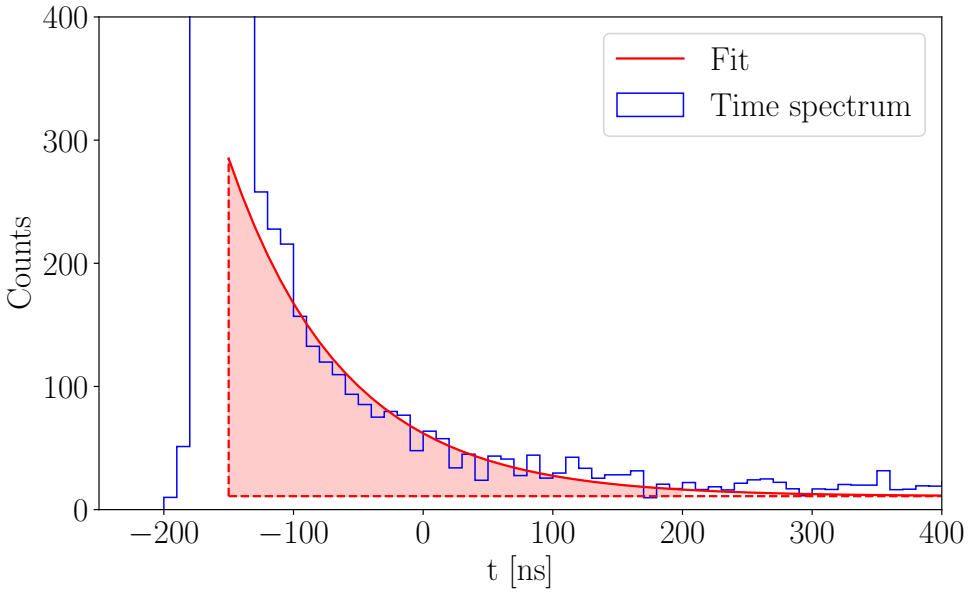

Figure 3.25: Time spectrum of the isomer deexcitation for ^{100}Cd. This is drawn using a gate on the 795 keV transition. Only the events with multiplicity ≤ 5 are selected. The background is subtracted from this spectrum. The light red area is the integrated area for the computation of the number of events.

the exponential decay, an equation of the shape $y = \exp(a - \lambda t) + b$ has been used. λ has been set as $\ln(2)/\tau$, and both parameters a and b are fitted to the histogram. b is an offset parameter representing the constant atomic background, visible at large t, while a is an amplitude parameter, correlated to the statistics of the ^{100}Cd isomer. To only account for the statistics of the isomer decay, $\tilde{y} = \exp(a - \lambda t)$ is integrated. The integral of the exponential yields,

$$I = \int_{t_1}^{t_2} \exp(a - \lambda t) dt = \frac{\exp(a - \lambda t_2) - \exp(a - \lambda t_1)}{-\lambda}. \tag{3.32}$$

Taking $t_1 = -90$ ns and $t_2 = -10$ ns (the cut applied on the data, represented by the green dashed lines in figure 3.23), I yields 7400±1900 events. To determine the total number of γ rays detected, the exponential presented previously needs to be integrated

from the center of the prompt peak to the end of the decay. The center of the prompt peak is considered to be at -150 ns, using the same units as figure 3.25. The integral I computed between these limits yields 24000±6400 events. The counts shown in figure 3.24 are then underestimated by a factor of 24000/7400 = 3.24±1.2. After taking into account this correction, the fit of the spectrum in figure 3.24 yields an isomeric ratio of 0.68(2)%. Extrapolating 50 cm before and after the target, taking into account the relativistic effects as discussed previously with equation (3.31), and correcting by the 3.24 factor, the percentage of isomer of ^{100}Cd decaying between -50 cm and 50 cm is 0.039(2)%.

In an analogous way to what has been done for ^{102}Sn, the γ rays emitted by the whole decay of the isomer state have been considered. As explained for the isomer of ^{102}Sn, the Doppler correction applied on γ rays emitted in a large range of values for the z-coordinate results in bad reconstruction of the energy, hence smeared out peaks. The resulting response functions for isomer emission before and after the target is shown in figure 3.26.

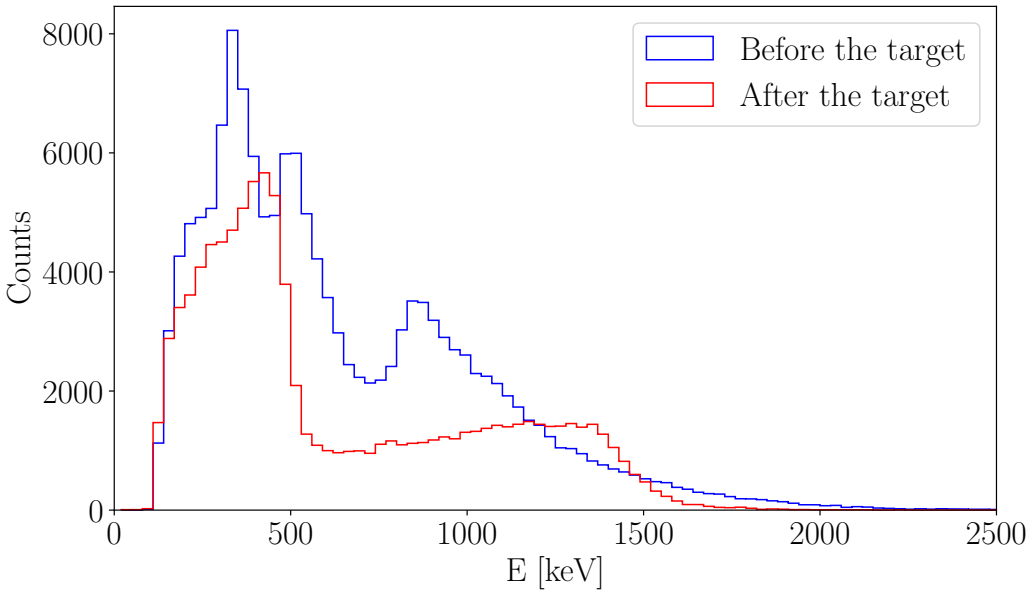

Figure 3.26: Doppler corrected response functions for isomer deexcitation of ^{100}Cd. In blue, the events have been generated in the 50 cm before the target to the target, in red, in the 50 cm after the target.

3.2.5 Half-life of excited states

For certain transitions in ^{100}Cd and ^{102}Sn, it has appeared that the photopeaks in the γ ray spectrum were broader than expected and had a slight shift in energy. A suitable explanation for this is considering that the decaying excited states have a non-zero half-life. This half-life is long enough so that the excited nucleus in the beam has time to travel a short distance before deexciting itself and emitting the γ ray, but not too long to not be another isomer state and still be detected by the DALI2 array. This way, the γ ray is emitted slightly after the target. As a consequence, a wrong angle would be taken into account for the Doppler correction which could decrease the resolution of the peak, and would shift it towards lower energies. The following paragraphs describe the method applied for the determination of the half-life in the case of two different states.

The 2_1^+ state in ^{100}Cd

The spectroscopic data for ^{100}Cd [73] indicate that the half-life of the first 2^+ state (also noted 2_1^+), noted here $\tau_{2_1^+}$, is above 1 ps. To determine the value of this half-life more precisely, several fits have been performed with $\tau_{2_1^+}$ as a free parameter. A χ^2 value has then been computed for each fit. To determine the error on the value of $\tau_{2_1^+}$, the χ^2 value has been turned into the probability of the chosen $\tau_{2_1^+}$ to be the true half-life of the state, using the following formula [76]:

$$p(\tau_{2_1^+}) \propto \exp\left(-\frac{\chi^2}{2}\right) \tag{3.33}$$

The retained value for $\tau_{2_1^+}$ is the one giving a minimal χ^2, or the maximal probability. The obtained probability distribution is multiplied by a normalization to guarantee that the integral of p is 1 on the range of values that has been chosen. The result of such a procedure is shown in figure 3.27.

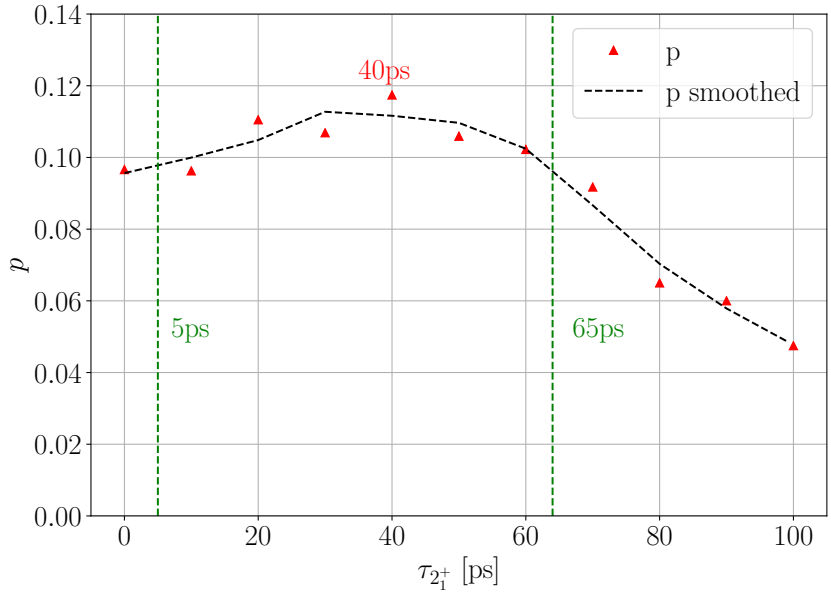

Figure 3.27: χ^2 probability as a function of $\tau_{2_1^+}$ for the CH_2 target. The black dashed line represents a smoothing of the data by a Savitzky-Golay filter [77]. The two green vertical dashed lines are the boundaries of the 68% confidence interval around the maximum at $\tau_{2_1^+}$=40 ps.

The green dashed lines represent the boundaries of the 1-σ confidence interval around the chosen half-life value. These boundaries, noted for the lower and higher value respectively τ_l and τ_h, have been determined such that:

$$\int_{\tau_l}^{\tau_h} p(\tau_{2_1^+}) = 0.68.$$

This procedure yields a half-life of $\tau_{2_1^+} = 40^{+25}_{-35}$ ps for the 2_1^+ state of ^{100}Cd.

The 4_1^+ state in ^{102}Sn

The spectroscopic data for ^{102}Sn in [78] do not provide any information about the half-life of the excited states in this nucleus. It is possible to apply the previous method with two

unknown half-life, and compute a χ^2 surface. However, it is possible to estimate the half-life for the 2_1^+ state from other data. Theoretical calculations for the proton transition matrix element M_p for ^{102}Sn provides a value of ∼0.1 eb [47]. As exposed in chapter 1, there is a link between the reduced transition probability $B(E2, 0_1^+ \rightarrow 2_1^+)$ and M_p given on equation (1.17). This gives an estimate of $B(E2, 0_1^+ \rightarrow 2_1^+) \sim 0.01$ e^{2}b^2, confirmed by recent shell model calculations [79]. One can relate the half-life of the excited state and the transition probability with the equation [80]:

$$B(E2, 0_1^+ \rightarrow 2_1^+) = 4.08 \cdot 10^{13} \frac{1}{E_\gamma \tau_\gamma}, \tag{3.34}$$

with E_γ the energy of the excited state in keV, and τ_γ the half-life in ps. In the end, this gives an estimate of $\tau_\gamma \sim 6$ ps. From what has been discussed in the previous paragraph on ^{100}Cd, such a half-life is too short to have a significant impact on the resolution and centroid of the photopeak. Moreover, from the figures shown for ^{100}Cd, the precision on this measurement of $\tau_{2_1^+}$ is not big enough to give a quantitative value. It then means that the shape of the photopeak for the $2_1^+ \rightarrow 0_1^+$ deexcitation is influenced by a longer half-life of the 4_1^+ state, as the $4_1^+ \rightarrow 2_1^+$ transition and the $2_1^+ \rightarrow 0_1^+$ transition are in a cascade. The same procedure as the one for the 2_1^+ state of ^{100}Cd has been applied to determine $\tau_{4_1^+}$ of ^{102}Sn. It yields $\tau_{4_1^+} = 450^{+385}_{-285}$ ps. The probability distribution is shown in figure 3.28.

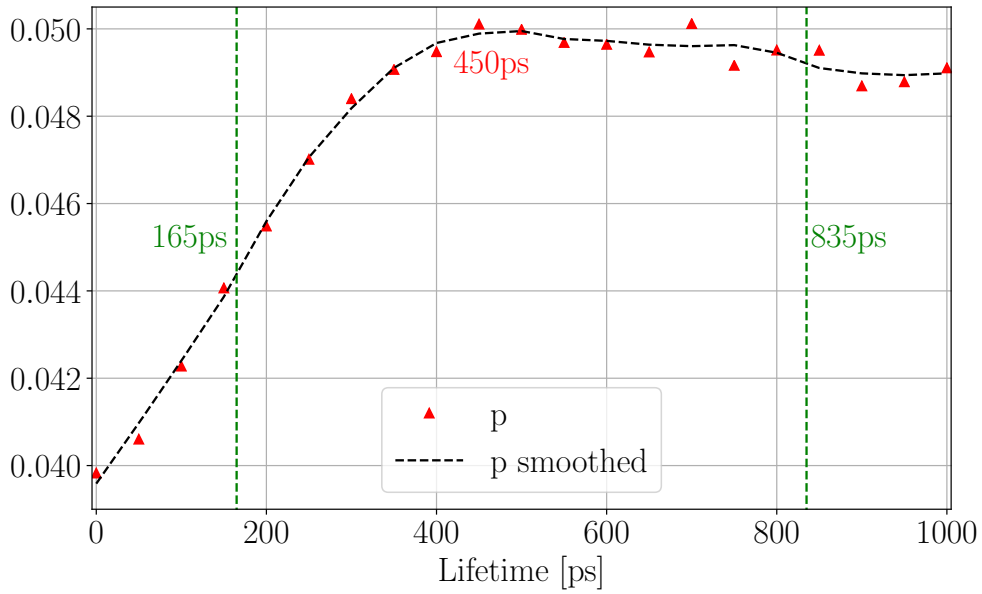

Figure 3.28: χ^2 probability as a function of $\tau_{4_1^+}$ for the CH_2 target. The black dashed line represents a smoothing of the data by a Savitzky-Golay filter [77]. The two green vertical dashed lines are the boundaries of the 68% confidence interval around the maximum at $\tau_{4_1^+}$=450 ps.

It is interesting to note at that point that, for the inelastic excitation of ^{102}Sn, all contributions to the γ spectrum are constrained, either by the implantation run performed during the same experiment (for the contribution of the isomer deexcitation) or by other reaction channels, namely the inelastic excitation of ^{100}Cd (for the C excitation and the double exponential background). This reinforces the confidence that their amplitude is not adjusted ad hoc to reproduce structures of the spectrum, which as a result increases the confidence on the cross-section.

3.2.6 Calculation of the cross-sections

The quantities of interest extracted from the data are the cross-section for inelastic excitation of ^{102}Sn and two other $N = 52$ isotones: ^{100}Cd and ^{98}Pd. Taking the 2^+ state of each of the aforementioned nuclei as an example, one can write the definition of the cross-section for inelastic excitation in the following way:

$$\sigma^{2^+} = \frac{N_p(2^+)}{N_i t_i}, \tag{3.35}$$

with $N_p(2^+)$ the number of 2^+ populated in the target, N_i the number of incident isotopes, and t_i the number of scattering centers in the considered target, expressed in number of atoms per cm^2. One can write these quantities as:

$$\begin{aligned} N_p(2^+) &= \frac{N_m(2^+)}{\varepsilon_t \varepsilon_{ZD} \varepsilon_{DALI}}, \\ N_i &= \frac{N_m(BR, ZD)}{\varepsilon_t \varepsilon_{ZD}}, \end{aligned} \tag{3.36}$$

with $N_m(2^+)$ the number of 2^+ measured, $N_m(BR, ZD)$ the number of isotopes measured with a gate on BigRIPS and ZeroDegree, ε_t the transmission, ε_{ZD} the acceptance of ZeroDegree, and ε_{DALI} the efficiency of DALI. Combining the two previous equations, one can write,

$$\sigma^{2^+} = \frac{N_m(2^+)/\varepsilon_{DALI}}{N_m(BR, ZD) t_i}. \tag{3.37}$$

$N_m(BR, ZD)$ is measured from the data, and the quantity $N_m(2^+)/\varepsilon_{DALI}$ is extracted from the fit of the experimental data with the simulation. The γ spectrum is fitted by a response function f of the type,

$$f(E) = B(E) + \sum_i p_i g_i(E), \tag{3.38}$$

with B the simulation of the background, g_i the response function for each transition and p_i the minimization coefficients. One can then write,

$$\frac{N_m(2^+)}{\varepsilon_{DALI}} = N_\gamma^{2^+} p_{2^+}, \tag{3.39}$$

with $N_\gamma^{2^+}$ the number of γ rays input in the simulation. Combined with equation (3.37), one can then write,

$$\sigma^{2^+} = \frac{N_\gamma^{2^+} p_{2^+}}{N_m(BR, ZD) t_i}. \tag{3.40}$$

The measurement presented here has been performed on a carbon target and a plastic (CH_2) target. The contribution of the nuclear excitation compared to the one of Coulomb excitation is optimal for very low Z, since Coulomb excitation cross-section is proportional to Z [81]. The idea is then to subtract the contribution of the reactions on C, measured with the pure C target, from the reactions on the CH_2 target, by subtracting the corresponding determined cross-sections. One can also directly subtract the γ energy spectra measured on C and CH_2 target, to reconstruct the spectra for inelastic excitation on an H target, and directly determine the cross-section on proton target from the fit of this spectrum. Those two methods yield the same quantity (the cross-section for inelastic excitation on H target) and more details on this procedure are given in appendix A.

Chapter 4

Results and discussion

Contents

The following sections are dedicated to displaying the fits of the γ energy spectra for the studied $N = 52$ isotones and the determined inelastic excitation cross-sections for the first excited 2^+ state on H target. The determination of this reaction cross-section requires the precise count of the γ rays detected, in this case, by the deexcitation of the 2_1^+ state to the 0_1^+ state. Furthermore, one has to take into account and subtract the contribution of the transitions corresponding to the decay of states lying at higher energy than the 2_1^+ state and possibly feeding it. Providing a γ energy spectrum showing structures as well separated as possible is the objective of the analysis presented in the previous chapter. The care given to the simulation and physical constraint of the isomer decay, exposed on subsection 3.2.4, is justified by the necessity to account only for the inelastic excitation towards the excited states of interest, and not for external background contributions. The background due to bremsstrahlung, high energy excited states, and the C excitation is also taken into account for the same reason. As explained in subsections 3.2.2 for bremsstrahlung and high energy excited states, these contributions will be left free for the fit of the ^{100}Cd spectrum. The resulting ^{100}Cd-constrained amplitudes will then be normalized and applied on ^{98}Pd, and ultimately to ^{102}Sn. This is why the results for the inelastic excitation of ^{100}Cd will be shown first, followed by the results for ^{98}Pd and ^{102}Sn. For each channel and each target, the intensities, noted Γ, are provided. They represent the number of γ rays measured corresponding to the $2_1^+ \rightarrow 0_1^+$ transition. Once the direct feeders of the 2_1^+ are identified, their respective Γ is subtracted from the intensity of the $2_1^+ \rightarrow 0_1^+$ transition, yielding the experimental cross-section for the inelastic excitation of the 2_1^+ state.

4.1 ^{100}Cd

The fit of the γ spectrum of ^{100}Cd on CH_2 target is displayed in figure 4.1, and the C target spectrum in figure 4.2. In this spectrum, only two known transitions are visible, corresponding to the $2_1^+ \rightarrow 0_1^+$ and the $4_1^+ \rightarrow 2_1^+$ transitions. Additionally, a 1230-keV transition, unreported in the data sheets [71], has been measured.

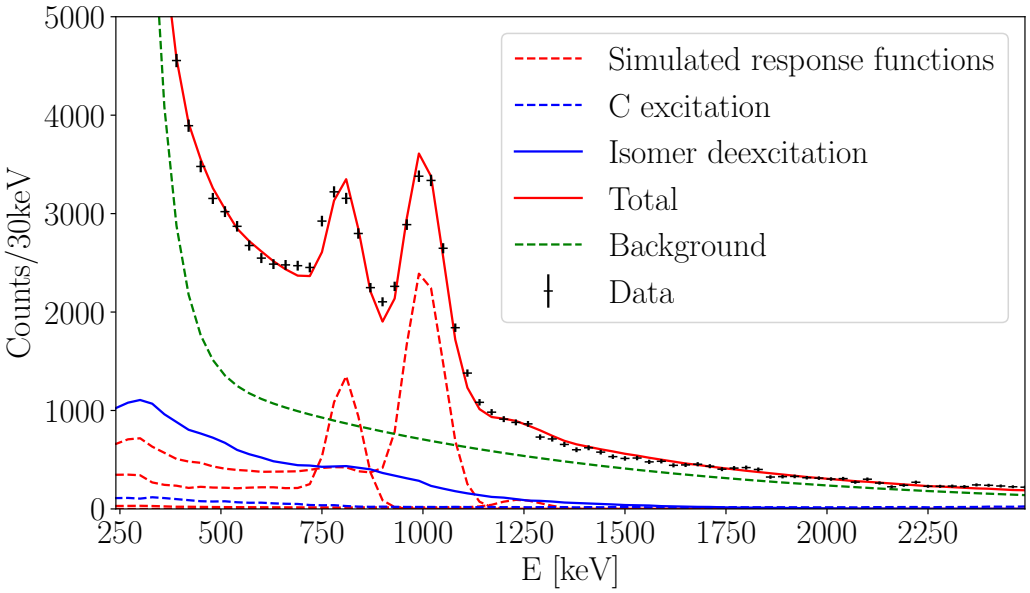

Figure 4.1: Doppler corrected energy spectrum for the inelastic excitation ^{100}Cd on CH_2 target. The red dashed lines are the response functions corresponding to the γ transitions fitted here at the energies of 795 keV, 1004 keV, 1230 keV. The green dashed line represents the double exponential background. The blue dashed line is the response function for the excitation of the C nuclei in the target. The solid blue line is the response function of the decay of the isomer state in ^{100}Cd. The solid red line is the sum of all the previously mentioned contributions. The data points are represented with their error bars as black crosses.

In these fits, eight parameters are left free:

- one for each response function of each of the three considered photopeaks,
- four parameters for the double-exponential background,
- one for the C excitation response function.

The only contribution that is fixed is the deexcitation of the isomer state, constrained by the isomeric ratio computed in subsection 3.2.4. The considered level scheme for ^{100}Cd has been shown previously in figure 3.22. From these two fits, one can note the importance of the isomer deexcitation as a background contribution. Even though the half-life of this isomer is rather short, compared to the distance between both targets, the isomeric ratio at the primary target is large enough that a significant amount of isomeric γ rays are detected by the DALI2 array. The fitted parameters for the double exponential, represented with green crosses, will be used as a constrain for the two other inelastic excitation channels.

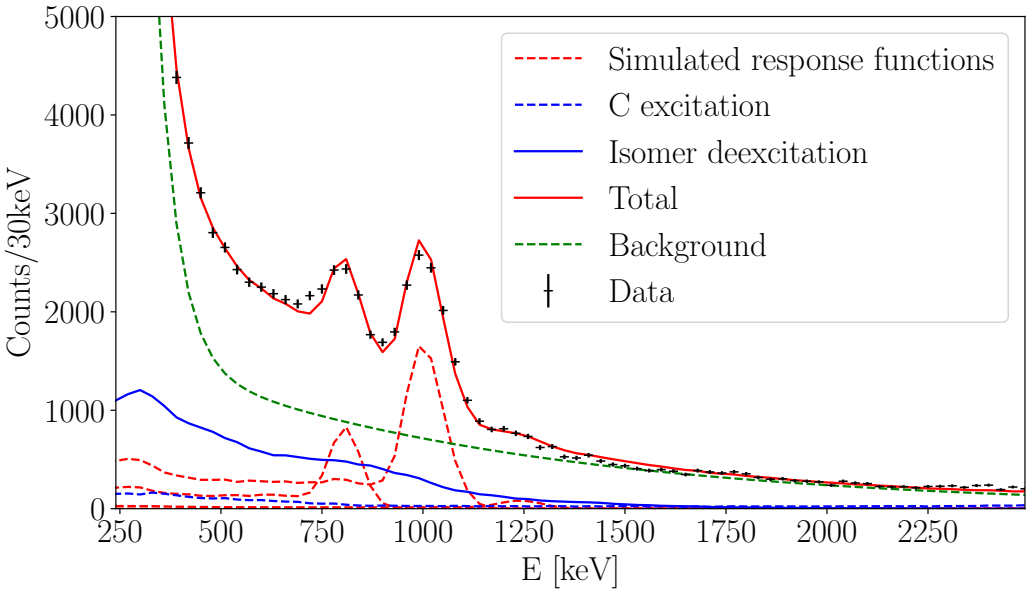

Figure 4.2: Doppler corrected energy spectrum for the inelastic excitation ^{100}Cd on C target. The red dashed lines are the response functions corresponding to the γ transitions fitted here at the energies of 795 keV, 1004 keV, 1230 keV. The green dashed line represents the double exponential background. The blue dashed line is the response function for the excitation of the C nuclei in the target. The solid blue line is the response function of the decay of the isomer state in ^{100}Cd. The solid red line is the sum of all the previously mentioned contributions. The data points are represented with their error bars as black crosses.

As explained in the beginning of the present chapter, one can note $\Gamma^{2^+\to 0^+}$ the cross-section for the deexcitation of the 2^+ state to the ground state, regardless of the process for populating the 2^+ state. One can similarly note $\Gamma^{4^+\to 2^+}$. The fit presented in figure 4.1 yields $\Gamma^{2^+\to 0^+}_{CH_2}$=17.8(8) mb and $\Gamma^{4^+\to 2^+}_{CH_2}$=7.6(7) mb. The fit presented in figure 4.2 yields $\Gamma^{2^+\to 0^+}_{C}$=25.5(13) mb and $\Gamma^{4^+\to 2^+}_{C}$=10.1(6) mb. One can then subtract $\Gamma^{4^+\to 2^+}$ from $\Gamma^{2^+\to 0^+}$, to remove the contribution of the feeding of the 2^+_1 by the 4^+_1 state, and obtain the experimental cross-section for the inelastic excitation of the 2^+ state, noted σ^{2^+}: $\sigma^{2^+}_{CH_2}$=10.3(10) mb and $\sigma^{2^+}_{C}$=15.4(14) mb. These two quantities yield the cross-section on H target, following the procedure detailed on appendix A: $\sigma^{2^+}_{H}$=7.7(17) mb.

4.2 ^{98}Pd

The level scheme of ^{98}Pd is shown in figure 4.3.

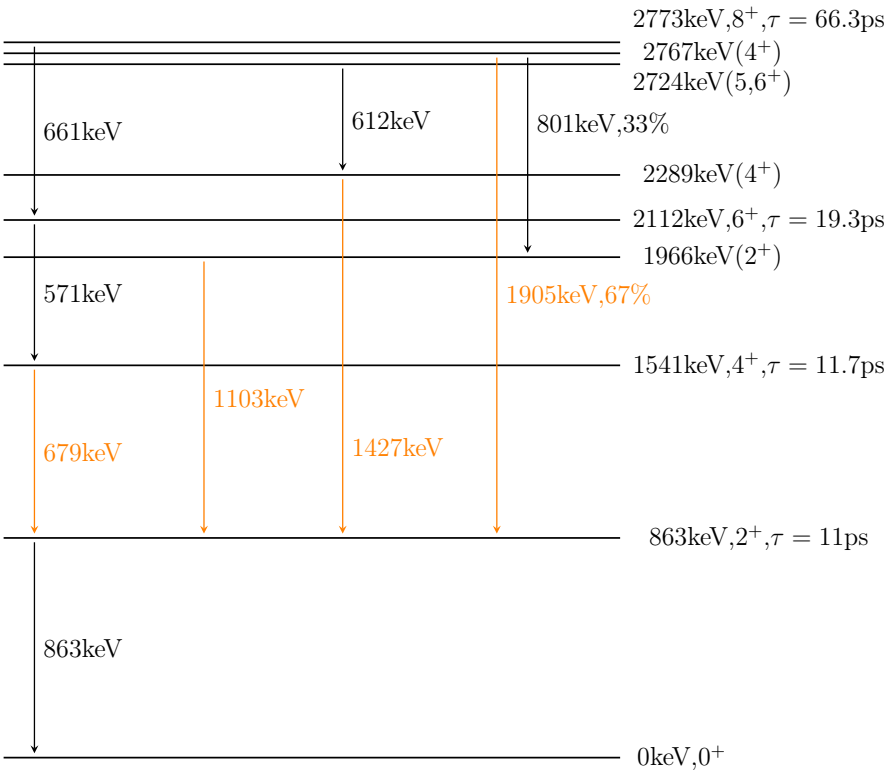

Figure 4.3: The level scheme of ^{98}Pd [82]. The yrast band is the cascade on the left of the scheme. The orange arrows point at the direct feeders of the first 2^+ state. The spin and parity assignments in parentheses are suggested in [82].

In both spectra, photopeaks at 863 keV, 801keV, 1103 keV and 1905 keV are visible corresponding to the $2_1^+ \rightarrow 0_1^+$, $4_3^+ \rightarrow 2_2^+$, $2_2^+ \rightarrow 2_1^+$ and $4_3^+ \rightarrow 0_1^+$ transitions, respectively. The photopeak at 1427 keV corresponding to the $4_2^+ \rightarrow 2_1^+$ transition is only visible in the CH_2 spectrum. Furthermore, a peak centered around 620 keV is visible on both spectra, and most likely contains the 679 keV, 571 keV and 661 keV photopeaks corresponding to the $4_1^+ \rightarrow 2_1^+$, $6_1^+ \rightarrow 4_1^+$ and $8_1^+ \rightarrow 6_1^+$ transitions, respectively. Experimentally, one cannot disentangle each contribution, but it is expected that the $4_1^+ \rightarrow 2_1^+$ transition is dominant. Calculations using the TALYS code [83] (described in more details in section 5.1) have been run and show that, in the case of inelastic excitation, the contribution of the $4_1^+ \rightarrow 2_1^+$ transition is 95% of the total. Since the uncertainty on the transition cross-section is much larger than 5%, and in order to avoid model dependent arguments, one can assume that the whole peak around 620 keV corresponds to the $4_1^+ \rightarrow 2_1^+$.

Unlike ^{100}Cd and ^{102}Sn, ^{98}Pd does not have any known isomer state. The remaining background contributions are the double exponential background and the C excitation. The double exponential background is, as described earlier, constrained from the results obtained for the inelastic excitation of ^{100}Cd, except for the amplitude of the high energy exponential, normalized by the statistics and charge number of both channels. The same procedure is applied for the amplitude of the C excitation contribution. As a result, there are seven free parameters for the γ spectra on CH_2 and C target:

- one for each response function of each of the photopeaks,
- one parameter for the double-exponential background.

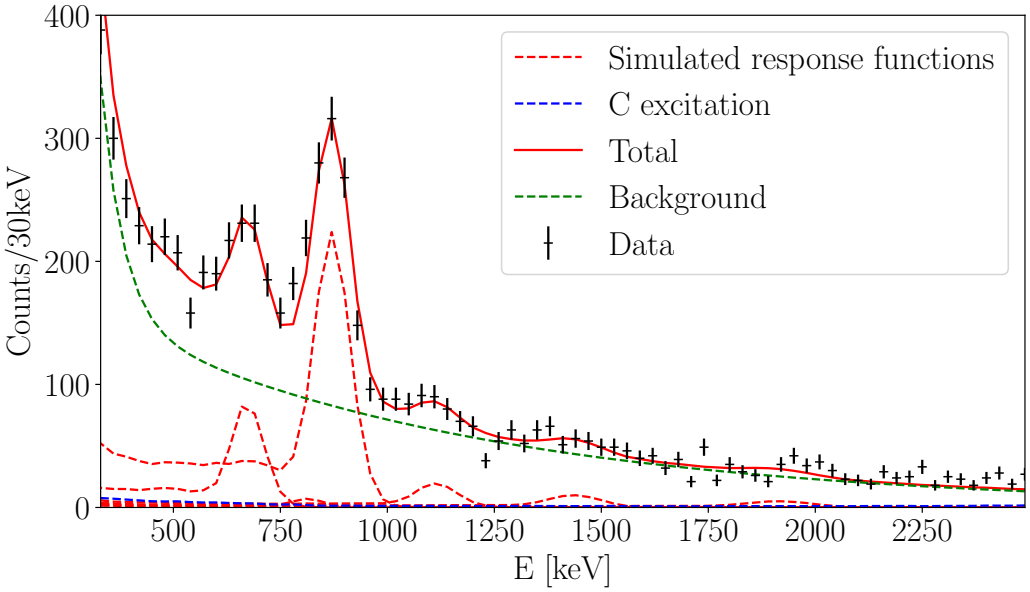

Figure 4.4: Doppler corrected energy spectrum for the inelastic excitation ^{98}Pd on CH_2 target. The red dashed lines are the response functions corresponding to the γ transitions fitted here at the energies of 801 keV, 863 keV, 1103 keV, 1427 keV, 1905 keV and of the $8_1^+ \rightarrow 6_1^+ \rightarrow 4_1^+ \rightarrow 2_1^+$ cascade. The green dashed line represents the double exponential background. The blue dashed line is the response function for the excitation of the C nuclei in the target. The solid red line is the sum of all the previously mentioned contributions. The data points are represented with their error bars as black crosses.

As it can be seen in figure 4.3, four excited states decay directly on the 2_1^+ state of ^{98}Pd. The corresponding Γ values are shown in table 4.1.

Transition energy (keV)	863	$4_1^+ \rightarrow 2_1^+$	1103	1427	1905
Γ_{CH_2} (mb)	21.5(14)	6.8(5)	2.4(3)	1.7(3)	1.2(3)
Γ_C (mb)	27.1(23)	10.7(12)	2.3(6)	0	4.3(9)

Table 4.1: Cross-sections for the transitions in ^{98}Pd, for CH_2 and C target. The 863keV-transition is the $2_1^+ \rightarrow 0_1^+$ transition. The other transitions are directly feeding the 2_1^+ state. The column "$4_1^+ \rightarrow 2_1^+$" is the estimate of the intensity for the $4_1^+ \rightarrow 2_1^+$ following the aforementioned method.

To extract the experimental cross-section, the intensity value for each feeder is subtracted from $\Gamma^{2_1^+ \rightarrow 0_1^+}$ for each target. This yields: $\sigma^{2^+}_{CH_2}$=9.3(16) mb and $\sigma^{2^+}_{C}$=9.9(26) mb. This yields for the hydrogen target: $\sigma^{2^+}_{H}$=9.0(27) mb.

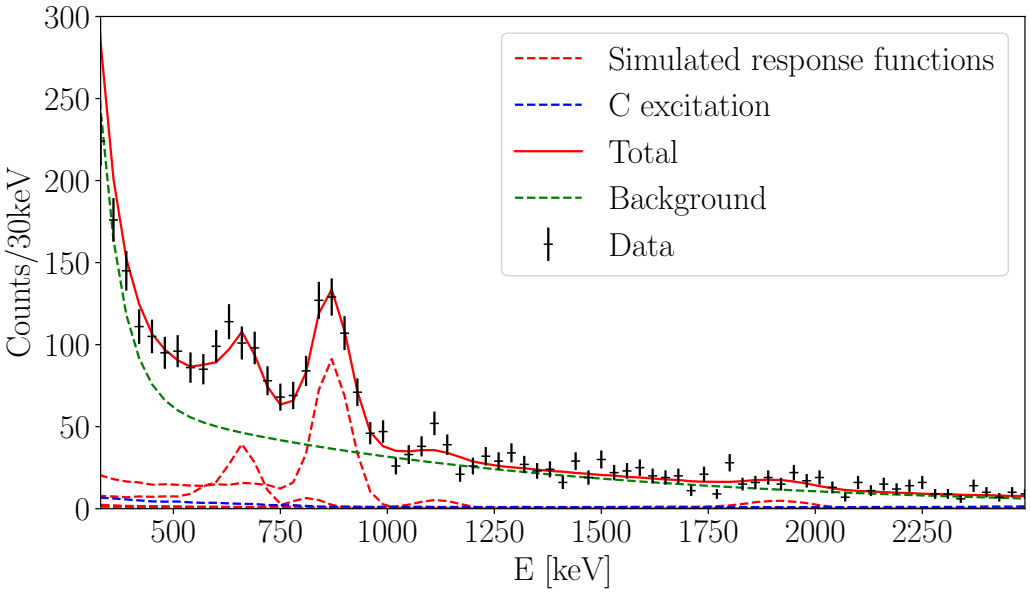

Figure 4.5: Doppler corrected energy spectrum for the inelastic excitation ^{98}Pd on C target. The red dashed lines are the response functions corresponding to the γ transitions fitted here at the energies of 801 keV, 863 keV, 1103 keV, 1905 keV and of the $8_1^+ \rightarrow 6_1^+ \rightarrow 4_1^+ \rightarrow 2_1^+$ cascade. The green dashed line represents the double exponential background. The blue dashed line is the response function for the excitation of the C nuclei in the target. The solid red line is the sum of all the previously mentioned contributions. The data points are represented with their error bars as black crosses.

4.3 ^{102}Sn

For the inelastic excitation of ^{102}Sn, the extraction of $\sigma_H^{2^+}$ has been done slightly differently from the two other channels. As the data for the C target had too low statistics to be fitted satisfactorily, the CH_2 and C target spectra have been subtracted to produce a reconstructed spectrum on H target. This spectrum has then been fitted directly, yielding the Γ values. This method is equivalent to fitting the CH_2 and C spectra, then subtracting the resulting cross-sections, as shown in appendix A. The fits for the CH_2 and the H target are displayed in figure 4.6 and 4.7 respectively. The γ energy spectrum for ^{102}Sn on C target can be seen in figure 4.8.

In an analogous way to the ^{98}Pd channel, the double exponential background is constrained by the one of the ^{100}Cd, as well as the C excitation. The isomer contribution is significant for this reaction channel and is constrained by the implantation runs, as exposed in subsection 3.2.4. This means that there are only three free parameters for these fits:

- one for the $2_1^+ \rightarrow 0_1^+$ transition,
- one for the $4_1^+ \rightarrow 2_1^+$ transition,
- one parameter for the double-exponential background.

Two response functions have been used to reproduce the photopeak around 1500 keV. One takes into account the direct population of the 2_1^+ state and its decay to the ground state. The other one takes into account the feeding of the 2_1^+ state from the decay of

the 4_1^+ state. Indeed, as the half-life of the 4_1^+ state is rather long (450 ps), the centroid and width of the two aforementioned response functions are different (the centroids are approximately 60 keV apart). For consistency, the amplitude of the response function for the $2_1^+ \rightarrow 0_1^+$ transition coming from the 4_1^+ state is set at the same value as the amplitude for the response function for the $4_1^+ \rightarrow 2_1^+$ transition. For the CH_2 target, the fit yields: $\Gamma_{CH_2}^{2_1^+ \rightarrow 0_1^+}$=6.9(18) mb and $\Gamma_{CH_2}^{4_1^+ \rightarrow 2_1^+}$=3.4(18) mb. For the H target, the fit yields: $\Gamma_H^{2_1^+ \rightarrow 0_1^+}$=7.3(29) mb and $\Gamma_H^{4_1^+ \rightarrow 2_1^+}$=5.5(29) mb. This yields the experimental cross-sections: $\sigma_{CH_2}^{2^+}$=3.4(5) mb and $\sigma_H^{2^+}$=1.8(4) mb.

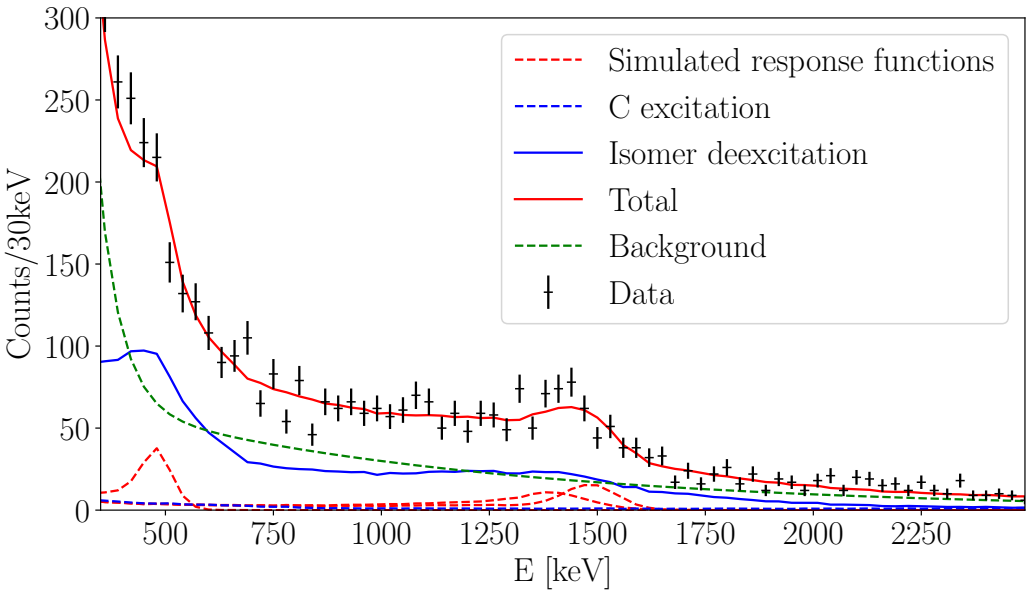

Figure 4.6: Doppler corrected energy spectrum for the inelastic excitation ^{102}Sn on CH_2 target. The red dashed lines are the response functions corresponding to the γ transitions fitted here at the energies of 1472 keV and 497 keV. The green dashed line represents the double exponential background. The blue dashed line is the response function for the excitation of the C nuclei in the target. The solid red line is the sum of all the previously mentioned contributions. The data points are represented with their error bars as black crosses.

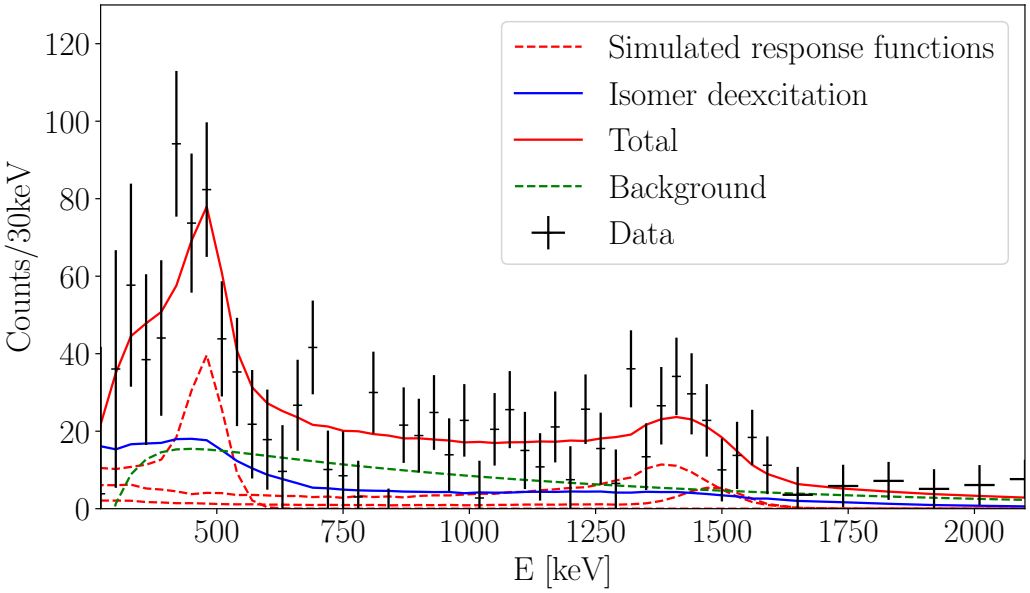

Figure 4.7: Doppler corrected energy spectrum for the inelastic excitation ^{102}Sn on H target. The red dashed lines are the response functions corresponding to the γ transitions fitted here at the energies of 1472 keV and 497 keV. The green dashed line represents the double exponential background. The blue dashed line is the response function for the excitation of the C nuclei in the target. The solid red line is the sum of all the previously mentioned contributions. The data points are represented with their error bars as black crosses.

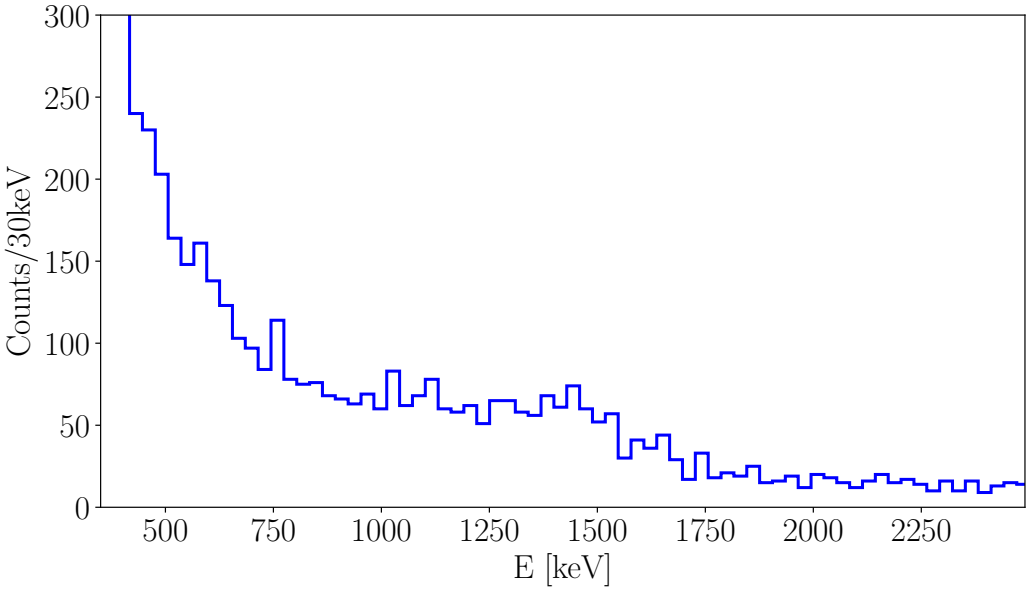

Figure 4.8: Doppler corrected energy spectrum for the inelastic excitation ^{102}Sn on C target.

4.4 Discussion

The intensities for the $2_1^+ \rightarrow 0_1^+$ and $4_1^+ \rightarrow 2_1^+$ transitions, and the experimental cross-sections of the inelastic excitation of the 2_1^+ state are summarized in table 4.2.

Isotone	^{98}Pd	^{100}Cd	^{102}Sn
$\Gamma_{\mathrm{H}}^{2^+\to 0^+}$ (mb)	18.7(24)	14.0(14)	7.3(29)
$\Gamma_{\mathrm{H}}^{4^+\to 2^+}$ (mb)	4.9(10)	6.4(11)	5.5(29)
$\sigma_{\mathrm{H}}^{2^+}$ (mb)	9.0(27)	7.7(17)	1.8(4)

Table 4.2: Summary of the intensities and cross-sections on H target for the three isotones N=52 of interest.

One can represent the experimental inelastic excitation cross-sections of the 2_1^+ state as a function of the atomic number Z. This is shown in figure 4.9 for the H target.

The systematic errors have been computed by varying of one standard deviation the amplitude of the contributions of σ^{2^+}, namely the intensities of the direct feeders of the 2_1^+ state and the background contributions, for $\sigma_{\mathrm{CH_2}}^{2^+}$ and $\sigma_{\mathrm{C}}^{2^+}$ of ^{98}Pd and ^{100}Cd, and for $\sigma_{\mathrm{CH_2}}^{2^+}$ and $\sigma_{\mathrm{H}}^{2^+}$ of ^{102}Sn. For the systematic error on $\sigma_{\mathrm{H}}^{2^+}$ of ^{98}Pd and ^{100}Cd, the systematic errors on $\sigma_{\mathrm{CH_2}}^{2^+}$ and $\sigma_{\mathrm{C}}^{2^+}$ have been combined according to the convolution formula [84]:

$$f_z(z) = \int f_x(x) f_y(z-x) dx. \tag{4.1}$$

This formula is written in the case of a quantity z written as the sum of two other quantities x and y, and uses their distribution noted f_i (with i being x, y, or z).

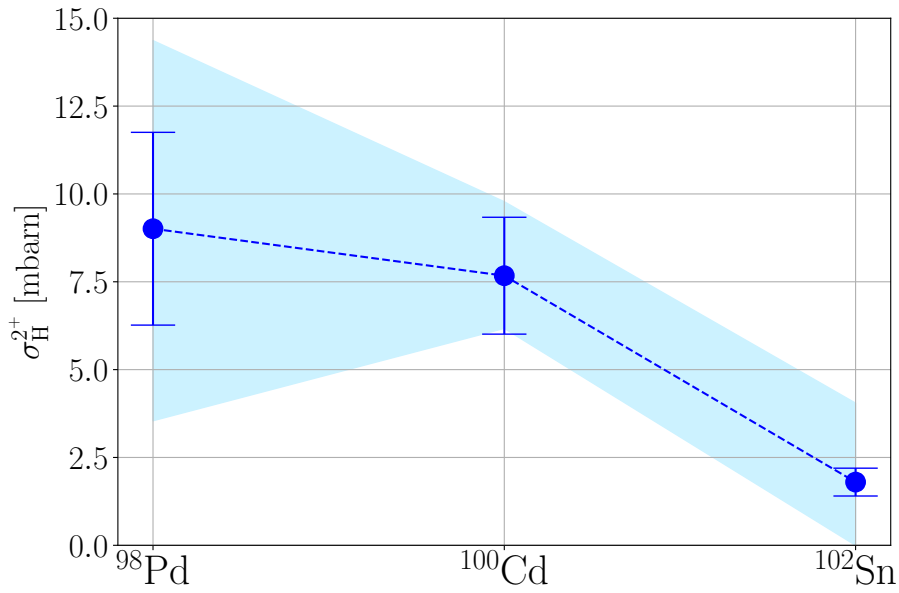

Figure 4.9: Cross-section for the inelastic excitation of the 2_1^+ state as a function of the charge number Z, on the H target. The error bars indicate the statistical errors, and the light blue area is the systematic error.

One can note that the systematic error for ^{98}Pd is larger compared to the one of the two other isotones. This can be explained by the high number of direct feeders for the 2_1^+ state. Indeed, these feeders are transitions yielding photopeaks with low amplitude, with rather large errors, in the γ spectra. Combining the errors on the amplitude of all these feeders increases the systematic error on the cross-section. Additionally, some

transitions between 600 and 900 keV have a large overlap, which increases the error on each amplitude.

Figure 4.9 shows a clear drop of the experimental inelastic excitation cross-section on H target going from Pd, Cd to Sn. This is the expected trend for this quantity. Indeed, the inelastic excitation translates into the collectivity of the 2_1^+ state, which is minimum in ^{102}Sn. At first approximation, if the $N = 50$ and $Z = 50$ shell closures are preserved, this state can be interpreted as formed via the excitation of the two neutrons above the $N = 50$ shell closure only.

The present measurement suggests that the $Z = 50$ shell closure is preserved to a certain extent for light Sn isotopes. To strengthen this statement, one could also look at the change in cross-sections with the neutron number N. This is shown on figure 4.10.

One should be aware that, in the case of ^{100}Cd and ^{98}Pd, the excitation of the 2^+ state can also arise from the recoupling of protons in the $g_{9/2}$ orbital, which is the one just below the $Z = 50$ shell gap. As a consequence, the information on the value of the transition matrix element M_n of the 2_1^+ state for open proton shells is less straightforward than the one of ^{102}Sn.

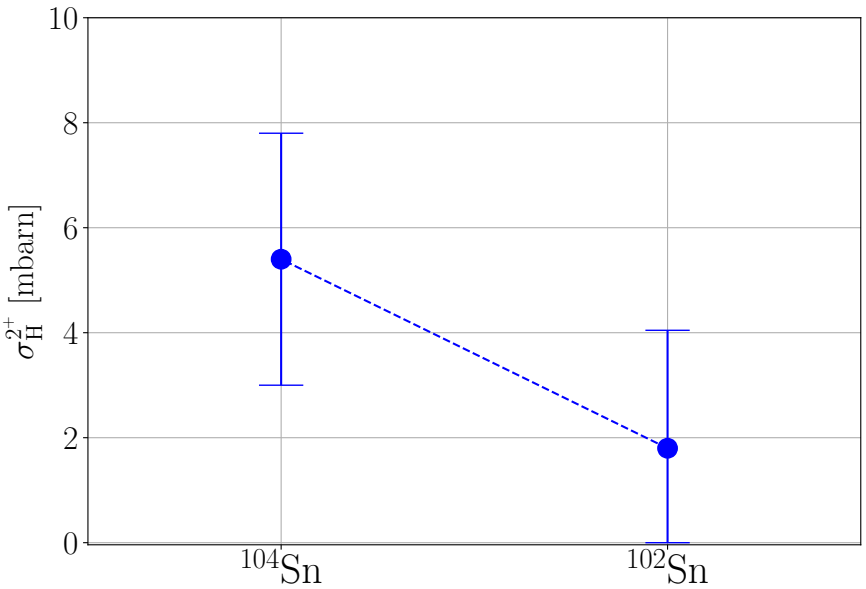

Figure 4.10: Cross-section for the inelastic excitation of the 2_1^+ state as a function of the neutron number N, on the H target. The value for ^{102}Sn is the one of the present work. The value for ^{104}Sn is taken from the work of A. Corsi *et al.* [47].

The inelastic excitation cross-section decreases approaching the $Z = N = 50$ shell closure, confirming the preservation of this shell closure. Hartree-Fock-Bogoliubov (HFB)+Quasi-particle Random Phase Approximation (QRPA) calculations using the Gogny D1M interaction have been performed by S. Péru and M. Dupuis (CEA-DAM, France). The parameters for the Gogny D1M interaction are fitted to all measured masses, with the constraints of providing reliable nuclear matter and neutron matter properties, as well as radii, giant resonance and fission properties for a given set of nuclei. The resulting potential is displayed in figure 4.11. One can see that the HFB potential is softening as Z decreases, so as one goes away from the $Z = 50$ shell closure, which agress with the

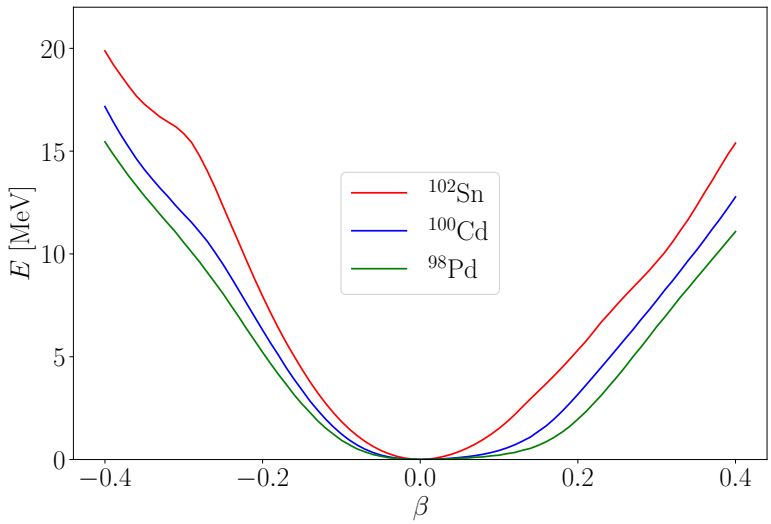

Figure 4.11: Theoretical HFB nuclear potential for ^{98}Pd, ^{100}Cd and ^{102}Sn. β is the quadrupole deformation parameter.

hints of preserved shell closure given by the experimental cross-sections. One-body neutron and proton local transition densities provided by QRPA and the semi-microscopic Jeukenne-Lejeune-Mahaux (JLM) optical potential [85, 86] have been used in a coupled -channels reaction calculations to obtain the theoretical estimate of the inelastic excitation cross-sections. The JLM potential is well suited for inelastic scattering on spherical and neaar-spherical nuclei with mass $40 < A < 209$, at energies up to 200 MeV/u. This method has already been used for ^{104}Sn [47], and for ^{72,74}Ni and ^{76,80}Zn [67]. The result of these calculations for both the systematics with respect to N and with respect to Z can be seen in figure 4.12.

The results of the theoretical calculations display a rather satisfactory qualitative reproduction for both the light Sn isotopes, and the $N = 52$ isotones. One can note that the theoretical values for the cross-sections are systematically lower than the experimental ones. An explanation for this discrepancy can be found in the fact that the experimental σ^{2^+} presented here is the intensity of the $2^+_1 \rightarrow 0^+_1$ transition, to which the intensities of the 2^+_1 feeders have been subtracted. This quantity is determined purely from experimental data, and these alone cannot take into account the feeding from the continuum of high excitation energy states. To estimate the contribution of this feeding, other theoretical calculations are needed, which are described in chapter 5. Subtracting this contribution from the experimental values will enable a quantitative comparison between theoretical and experimental results.

Both experimental and theoretical results point towards a preservation of the $Z = N = 50$ shell closure. To which extent the shell closure is preserved, e.g. regarding its softness, is an open debate (see the work of Togashi *et al.* [55] and references therein) and requires a more thorough comparison between theory and experiment, as well as additional data. These go beyond the scope of the present thesis.

Along C and CH_2 targets, a 0.5 mm Au target has been used during this experiment and the analysis of these data is performed by another collaborator, namely M.L. Cortes. From these runs, an experimental value for the $B(E2, 2^+ \rightarrow 0^+)$ will be provided. Combined with the results for the inelastic excitation, the transition matrix elements M_n and M_p

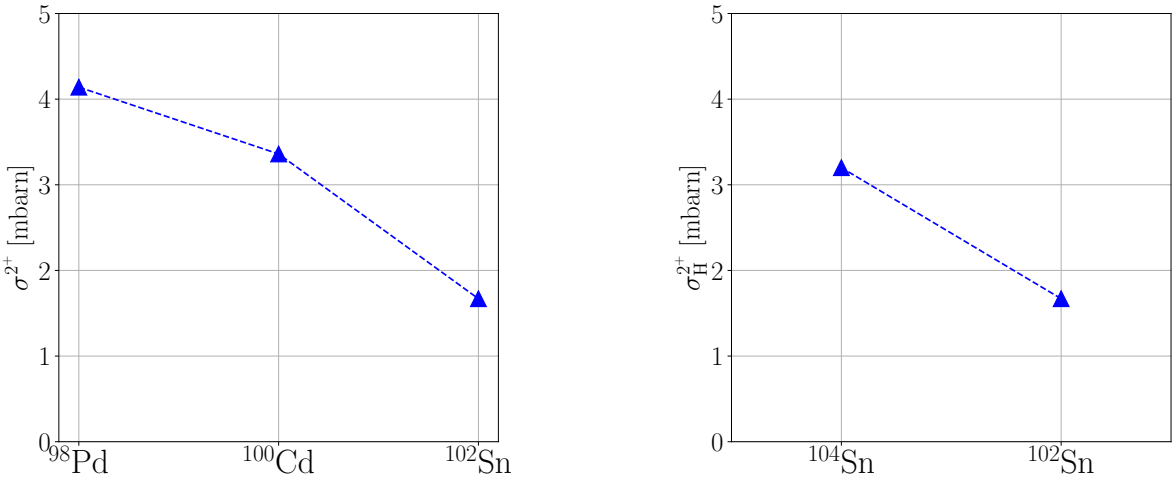

Figure 4.12: Theoretical QRPA-JLM calculations for the inelastic excitation cross-section of the 2_1^+ state for $N = 52$ isotones and $Z = 50$ isotopes. (a) Theoretical QRPA-JLM calculations for the inelastic excitation cross-section of the 2_1^+ state for ^{98}Pd, ^{100}Cd and ^{102}Sn. (b) Theoretical QRPA-JLM calculations for the inelastic excitation cross-section of the 2_1^+ state for ^{102}Sn and ^{104}Sn. The value for ^{104}Sn is taken from the work of A. Corsi *et al.* [47].

will be determined, and will provide a global view on the collectivity of light Sn isotopes.

Chapter 5

Conclusion and perspectives

5.1 Interpretation of the inelastic excitation cross-section

The experimental inelastic excitation cross-sections $\sigma_{\mathrm{H}}^{2^+}$ for the three isotones $N = 52$, namely ^{98}Pd, ^{100}Cd, and ^{102}Sn, have been determined. Figure 4.9 displays a clear decrease at the $Z = 50$ shell closure. This decrease can also be seen when changing the neutron number N, as the results from this work have been compared with previous ones on ^{104}Sn. These experimental results have been compared to theoretical calculations combining HFB calculations with QRPA, together with a semi-microscopic JLM potential. A satisfactory qualitative agreement is shown.

To improve the estimate of the inelastic excitation cross-section, and be able to quantitatively compare, it is planned to attempt to evaluate the contribution of feeding from the continuum. At high excitation energy, below the one-proton separation energy, the excited states are so close to each other that they form a continuum of states. During the reaction, this continuum can be populated and decay to lower states. Unlike the aforementioned transitions, these decays do not exhibit clear photopeak structures in the γ energy spectra. We plan to use the TALYS reaction code, developed by A. Koning, S. Hilaire and S. Goriely, to estimate this contribution [83].

TALYS uses the implementation of several nuclear reaction models allowing the calculation of cross-sections and Γ intensities for nuclear reactions involving nuclei with $12< A <339$ at the energy E between 1 keV and 200 MeV. It can be used as a nuclear reaction tool, to compare experimental results with the predictions of theoretical models, but it can also be used as a nuclear data tool. Indeed, TALYS also features large data libraries of both experimental and calculated values of observables, such as exclusive channel cross-sections, isomeric cross-sections, angular distributions, or yields for the production of medical isotopes. After selecting the adequate set of input parameters, such as the target, beam energy and projectile used in the reaction of interest, or the level density and pre-equilibrium parameters, one can generate data for further uses in nuclear reactor sizing, radiation shielding or nuclear waste disposal for instance. First, a sensitivity study of the effect of the different models for the level density, the photon strength function will be performed. Another relevant quantity in this process is the spin cutoff parameter, as it describes the spin structure of the continuum. This quantity is defined in the context of the pre-equilibrium exciton model [87]. This model, suitable for reaction energies above

10 MeV, considers the target+beam system, in which excited states are created step by step, characterized by their number of excitons, a general term to refer to particles and holes. One can note the exciton number $n = h+p$, h being the number of holes below the Fermi level and p the number of particles above the Fermi level. Within this framework, the level density is given by [88]:

$$R_n(J^\Pi) = \frac{1}{2} \cdot \frac{2J+1}{\sqrt{\pi n^3}\sigma_n^3} \exp\left(-\frac{(J+1/2)^2}{n\sigma_n^2}\right), \tag{5.1}$$

with J^Π the spin-parity assignment of the excited state of the nucleus of interest, n the exciton number, and σ_n the spin cutoff. The definition of the spin cutoff is:

$$\sigma_n = snA^{2/3}, \tag{5.2}$$

with A the mass number of the nucleus of interest and s the spin cutoff parameter. σ_n is the width of the angular momentum distribution of the states populated via the reaction of interest. The value of 0.24 is proposed for s, following the recent study by M. Kerveno *et al.* [88]. An improvement can be the use of microscopic calculations to determine a value of s for the energy used in this experiment. This procedure is expected to yield an experimental cross-section, corrected with theoretical reaction calculations, noted $\sigma^{2^+}_{exp-th}$. Eventually, a comparison will be made between the three values of $\sigma^{2^+}_{\mathrm{H}}$, $\sigma^{2^+}_{th}$ and $\sigma^{2^+}_{exp-th}$.

5.2 Other investigations in the ^{100}Sn region

This experiment was also meant to evaluate the production cross-section of ^{100}Sn in order to perform its first spectroscopy. The production of ^{100}Sn has been estimated to be 9.1(14) mb on C target and 5.1(15) on H target, via the one-neutron knockout reaction on ^{101}Sn [89]. The estimate is 0.5(1) mb on C target for the production via the two-neutron knockout reaction on ^{102}Sn. The goal of this experiment is the measurement of the half-life of the ground state of ^{100}Sn and the energy of its first excited state, namely its $E(2^+_1)$. This new experiment will benefit from a longer beam time than the experiment presented here improving the statistics of the resulting spectra.

Part II

Two-neutron decay of ^{13}Li and ^{11}Li

うぐひすの鳴そこなへる嵐かな　長良若風

Of the nightingale,

It has troubled the song —

The gusty wind.

Nagara no Jakufū, 1689

Chapter 6

Neutron-neutron correlations

Contents

The light neutron-rich nuclei display a wide variety of exotic structures, such as halo or Borromean features, as it is shown in figure 6.1. These effects emerge for systems with a limited number of nucleons, as little as 6 in the case of ^{6}He, and they push the limits of nuclear existence on the neutron-rich side of the nuclide chart, namely the position of the neutron drip line. The position of the neutron drip line is dictated by the smallest x-neutron separation energy S_{xn}. A negative S_{xn} would indeed mean that the emission of x neutron is energetically favorable, and imply that the given nucleus is unbound. A definition of the (one-neutron) separation energy for a given nucleus ${}^A_Z\mathrm{X}_N$ is:

$$S_n = B(A,Z) - B(A-1,Z), \tag{6.1}$$

with $B(A,Z)$ the binding energy of ${}^A_Z\mathrm{X}_N$, and $B(A-1,Z)$ the binding energy of ${}^{A-1}_Z\mathrm{X}_{N-1}$. A simple formula for the binding energy, provided by the liquid-drop model, is the Weizsäcker semi-empirical mass formula [91]:

$$B(A,Z) = a_V A - a_s A^{2/3} - a_C \frac{Z(Z-1)}{A^{1/3}} - a_A \frac{(N-Z)^2}{A} + a_P \delta_0(N,Z), \tag{6.2}$$

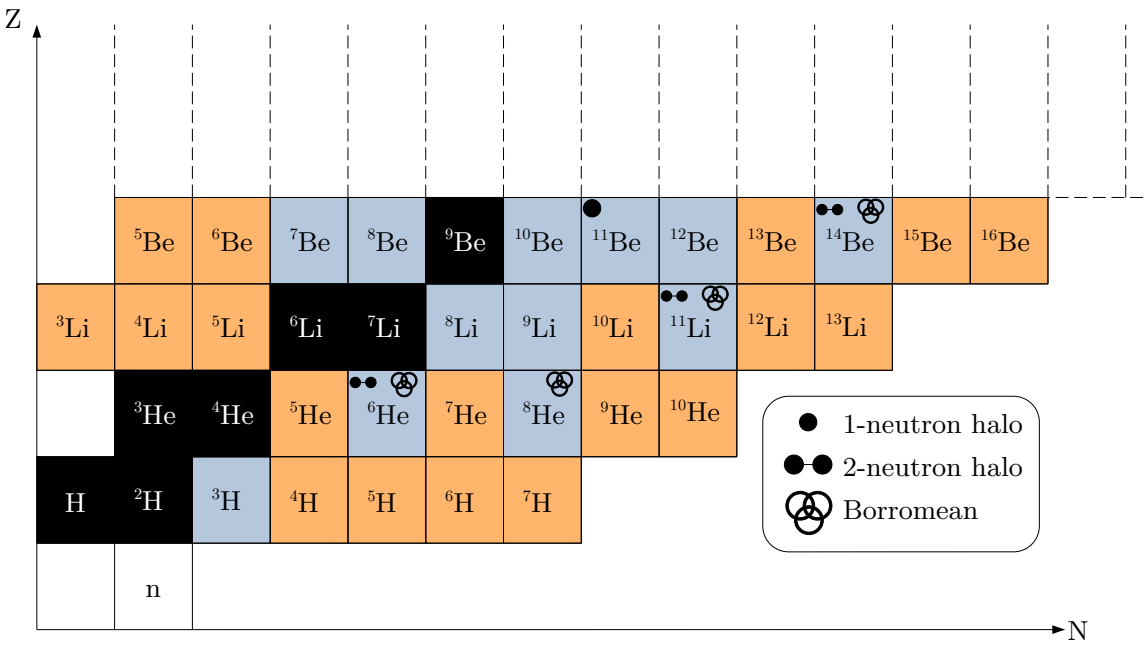

Figure 6.1: Portion of the nuclide chart with $0 \leq Z \leq 4$. The black nuclei are stable. The blue nuclei are exotic and bound, the orange ones are unbound. One can see the different Borromean systems mentioned in the text, such as ^{6}He, and ^{11}Li. This scheme also shows other examples of Borromean nuclei close to $Z = 3$, such as ^{14}Be [90].

with, for instance, a_V=15.75 MeV, a_s=17.8 MeV, a_C=0.711 MeV, a_A=15.75 MeV, a_P=11.18 MeV, and

$$\delta_0 = \begin{cases} A^{-1/2} & \text{if } N \text{ and } Z \text{ are even,} \\ -A^{-1/2} & \text{if } N \text{ and } Z \text{ are odd,} \\ 0 & \text{if } A \text{ is odd.} \end{cases}$$

Several sets of these parameters exist. The numerical values for the constants a_i are fitted to the experimental binding energy per nucleon of stable nuclei. These computed values can be compared to experimental data, as it is shown in figure 6.2. It appears that the Weizsäcker formula predicts unbound ^{8}He and ^{11}Li, while their measured S_n is positive, 2.535(8) MeV and 0.396(13) MeV, respectively. More complete descriptions of these nuclei are needed to get the correct sign for S_n. The pioneering study on Borromean nuclei by M.V. Zhukov *et al.* [92] mentions the neutron-neutron (n-n) correlations as carrying "more clear fingerprints of the underlying nuclear structure".

Correlations between nucleons are an important and complex phenomenon for the structure of the atomic nucleus, and their study has driven the scientific community to refine and to push the limits of the existing experimental setups. The decay of unbound nuclei is a way to study these correlations. Proton-proton (p-p) correlations have been studied via the two-proton decay of exotic nuclei since the early 2000s in systems such as the proton-rich ^{45}Fe [93], and later in the unbound ^{6}Be [94]. It is a decade later that the first results are produced on the two-neutron decay of unbound nuclei on ^{16}Be [95, 96] and ^{13}Li [97].

This chapter will first briefly describe the two special structures mentioned in the previous paragraph, namely halo and Borromean nuclei. Then, the particular study cases of ^{11}Li

and ^{13}Li will be discussed in more details, while presenting the motivations and objectives of this thesis.

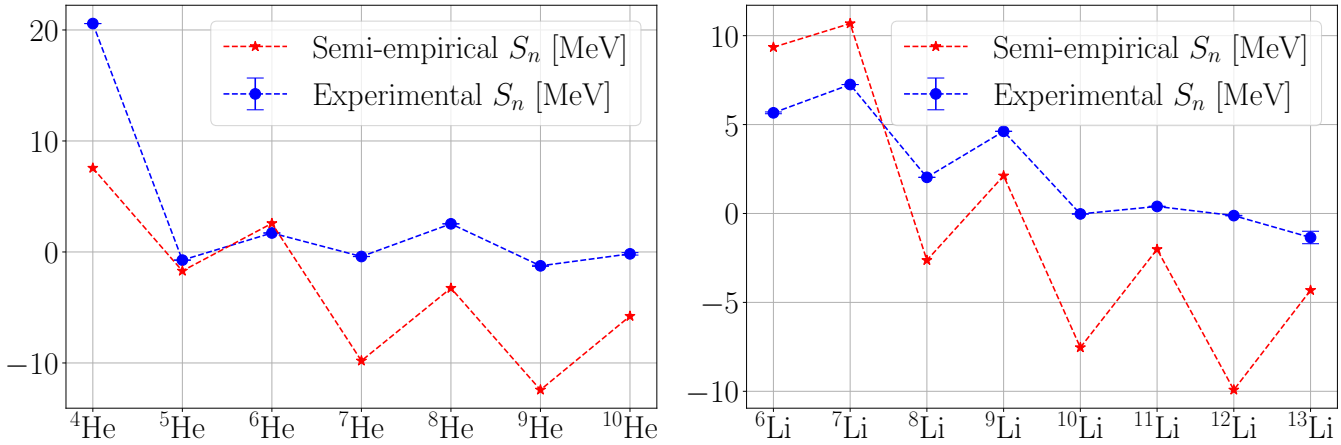

Figure 6.2: Comparison between the experimental and computed values for S_n for the He (a) and Li (b) isotopic chains. The blue dots are the experimental values, taken from [74], while the red stars are the computed values. (a) S_n for the He isotopes. (b) S_n for the Li isotopes.

6.1 Special nuclear structures in neutron-rich Li isotopes

6.1.1 Halo nuclei

The halo effect has first been discovered in 1985 by I. Tanihata *et al.* [98], with the measurement of a surprisingly large interaction cross-section of ^{6}He and ^{11}Li on a C target, suggesting a larger radius than expected. Two years later, the term "halo" is used for the first time by P. G. Hansen and B. Jonson [99], describing two neutrons of ^{11}Li bound weakly with a core of ^{9}Li. This results in a halo of matter around the core of the nucleus extending significantly further than the nuclear radius. This can be quickly appreciated by computing the radius of ^{6}He and ^{11}Li with the empirical radius formula, $R_{^{11}\mathrm{Li}} = r_0 \cdot A^{1/3} = 2.67$ fm and $R_{^{6}\mathrm{He}} = 2.18$ fm, and comparing it with the value measured in [98] of 3.27(24) fm and 2.73(4) fm for ^{11}Li and ^{6}He, respectively. The numerical values measured in [98] can be found in figure 6.3.

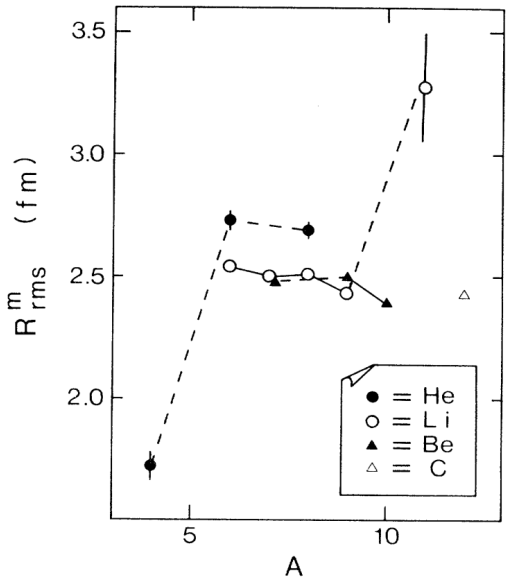

Figure 6.3: Matter rms radius R^m_{rms} as a function of the mass number A, for He isotopes, Li isotopes, Be isotopes and ^{12}C. Picture from [98].

With these pioneering studies, ^{11}Li has become one of the canonical examples for halo nuclei. ^{11}Li and ^{6}He previously mentioned are two-neutron halo nuclei, meaning that they are formed by a weakly bound core+neutron+neutron system. There also exists one-neutron halo nuclei, such as ^{11}Be, for which hints of an unusual structure have been found before Tanihata's work (see [100]). Some two-neutron halo nuclei have the other structural particularity of being Borromean nuclei, an effect explained in the following paragraph.

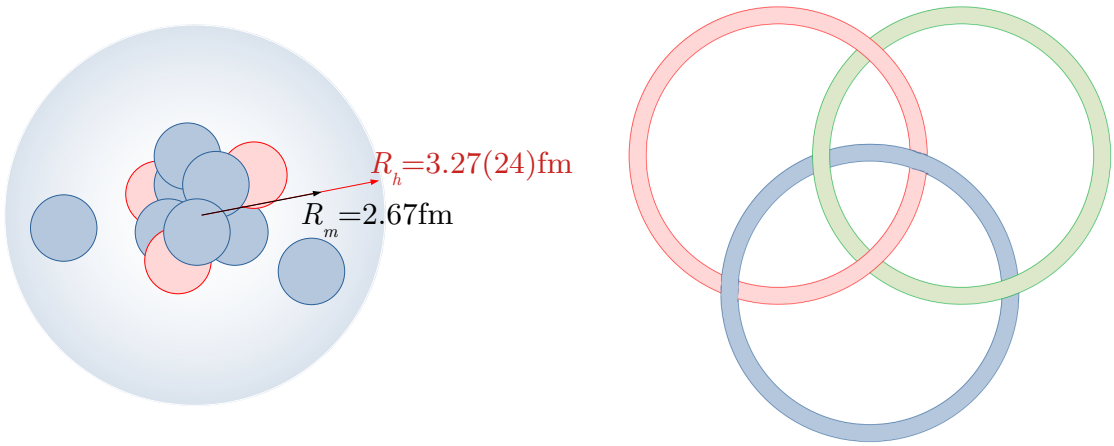

(a) (b)

Figure 6.4: (a) Schematic view of ^{11}Li as a halo nucleus. R_m is the matter radius and R_h is the halo radius, both have been exposed in the text. The red circles symbolize the protons, and the blue circles symbolize the neutrons. (b) Schematic view of the Borromean rings. Removing one ring also detaches the two others, while the three interlaced rings hold together.

6.1.2 Borromean nuclei

Borromean nuclei are named after the mathematical structure of the Borromean rings, referring to the emblem of the aristocratic Borromeo family rooted in Northern Italy [101]. Analogously to the rings, Borromean nuclei are bound three parts systems for which removing one part unbounds the structure. This is already described by Hansen and Jonson in [99], where it is exposed that a ^{9}Li core cannot bind a single neutron and that the binding between two neutrons is too weak to form a dineutron. However, these three bodies can be weakly bound together in a core bound to a dineutron. The first structure calculations for Borromean nuclei have been performed in 1993 by M.V. Zhukov *et al.* in [92] on ^{6}He and ^{11}Li, using for the first time the adjective "Borromean". As mentioned in the beginning of chapter 6, this work concludes on n-n correlations as a relevant source of information on the structure of Borromean nuclei. It also points out the sensitivity of these systems to the fragment-neutron correlations. This study ends on the necessity for experiments to provide complete measurements of reactions with Borromean and halo nuclei, a challenging endeavor that benefits from the support and the close connection with new theoretical models. In that context, it is important to consider observables that reveal not only n-n interactions but also fragment-neutron interactions, accessible experimentally, and relevant from the theoretical point of view. The following paragraphs describe such quantities, used in the following study, namely the relative energy and the Jacobi coordinates.

6.1.3 Invariant mass and relative energy

The invariant mass of the three-body (fragment+n+n) system is defined as follows:

$$M_{inv,3B} = \sqrt{E_{tot,3B}^2 - \overrightarrow{P}_{tot,3B}^2}, \tag{6.3}$$

with:

$$\begin{aligned} E_{tot,3B} &= E_f + E_{n_1} + E_{n_2}, \\ \overrightarrow{P}_{tot,3B} &= \overrightarrow{P}_f + \overrightarrow{P}_{n_1} + \overrightarrow{P}_{n_2}, \end{aligned} \tag{6.4}$$

with $E_{tot,3B}$ the total energy of the 3-body system, computed with E_f the energy of the fragment, E_{n_1} and E_{n_2} the energy of each neutron, and $\overrightarrow{P}_{tot,3B}$ the total momentum of the 3-body system, computed with $\overrightarrow{P}_f$ the momentum of the fragment, $\overrightarrow{P}_{n_1}$ and $\overrightarrow{P}_{n_2}$ the momentum of each neutron. The invariant mass relates the energies and momenta of the relativistic system. From this quantity, one can compute the relative energy of the system:

$$E_{rel,3B} = M_{inv,3B} - (m_f + 2m_n), \tag{6.5}$$

with m_n the neutron mass and m_f the fragment mass. Subtracting the rest mass of each part from the invariant mass yields the relative energy, which is the energy that is to be shared in the two-neutron decay. In a similar way, it is also possible to define the invariant mass and relative energy of both two-body systems: the fragment-neutron system (noted with the subscript '$2B, fn$') and the neutron-neutron system (noted with the subscript '$2B, nn$'). One can also define the two reduced relative energies that will be used for the

interpretation of the data:

$$\begin{aligned} \epsilon_{fn} &= \frac{E_{rel,2B,fn}}{E_{rel,3B}}, \\ \epsilon_{nn} &= \frac{E_{rel,2B,nn}}{E_{rel,3B}}. \end{aligned} \tag{6.6}$$

Peaks in the relative energy spectrum of the three-body system are hints that resonant states may organize the structure of the isotopes of interest. Peaks in the relative energy spectrum of the two-body (fragment+n) system are hints that the decay energy is not shared democratically among the fragment and the neutrons. These peaks also give indications that the intermediate systems may also be structured by resonant states. These considerations can also be made using correlated observables such as the Jacobi coordinates.

6.1.4 Jacobi coordinates

One can choose specific descriptions and parametrizations for the three-body system to compute correlations between parts of this system, e.g. the two neutrons emitted by the decay. A common choice for the type of decay presented in this study is the Jacobi coordinates [102]. One can first consider the momenta k_1,k_2 and k_3 of the three bodies and their respective masses m_1, m_2 and m_3 in a general manner. It is then possible to write the two following quantities:

$$\begin{aligned} \overrightarrow{k}_x &= \frac{m_2 \overrightarrow{k}_1 - m_1 \overrightarrow{k}_2}{m_1 + m_2}, \\ \overrightarrow{k}_y &= \frac{m_3 \left(\overrightarrow{k}_1 + \overrightarrow{k}_2 \right) - (m_1 + m_2) \overrightarrow{k}_3}{m_1 + m_2 + m_3}. \end{aligned} \tag{6.7}$$

One can now compute the two following quantities:

$$\begin{aligned} E_x &= \frac{(m_2 + m_1) k_x^2}{2 m_1 m_2}, \\ \cos\theta_k &= \frac{\overrightarrow{k}_x \cdot \overrightarrow{k}_y}{k_x k_y}. \end{aligned} \tag{6.8}$$

E_x is the energy associated with the momentum $\overrightarrow{k}_x$ and θ_k is the angle between $\overrightarrow{k}_x$ and $\overrightarrow{k}_y$. Applying these equations to the case of the three-body decay of ^{13}Li, two different systems are used:

- the T system, where 1 and 2 are both neutrons, labeled as n_1 and n_2, and 3 is ^{11}Li,
- the Y system, where 1 and 3 are both neutrons, and 2 is ^{11}Li.

A visualization of both systems, of the different momenta and of θ_k is provided in figure 6.5. In the proposed T system, equations (6.7) become:

$$\begin{aligned} \overrightarrow{k}_{x,T} &= \frac{\overrightarrow{k}_{n_1} - \overrightarrow{k}_{n_2}}{2}, \\ \overrightarrow{k}_{y,T} &= \frac{m_{^{11}Li} \left(\overrightarrow{k}_{n_1} + \overrightarrow{k}_{n_2} \right) - 2 m_n \overrightarrow{k}_{^{11}Li}}{2 m_n + m_{^{11}Li}}. \end{aligned} \tag{6.9}$$

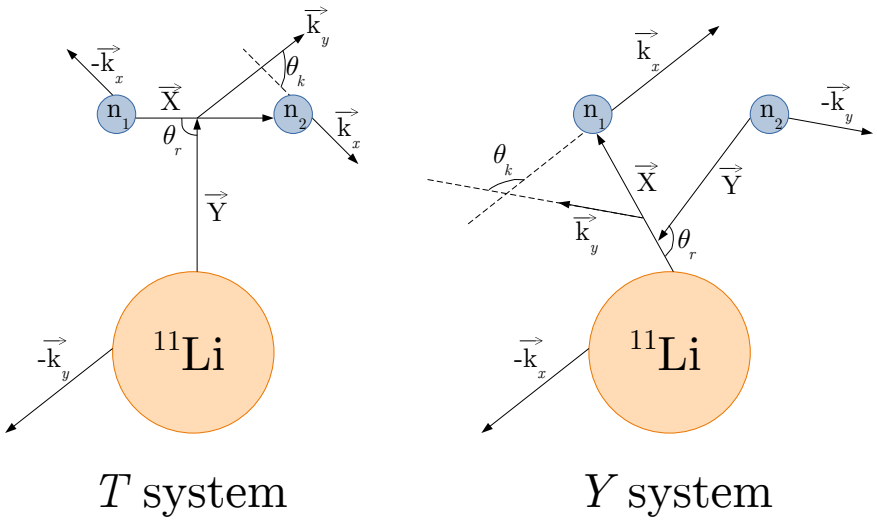

Figure 6.5: Schematic representation of the Jacobi coordinates in the T and Y systems, in the case of the decay of ^{13}Li.

Similarly, for the proposed Y system, equation (6.7) become:

$$\begin{aligned} \vec{k}_{x,Y} &= \frac{m_{^{11}Li}\,\vec{k}_{n_1} - m_n\,\vec{k}_{^{11}Li}}{m_n + m_{^{11}Li}}, \\ \vec{k}_{y,Y} &= \frac{m_n\left(\vec{k}_{n_1} + \vec{k}_{^{11}Li} - \vec{k}_{n_2}\right) - m_{^{11}Li}\,\vec{k}_{n_2}}{2m_n + m_{^{11}Li}}. \end{aligned} \tag{6.10}$$

In equations (6.9) and (6.10), $m_{^{11}Li}$ and m_n are respectively the mass of ^{11}Li and the neutron mass, and $\vec{k}_{^{11}Li}$, $\vec{k}_{n_1}$ and $\vec{k}_{n_2}$ the momenta of ^{11}Li, the first neutron and the second neutron respectively. For E_x, one can write:

$$\begin{aligned} E_{x,T} &= \frac{k_{x,T}^2}{m_n}, \\ E_{x,Y} &= \frac{(m_n + m_{^{11}Li})\,k_{x,Y}^2}{2m_n m_{^{11}Li}}. \end{aligned} \tag{6.11}$$

Replacing $m_{^{11}Li}$ by the mass of ^{9}Li, $m_{^{9}Li}$, one obtains the Jacobi coordinates for the decay of ^{11}Li.

The information about correlations among the three bodies is contained in $E_x/E_{rel,3B}$ and θ_k. The use of both systems is relevant to view different correlations among the three bodies. $E_{x,T}/E_{rel,3B}$ and $\cos(\theta_{k,Y})$ would highlight the correlations between the two neutrons, while $E_{x,Y}/E_{rel,3B}$ and $\cos(\theta_{k,T})$ would give clues on the nature of the decay process of ^{13}Li and ^{11}Li. The analysis, presented in chapter 8, will then rely on the four quantities $E_{x,T}/E_{rel,3B}$, $E_{x,Y}/E_{rel,3B}$, $\cos(\theta_{k,T})$ and $\cos(\theta_{k,Y})$, as well as on the relative two-body and three-body energies presented earlier.

6.2 State of the art

It has been suggested that the study of halo and Borromean nuclei, because of their weak neutron binding and their two-neutron decay scheme, is a great opportunity to extend the knowledge on neutron correlations in the atomic nucleus [92, 99]. Since the studies cited earlier have been made, experimental data have been made available on ^{10}Li, ^{11}Li, ^{12}Li and ^{13}Li. Some of these results are presented in the following paragraphs, selected based on their link to the present work (a similar method has been used, or information relevant for the analysis of the results shown later are provided).

6.2.1 ^{10}Li

D.R. Tilley *et al.* [103] propose a review of numerous studies on ^{10}Li populated via fragmentation or knockout reactions produced before 2004. More recent measurements have then been made performing knockout reactions with ^{11}Li beams by H. Simon *et al.* in 2007 [104], and Yu. Aksyutina *et al.* in 2008 [105], providing the measurement of a sharp s-wave virtual state as the ground state of ^{10}Li, and of a broader resonance centered around 500 keV. They respectively result in a value of -30^{+12}_{-31} fm and -22.4(48) fm for the scattering length of the s-wave ground state, and a resonance energy of 0.510(44) MeV and 0.566(14) MeV for the resonant state. A more precise measurement of the ground state of ^{10}Li has also been provided in 2015 by Y. Kubota *et al.* [106]. This study confirms the assigned angular momentum, and corresponds to a value of -17.0(25) fm for the scattering length. The relative energy spectrum for the ^{10}Li+n system from this study is shown in figure 6.6.

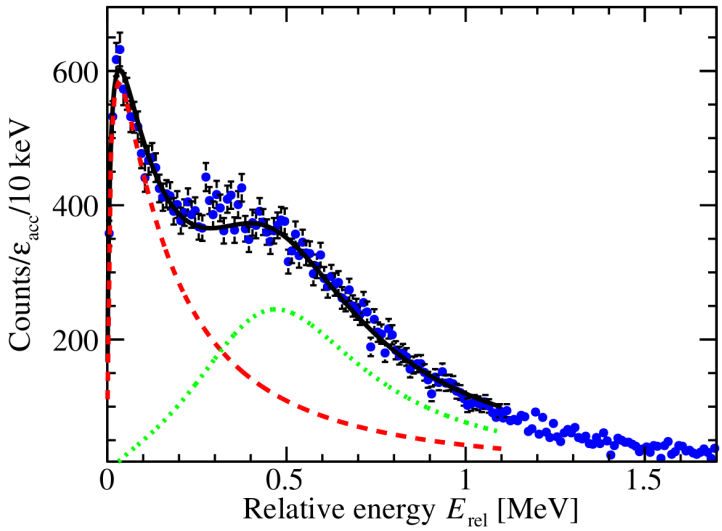

Figure 6.6: Relative energy spectrum of ^{10}Li. The red dashed line is an s-wave virtual state with a scattering length of -17.0(25) fm. The green dotted line is a p-wave with a resonance energy of 0.514(6) MeV and a width of 0.38(19) MeV. The black line is the sum of both contributions. Figure from [106].

6.2.2 ^{11}Li

As explained earlier, ^{11}Li has been studied numerous times in the past years. A selection of studies linked to the present work is proposed in the following paragraph. These works

bring spectroscopic information on the resonant states of ^{11}Li, or information on the n-n correlations in this system.

M. Zinser *et al.* performed in 1997 the break-up of a ^{11}Li beam on C and Pb targets, to measure the invariant mass spectrum of this Li isotope [107]. It provides the measurement of two wide resonant states at 1.0(1) and 2.4(2) MeV. A.A. Korsheninnikov *et al.*, the same year, confirm this statement by measuring an excited resonant state at around 1.3 MeV, assigning an orbital angular momentum of $l = 1$ [108]. H. Simon *et al.* confirmed these measurements by fitting the invariant mass spectrum of ^{11}Li, obtained by fragmentation of a ^{11}Li on a C target [104]. They provide a resonance energy of 1.24(5) MeV and 2.45(27) MeV for the two excited states, as well as the cross-section for populating these two states.

The characterization of the correlations in ^{11}Li can be done by considering angle distributions between the two neutrons [109]. One way is to consider the opening angle between the two neutrons, usually noted θ_{12}. It is related to the distance between the ^{9}Li core and the center of mass of the two neutrons, noted $r_{c,2n}$, as well as the neutron-neutron distance, noted r_{nn}. A schematic view of the different relevant quantities is shown in figure 6.7.

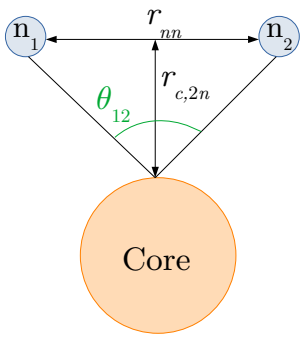

Figure 6.7: Schematic view of the opening angle, r_{nn}, and $r_{c,2n}$ in the core+n+n system.

The opening angle is expected to be around 90° without correlations and <90° with correlations, which also links a small r_{nn} with the presence of correlations. The link between the opening angle and the value of the reduced electric transition probability $B(E1)$ in the case of ^{11}Li has been provided by calculations performed by H. Esbensen and G.F. Bertsch in [110]. A measurement of the $B(E1)$ via Coulomb excitation of ^{11}Li on a Pb target has been performed in 2006 by T. Nakamura *et al.* [111]. The result of this experiment is the measurement of a strong soft $B(E1)$ transition, as predicted by Esbensen and Bertsch, typical of halo nuclei. It yields an opening angle of $\langle\theta_{12}\rangle = 48^{\circ}{}^{+14}_{-18}$, and a value for $\sqrt{\langle r^2_{c,2n}\rangle}$ of 5.01(32) fm. The large value for $\sqrt{\langle r^2_{c,2n}\rangle}$ confirms once more the correct representation of ^{11}Li as a halo nucleus. The low value for the opening angle provides a hint of strong n-n correlations. This has been nuanced in 2020 by Y. Kubota *et al.*, who performed quasi-free scattering with a ^{11}Li beam [112]. The angle considered in this study is noted θ_{fn}, and is almost the analog of θ_{12} in momentum coordinates. It

is defined as follows:

$$\cos(\theta_{fn}) = \frac{(\overrightarrow{k}_{n_1} + \overrightarrow{k}_{^9Li}) \cdot \overrightarrow{k}_{x,Y}}{\| \overrightarrow{k}_{n_1} + \overrightarrow{k}_{^9Li} \| k_{x,Y}}, \tag{6.12}$$

using the notations of subsection 6.1.4. The relationship $\theta_{fn} = 90° - \theta_{12}$ implies that $\theta_{fn} < 90°$ is the sign of the existence of correlations. The result of the experiment is a peak in $\langle\theta_{fn}\rangle$ for a missing momentum k of $\sim$3 fm^{-1} with a value of $\sim$101°, equivalent to θ_{12} $\sim$79°. This value for the missing momentum is equivalent to a distance of $\sim$3.6 fm from the core for the two correlated neutrons.

The characterization of the n-n correlations used in the present work, based on the formalism of R. Lednicky and V.L. Lyuboshits [113] (detailed in subsection 8.4.4), relies on the value of r_{nn}. In 2000, F.M. Marqués *et al.* used this formalism, implemented via an iterative method, to produce n-n correlations in momentum space and compare them to experimental data on ^{11}Li obtained by two-neutron interferometry, to deduce a value of r_{nn} [114]. This yields a value of r_{nn} = 6.6(15) fm for ^{11}Li, revealing rather strong n-n correlations. In 2016, J.K. Smith *et al.* proposed a study of the two-neutron decay of ^{11}Li using a Monte Carlo GEANT4-based simulation of the n-n correlations, also described using the Lednicky-Lyuboshits formalism [115]. The procedure described in the present thesis is very similar to the one applied there. Starting from the level scheme of ^{11}Li, several decay paths have been taken as an ansatz and simulated. The Jacobi coordinates of the ^{9}Li+n+n system are then fitted by these response functions. The conclusion of this work is that the data are best reproduced by the simultaneous emission of two correlated neutrons. These results can be seen in figure 6.8.

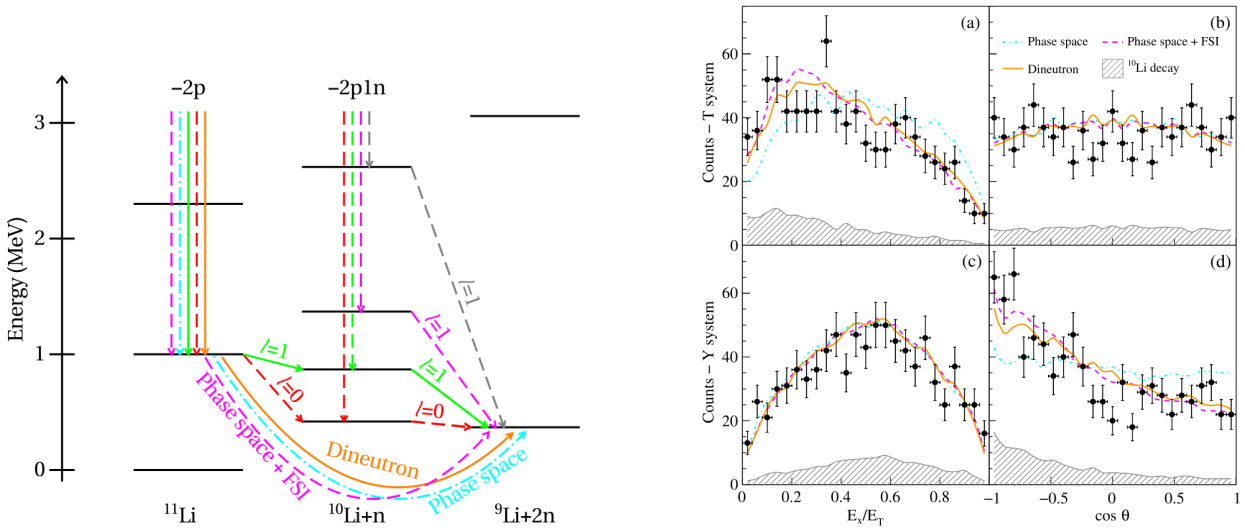

Figure 6.8: (a) Level scheme for the population and decay of ^{10}Li and ^{11}Li showing the decay paths used in their simulation by J.K. Smith *et al.* in [115]. Figure from [115]. (b) Fit of the Jacobi coordinates of the ^{9}Li+n+n system by J.K. Smith *et al.*, considering a simultaneous emission of two correlated neutrons. The top row displays coordinates for the T system, and the ones for the Y system are on the bottom row. The left column shows $E_x/E_{rel,3B}$, and the right column shows cos(θ). Figure from [115].

6.2.3 ^{12}Li

All the works mentioned in this paragraph study the one-neutron decay of ^{12}Li to obtain spectroscopic information on this nucleus. The first measurement of the ground state of ^{12}Li, produced via (p,2pn) on ^{14}Be, has been performed in 2008 by Yu. Aksyutina *et al.* [105]. This study shows that the ground state of ^{12}Li can be described as a virtual s-wave state with a scattering length of -13.7(16) fm. This value has then been challenged in 2013 by Z. Kohley *et al.*, who populated ^{12}Li in the same way, and who fitted the ground state with a virtual s-wave state with a scattering length greater than 4 fm [97]. Two excited states have then been measured by C.C. Hall *et al.* in 2010, which uses two-proton removal on ^{14}B to populate these states [116]. The resonance energy for these states are 0.25(2) MeV and 0.555(20) MeV. The relative energy spectrum for ^{12}Li proposed by C.C. Hall *et al.* is shown in figure 6.9.

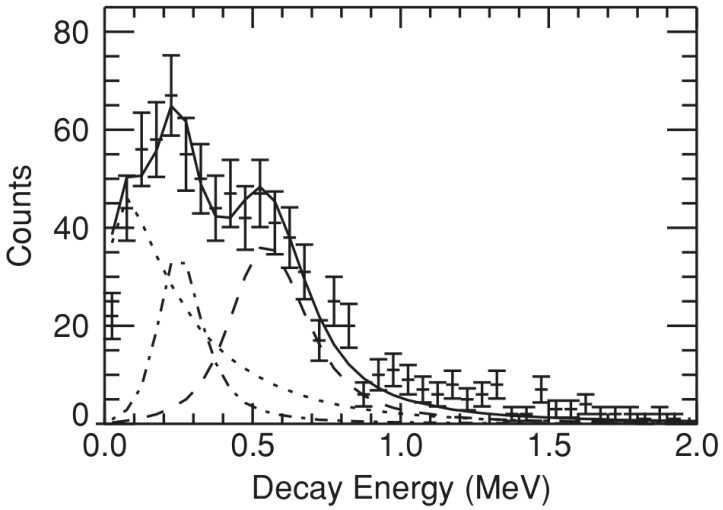

Figure 6.9: Relative energy spectrum of ^{12}Li. The dotted line is an s-wave virtual state with a scattering length of -13.7(16) fm. The dotted dashed line is a resonance state with a resonance energy of 0.25(2) MeV. The dashed line is a resonance state with a resonance energy of 0.555(20) MeV. The black line is the sum of all these contributions. Figure from [116].

6.2.4 ^{13}Li

The two studies shown here, as well as the present thesis, populate various states of ^{13}Li via a (p,2p) reaction on ^{14}Be. The first measurement of a resonant state in ^{13}Li has been performed by Yu. Aksyutina *et al.* in 2008, and fitted by a resonance energy of 1.47(31) MeV [105]. Two years later, the same data has been used by H.T. Johansson *et al.* to compute the Jacobi coordinates of the three-body system [117]. The ground state has then been measured in 2013 by Z. Kohley *et al.*, with a resonant energy of $0.12^{+0.06}_{-0.08}$ MeV [97]. In this study, the Jacobi coordinates have also been computed and fitted, supposing the simultaneous emission of two correlated neutrons. These results are shown in figure 6.10.

6.3 Objectives of the present thesis

The present work will focus on the detected two-neutron events. This way, only the n-n correlations in the pair emitted by the isotopes of interest and the process for the emission

of two neutrons are considered. As mentioned in the previous paragraphs, the present thesis presents the study of the two-neutron decay of ^{11}Li and ^{13}Li, both populated via a (p,2p) reaction, on ^{12}Be and ^{14}Be, respectively.

The energies and momenta of the fragment and the two neutrons are all measured, and the relative energy spectra for the fragment+neutron+neutron (f+n+n) and the fragment+neutron (f+n) systems, as well as the Jacobi coordinates, are reconstructed. Thanks to the experimental setup, presented in the following chapter, and the high intensity of the exotic beam, the resolution and statistics are higher than for the aforementioned studies. The resonant states in the f+n+n relative energy spectra will then be fitted. With the help of a GEANT4-based simulation package, named SAMURAI-SIM, the response functions for the simultaneous decay of two correlated neutrons (also referred to as direct decay), or the delayed decay of two correlated neutrons (also referred to as sequential decay), will be simulated for each of the fitted resonant states. The f+n relative energy spectra will be fitted to constrain the potential resonant states populated in the intermediate systems, namely ^{10}Li and ^{12}Li. These response function will then be used to fit the Jacobi coordinates, for various ranges of f+n+n relative energy. This set of observables is sensitive to the nature of the decay, direct or sequential, and also to the strength of the n-n correlations.

These fits will then provide information on the proportion of sequential or direct decay for a given resonant state in a given f+n+n relative energy range. The radius r_{nn} mentioned previously will be left as a free parameter in the simulation to provide a characterization of the correlations in the two Li isotopes of interest.

The following chapters will first describe the experimental setup used for this work. As exposed in sections 6.1.3 and 6.1.4, the considered observables require the measurement of the energy and momenta of each particle involved in the decay, requiring a substantial variety of detectors. Then, the treatment that has been performed on the data will be exposed, as well as the different observables considered in the analysis. Eventually the results will be shown and discussed.

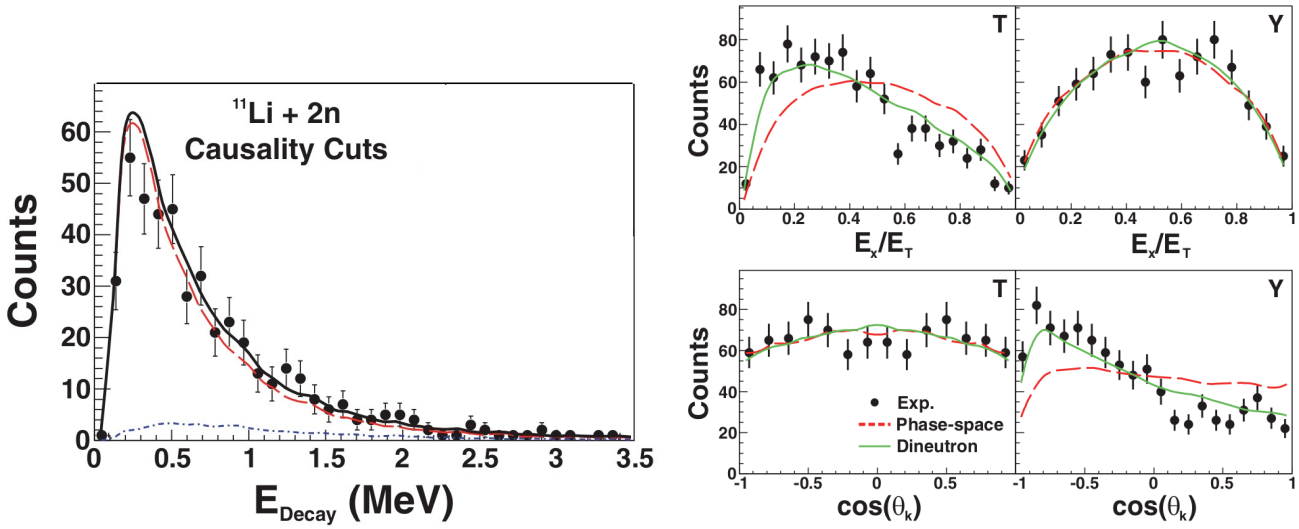

(a) (b)

Figure 6.10: (a) Relative energy spectrum for the ^{11}Li+n+n system proposed by Z. Kohley *et al.*. The red dashed line is the contribution of the two-neutron decay of ^{13}Li. The blue dotted dashed line is the contribution of the one-neutron decay of ^{12}Li. The black line is the sum of these contributions. Figure from [97]. (b) Fit of the Jacobi coordinates of the ^{11}Li+n+n system by Z. Kohley *et al.*. In solid green is the simulation for a simultaneous emission of two correlated neutrons. In dotted dashed red is the simulation for a simultaneous emission without correlations (also named phase space distribution). The left column displays coordinates for the T system, and the ones for the Y system are on the right column. The top row shows $E_x/E_{rel,3B}$, and the bottom row shows $\cos(\theta)$. Figure from [97].

Chapter 7

Experimental setup

Contents

The data analyzed in this study have been acquired at RIBF, at the RIKEN Nishina Center, as part of the s018 campaign, using a beam-line that is very similar to the one presented in part I. Here, a beam of ^{48}Ca was fired at an energy of 345 MeV/nucleon and an intensity of 400 pnA on a primary ^{9}Be target. This yielded a cocktail beam mainly composed of ^{11}Li, ^{14}Be and ^{17}B, and of ^{12}Be in a lesser proportion [118]. These three nuclei then impinge on the MINOS liquid hydrogen target at an energy of 246, 265 and 277 MeV/nucleon respectively. The reactions of interest in MINOS are for this study ^{14}Be(p,2p)^{13}Li$\rightarrow$ ^{11}Li+2n and ^{12}Be(p,2p)^{11}Li$\rightarrow$ ^{9}Li+2n. The whole beam line is displayed on figure 7.1. One can describe the experimental setup in three parts in an analogous way as what is done in part I. The two first parts are the acceleration stage and BigRIPS, and have been already described in part I. The third part of the setup is however different from the one introduced before, as the Superconducting Analyzer for MUlti particles from RAdio Isotope Beams (SAMURAI) is used here. The next sections will then be focused on the description of the different devices composing this spectrometer.

7.1 The SAMURAI magnet

The SAMURAI spectrometer is a set of detectors used in this experiment to detect each particles or radiation produced by the reaction of interest, and reconstruct observables such as momenta for all the reaction products [119]. A schematic view of the spectrometer is shown in figure 7.2.

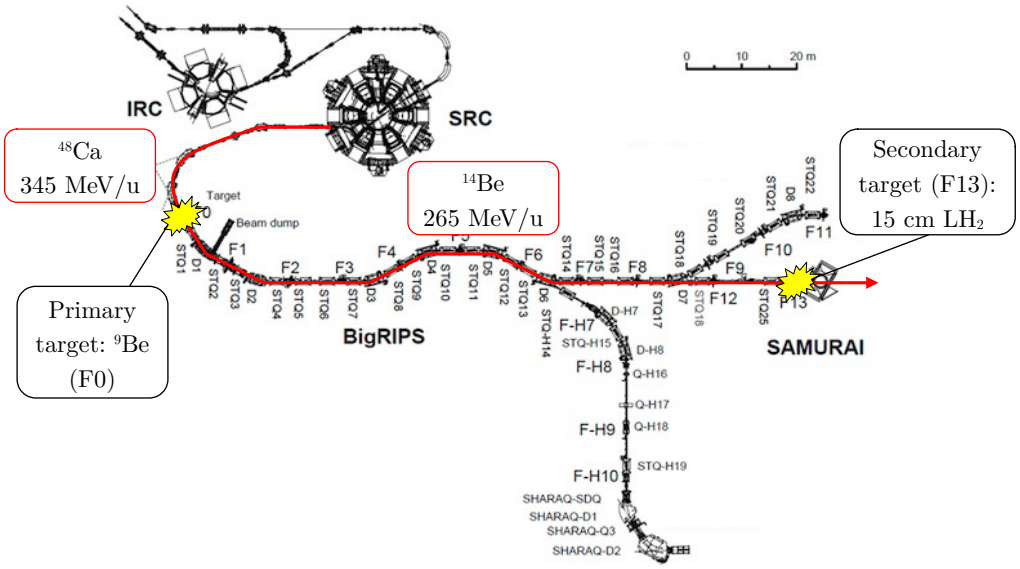

Figure 7.1: Schematic view of the BigRIPS-SAMURAI beam-line at RIBF. IRC stands for Intermediate stage Ring Cyclotron, and SRC for Superconducting Ring Cyclotron. These are parts of the accelerators used before BigRIPS. The primary and secondary targets are indicated, as well as the primary and secondary beam energies. Image from [57].

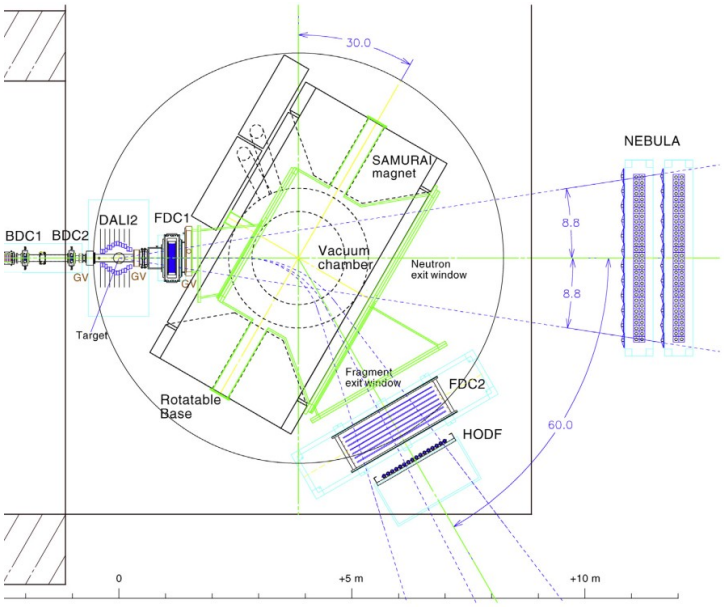

Figure 7.2: Plan of the SAMURAI spectrometer around the SAMURAI magnet. Figure from [120].

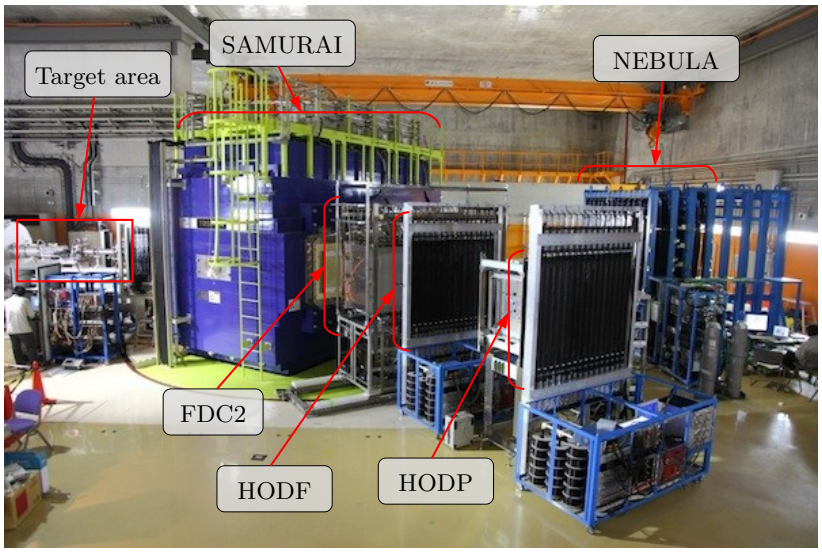

Figure 7.3: Picture of the SAMURAI magnet, as well as some other detectors composing the SAMURAI spectrometer. Picture from [121].

The nuclei in the cocktail beam impinge on the MINOS target. The electromagnetic radiations that can be emitted during the reaction between the beam and the target are detected in the DALI2 array, that has been described in section 2.3. One can note that, for this experiment, the DALI2 detector was used in a reduced version with 68 crystals. Figure 7.4 displays a picture of this configuration.

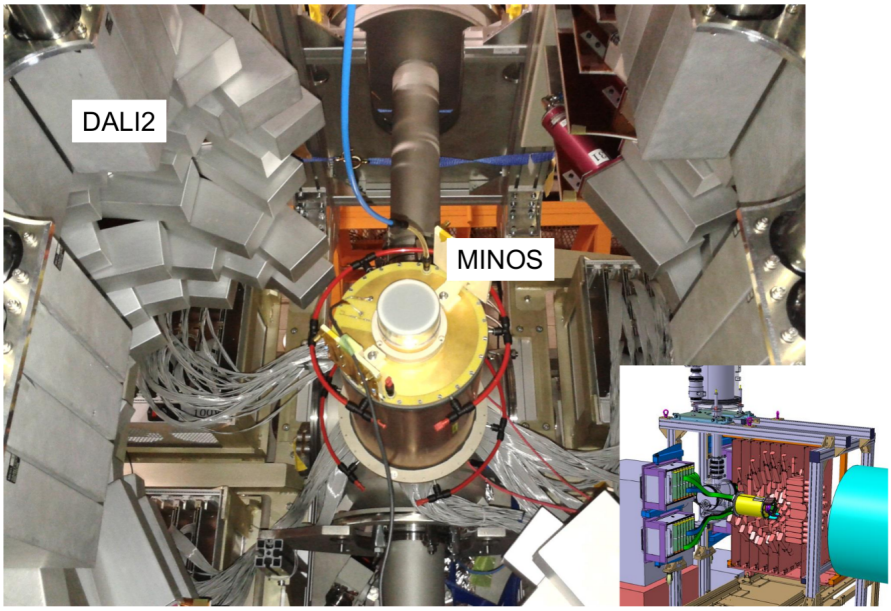

Figure 7.4: Picture of half of the DALI2 array in the s018 experiment. The cylinder in the middle is the MINOS TPC. For the configuration of DALI2 during beam time, both halves of DALI2 are put together to enclose the MINOS TPC. The bottom right corner is a 3D zoomed out view of the array. Picture by the SAMURAI collaboration.

The decay neutrons then go through the SAMURAI magnet before hitting the NEBULA

array. The charged particles are deflected by the magnetic field in the magnet and go into the fragment and proton hodoscopes. Before and after the magnet, forward drift chambers are placed to measure the position of the beam. Details on these detectors are given in the following sections.

The central piece of the SAMURAI spectrometer is the SAMURAI magnet. It is a superconducting dipole magnet measuring 6.7×3.5×4.64 m^3, able to provide a maximum magnetic field of 3.08 T at 563 A giving a bending power of 7.05 Tm [122].

7.2 MINOS

The MINOS (that stands for "nuclear MagIc Numbers Off Stability") device is a liquid hydrogen target coupled with a tracking system [123]. A schematic view of this system can be found in figure 7.5.

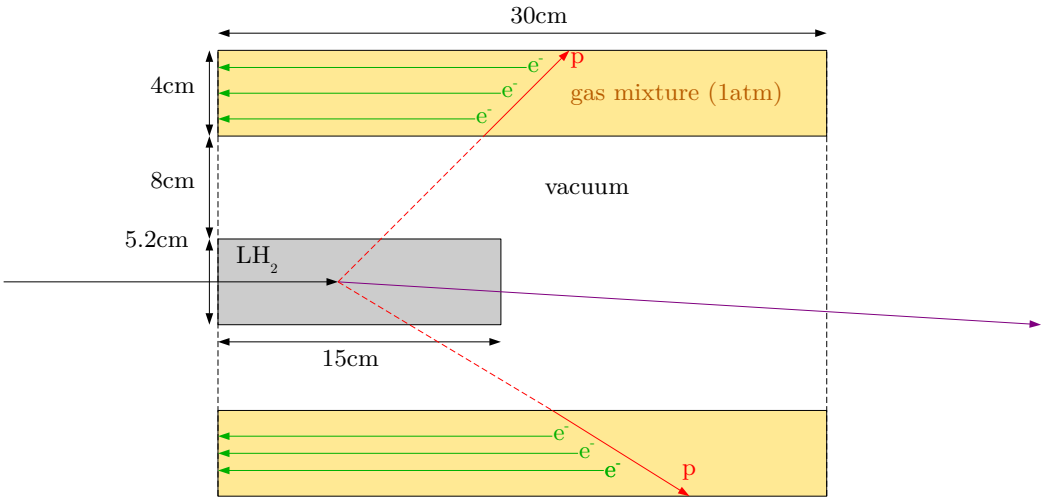

Figure 7.5: Schematic view of the MINOS target.

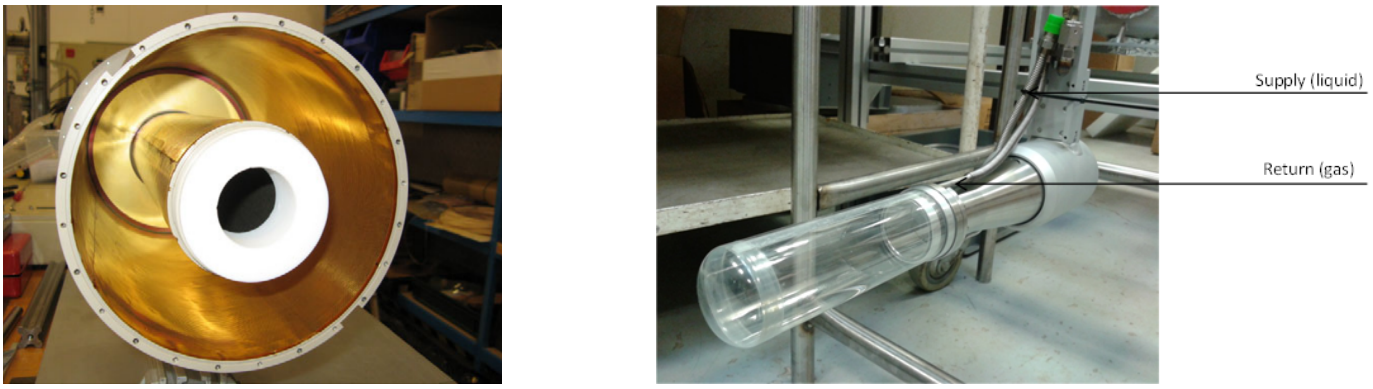

(a) (b)

Figure 7.6: (a) The MINOS field cage. Taken from figure 10 in [123]. (b) The cell which contains the liquid hydrogen target. Taken from figure 12 in [123].

The liquid hydrogen is contained in a cylindrical cell of 15 cm in length and 5.2 cm in diameter. This cell is placed in a vacuum tube of 80 mm in diameter. Around it is the time projection chamber (TPC) dedicated to the tracking of the recoil proton and, in our case, the knocked-out proton. This part of the device is filled with a gas mixture of Ar (82%), isoC_4H_{10} (3%) and CF_4 (15%) at a pressure of 1 atm. The two plates at each end of the TPC are powered with a voltage difference of approximately 6 kV, creating an electric field of around 180 V/cm. When the beam is on, it impinges on the target and may react with the liquid hydrogen in the cell.

In the case of ^{14}Be(p,2p)^{13}Li and ^{12}Be(p,2p)^{11}Li, one proton is knocked out of the beryllium isotope and one from the target recoils. Both protons go through the tracking system and ionize the gas in it. The electrons resulting from the ionization then drifts thanks to the action of the electric field. The position and timing of the drifting electrons on the plate enable the reconstruction of the trajectory of each proton. Intersecting these trajectories with each other and with the trajectory of the beam provides the position of the interaction vertex.

7.3 WINDS and RP detector

Two detectors were located on each side of the target. One of them, called WINDS (Wide-angle Inverse-kinematices Neutron Detectors for SHARAQ) , is an array of plastic scintillators covering angles between 20° and 60°, and is used for the detection of knocked-out neutrons, in the case of a (p,pn) reaction in the target for example [124]. The reaction of interest for the present work being (p,2p), the information from this detector has not been used.

The other detector is the Recoil Proton (RP) detector, which covers angles between 30° and 65°, and is used for the tracking of the recoil proton in the case of a (p,2p) reaction in the target for example [118]. It is composed of multi-wire drift chambers (MWDC), used for the tracking of the trajectory of the recoil proton, and of an array of plastic scintillators for time-of-flight measurements. The data acquisition is triggered when a proton is detected in the RP detector, ensuring the selectivity for the quasi-free scattering (QFS) process. This is detailed in section 8.1.

7.4 NEBULA

The NEBULA detector (NEutron-detection system for Breakup of Unstable nuclei with Large Acceptance) [120] is an array of plastic scintillators used for the detection of neutrons at the RIBF facility. These scintillators are plastic bars measuring $12\times12\times180$ cm^3. They are distributed into two walls composed themselves by two layers of 30 scintillators, with a PMT on each end of the bar.

The studied reactions yield two neutrons that go through the SAMURAI magnet and hit the detectors of NEBULA. An incident neutron then knocks out a proton from the plastic of the scintillators that will excite the surrounding material, triggering the fluorescence mechanism. By looking at which scintillators are hit, this provides the time-of-flight, the position and the deposited charge in the plastic scintillators of the incident neutrons.

The discrimination between an incident charged particle or an incident neutron can be

done via the use of VETO walls. These additional walls are positioned before each wall of the NEBULA array and are made of 1 cm thick plastic scintillators. The neutron detection efficiency for the VETO walls is very low due to the thinness of the detectors. This width is however large enough to detect charged particles. A signal in these walls would result in the rejection of the event.

7.5 Fragment and proton hodoscopes

The fragment and proton hodoscopes (HODF and HODP respectively) are detectors placed after the SAMURAI magnet [120]. These devices are identical and are arrays of 16 plastic scintillators placed next to each other. Each plastic module measures $10\times120\times1$ cm^3, for a wall with a total length of 160 cm. The HODF wall is not exactly aligned with the HODP wall, as the magnetic rigidity of the different charged fragments, ^{9}Li and ^{11}Li in this case, are different, and the acceptance needs to be maximized. Each module is coupled with two photomultiplier (reference R7195 Assy), one up and one down, to amplify the fluorescence signal triggered by the charged particle.

7.6 Drift chambers

Multi-wire proportional drift chambers (MWPC) are used to track the position of the beam at a given point in the setup [120]. For the SAMURAI spectrometer, one can distinguish beam drift chambers (BDCs) and forward drift chambers (FDCs). BDCs are placed before the MINOS target to measure the position of the beam before the reaction. They are $320\times320\times120$ mm^3 boxes filled with isoC_4H_{10} gas. In this setup, one FDC is placed right before the SAMURAI magnet (and is denoted FDC1) and one FDC right after the SAMURAI magnet (denoted FDC2). The FDC1 features a rectangular opening window measuring 62×34 cm^2, with an effective area of 31.5 cm in diameter in the middle, and measures the angle of emission for the charged heavy fragments after the reaction (^{9}Li and ^{11}Li in the case of this study). This chamber uses isoC_4H_{10} as the ionizing gas. The FDC2 is placed on the trajectory of the charged particles after SAMURAI and is much larger than the FDC1, to detect all charged reaction products. Its effective volume measures $220\times80\times80$ cm^3 and is filled with a mixture of 40% of He and 60% of isoC_4H_{10} as the ionizing gas. Both FDCs are used for the analysis of the magnetic rigidity of the fragments.

Chapter 8

Data Analysis

Contents

The s018 campaign took place in 2014. The present work is not the first analysis performed on s018 data. The study of (p,pn) knockout on ^{11}Li by Y. Kubota *et al.* presented earlier [112] is, for instance, a result from the s018 campaign. As a consequence, detector calibrations were already performed when the present work has been started. The following paragraphs expose the parts of the analysis that have been done specifically for the two decays of interest, namely the neutron cross-talk rejection in the NEBULA array, the fragment-neutron alignment and the simulations of two-neutron decay.

8.1 Selectivity on the reaction

One improvement with respect to the previous studies mentioned in subsections 6.2.2 and 6.2.4 is the selectivity on the (p,2p) reactions producing both ^{11}Li and ^{13}Li. In the work of Smith *et al.* on ^{11}Li [115], the reaction leading to the population of ^{9}Li is not guaranteed to be the two-neutron decay of ^{11}Li. The one-neutron decay of ^{10}Li, populated via ^{13}B(p,p2pn)^{10}Li, needs to be considered. In an analogous way, in the work of Kohley *et al.* on ^{13}Li [97], the one-neutron decay of ^{12}Li, populated via ^{14}Be(p,2pn)^{12}Li, needs to

be considered for the population of the ground state of ^{11}Li. These alternative scenarios also yield ^{9}Li and ^{11}Li, as well as signals in the array used for neutron detection, meaning that without further information, these contributions need to be taken into account.

In the present setup, the MINOS device was used to track the recoil and knocked-out protons involved in the (p,2p) reaction. Furthermore, as stated in section 7.3, the main data acquisition trigger required the measurement of a proton between 30° and 60°, ensuring the QFS condition. One can note that this trigger condition was needed to allow taking data with a reasonable dead time, but makes the extraction of cross-sections more delicate, and beyond the scope of the present thesis. Measuring the kinematics of the two protons provides a way of ensuring that most selected events with an incoming ^{14}Be (respectively ^{12}Be) and an outgoing ^{11}Li (respectively ^{9}Li) went through the desired (p,2p) reaction.

One can define θ_1, and θ_2 the angle between the trace of the recoil proton, knocked-out proton, respectively, and the beam. A signature of the QFS reactions such as (p,2p) reaction is a linear correlation between these two quantities. This has been first observed experimentally in inverse and complete kinematics in [125]. This correlation has also been observed in previous studies of the s018 campaign, regarding notably ^{17}B [126]. This angular correlation in the case of ^{11}Li and ^{13}Li is displayed in figure 8.1.

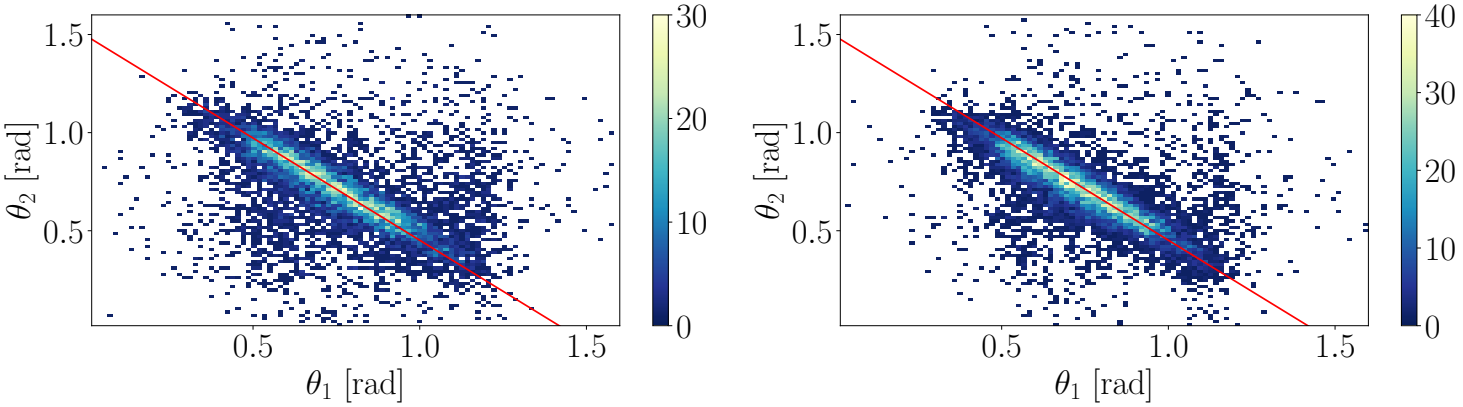

Figure 8.1: (a) θ_2 as a function of θ_1, considering impinging ^{12}Be and outgoing ^{9}Li. The linear correlation has been fitted, and the result is shown by the straight red line. (b) θ_2 as a function of θ_1, considering impinging ^{14}Be and outgoing ^{11}Li. The linear correlation has been fitted, and the result is shown by the straight red line.

These two plots show that most of the events, for the two isotopes of interest, results from the (p,2p) reaction of interest, and that the contamination by the other reaction channels mentioned above is negligible. In addition to this correlation, the opening angle for the two protons, noted $\theta_{p,12}$ has been computed using a (p,2p) kinematics calculator, provided by the R^{3}B (Reactions with Relativistic Radioactive Beams) collaboration in GSI, Germany [127]. This program computes the angles and momenta of the particles involved in a quasi-free scattering reaction, such as the one used to populate the unbound states of ^{11}Li and ^{13}Li. The computed and measured values are summed up in table 8.1.

	Computed $\theta_{p,12}$ (in degrees)	Measured $\theta_{p,12}$ (in degrees)
^{14}Be(p,2p)^{13}Li	81.2	81(3)
^{12}Be(p,2p)^{11}Li	81.8	82(4)

Table 8.1: Computed and measured opening angle for the protons of the (p,2p) reactions on ^{14}Be and ^{12}Be.

The computed and measured values are in very good agreement, confirming the fact that the reaction process is essentially QFS at the present beam energies.

8.2 Neutron cross-talk

The detection of neutrons in NEBULA relies mainly on the (n,p) reaction between the plastic of the scintillators and the incident neutron. The recoil proton triggers the scintillation process, but other reactions occur consequently. As a result, a single neutron can yield several signals in the NEBULA array. This phenomenon is called cross-talk and is common in arrays where the detectors are close to each other. As the studied reactions yield several neutrons, it is very important to first remove the cross-talk events that could be misinterpreted as two-neutrons events. The algorithm used to perform this event rejection checks whether every hit making up a given event satisfy a set of conditions. The conditions and selections applied on data for the cross-talk rejection are exposed in the following subsections.

8.2.1 Same-wall cut

As mentioned in the previous paragraph, the recoil proton triggers the scintillation process in the plastic detectors of the NEBULA array. As it travels in the scintillating material, it is slowed down and emits bremsstrahlung radiation. This radiation can be detected in the neighbouring plastic bars of the same wall, close to the one initially hit by the incident neutron. This is represented schematically in figure 8.2.

Keeping the same notations as in [119], the first event occurs at a time t_1 and at the position $\overrightarrow{r_1}$. Analogously, the second event occurs at a time t_2 and position $\overrightarrow{r_2}$. The events that are too close to each other spatially (typically in scintillators that are touching each other) and that are detected almost at the same time are heavily suspected to be cross-talk events, and are therefore removed. To quantify this, one can consider the following differences (also from [119]):

$$\begin{aligned} dt &= t_2 - t_1, \\ dr &= |\overrightarrow{r_2} - \overrightarrow{r_1}|. \end{aligned} \tag{8.1}$$

In the (dr, dt) space, the events that are close to each other and next to $(0, 0)$ are then rejected. The border of this area can be described by the following ellipse [119]:

$$\sqrt{\left(\frac{dr - dr_0}{R}\right)^2 + \left(\frac{dt - dt_0}{T}\right)^2} = 1, \tag{8.2}$$

with $(dr_0, dt_0) = (158, 0.34)$ the coordinates of the center of the ellipse, and $R = 221$ mm and $T = 2.57$ ns the semi-major axis and semi-minor axis respectively. These values are

empirical and are the most suitable for this study among the different sets of values that have been tried (see subsection 8.2.4). This cut can be seen in figure 8.3.

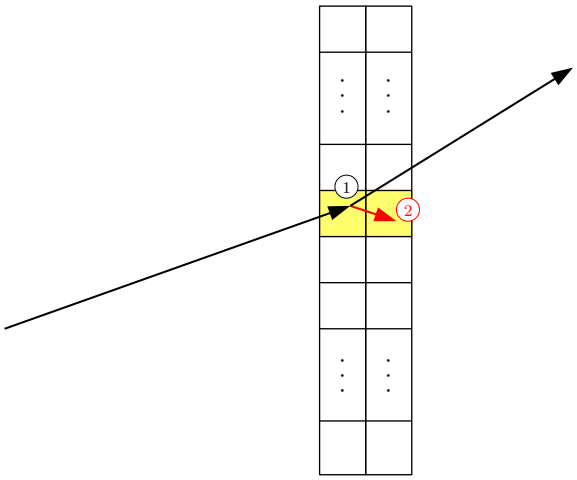

Figure 8.2: Schematic view of a cross-talk event occuring in the same wall. One signal is detected in the first layer of the wall, and a second one is detected in a neighboring bar in the second layer of the wall. The hit bars are highlighted in yellow.

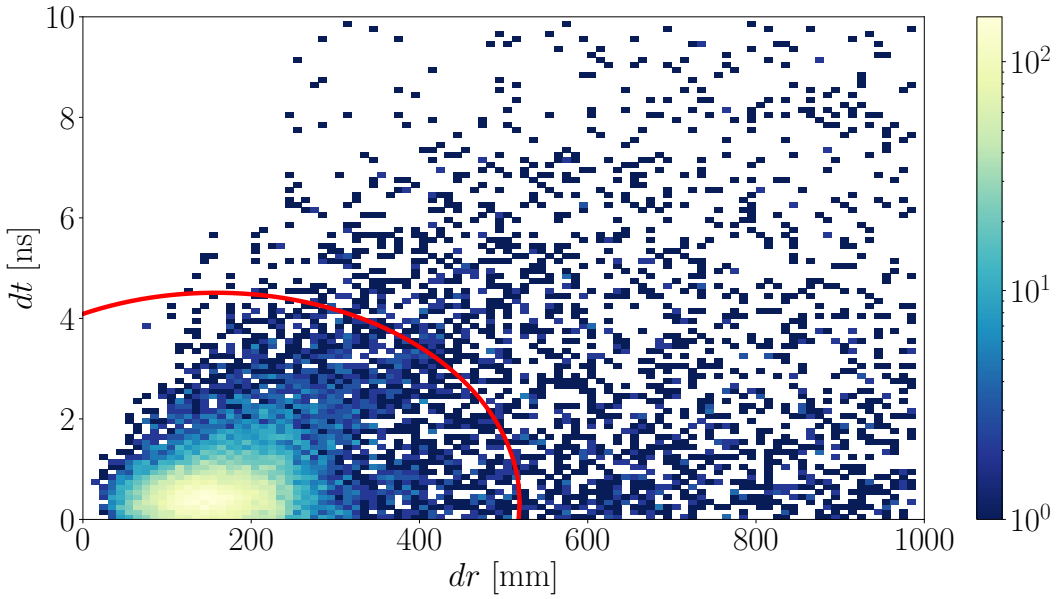

Figure 8.3: dt as a function of dr. The red line shows the elliptic cut that is applied on this study. The events shown have been selected via the reaction channel ^{13}Li $\rightarrow$ ^{11}Li + 2n. This plot presents approximately half the available statistics.

8.2.2 Causality cuts

The incident neutron almost never deposits its full energy in the bar of the NEBULA array that it interacts with, and, as a consequence, keeps on traveling after the hit. The

traveling neutron can then interact again in another scintillator, that can be in a different wall of the array, quite far from the original hit. This is represented schematically in figure 8.4. One way to put aside these different wall cross-talk events is to apply a causality condition on the events. This selection guarantees that the velocity does not decrease too much between the first wall and the second wall of scintillators, which would indicate that the second signal is most likely caused by the same neutron as the first signal. The velocity measured between the target and the first wall would then be greater than the one measured between the first and the second wall, which would not necessarily be the case for an actual two-neutrons event.

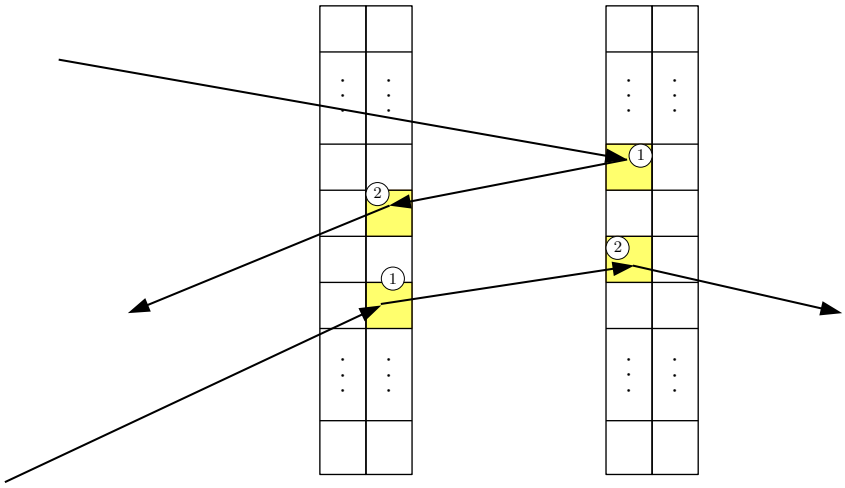

Figure 8.4: Schematic view of a cross-talk event occuring in different walls. Here are shown the two main scenarios. Black: A neutron deposits part of its energy in the first wall and part of its energy in the second wall. Orange: the neutron leaves deposits energy in the second wall and is scattered back into the first wall, producing a second signal. In both cases, one neutron produces two signals in the NEBULA array.

To apply this event selection, one can first write β_{01} the velocity measured between the target and the first hit scintillator, and β_{12} the velocity measured between the first and the second hit scintillator. When the first wall is hit first, β_{12} is positive. However, if the second wall is hit first, this quantity becomes negative. One can also note Q_1 and Q_2 the charge deposited in the first and second wall respectively. One can then display the causality cut used for this study in the $(\beta_{01}/\beta_{12}, Q_1)$ plane, as it is shown in figure 8.5. On this figure, the events with a negative β_{01}/β_{12} ratio are the ones where the first signal is detected in the second wall and the second signal is detected in the first wall. Cross-talk events with a negative velocity ratio undergo a process like the one depicted in figure 8.4 with the orange arrows: the neutron deposits energy in the second wall and is scattered backwards, and deposits energy in the first wall.

As explained previously, the cross-talk events are characterized here by $|\beta_{01}/\beta_{12}| > 1$. This would yield a vertical line in the $(\beta_{01}/\beta_{12}, Q_1)$ plane. The boundaries chosen for this study are slightly tilted to take into account that a neutron leaving a lot of energy in the first wall (with a high Q_1) will see its velocity between both modules decrease accordingly (yielding a lower β_{12}, so a higher β_{01}/β_{12}).

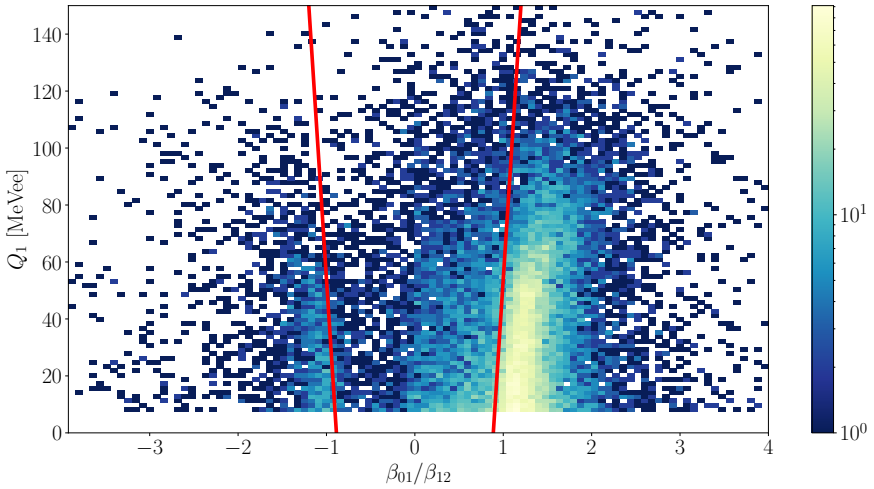

Figure 8.5: Q_1 as a function β_{01}/β_{12}. The events shown have been selected via the reaction channel ^{13}Li $\rightarrow$ ^{11}Li + 2n. This plot presents approximately half of the available statistics. The cross-talk events are the ones outside of the area delimited by the red lines.

8.2.3 Cuts on γ rays

The plastic scintillators that make up the NEBULA array are not only sensitive to neutrons but also to γ rays. It is therefore necessary to remove the events caused by these radiations. As they deposit less energy in the scintillators than neutrons, all hits with an energy deposited smaller than 6 MeVee are considered γ rays and, as a consequence, removed. This condition can be seen in figure 8.5 where no events are displayed below 6 MeVee. For the remaining γ ray events, another cut is applied. As one wants to remove the cross-talk events, one can consider the quantity $1/\beta_{12}$. This ratio compares the velocity of particle between the first hit scintillator and the second hit scintillator to the speed of light. Thus, the events with $1/\beta_{12} \simeq 1$ are most probably events for which a γ ray is produced in the scintillators of the NEBULA array, and can be considered as cross-talk γ ray events. Such events can be seen in the $(1/\beta_{12}, Q_2)$ plane, as shown in figure 8.6.

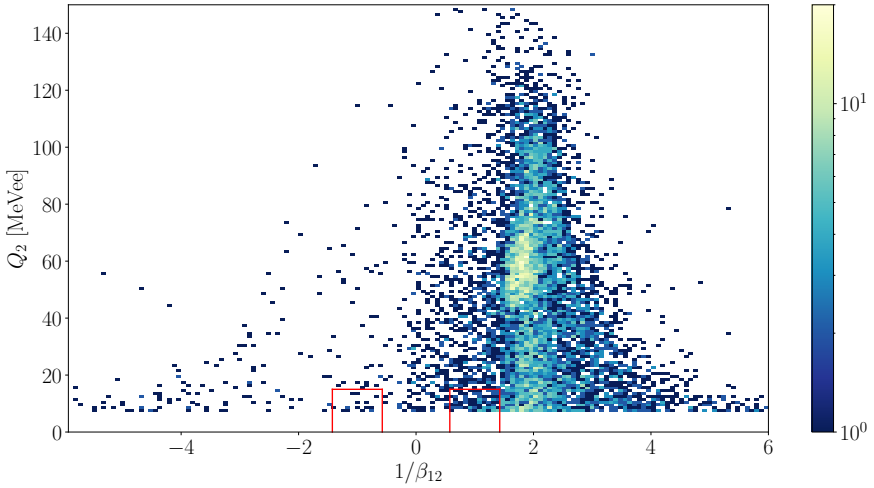

Figure 8.6: Q_2 as a function $1/\beta_{12}$. The events shown have been selected via the reaction channel ^{13}Li $\rightarrow$ ^{11}Li + 2n. This plot presents approximately half of the available statistics. The cross-talk events, due to the production of a γ ray in the interaction with the first neutron, are the ones inside of the area delimited by the two red boxes.

One can note that these selections are not, strictly speaking, part of the cross-talk rejection procedure. Their description is however included in this chapter as γ rays yield signals in the NEBULA array that can be falsely attributed as true two-neutron events.

8.2.4 Performances

Cross-talk rejection is crucial when studying two-neutron decay reaction channels to remove events with high multiplicity due to only one neutron, falsely interpreted as two-neutron events. It is then necessary to choose the set of parameters for the cuts presented previously that provides the best performances. In the case of cross-talk rejection, this can be quantified by looking at the amount of events of multiplicity strictly greater than one (noted $M > 1$ in this paragraph) remaining before and after the cuts have been applied. In the case of a one-neutron decay reaction channel, the amount of events with $M > 1$ remaining must be minimal. T. Nakamura and Y. Kondo in [119] report 2.9 % of events with $M > 1$, with potential cross-talk happening, remaining after their analysis (also called survival rate), which is the order of magnitude chosen here for efficient cross-talk rejection cuts. As the channels of interest are two-neutron decay reaction channels, it is important that the chosen cuts do not accidentally remove too many $M > 1$ true two-neutron events, which constitute the statistics for the relative energy spectra. The cuts are first drawn on simulated data sets, before being drawn and assessed on experimental data. To quantify the performances, one can write:

$$r = \frac{N(M > 1, \text{After CT rejection})}{N(M > 1, \text{Before CT rejection})}, \tag{8.3}$$

with $N(M > 1, \text{After CT rejection})$ and $N(M > 1, \text{Before CT rejection})$ the number of events with $M > 1$ after and before the rejection of cross-talk events, respectively. Furthermore, one can note r_1 and r_2 the ratio previously defined for a one-neutron decay channel and a two-neutron decay channel, respectively. Eventually, one can note r_{21} the ratio r_2/r_1. r_{21} can be a suitable index for the performances of the proposed cross-talk rejection cuts. The optimal cut would minimize r_1, as the survival rate should be as low as possible for a one-neutron decay channel, thus checking that the cross-talk rejection is efficient. It would also maximize r_2, in order to make sure that a sufficient number of events in the two-neutron decay channel is preserved. The combination of both these trends results in a maximized r_{21} for the suitable set of cross-talk cuts.

The ratio r_2 is meaningful as the analog of r_1. One could prefer the use of r'_2, more tailored for the case of a two-neutron decay channel, defined as:

$$r'_2 = \frac{N(M = 2, \text{After CT rejection})}{N(M > 1, \text{Before CT rejection})}, \tag{8.4}$$

as $N(M = 2, \text{After CT rejection})$ is the number of events of interest. Similarly, one can define r'_{21} as the ratio r'_2/r_1. In the following paragraphs, several parameters are compared for the same-wall cut and the causality cut. To compute the different ratios, the considered one-neutron decay channel is the reaction ^{11}Li(p,pn)^{10}Li $\rightarrow$ ^{9}Li + n. The chosen two-neutron decay channel is the reaction of interest ^{14}Be(p,2p)^{13}Li $\rightarrow$ ^{11}Li + 2n.

Same-wall cut

For a given causality cut, several ellipses have been tried for the same-wall cut. All these ellipses are centered in (158,0.34) in the (dr, dt) plane (see subsection 8.2.1) but have

different semi-major and semi-minor axis. The values for r_{21} for the different cuts are shown in figure 8.7. On this figure, each same-wall cut is characterized by the semi-major axis R and the semi-minor axis T (written on the x-axis as (R, T)). The different cuts are ordered by increasing size of the ellipse. It now appears that the most efficient same-wall cross-talk cut is the one with $(R, T) = (221, 2.57)$, which is the one displayed in figure 8.8).

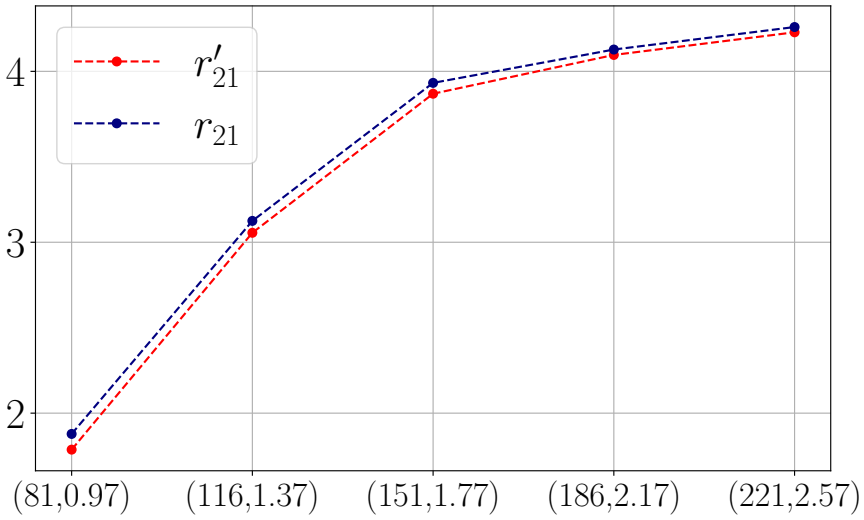

Figure 8.7: The different values of r_{21} and r'_{21} for each same-wall cut, and the (1442.3,-1364.3) causality cut.

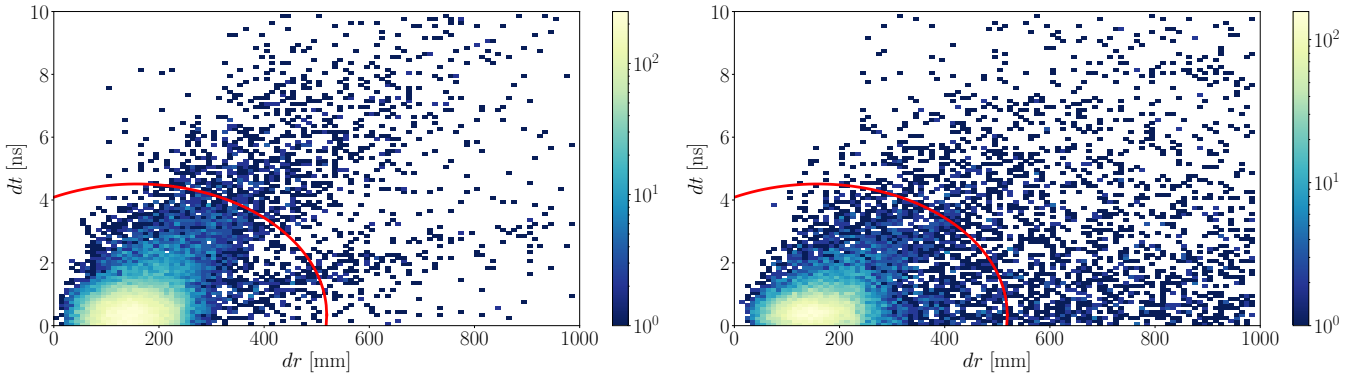

(a) (b)

Figure 8.8: Comparison of the (dr, dt) plot, used to represent the same-wall cut, produced using data or simulating events with the SMSIMULATOR package. (a) dt as a function of dr for the one-neutron decay of ^{12}Li, simulated with the SMSIMULATOR package. (b) dt as a function of dr, made from the data of the two-neutron decay of ^{13}Li. Same figure as figure 8.3.

Causality cut

One can now fix the same-wall cut as the one chosen in the previous paragraph and compare different causality cuts in an analogous way. The cuts are here characterized by the slope and the offset of the straight line that is the causality cut (the one for negative values of β_{01}/β_{12} is the symmetry of the other one with respect to the y-axis), with the format (slope,offset). The result can be seen in figure 8.9.

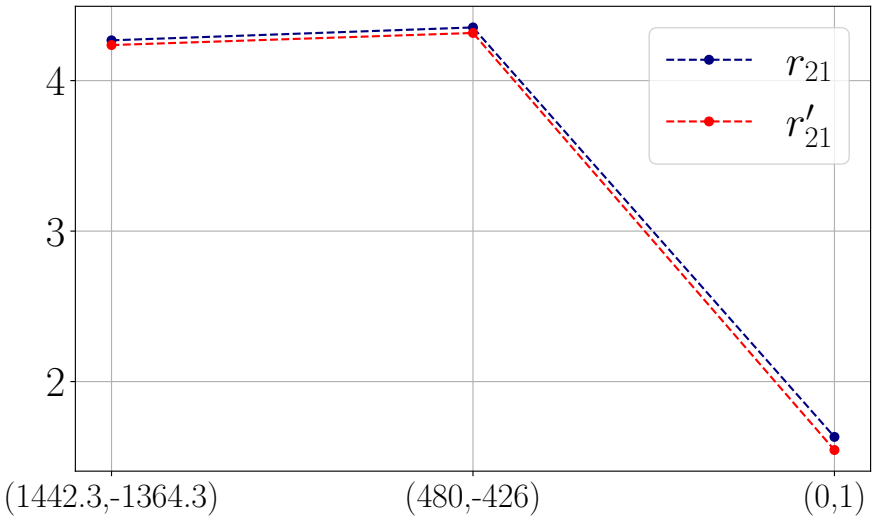

Figure 8.9: The different values of r_{21} and r'_{21} for each causality cut, and the (151,1.77) same-wall cut.

The cuts presented on this figure are steeper and steeper, until the vertical line $\beta_{01}/\beta_{12} = 1$. It now appears that the most efficient causality cut is the one with the coefficients (480,-426), which is displayed in figure 8.5.

The chosen cuts yield a survival rate of 2.32 % for the one-neutron decay channel. This rate is similar to the one that was achieved in [119]. For the two-neutron decay channel, the survival rate is 10.1 %, which gives $r_{21} = 4.35$.

The aforementioned conditions used for cross-talk rejection also confirm that the SMSIMULATOR package is suitable to simulate the two-neutron decay in the SAMURAI setup, as the results yielded by the different cross-talk cuts are very similar between simulation and data. This can be seen in figure 8.10. The SMSIMULATOR package is described with more details in subsection 8.4.1.

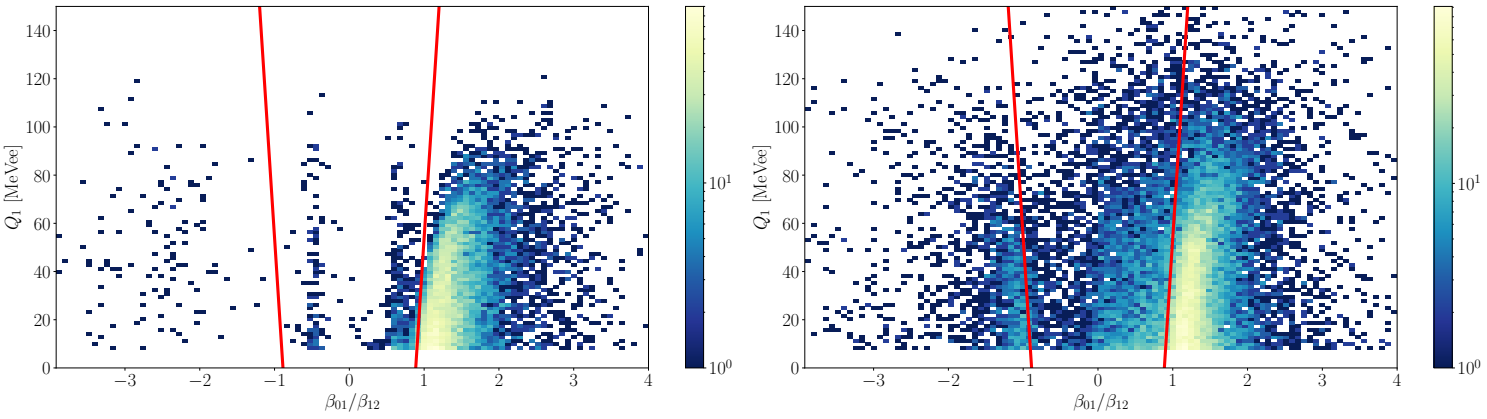

(a) (b)

Figure 8.10: Comparison of the charge $Q1$ against β_{01}/β_{12} plot, used to represent the causality cut, produced using data or simulating events with the SMSIMULATOR package. (a) $Q1$ as a function of β_{01}/β_{12} for the one-neutron decay of ^{12}Li, simulated with the SMSIMULATOR package. (b) $Q1$ as a function of β_{01}/β_{12}, made from the data of the two-neutron decay of ^{13}Li. Same figure as figure 8.5.

8.3 Fragment-neutron alignment

After selecting events using the cross-talk cuts as described in section 8.2, a further correction can be performed referred to as fragment-neutron alignment. It is necessary to guarantee a correct reconstruction of the momentum of the fragment and the neutrons resulting from the decay. Due to small systematic errors in the calibration of the various detectors of the setup, the measurement of the momentum can be slightly imprecise and lead to incorrect reconstruction of the relative energy. To tackle this issue, one can make sure that, on average, the reconstructed velocities of the neutrons and the fragment is the same, as they are emitted from the same decay. This distribution for the neutrons is provided by the measurement of their time of flight. The NEBULA array can detect γ rays and the resulting peak in the velocity distribution is centered exactly at $\beta = 1$. These aspects make the velocity distribution for neutrons more reliable and robust than the one for the fragment, which suffers more from the aforementioned errors. As a result, one can align the velocity distribution for the fragment on the one of the neutrons.

The momentum for the fragment can be computed with the following formula:

$$\begin{aligned} P_f &= E_f \cdot \beta_f, \\ E_f &= m_f \cdot \gamma_f, \end{aligned} \tag{8.5}$$

with E_f the energy of the fragment, β_f its velocity, γ_f the Lorentz factor associated to its velocity and m_f its mass. The same equations also apply for the neutrons. To perform the alignment, a small shift $\Delta\beta_f$ (usually of the order of 5‰ of the value of β_f) is applied to β_f. For this study, the value of $\Delta\beta_f$ has been computed by determining its effect on the value of $\Delta\beta_{nf}$, the difference between the neutron velocity and the fragment velocity, and on the value of $P^f_{z,n}$, the momentum of the neutron boosted in the frame of the fragment, and projected on the z-axis. The distribution of both these quantities, for a given $\Delta\beta_f$, are Gaussian-like. After fitting them, the centroid of the distribution is then plotted versus $\Delta\beta_f$. The result of this procedure can be seen in figure 8.11 for the case of the reaction ^{13}Li $\rightarrow$ ^{11}Li+2n. From the linear fits shown in figure 8.11, $\Delta\beta_{fn} = 0$ for $\Delta\beta_f = 0.00486(3)$, and $P^f_{z,n} = 0$ for $\Delta\beta_f = 0.0058(1)$. The value eventually used in this study is the average of these two numbers and is 0.00534.

8.4 Simulation of the neutron resonances

In the following subsections, details about the shape of the neutron resonances and about their fit to the data are given.

8.4.1 The SMSIMULATOR simulation package

The SMSIMULATOR simulation package developed by R. Tanaka and Y. Kondo [128] is a simulation code developed to simulate the response of the NEBULA array. It is divided into three parts, in an analogous way to the SHOGUN simulation package (see subsection 3.2.1).

- The first part of the code is an event generator, which task is to generate events at a given relative energy, for the desired beam isotope, fragment isotope and beam energy.

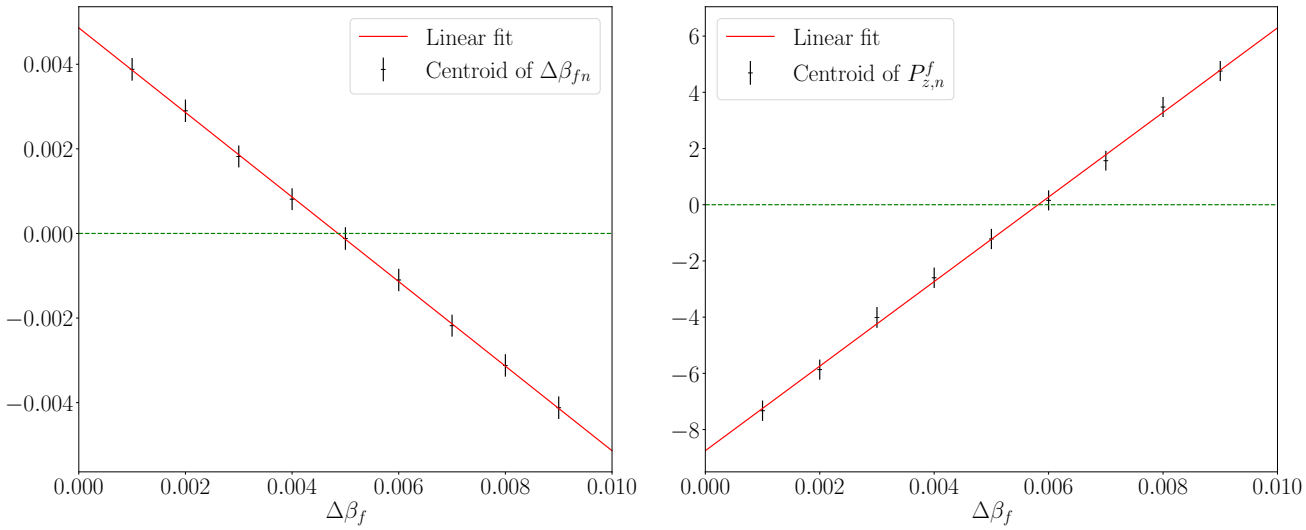

(a) (b)

Figure 8.11: (a) $\Delta\beta_{nf}$ as a function of the shift $\Delta\beta_f$, fitted by a linear function. (b) $P^f_{z,n}$ as a function of the shift $\Delta\beta_f$, fitted by a linear function.

- The second part is an event builder, which takes the output of the event generator as an input. It simulates the trajectory of the different particles through the SAMURAI magnet and the response of the NEBULA detector to the event previously generated.
- The third part is an event reconstructor, which takes the output of the event builder as an input and reproduces the analysis performed on the experimental data. Indeed, the cross-talk removal selection is applied to the simulated data, and the observables of interest, such as the invariant mass of the system and the relative energy, are computed.

8.4.2 Resolution and efficiency of the NEBULA detector

Before considering the shape of the resonances, it is necessary to determine the resolution and the efficiency of the NEBULA detector as a function of the energy. To do so, some response functions of the NEBULA detector have been simulated for a wide range of input relative energy E_{rel}. The input relative energy distribution is set as a Dirac function in the event generator. As the response of the detector is computed, this distribution widens and can be described by a Gaussian curve (except for small relative energy). The standard deviation σ of the output Gaussian curve depends on the input relative energy, and $\sigma(E_{rel})$ is then fitted. The default Gaussian fit function in ROOT has the following form:

$$\mathcal{G}(E_{rel}) = p_0 \exp\left(-\frac{1}{2}\left(\frac{E_{rel} - p_1}{p_2}\right)^2\right), \tag{8.6}$$

with p_i being the fit parameters. One can directly identify the standard deviation with the parameter p_2. The NEBULA resolution is then fitted with the following function:

$$\sigma(E_{rel}) = a \cdot E_{rel}^b = p_2(E_{rel}), \tag{8.7}$$

with a and b the fit parameters. This is displayed in figure 8.12.

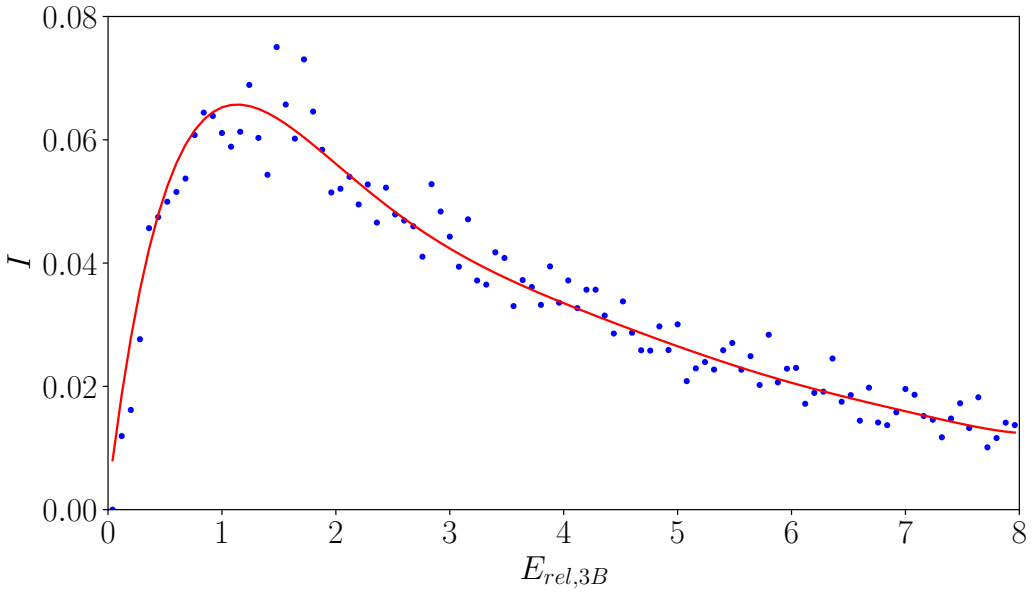

Figure 8.13: Fit of the efficiency of the NEBULA array computed with the SMSIMULATOR simulation package.

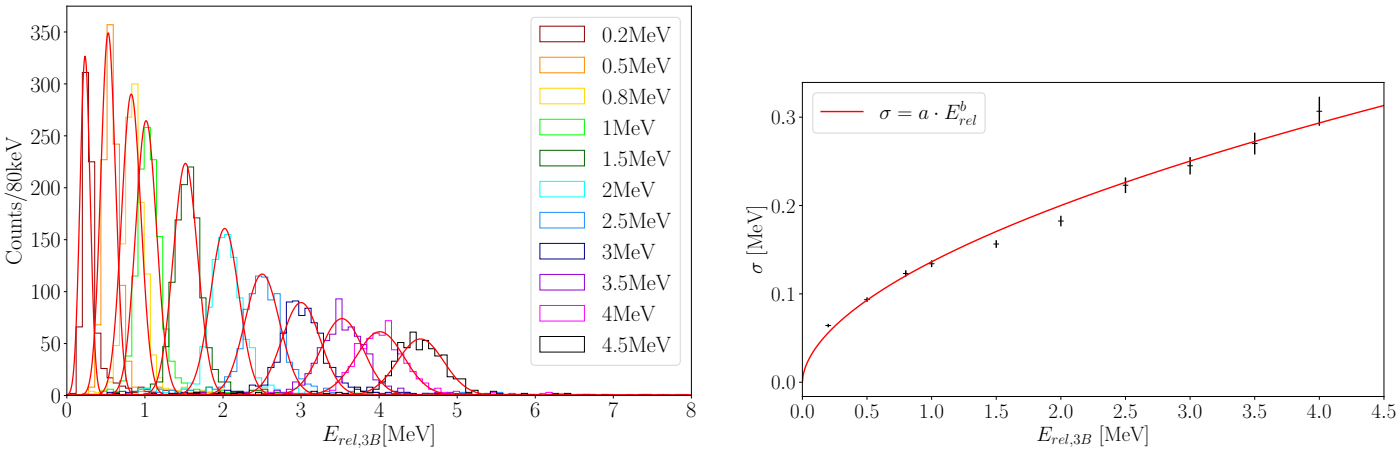

(a) (b)

Figure 8.12: Determination of the resolution of the NEBULA array using Dirac-shaped related energy distributions input for the SMSIMULATOR package. (a) Gaussian fit of the simulated response functions for a monoenergetic input. The caption provides the energy for which the input events have been generated. (b) Resolution as a function of the input relative energy, extracted from the Gaussian fit in figure 8.12a.

While the input E_{rel} distribution is a Dirac distribution to compute the resolution of the detector, a uniform distribution is taken as an input in order to compute the efficiency of the NEBULA array, denoted I. After going through the generator, the builder and the reconstructor of the SMSIMULATOR package, this shape of the distribution is now the one of I as a function of E_{rel}. The content of each bin of this distribution is divided by the one given as an input, and fitted by an seventh-degree polynomial function. The result of this procedure is shown in figure 8.13.

8.4.3 Shape of the response functions

The neutron resonances have the shape of the Breit-Wigner distribution [129, 130]. The shape of the resonance depends on the orbital angular momentum l. One can first define the wave number k as follows:

$$k(E_{rel}) = \frac{\sqrt{2E_{rel}\mu}}{\hbar}, \tag{8.8}$$

with μ the reduced mass of the system. The considered system is composed of two neutrons and a fragment. μ is then defined as:

$$\frac{1}{\mu} = \frac{1}{m_n} + \frac{1}{m_n} + \frac{1}{m_f} \Leftrightarrow \mu = \frac{m_f m_n^2}{2m_f m_n + m_n^2}, \tag{8.9}$$

with m_n the mass of the neutron, and m_f the fragment mass.

For the s-wave distribution, so for $l = 0$, the shape of the virtual state is given by its asymptotic formula [129]:

$$\mathcal{S} = \frac{d\sigma}{dE} \propto k \left(\frac{1}{\alpha^2 + k^2}\right)^2 \left(\cos(ka) - \frac{\alpha}{k}\sin(ka)\right)^2, \tag{8.10}$$

with α the falloff parameter, and a the scattering length. For $l \neq 0$, the usual Breit-Wigner distribution formula has been used [130]:

$$\mathcal{B}_l = \frac{d\sigma}{dE} \propto \frac{\Gamma_l(E_{rel})}{(E_{res} + \Delta_l(E_{rel}) - E_{rel})^2 + \frac{1}{4}\Gamma_l(E_{rel})^2}, \tag{8.11}$$

with E_{res} the resonance energy, Γ_l the width of the resonance and Δ_l the resonance shift. These quantities are defined using Bessel functions [131]. One first defines the following quantities:

$$\begin{aligned} F_l &= \sqrt{\frac{\pi kR}{2}} J_{l+\frac{1}{2}}(kR), \\ G_l &= (-1)^l \sqrt{\frac{\pi kR}{2}} J_{l-\frac{1}{2}}(kR), \end{aligned} \tag{8.12}$$

with R the radius of the fragment as $R = 1.25A^{\frac{1}{3}}$ in fm, with A the number of mass of the fragment, and $J_{l\pm\frac{1}{2}}$ the spherical Bessel functions. These functions are the regular and irregular solutions of the radial Schrödinger equation. In the case of neutron decay, the penetrability P_l can be written with these solutions using the following approximation:

$$P_l \approx |2l + 1| \frac{F_l}{G_l}. \tag{8.13}$$

The penetrability is then used to define the width of the resonance:

$$\Gamma_l = 2\gamma^2 P_l, \tag{8.14}$$

with γ^2 the reduced penetrability.

The resonance shift is defined with the shift function S_l:

$$\Delta_l = -\left(S_l(E_{rel}) - S_l(E_{res})\right)\gamma^2. \tag{8.15}$$

In [131], a recursion formula has been derived to link S_l and P_l using the Powell recursion formulas [132]. In the case of neutrons, one can then write:

$$\begin{aligned} P_l &= (kR)^2 P_{l-1} \frac{1}{(l - S_{l-1})^2 + P_{l-1}^2} \\ \Leftrightarrow S_l &= (l+1) - \sqrt{\frac{(kR)^2 P_l}{P_{l+1}} - P_l^2}. \end{aligned} \tag{8.16}$$

The formulas for $\mathcal{S}$ and $\mathcal{B}_l$ contain the physics of the scattering problem with a fragment and two neutrons. To fit the invariant mass spectrum and encompass the whole experimental system in the shape of the resonances, it is necessary to take into account detector properties such as the resolution and the efficiency, as previously mentioned (see subsection 8.4.2). The Breit-Wigner distribution is then convoluted to a Gaussian curve $\mathcal{G}$, to take into account the detector resolution at a given E_{rel}, and is multiplied to the detection efficiency. This yields:

$$\begin{aligned} \tilde{\mathcal{S}} &= (\mathcal{S} * \mathcal{G})\epsilon, \\ \tilde{\mathcal{B}}_l &= (\mathcal{B}_l * \mathcal{G})\epsilon. \end{aligned} \tag{8.17}$$

$\tilde{\mathcal{S}}$ and $\tilde{\mathcal{B}}_l$ are an analytical form of the distributions for the f+n+n relative energies, that contain both the physics of the system and the characteristics of the neutron detector. These formulas offer a rather convenient and fast way of finding values for E_{res} and $\Gamma_l(E_{res})$. Instead of generating a grid of response functions for different (E_{res},$\Gamma_l(E_{res})$), one can directly implement these formulas along with a χ^2 minimization procedure. However, using the proposed convolution to take into account the resolution of the NEBULA array is approximate, as, for low relative energies, the response function of a monoenergetic input is not Gaussian. This effect can be seen with the red histogram in figure 8.12a. As a consequence, the method used in the present work to generate the simulated response functions relies on a fit of the relative energy spectrum using $\tilde{\mathcal{S}}$ and $\tilde{\mathcal{B}}_l$ for the determination of (E_{res},$\Gamma_l(E_{res})$), and the use of the SMSIMULATOR package to generate the response functions actually used in the fit.

8.4.4 Phase-space decay and n-n correlations

^{10}Li, ^{12}Li and ^{13}Li are unbound systems. The half-life of the ground state of ^{11}Li is 8.75(14) ms [133]. The excited states of ^{11}Li are all unbound. In the case of a direct decay, namely both neutrons emitted at the same time, the three-body relative energy needs to be distributed among the fragment and the two neutrons. One can first consider that the neutrons are not interacting with each other, in which case, the neutrons will share the available energy randomly, following a phase-space decay. However, the two emitted neutrons originate from the same system and therefore may be correlated, the phase-space decay thus constituting a limit case for which the two neutrons are not correlated at all.

One way to take into account these correlations is to use the correlation function proposed in [134]. The formalism developed in [113] by R. Lednicky and V.L. Lyuboshits makes it possible to compute such a quantity, and an example for an application in the case of neutron-neutron correlations can be found in [90]. According to [90], the correlation function, noted C_{nn}, can be written as:

$$C_{nn} = \frac{d^2n/dp_{n_1}dp_{n_2}}{(dn/dp_{n_1})(dn/dp_{n_2})}, \tag{8.18}$$

with p_{n_1} and p_{n_2} the momentum for both neutrons, and n the particle count. This means that the correlation function is the ratio between the measured two-particle distribution on the numerator, and the product of both single particle distributions on the denominator. An integral formula is proposed in [113] for the computation of the correlation function:

$$C_{nn} \simeq \int W(\vec{r}, t, r_0, \tau_{nn}) F(\vec{r}, q_{nn}, r_0) \mathrm{d}t \mathrm{d}\vec{r}, \tag{8.19}$$

with W the spatial and time distribution of the neutron source, and F the final state interaction, containing the scattering amplitude. $\vec{r}$ and t are respectively the space and time coordinate, and $q_{nn} = |p_{n_1} - p_{n_2}|$. This approximation is valid under certain assumptions regarding the characteristics of the neutron source. The first one is that the source does not depend on the neutron momenta, which means that no structural elements are included in this description. The source is also considered Gaussian, in order to have analytical formulas, and the distance distributions for the neutrons should not overlap. As a result, W is usually characterized by its spatial variance of $\sqrt{2}r_0$. In this context, r_{nn} is the rms, effective n-n distance equal to $\sqrt{6}r_0$.

One can now note that C_{nn} depends on the space parameter r_{nn} and the time parameter τ_{nn}, which characterize the neutron source: r_{nn} is the distance between the two neutrons, and τ_{nn} the delay between the emission of both neutrons, i.e. the lifetime of the intermediate state in the fragment+neutron system. In the case of a direct decay, the value of τ_{nn} is 0. In the case of a sequential decay, the value of τ_{nn} depends on the width of the intermediate state with the formula:

$$\tau_{nn} = \frac{\hbar c}{\Gamma_{l,i}(E_{res})}, \tag{8.20}$$

with $\Gamma_{l,i}(E_{res})$ the width of the intermediate state at $E_{rel} = E_{res}$, with the same notation as in equation (8.11). In both cases, the value of r_{nn} is fitted to the experimental data. A small n-n distance indicate strong correlations, and the minimal value for equation (8.19) to hold is $r_{nn} \simeq 3.67$ fm. Indeed as mentioned before, the distance distributions for the neutrons should not overlap and keeping the value of the spatial parameter r_0 above 1.5 fm ensures this. Similarly, a larger r_{nn} indicates weak correlations and the limiting case of the absence of correlations is equivalent to $r_{nn} \to \infty$.

Practically, the momentum distributions for both neutrons, and the fragment are generated without any correlations, from the Breit-Wigner-shaped relative energy distributions described in subsection 8.4.3. The inverse sampling method is then used to take the correlations into account: the correlation function is computed using the aforementioned formalism, normalized, and used as the cumulative distribution. These correlated distributions are used as an input for the SMSIMULATOR package, which applies the effects of the resolution and efficiency of the NEBULA array. The final step is applying the same analysis as the one performed on the data, namely applying the cross-talk cuts detailed in section 8.2. Regarding the notations for the quantification of the n-n correlations, r_0 has been used for the generation of the response functions, but r_{nn} will be used to present the results, as it is an effective parameter, that can be compared to the results of other studies on neutron-rich light nuclei, which also use the Lednicky-Lyuboshits formalism (see references [114, 135, 136]).

Chapter 9

Results

Contents

After exposing the different treatments performed on the data, this chapter displays the different results regarding the decay of two neutron-rich Lithium isotopes: ^{11}Li and ^{13}Li, produced via (p,2p) reaction on ^{12}Be and ^{14}Be, respectively. Both nuclei will be presented in the same way. First, the three-body invariant mass spectrum is fitted. Based on this, spectroscopic information are extracted and used to select a range in three-body energy, from which the two-body invariant mass spectrum and the Jacobi coordinates will be displayed. Doing so, it is possible to show which decay process (direct or sequential) is preferred for each resonant state in ^{13}Li and ^{11}Li.

9.1 Two-neutron decay of ^{13}Li

9.1.1 Three-body relative energy spectrum

Figure 9.1a shows the three-body invariant mass spectrum for ^{13}Li, and figure 9.1b shows the same spectrum for events with two neutrons detected in different walls. On the latter, the presence of a low-lying resonant state in the spectrum of ^{13}Li is clear. Table 9.1 sums up the different energies and width of the resonances that have been used to fit the three-body invariant mass spectrum. These resonances appear in green in figure 9.1b and they are p-waves, so Breit-Wigner distributions with $l = 1$, with the same notation as in equation (8.11). A virtual state, in blue in figure 9.1b, has also been used to fit the invariant mass spectrum, with a scattering length of $a_s = -4$fm. As shown in table 9.2, resonance 1 in table 9.1 have already been measured in [97] and resonance 3 is first mentioned in [105], while resonances 2 and 4 are newly observed. One can then note that the spectrum and the proposed fit from figure 9.1b gather the existing spectroscopic

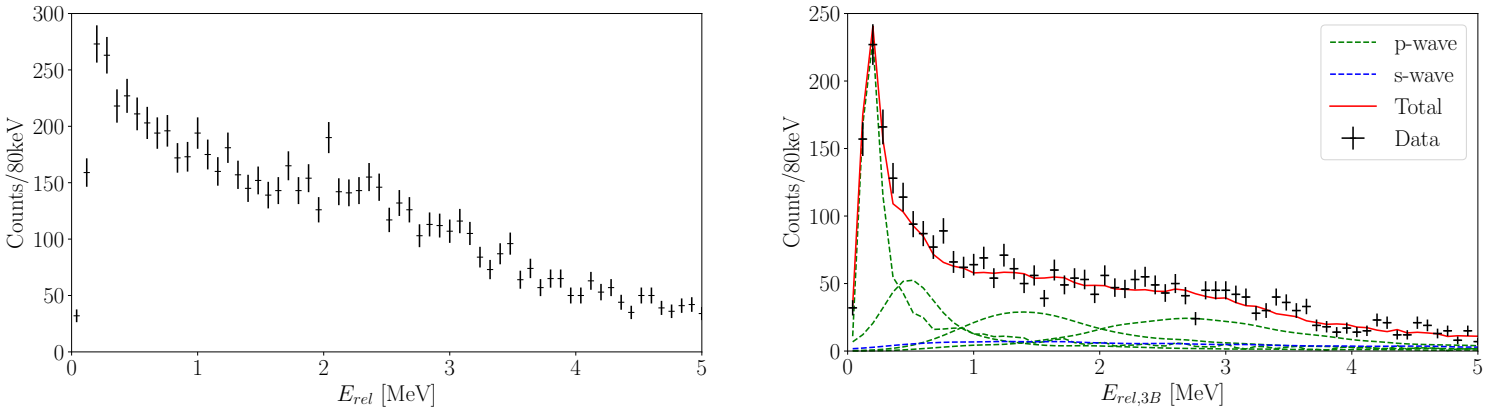

(a) (b)

Figure 9.1: (a) Three-body invariant mass spectrum of ^{13}Li, for both different wall and same wall events. (b) Three-body invariant mass spectrum of ^{13}Li for different wall events, fitted with Breit-Wigner distributions, in green, and a virtual state, in blue. In red is the sum of all contributions, and in black are the experimental data points.

	1	2	3	4
E_{res} (MeV)	0.16(1)	0.45(6)	1.47(31)	2.8(2)
Γ_{res} (MeV)	0.16(4)	0.26(11)	1.7(7)	1.7(7)

Table 9.1: Parameters for the p-waves used to fit the spectrum in figure 9.1b. E_{res} is the resonance energy, and Γ_{res} is the width of the distribution at the resonance energy. Recalling the notation from equation (8.11), $\Gamma_{res} = \Gamma_1(E_{res})$.

	1 in [97]	3 in [105]
E_{res} (MeV)	$0.12^{+0.6}_{-0.8}$	1.47(31)
Γ_{res} (MeV)	$0.125^{+0.6}_{-0.4}$	1-3

Table 9.2: Parameters for the p-wave states in ^{13}Li from previous studies. E_{res} is the resonance energy, and Γ_{res} is the width of the distribution at the resonance energy. Recalling the notation from equation (8.11), $\Gamma_{res} = \Gamma_1(E_{res})$.

information on ^{13}Li from two different studies, and complete it by proposing the addition of two new resonances.

Now that some resonant excited states have been identified in ^{13}Li above the two-neutron emission threshold, it is possible to check the two-body energy spectrum and the Jacobi coordinates by selecting a range of three-body relative energy where the energy available for the decay is the one of the considered resonance. The emitted particles will either populate the excited states of ^{12}Li, implying structures in the two-body plots, or decay directly to the ground state of ^{11}Li.

9.1.2 Two-body invariant mass spectrum and Jacobi coordinates

As previously exposed in section 8.4.4, the neutron correlation function in the case of a direct decay depends on the neutron distance r_{nn}, under the assumptions of the formalism [113]. This parameter is fitted to the data. Therefore, the Jacobi coordinates for ^{13}Li have been fitted for several values of r_{nn}. A χ^2 has been extracted for each fit and represented in figure 9.2 as a function of r_{nn}.

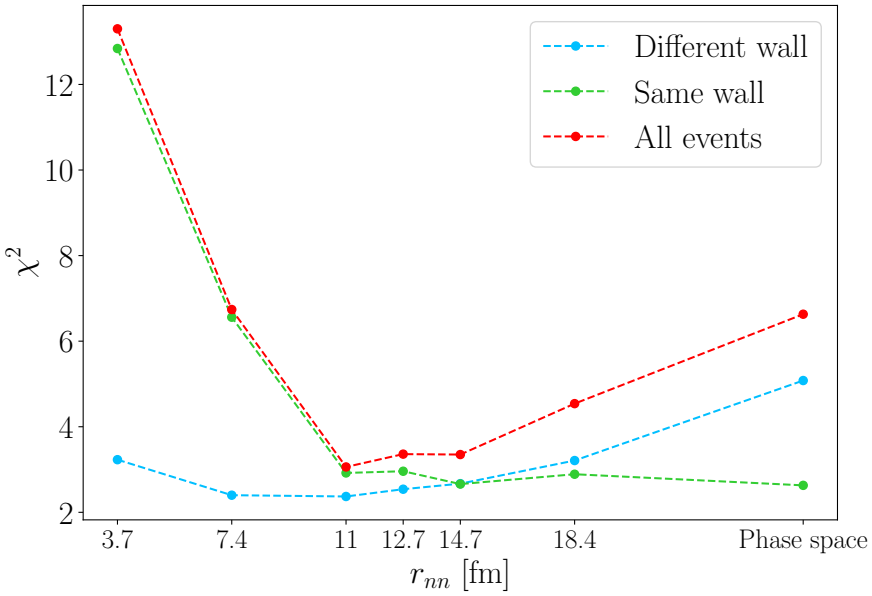

Figure 9.2: χ^2 as a function of r_0. The blue dots are for the fits on different wall events, and the green dots for the fit on same wall events. The red dots represent the fit on the whole statistics. The black stars are the average between the three values of χ^2 aforementioned for each r_0.

The χ^2 curve shown in figure 9.2 shows a minimum between $r_{nn} = 11$ fm and $r_{nn} = 14.7$ fm. In this range, χ^2 is rather flat meaning that all these values of r_{nn} yield an equivalent goodness of fit, which justifies the median value of $r_{nn} = 12.7$ fm for the rest of the study. The sensitivity on the value of r_{nn} is limited, but it is clear that the emitted neutrons are correlated, as the response functions for the phase space distribution clearly yield a higher χ^2 value. Similarly, it is clear that the correlation are not extreme, as the χ^2 value is also clearly higher for values of r_{nn} close to the limit value of 3.7 fm. The three-body invariant mass spectrum of ^{13}Li has been divided into four sections. This is shown in figure 9.3. A gate corresponding to each section is applied on the three-body relative energy. With this condition, the two-body energy spectrum for the fragment-neutron system is built, and

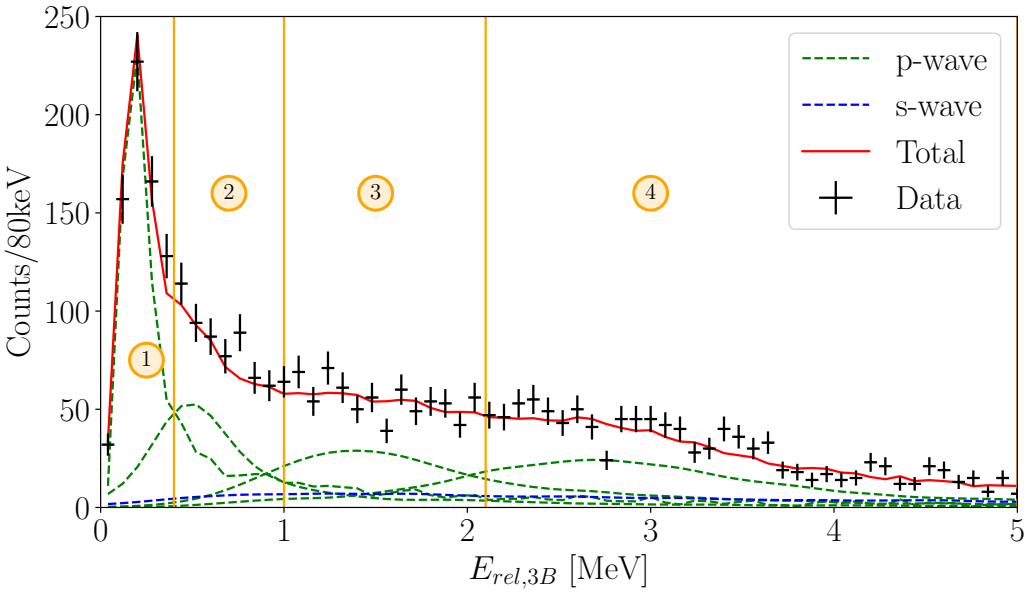

Figure 9.3: Fit of the three-body invariant mass spectrum of ^{13}Li, for different wall events. The orange vertical lines divide the four sections considered for the rest of the analysis. Section 1 goes from 0 keV to 400 keV, section 2 from 400 keV to 1 MeV, section 3 from 1 MeV to 2.1 MeV, and section 4 from 2.1 MeV to 5 MeV.

the Jacobi coordinates are computed and fitted. One can first assume that ^{13}Li decays directly to ^{11}Li. This assumption is based on the fact that no clear structure is visible in the two-body relative energy spectrum of ^{11}Li+n, displayed in figure 9.4.

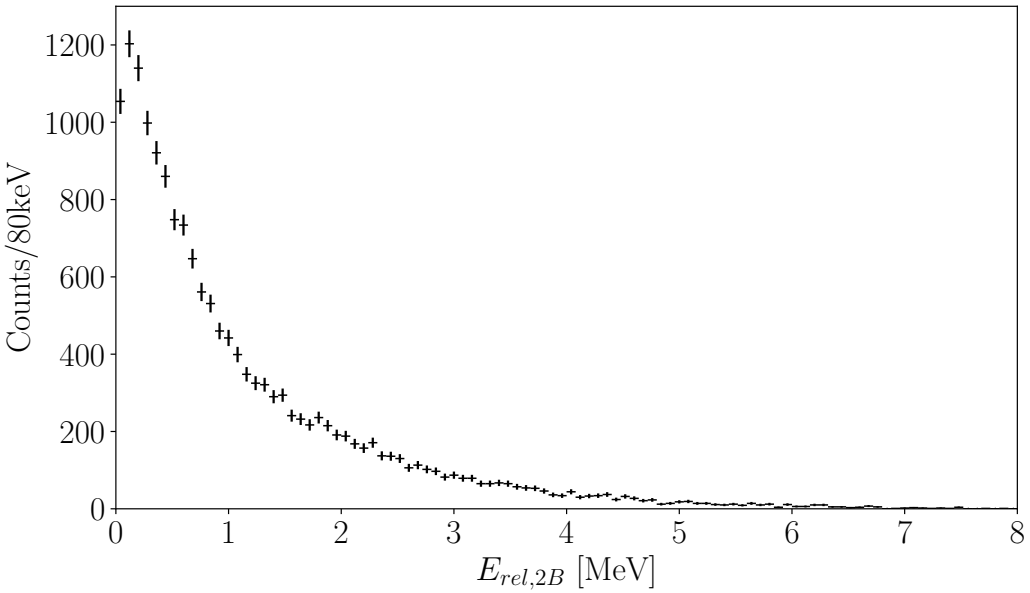

Figure 9.4: Relative energy spectrum for the ^{11}Li+n system. This spectrum displays both different and same wall events. The two-body relative energy has been calculated with both decay neutrons and added to this histogram.

For each gate showed in figure 9.3, the Jacobi coordinates have been reproduced considering a direct decay with $r_n = 12.7$ fm. The results for section 1 are displayed in figure

9.5, the ones for section 2 in figure 9.6, the ones for section 3 in figure 9.7, and the ones for section 4 in figure 9.8. One can first note that the amplitude of the simulation as superimposed with the data on these figures is not fitted to the data. For each section, the integral of each component of the fit displayed in figure 9.1b is computed. This integral is then used as a normalization for the contributions of these components in the response function of the Jacobi coordinates. As a consequence, there are no free parameters in figure 9.5, 9.6, 9.7 and 9.8.

Considering the direct decay only allows to reproduce the experimental data for the three first considered sections. One can see in figure 9.8 that some structures, especially for $\cos(\theta_T)$ and $E_{x,Y}/E_{rel,3B}$, are not well reproduced by the simulation. This questions the assumption of the direct decay as the only decay process in this energy range. Some resonant states have already been measured in ^{12}Li [97] and can be considered as intermediate states in the case of a sequential decay from ^{13}Li to ^{12}Li to ^{11}Li. The parameters chosen in this study and their comparison with the results from previous studies are summed up in table 9.3. These parameters have been found by varying the resonance energy and fitting the two-body spectrum, and using χ^2 as a goodness-of-fit criterion. The resulting χ^2 surface can be found in figure 9.9. For this figure, the fits have been performed on the two-body (f+n) spectrum with a narrower gate, between 2760 and 3360 keV, helping enhance the ^{12}Li structures. The fit with the lowest χ^2 is displayed in figure 9.10.

	1	2	1 in [97]	2 in [97]
E_{res} (MeV)	0.15	0.5	0.21(3)	0.525(25)

Table 9.3: Parameters for the intermediate p-wave states in ^{12}Li (used as intermediate decay states to fit figure 9.10 shown later). The left-hand side of the table shows the parameters for this study, while the right-hand side shows the parameters from [97]. E_{res} is the resonance energy.

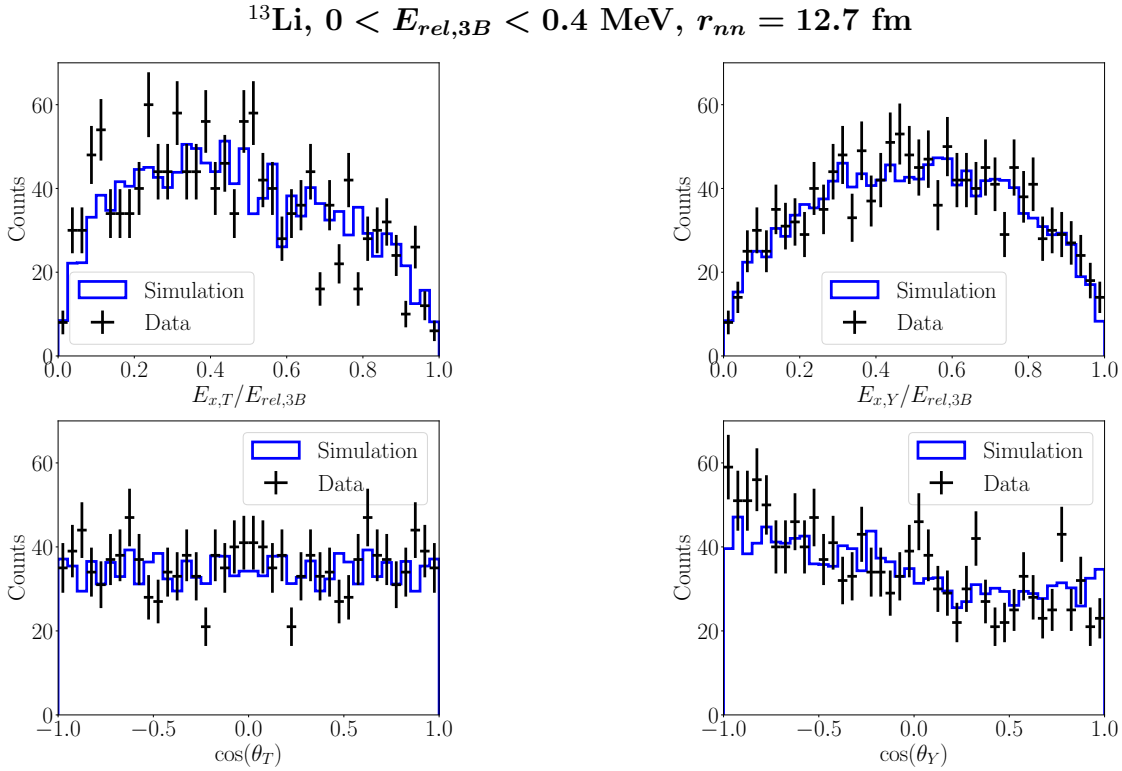

Figure 9.5: The Jacobi coordinates for the decay of ^{13}Li→ ^{11}Li+n+n, with a selection of the events with a three-body relative energy between 0 and 400 keV. The simulation are performed assuming a direct decay of ^{13}Li to ^{11}Li, with $r_{nn} = 12.7$ fm.

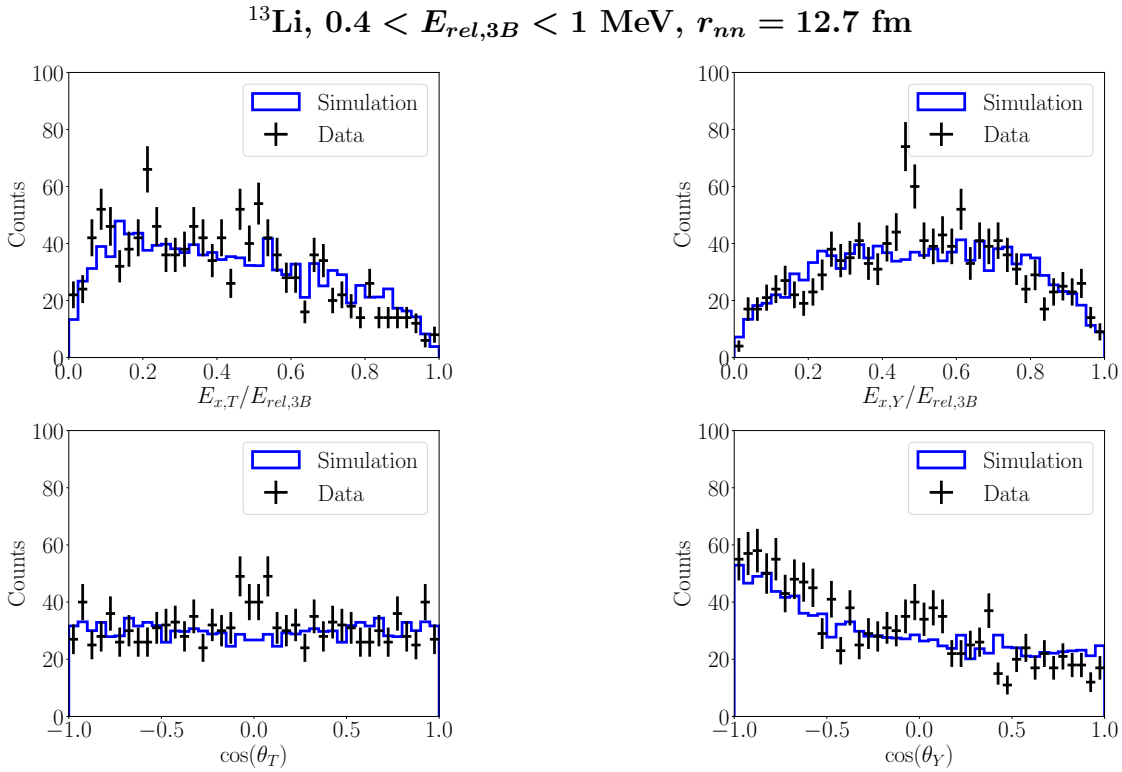

Figure 9.6: The Jacobi coordinates for the decay of ^{13}Li, with a selection of the events with a three-body relative energy between 400 and 1000 keV. The simulation are performed assuming a direct decay of ^{13}Li to ^{11}Li, with $r_{nn} = 12.7$ fm.

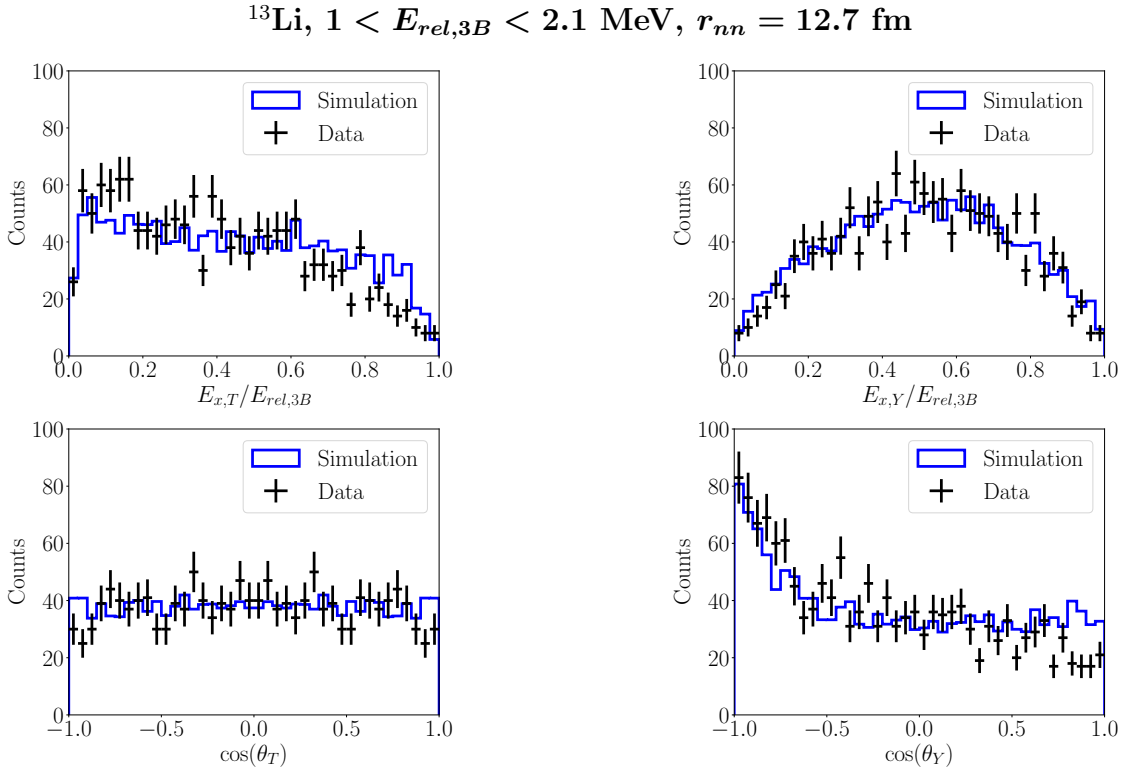

Figure 9.7: The Jacobi coordinates for the decay of ^{13}Li, with a selection of the events with a three-body relative energy between 1 and 2.1 MeV. The simulation are performed assuming a direct decay of ^{13}Li to ^{11}Li, with $r_{nn} = 12.7$ fm.

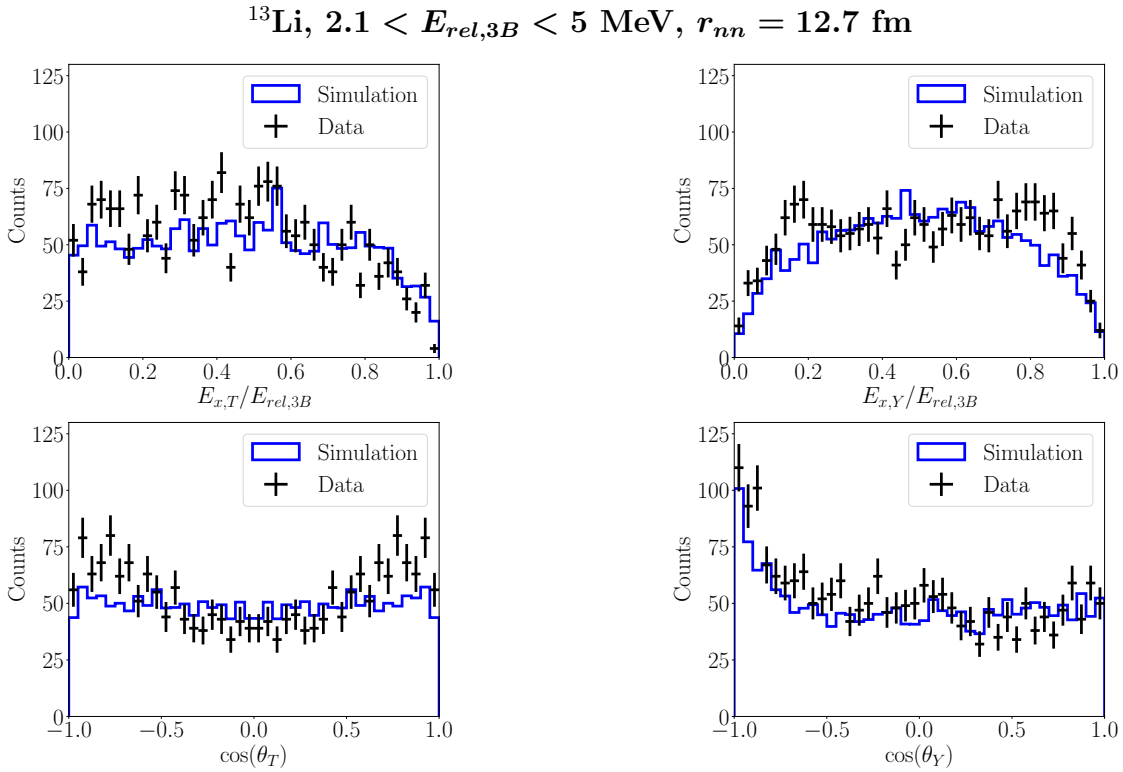

Figure 9.8: The Jacobi coordinates for the decay of ^{13}Li, with a selection of the events with a three-body relative energy between 2.1 and 5 MeV. The simulation are performed assuming a direct decay of ^{13}Li to ^{11}Li, with $r_{nn} = 12.7$ fm.

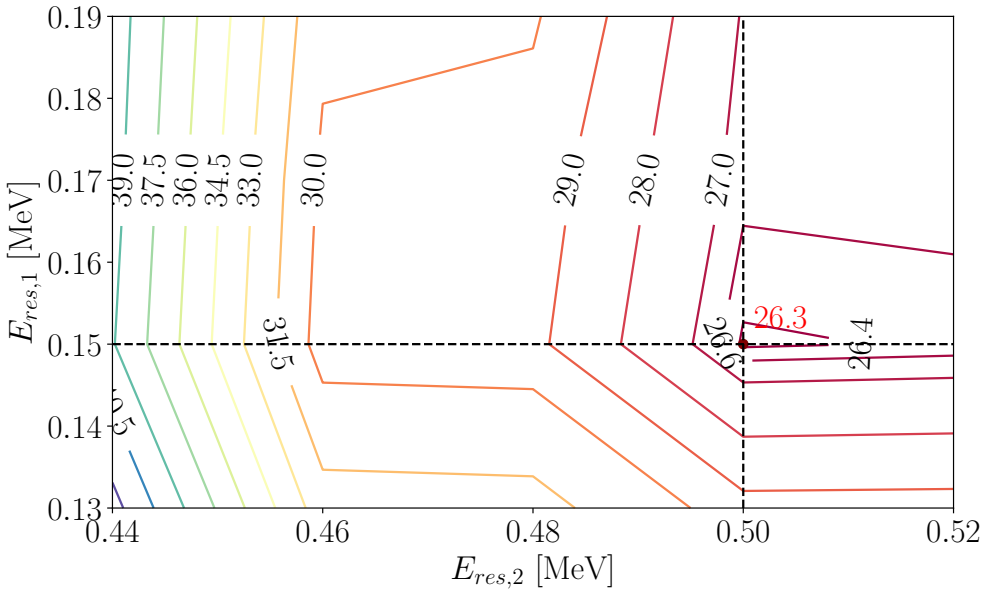

Figure 9.9: χ^2 surface for the determination of the resonance energy of the two intermediate states in ^{12}Li. The y-axis and the x-axis are the resonance energies of the two intermediate states in ^{12}Li. The z-axis is the χ^2 for each fit. The minimal χ^2 can be found at [0.15,0.5] with χ^2=26.3.

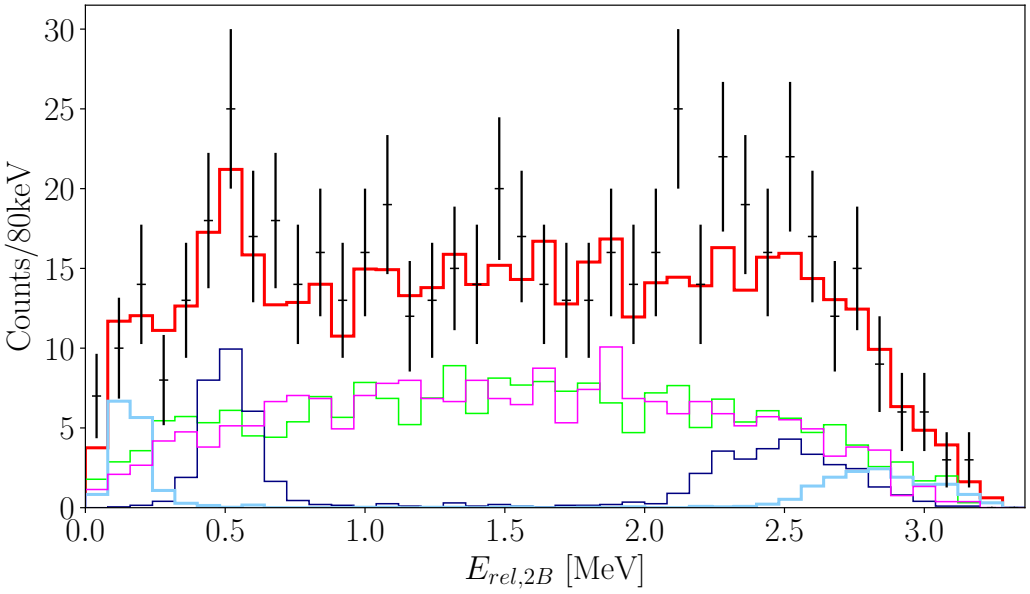

Figure 9.10: Fit of the two-body (f+n) relative energy spectrum in the 2760-3360 keV gate on the three-body relative energy. The black crosses are the data points with their error bars. The light blue and the navy blue histogram are the response functions for the intermediate decay from the 2.13 MeV state in ^{13}Li through the 0.15 keV and the 0.5 keV intermediate state, respectively. The pink histogram is the response function for the direct decay of the 2.13 MeV state in ^{13}Li. The green histogram is the response function for the direct decay of the remaining states in ^{13}Li in the considered gate. The red histogram is the sum of all the previously mentioned contributions.

In figure 9.10, the amplitudes of each contribution are not fitted freely to the data. For a given energy range, one can note that the fit in figure 9.1b proposes values for each amplitudes. As a consequence, the integral of the different contributions in figure 9.10 should be consistent with the ones found in the 2760-3360 keV range for the three-body spectrum, and the integral of the data in that range should be used as a normalization factor. As now, one considers that the 2.13 MeV resonance in ^{13}Li can decay both directly to ^{11}Li and sequentially through ^{12}Li, the fitted parameters are the following ones:

- the proportion of events decaying through the resonant state with $E_{res} = 0.5$ MeV in ^{12}Li, noted a_1,
- the proportion of events decaying through the resonant state with $E_{res} = 0.15$ MeV in ^{12}Li, noted a_2,
- the proportion of events decaying directly to ^{11}Li, noted $a_3 = 1 - a_1 - a_2$.

In figure 9.10, the following parameters yield the lowest χ^2: $a_1 = 0.2$, $a_2 = 0.1$, and $a_3 = 0.7$. One can apply these proportions to the Jacobi coordinates in the same 2760-3360 keV gate. The result is given in figure 9.11.

^{13}Li, 2.76 < $E_{rel,3B}$ < 3.36 MeV, r_{nn} = 12.7 fm

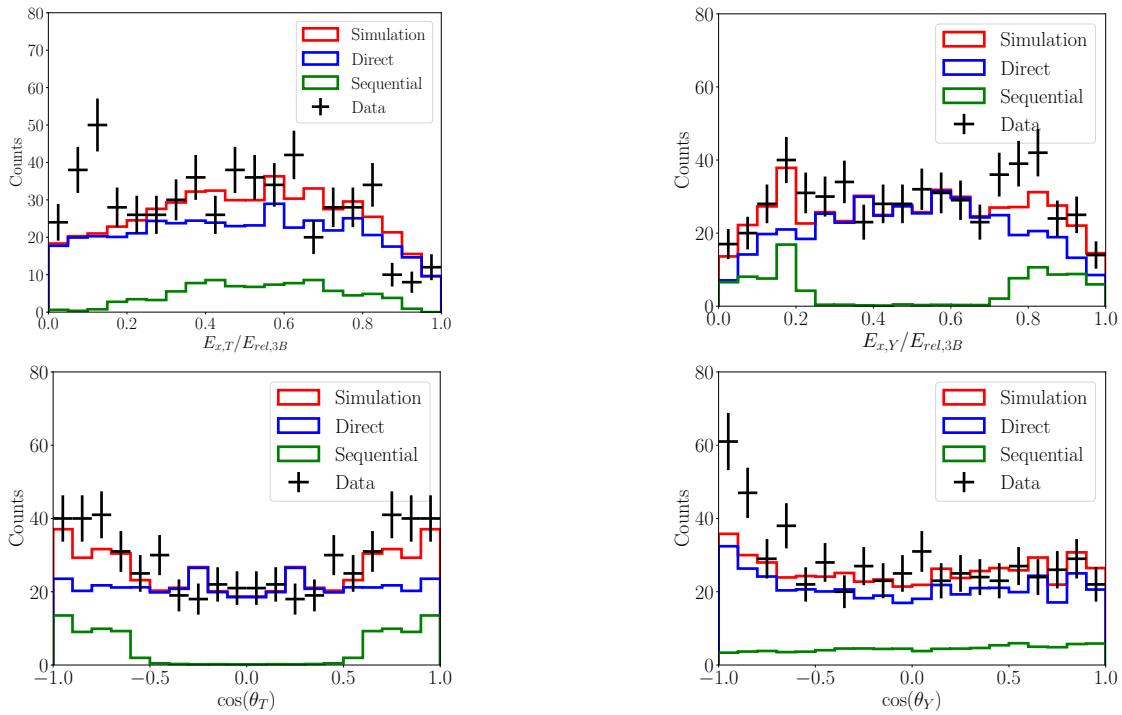

Figure 9.11: The Jacobi coordinates for the decay of ^{13}Li, with a selection of the events with a three-body relative energy between 2760 and 3360 keV. The simulation are performed with $r_{nn} = 12.7$ fm. The blue response function corresponds to the direct decay, and the green response function to the sequential decay. The red histogram is the sum of the two latter contributions.

Fitting the Jacobi coordinates in each of the proposed gates enabled the determination of the decay process of each resonant states in ^{13}Li. This shows evidences of sequential decay at high three-body relative energy. The selection between 2760 and 3360 keV made it possible to have a measurement of the resonance energy of the two observed states in

^{12}Li. It also gave hints of a sequential behavior in this range of the three-body relative energy. Using the same method for section 4 in figure 9.1b makes it possible to fit the areas that were poorly reproduced in figure 9.8, on the $\cos(\theta_T)$ and the $E_{x,Y}$ coordinates. The lowest χ^2 for the Jacobi coordinates in section 4 is found for $a_1 = 0.3$, $a_2 = 0.1$ and $a_3 = 0.6$. The corresponding fit is displayed in figure 9.12.

The information about the decay processes and the resonance energy of the excited states can be summed up in the level scheme in figure 9.13a. It can be compared to the one proposed by Z. Kohley *et al.* in [97], displayed in figure 9.13b.

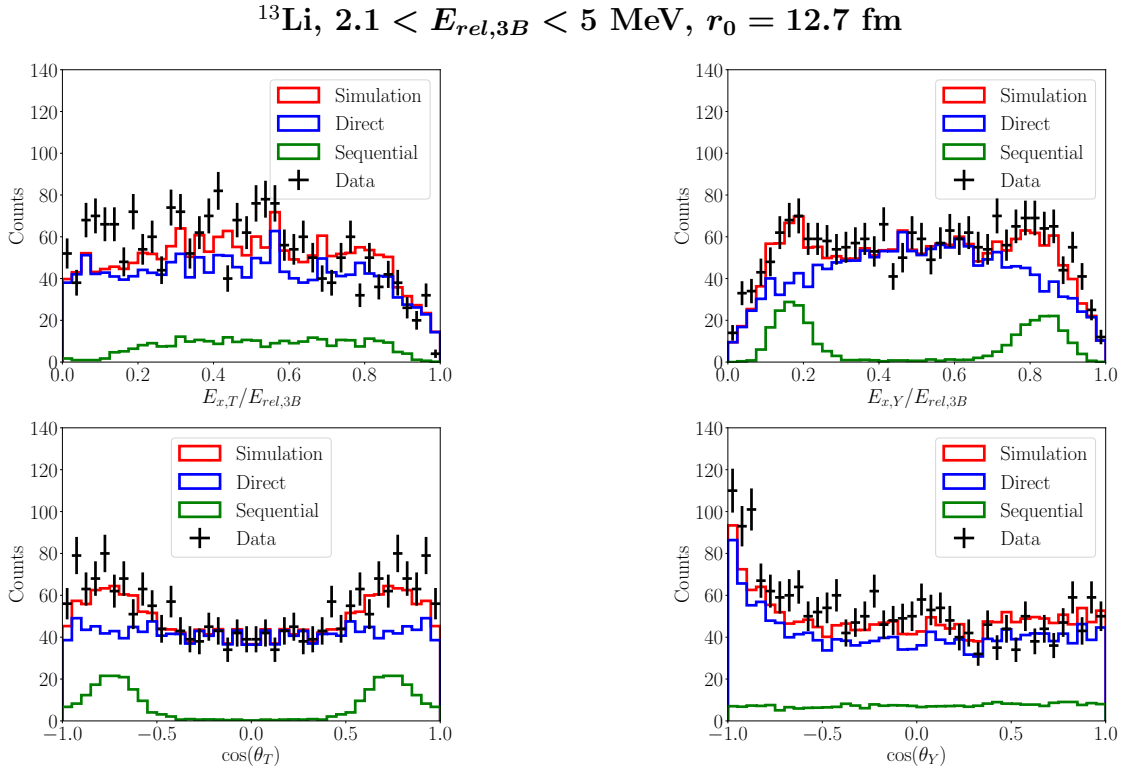

Figure 9.12: The Jacobi coordinates for the decay of ^{13}Li, with a selection of the events with a three-body relative energy between 2.1 and 5 MeV. The simulation are performed with $r_{nn} = 12.7$ fm. The blue response function corresponds to the direct decay, and the green response function to the sequential decay. The red histogram is the sum of the two latter contributions.

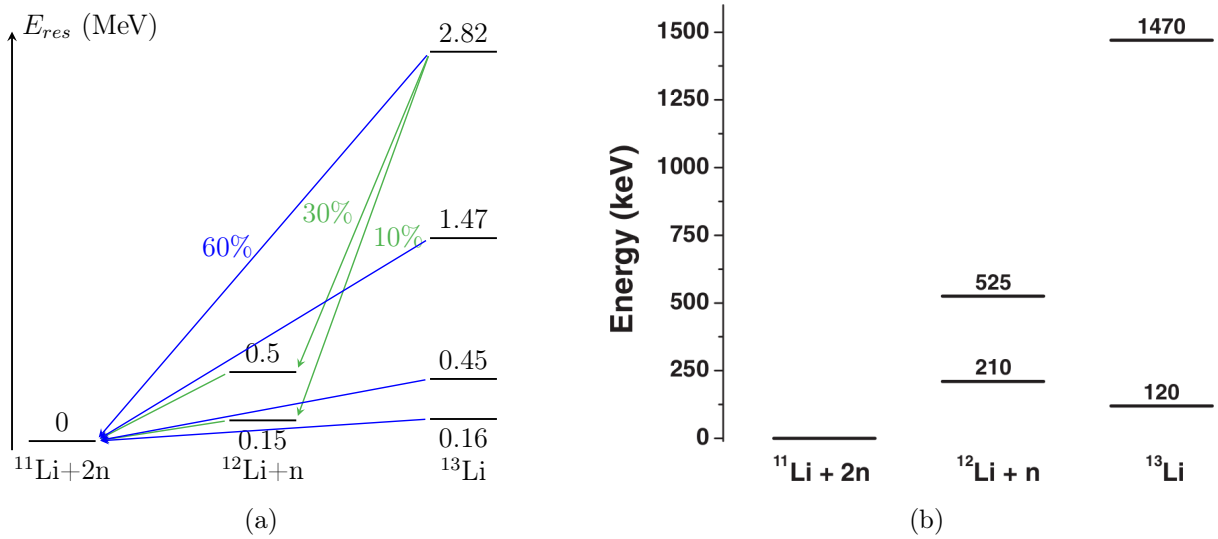

Figure 9.13: (a) Level scheme for the decay of ^{13}Li from the results of the present work. The blue arrows represent the direct decay, and the green arrows the sequential decay. The percentages on the arrows starting on the 2.13 MeV indicate the proportion of each type of decay for this resonant state. (b) Level scheme for the decay of ^{13}Li, proposed by Z. Kohley *et al.* in [97].

9.2 Two-neutron decay of ^{11}Li

A similar study as the one conducted for ^{13}Li has been performed in the case of the two-neutron decay of ^{11}Li. The three-body relative energy spectrum is displayed in figure 9.14, as well as the gates used for the rest of this study.

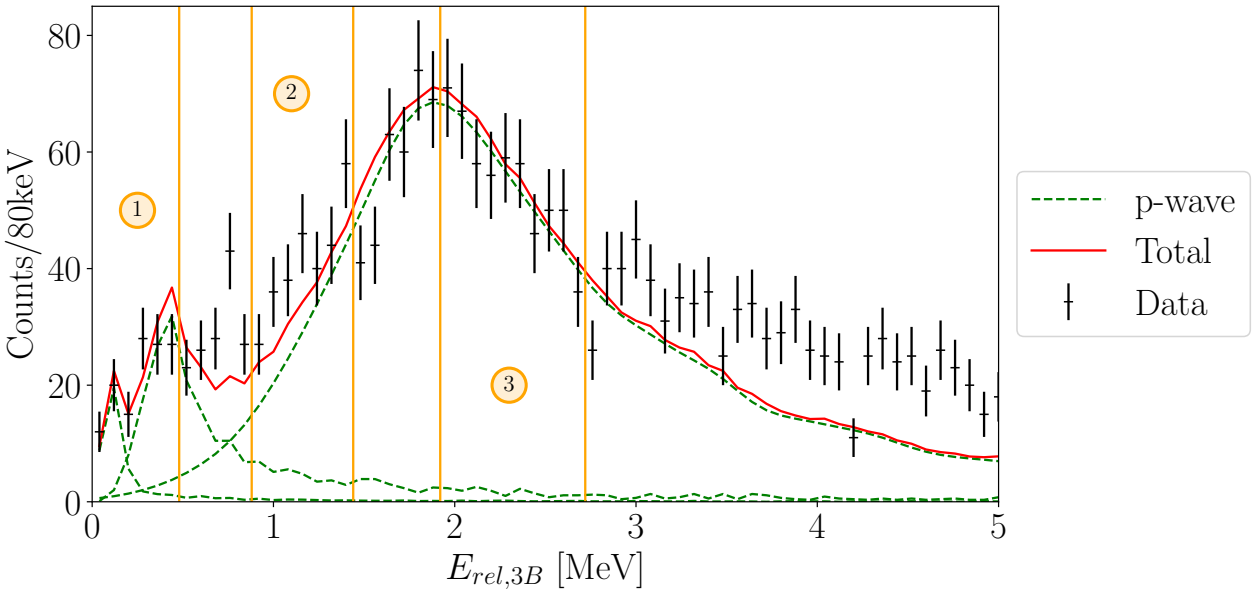

Figure 9.14: Three-body invariant mass spectrum of ^{11}Li for different wall events, fitted with Breit-Wigner distributions in green. In red is the sum of all contributions, and in black are the experimental data points. The vertical orange lines show the limits of the gates applied on the data. Section 1 ranges from 0 to 0.48 MeV. Section 2 ranges from 0.88 to 1.44 MeV. Section 3 ranges from 1.92 to 2.72 MeV.

Section 1: $0 < E_{rel,3B} < 0.48$ MeV

Section 1 considers events with $0 < E_{rel,3B} < 0.48$ MeV. Two p-wave resonances have been used to reproduce the data in this energy range. The fit is shown in figure 9.15.

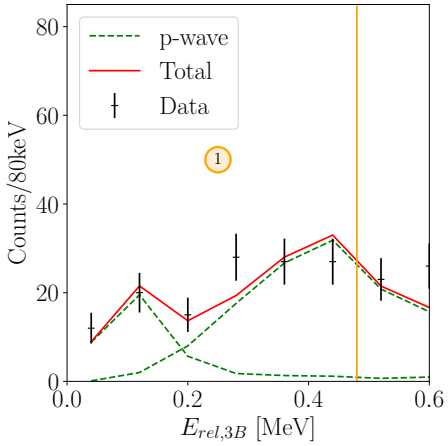

Figure 9.15: Fit of the three-body invariant mass spectrum of ^{11}Li, for different wall events in the $0 < E_{rel,3B} < 0.48$ MeV range.

	1	2
E_{res} (MeV)	0.08(2)	0.39(6)
Γ_{res} (MeV)	0.010(3)	0.7(4)

Table 9.4: Parameters for the resonances used in the fit of figure 9.15. E_{res} is the resonance energy, and Γ_{res} is the width at E_{res}.

One can first note that a similar resonance to resonance 2 in table 9.4 has been detected previously in [111]. In a similar way to what has been done in subsection 9.1.2, several possibilities for the decay of these two resonant states have been taken into account. The corresponding response functions have been used to fit the two-body (^{9}Li+n) relative energy spectrum, with the constraint of the integral of the resonant state in ^{11}Li. The result of this fit is displayed in figure 9.16. The different parameters for the resonances in ^{10}Li considered for the fit are gathered in table 9.5.

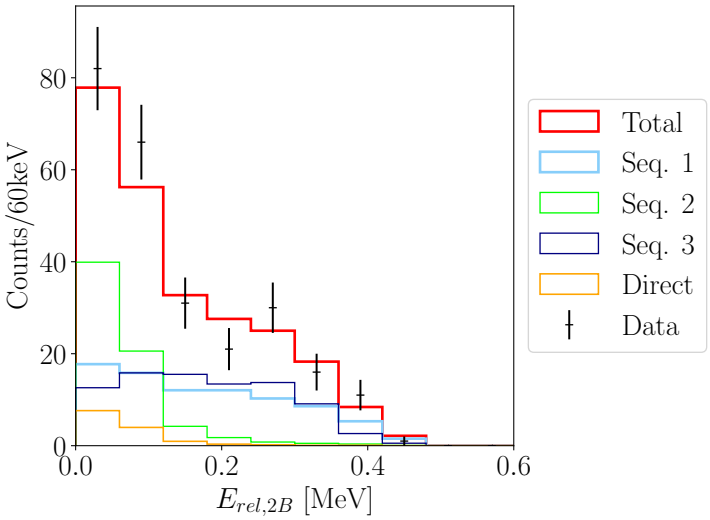

Figure 9.16: Fit of the two-body (^{9}Li+n) invariant mass spectrum, for different wall events in the $0 < E_{rel,3B} < 0.48$ MeV range. The light blue histogram is the response function for the sequential decay of resonance 2 in ^{11}Li through resonance 1 in ^{10}Li. The navy blue histogram is the response function for the sequential decay of resonance 2 in ^{11}Li through resonance 2 in ^{10}Li. The light green histogram is the response function for the sequential decay of resonance 1 in ^{11}Li through resonance 1 in ^{10}Li. The orange histogram is the response function for the direct decay of resonance 1 in ^{11}Li. The red histogram is the sum of all the aforementioned contributions.

	1		2
a_s (fm)	-30	E_{res} (MeV)	0.3
		Γ_{res} (MeV)	0.14

Table 9.5: Parameters for the intermediate ^{10}Li resonances used in the fit of figure 9.16. Resonance 1 is an s-wave state, given with its scattering length a_s. For resonance 2, E_{res} is the resonance energy, and Γ_{res} is the width at E_{res}.

Resonance 1 in ^{10}Li is an s-wave state that has been measured in previous studies, notably in [104] where the scattering length a_s is the same as the one used in this study. Resonance 2 is consistent with a p-wave resonant state with $E_{res} = 0.21(12)$ MeV previously measured in [107]. In an analogous way as what was described for ^{13}Li in subsection 9.1.2, what is minimized here are the proportions of sequential and direct contribution for each resonant state in ^{11}Li. The result of this procedure applied on the two-body relative energy spectrum is that the decay of resonance 2 in ^{11}Li is sequential through resonance 1 in ^{10}Li with an intensity of 50%, and through resonance 2 in ^{10}Li with an intensity of 50%. Resonance 1 in ^{11}Li decays sequentially through resonance 1 in ^{10}Li with an intensity of

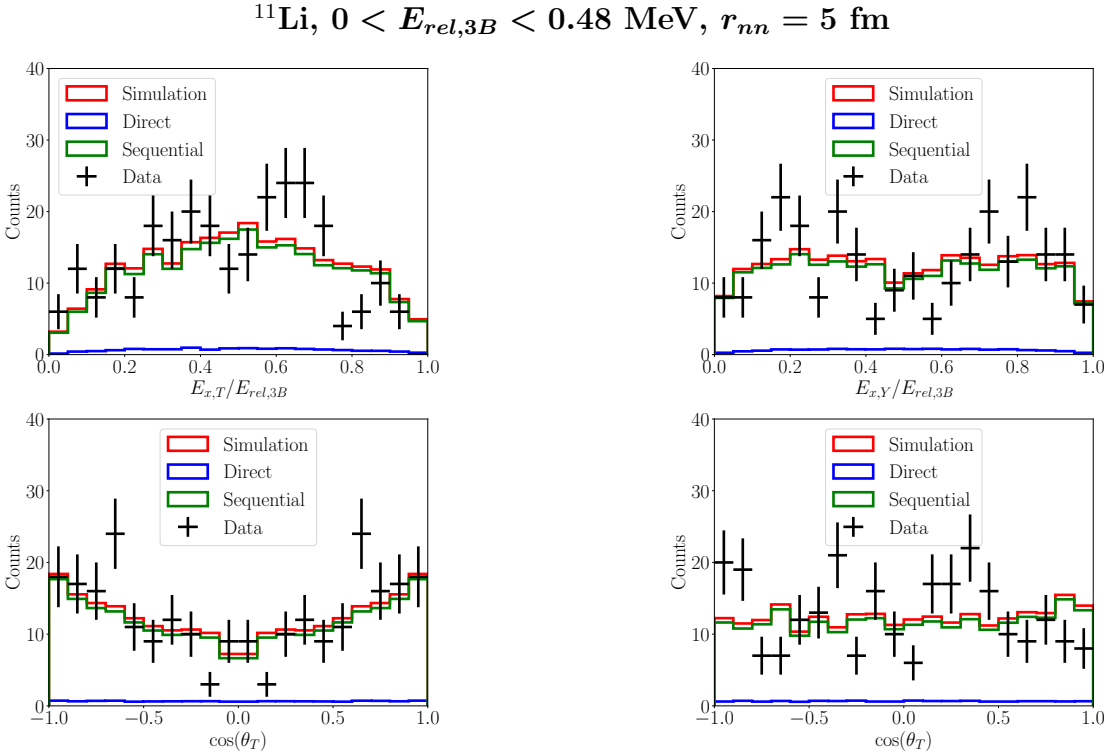

Figure 9.17: The Jacobi coordinates for the decay of ^{11}Li, with a selection of the events with a three-body relative energy between 0 and 0.48 MeV. The simulation are performed with $r_{nn} = 5$ fm. The blue response function corresponds to the direct decay, and the green response function to the sequential decay. The red histogram is the sum of the two latter contributions.

84% and decays directly with an intensity of 16%. One can apply the same proportions to reproduce the Jacobi coordinates. This is shown in figure 9.17. The different sequential and direct contributions in figure 9.16 are summed into one total sequential and one total direct contribution, which then represent 92% and 8% of the statistics respectively, in the fit of the Jacobi coordinates.

Section 2: 0.88<$E_{rel,3B}$<1.44 MeV

The analysis conducted on section 1 has also been done on section 2, for which $0.88 < E_{rel,3B} < 1.44$ MeV. The work hypothesis for this range of three-body relative energy is that the events in section 2 make up the low energy tail of a resonance at higher energy. The resulting fit is given in figure 9.18, and the parameters of this resonance are given in table 9.6.

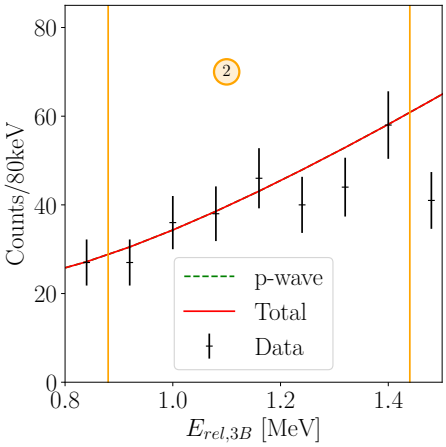

Figure 9.18: Fit of the three-body invariant mass spectrum of ^{11}Li, for different wall events in the $0.88 < E_{rel,3B} < 1.44$ MeV range.

	3
E_{res} (MeV)	2.1(3)
Γ_{res} (MeV)	2.7(5)

Table 9.6: Parameters for the resonances used in the fit of figure 9.18. E_{res} is the resonance energy, and Γ_{res} is the width at E_{res}.

Resonance 3, indicated in table 9.6, is coherent with a resonance previously measured in [107]. The two-body (fragment+neutron) relative energy spectrum in the considered gate is then fitted, considering the sequential decay and the direct decay of resonance 3 in ^{11}Li. The fit is shown in figure 9.19, and the parameters for the considered intermediate resonances is indicated in table 9.7.

	1		2	3	4
a_s (fm)	-30	E_{res} (MeV)	0.3	0.62	1.05
		Γ_{res} (MeV)	0.14	0.06	0.03

Table 9.7: Parameters for the intermediate ^{10}Li resonances used in the fit of figure 9.19. Resonance 1 is an s-wave state, given with its scattering length a_s. For resonance 2, 3 and 4, E_{res} is the resonance energy, and Γ_{res} is the width at E_{res}.

Resonances 1 and 2 in ^{10}Li indicated here are the same intermediate resonances as in table 9.5. Resonance 3 in ^{10}Li is consistent with a resonant state previously measured in [107], and resonance 4 is consistent with a previously measured resonance in [137]. In a similar way as what has been exposed for section 1, the integral of the fitted response function in figure 9.18 constrains the integral of the total response function in figure 9.19. Therefore, the different sequential and direct contributions are fitted with amplitudes that are lower than 1, and for which the sum is equal to 1. As a result, this fitting procedure yields that, for $0.88 < E_{rel,3B} < 1.44$ MeV, the decay of resonance 3 in ^{11}Li is fully sequential. The percentage of sequential decay through resonance 1, 2 and 3 in ^{10}Li is 30% for each decay. The remaining 10% is the proportion of sequential decay through resonance 4 in ^{10}Li. These proportions have been applied on the Jacobi coordinates and the result is shown in figure 9.20.

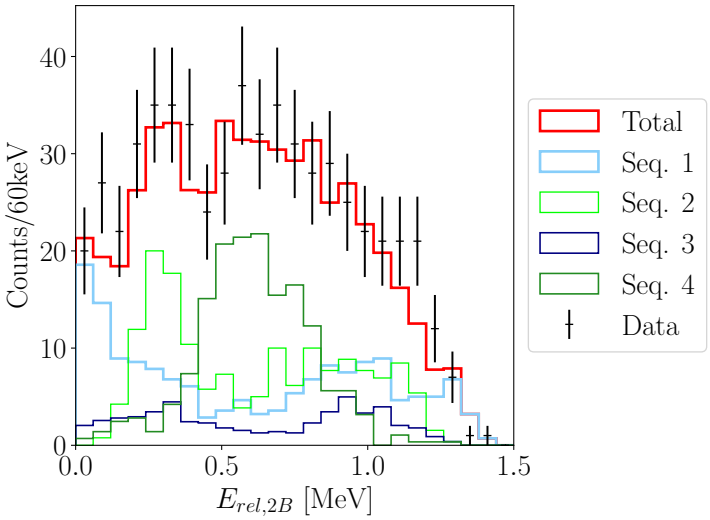

Figure 9.19: Fit of the two-body (^{9}Li+n) invariant mass spectrum, for different wall events in the $0.88 < E_{rel,3B} < 1.44$ MeV range. The light blue histogram is the response function for the sequential decay of resonance 3 in ^{11}Li through resonance 1 in ^{10}Li. The light green histogram is the response function for the sequential decay of resonance 3 in ^{11}Li through resonance 2 in ^{10}Li. The dark green histogram is the response function for the sequential decay of resonance 3 in ^{11}Li through resonance 3 in ^{10}Li. The navy blue histogram is the response function for the sequential decay of resonance 3 in ^{11}Li through resonance 4 in ^{10}Li. The red histogram is the sum of all the aforementioned contributions.

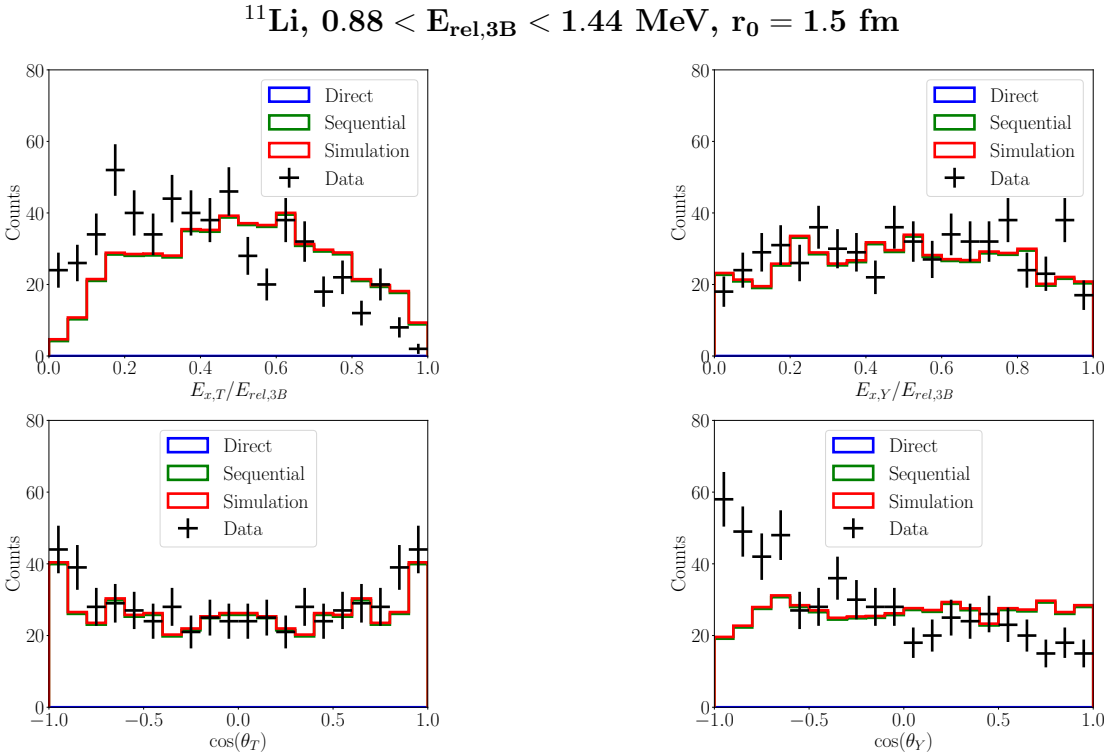

Figure 9.20: The Jacobi coordinates for the decay of ^{11}Li, with a selection of the events with a three-body relative energy between 0.88 and 1.44 MeV. The simulation are performed with $r_{nn} = 3.7$ fm. The green response function corresponds to the sequential decay. The red histogram is the sum of the two latter contributions. The proportions for the sequential and direct contributions are taken directly from the fit in figure 9.19.

The fit is rather satisfactory and reproduces the main features of $E_{x,Y}/E_{rel,3B}$ and $\cos(\theta_T)$. However, the two other Jacobi coordinates appear to not be fitted very well with some features of the plot not being reproduced, like the increasing number of counts for low $\cos(\theta_Y)$ for example. One explanation for this is the fact that $E_{x,Y}/E_{rel,3B}$ and $\cos(\theta_T)$ are more dependent on the sequential or direct nature of the decay process, while $E_{x,T}/E_{rel,3B}$ and $\cos(\theta_Y)$ are more dependent on the neutron correlations.

In this work, neutron correlations are taken into account with the correlation function and the r_{nn} parameter, as described in subsection 8.4.4. For this range of three-body relative energy, the value that appears more suitable to reproduce the data is 3.7 fm, which is the minimum value of r_{nn} for which the chosen formalism holds. Moreover, the resonant peaks visible in figure 9.19 are directly linked to the resonance energy and the width of the intermediate states in ^{10}Li. On the one hand, it then appears reasonable that the different proportions determined by the fit on the two-body spectrum reproduce well the Jacobi coordinates that rely on the nature of the decay process. On the other hand, the neutron correlations being at their limit of validity, it also appears reasonable that the Jacobi coordinates relying on the neutron correlations parameter are not well reproduced in that case.

The minimization procedure described earlier in this paragraph has been applied directly on the Jacobi coordinates, and the result is displayed in figure 9.21. Then, the resulting coefficients for each decay process have been applied to the corresponding response functions for the two-body relative energy spectrum. This is shown in figure 9.22. The resulting distribution does not reproduce the two-body relative energy spectrum in a satisfactory way. One set of parameters reproduces the two-body relative energy spectrum but fails to reproduce the features of $E_{x,Y}/E_{rel,3B}$ and $\cos(\theta_T)$, while another set of parameters reproduces the four considered quantities in Jacobi coordinates but does not fit the two-body relative energy spectrum.

A way to reconcile both results from the minimization on the two-body relative energy spectrum, and the minimization on the Jacobi coordinates, could be a description of the neutron correlations that takes into account more strongly correlated particles than the one used here. With such a method, it could be possible to capture both the neutron correlations and the different nature of the processes that build the two-neutron decay of ^{11}Li.

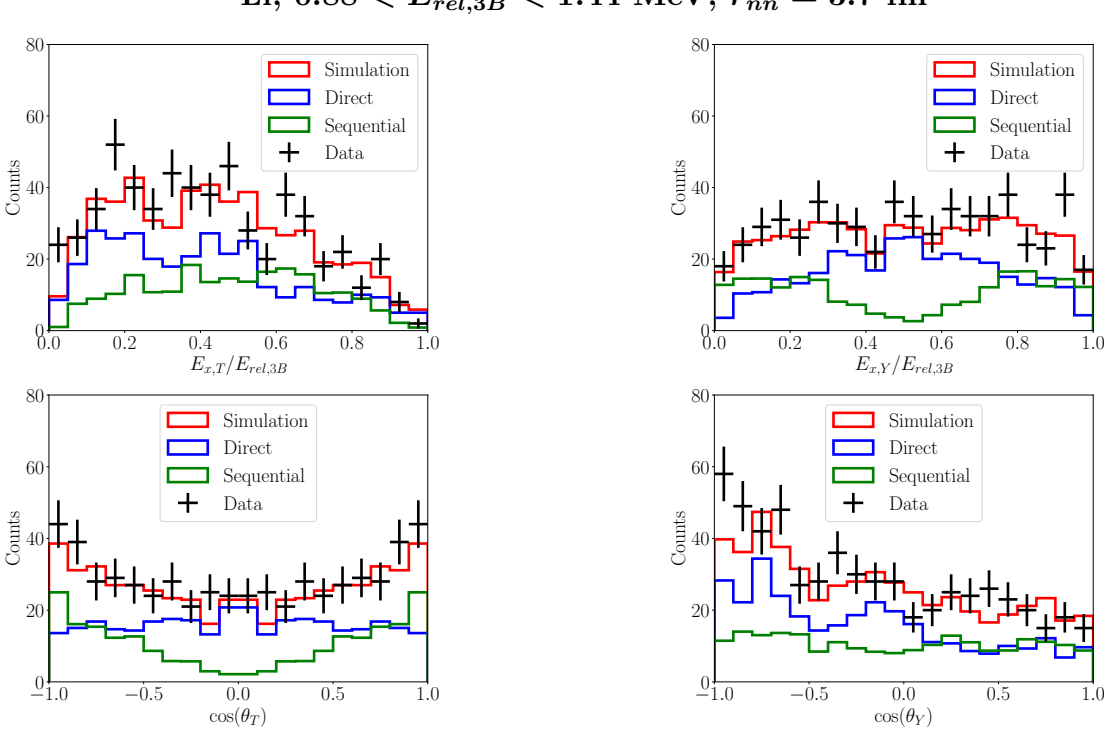

Figure 9.21: The Jacobi coordinates for the decay of ^{11}Li, with a selection of the events with a three-body relative energy between 0.88 and 1.44 MeV. The simulation are performed with r_{nn} = 3.7 fm. The blue response function corresponds to the direct decay, and the green response function to the sequential decay. The red histogram is the sum of the two latter contributions. The proportions for the sequential and direct contributions are fitted to the data.

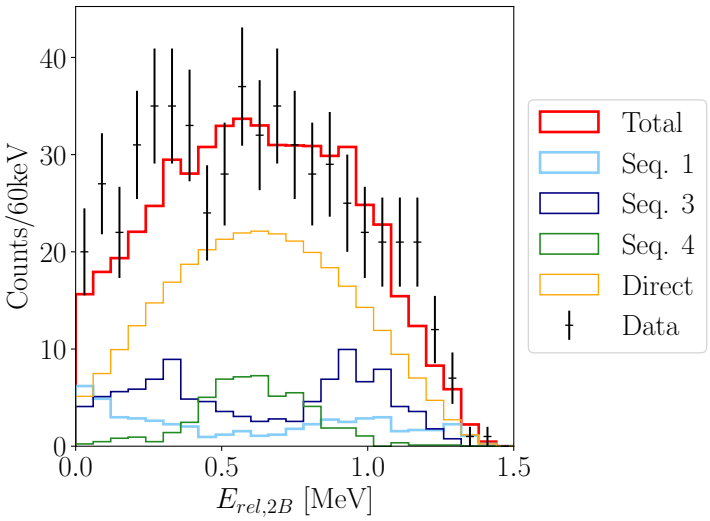

Figure 9.22: Fit of the two-body (^{9}Li+n) invariant mass spectrum, for different wall events in the 0.88 < $E_{rel,3B}$ < 1.44 MeV range. The light blue histogram is the response function for the sequential decay of resonance 3 in ^{11}Li through resonance 1 in ^{10}Li. The dark green histogram is the response function for the sequential decay of resonance 3 in ^{11}Li through resonance 3 in ^{10}Li. The navy blue histogram is the response function for the sequential decay of resonance 3 in ^{11}Li through resonance 4 in ^{10}Li. The orange histogram is the response function for the direct decay of resonance 3 in ^{11}Li The red histogram is the sum of all the aforementioned contributions.

Section 3: 1.92<$E_{rel,3B}$<2.72 MeV

Eventually, one last section has been considered for which 1.92<$E_{rel,3B}$<2.72 MeV. Resonance 3 in ^{11}Li (see table 9.6) has also been considered for the fit of the three-body relative energy spectrum, as it is shown in figure 9.23.

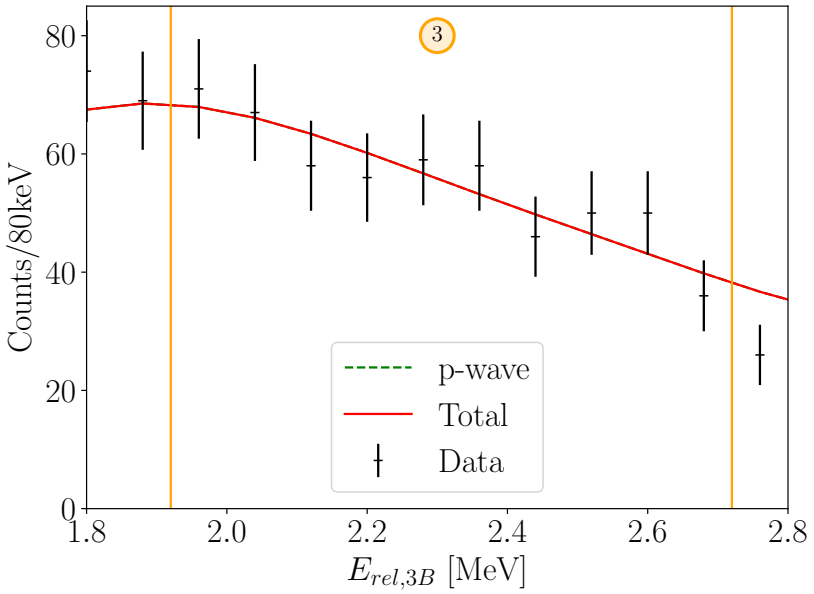

Figure 9.23: Fit of the three-body invariant mass spectrum of ^{11}Li, for different wall events in the 1.92 < $E_{rel,3B}$ < 2.72 MeV range.

The same intermediate resonances as in table 9.7 have been considered for the fit of the two-body relative energy spectrum. The result of this fit can be seen in figure 9.24.

The same minimization procedure than for section 1 and 2 has been applied. This yields that, for 1.92<$E_{rel,3B}$<2.72 MeV, resonance 3 in ^{11}Li decays sequentially through resonance 1 in ^{10}Li with an amplitude of 30%, through resonance 2 in ^{10}Li with an amplitude of 10%, through resonance 3 in ^{10}Li with an amplitude of 20%, and through resonance 4 in ^{10}Li with an amplitude of 20%. It also decays directly with an amplitude of 20%. These proportions have been applied to the Jacobi coordinates. The result is shown in figure 9.25.

As explained previously, $E_{x,Y}/E_{rel,3B}$ and $\cos(\theta_T)$ are well reproduced with the parameters given by the minimization on the two-body relative energy spectrum, as these Jacobi coordinates are mainly sensitive to the structure of the intermediate ^{10}Li. The two other coordinates are more sensitive to the neutron correlations. The minimization has then been performed on the Jacobi coordinates and the results are given in figure 9.26.

Instead of an 80% sequential and 20% direct decay of resonance 3 in ^{11}Li, the minimization on the Jacobi coordinates yields a 30% sequential and 70% direct decay. In a similar fashion to what has been done for 880 < $E_{rel,3B}$ < 1440 keV, these coefficients have been used as constraints for the fit of the two-body relative energy spectrum. The result of this procedure is shown in figure 9.27.

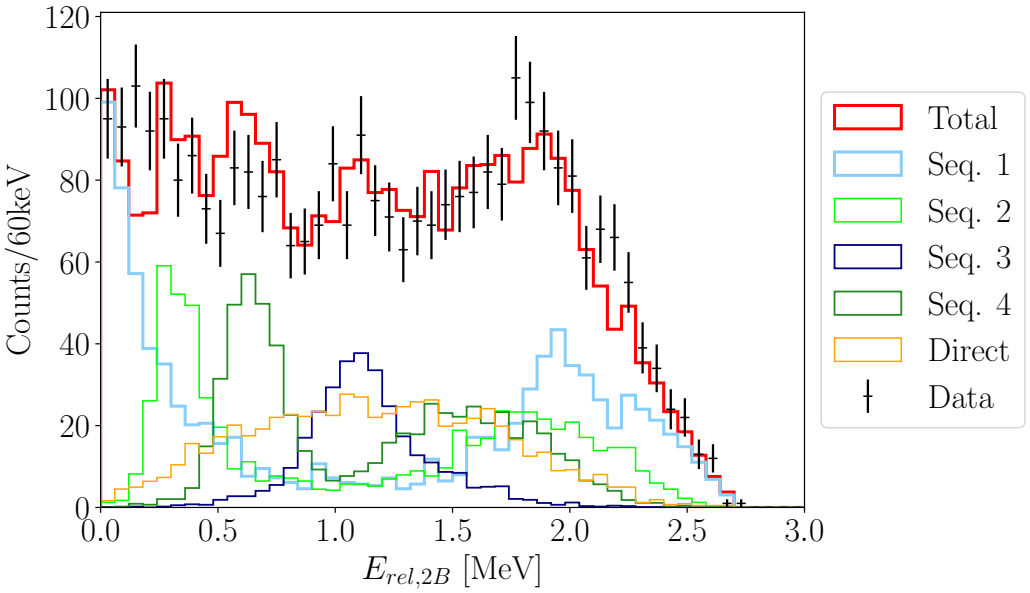

Figure 9.24: Fit of the two-body (^{10}Li+n) invariant mass spectrum, for all events in the $1.92 < E_{rel,3B} < 2.72$ MeV range. The light blue histogram is the response function for the sequential decay of resonance 3 in ^{11}Li through resonance 1 in ^{10}Li. The light green histogram is the response function for the sequential decay of resonance 3 in ^{11}Li through resonance 2 in ^{10}Li. The dark green histogram is the response function for the sequential decay of resonance 3 in ^{11}Li through resonance 3 in ^{10}Li. The navy blue histogram is the response function for the sequential decay of resonance 3 in ^{11}Li through resonance 4 in ^{10}Li. The orange histogram is the response function for the direct decay of resonance 3 in ^{11}Li. The red histogram is the sum of all the aforementioned contributions.

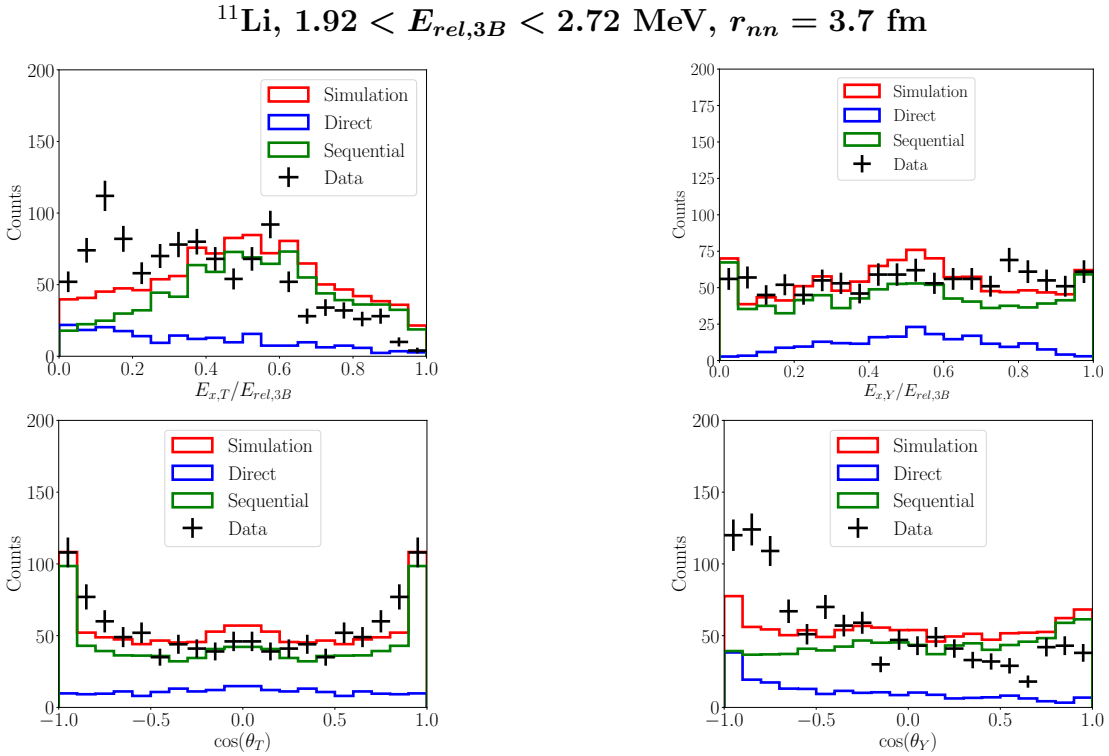

Figure 9.25: The Jacobi coordinates for the decay of ^{11}Li, with $1.92 < E_{rel,3B} < 2.72$ MeV. The simulation are performed with $r_{nn} = 3.7$ fm. The green response function corresponds to the sequential decay. The red histogram is the sum of the two latter contributions. The proportions for the sequential and direct contributions are taken directly from the fit in figure 9.24.

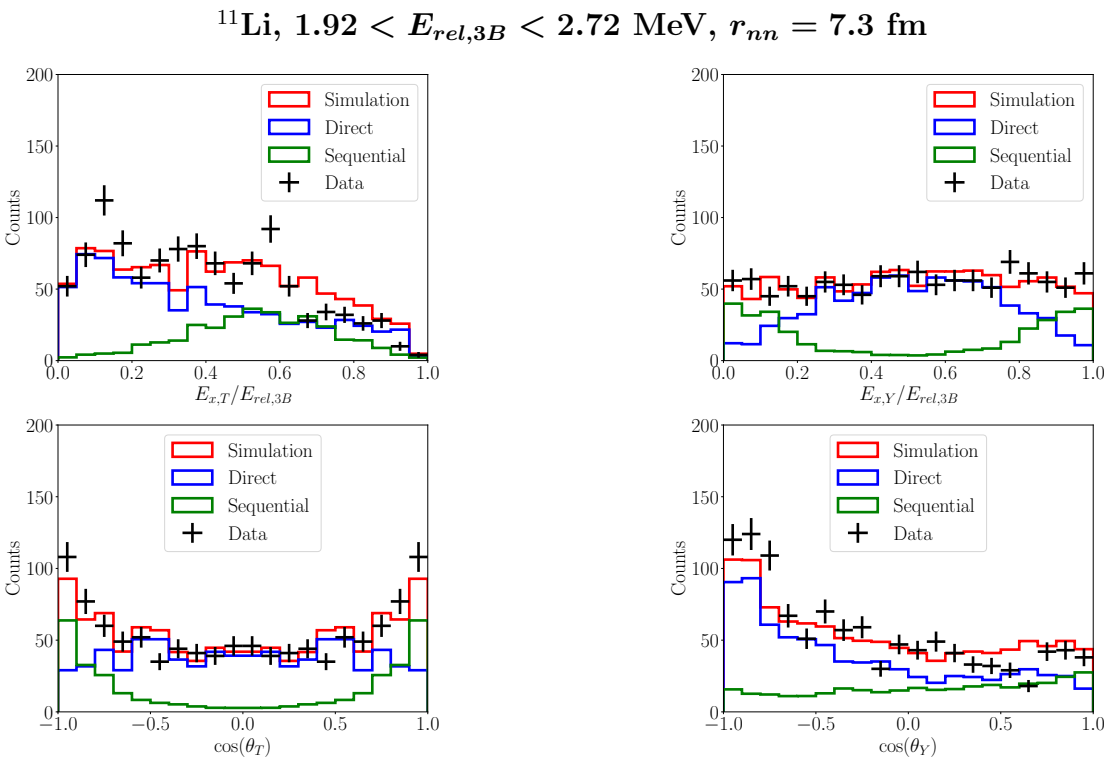

Figure 9.26: The Jacobi coordinates for the decay of ^{11}Li, with with 1.92<$E_{rel,3B}$<2.72 MeV. The simulation are performed with r_{nn} = 7.3 fm. The blue response function corresponds to the direct decay, and the green response function to the sequential decay. The red histogram is the sum of the two latter contributions. The proportions for the sequential and direct contributions are fitted to the data.

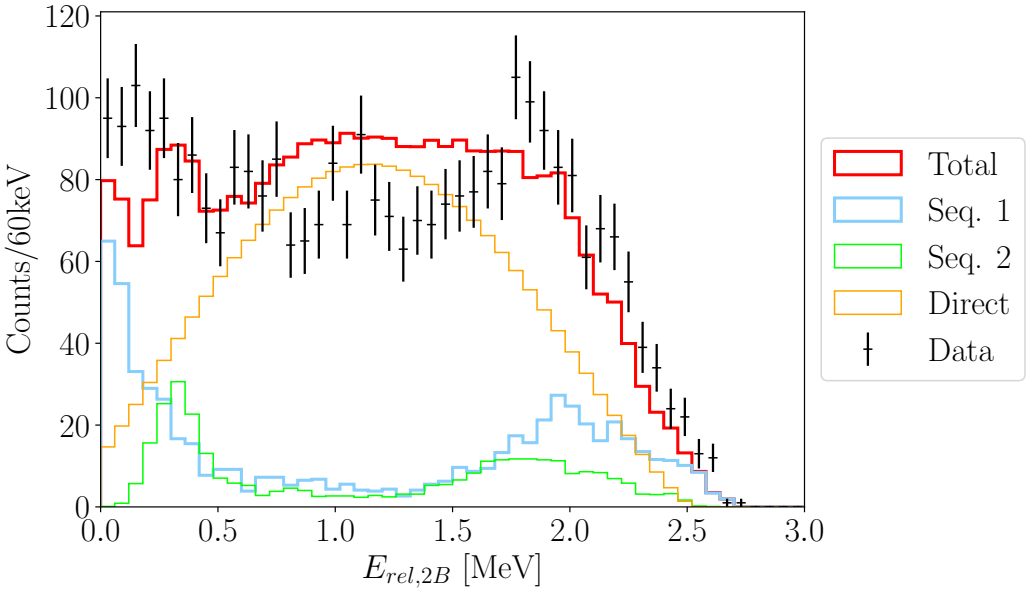

Figure 9.27: Fit of the two-body (^{10}Li+n) invariant mass spectrum, for all events in the 1.92 < $E_{rel,3B}$ < 2.72 MeV range. The light blue histogram is the response function for the sequential decay of resonance 3 in ^{11}Li through resonance 1 in ^{10}Li. The light green histogram is the response function for the sequential decay of resonance 3 in ^{11}Li through resonance 2 in ^{10}Li. The orange histogram is the response function for the direct decay of resonance 3 in ^{11}Li. The red histogram is the sum of all the aforementioned contributions.

When performing the minimization on the Jacobi coordinates, the correlation parameter r_{nn} does not need to be put at its lower limit to reproduce the structures of $E_{x,T}$ and $\cos(\theta_Y)$. It appears in figure 9.25 that, even with the lowest r_{nn} possible, these two quantities are not fitted in a satisfactory way using the coefficients found with the minimization on the two-body relative energy spectrum. Similarly to the $0.88 < E_{rel,3B} < 1.44$ MeV gate, the coefficients found when minimizing on the energy and angle in Jacobi coordinates do not reproduce the features of the two-body relative energy spectrum.

This discrepancy may originate from the initial work hypothesis made on the three-body relative energy spectrum. Indeed, it has been assumed that a single large p-wave resonance reproduced the data in this gate. However, one could decide to fit this part of the spectrum with two (or more) narrower, but overlapping, resonances. In this study, no hint of such structures has been found, making it possible to only constrain properly the resonance that has been assumed here, namely resonance 3 in ^{11}Li.

This indicates that the two-neutron decay of ^{11}Li in these ranges may not be understood in its entirety. However, the two explanations proposed in the previous paragraphs, namely the formalism of the neutron correlations and the assumptions on the three-body relative energy spectrum both reaching their limits of validity, imply phenomena and changes that go beyond the data shown here. Moreover, the scheme obtained using the two-body spectra provides a satisfactory reproduction of most considered observables, which strengthens these results, summed up in the following paragraph.

Summary

In the previous paragraphs, the two-body (fragment+n) relative energy spectrum and the Jacobi coordinates have been fitted by simulated response functions of the sequential or direct decay of resonant states in ^{11}Li, in three different ranges of three-body relative energy. From these fits, a scheme for the nature of the decay of ^{11}Li is proposed, i.e. proportions of sequential and direct decay for each assumed resonant state. For each section in the three-body spectrum, a level scheme summing up the decay process is proposed in figure 9.28. The proportions shown here are the one taken from the minimization on the two-body relative energy spectrum, as it is more sensitive to the decay process than the Jacobi coordinates. Reciprocally, the Jacobi coordinates are more sensitive to n-n correlations, and therefore, the determination of the r_{nn} parameter for each gate has been done using the results of the minimization on $E_{x,T}$, $E_{x,Y}$, $\cos(\theta_T)$ and $\cos(\theta_Y)$.

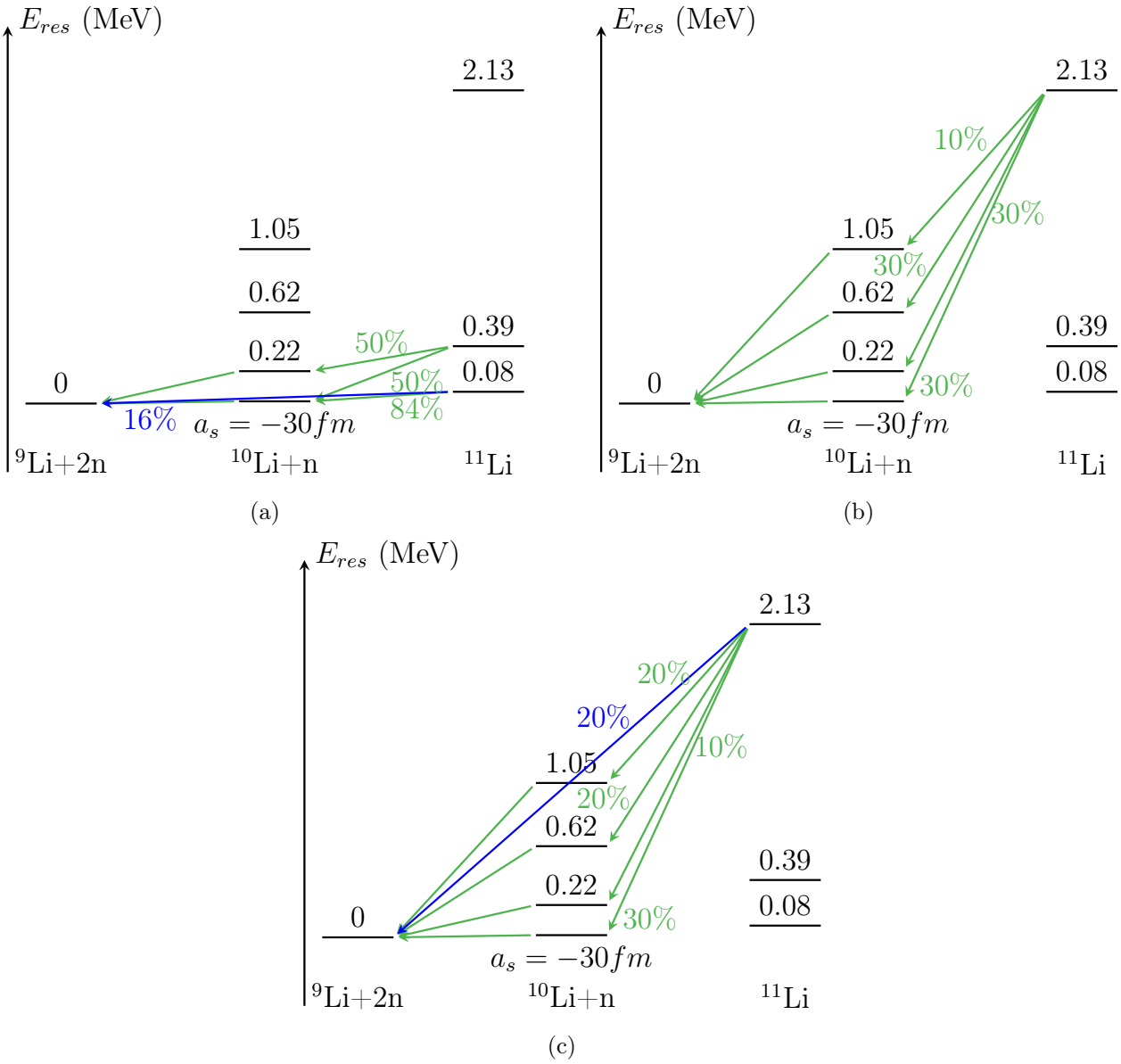

Figure 9.28: (a) Level scheme for the decay of ^{11}Li for $0<E_{rel,3B}<0.48$ MeV. The blue arrow represents the direct decay, and the green arrows the sequential decay. The percentages are the proportions for each decay. (b) Level scheme for the decay of ^{11}Li for $0.88<E_{rel,3B}<1.44$ MeV. The green arrows the sequential decay. The percentages are the proportions for each decay. (c) Level scheme for the decay of ^{11}Li for $1.92<E_{rel,3B}<2.72$ MeV. The blue arrow represents the direct decay, and the green arrows the sequential decay. The percentages are the proportions for each decay.

9.3 Core excitation of ^{9}Li

It has been assumed, for the interpretation of the results exposed in the previous paragraphs, that the two-neutron decay of ^{11}Li would leave ^{9}Li in its ground state. This assumption can be checked by looking at the γ rays emitted in coincidence with two-neutron events. As explained in section 7.1, a reduced configuration of the DALI2 array was placed around the MINOS device. Thanks to this setup, the γ rays emitted at the target can be measured. ^{9}Li has one known bound excited state at the energy of 2691(5) keV [74], which decays to the ground state via the emission of a γ ray.

Thanks to the MINOS system, the position of the reaction vertex is reconstructed. One can then apply a Doppler correction to the data, similar to the one presented in subsection 3.1.5, using this position for the computation of the angle between the beam and the γ ray. The resulting spectrum is shown in figure 9.29.

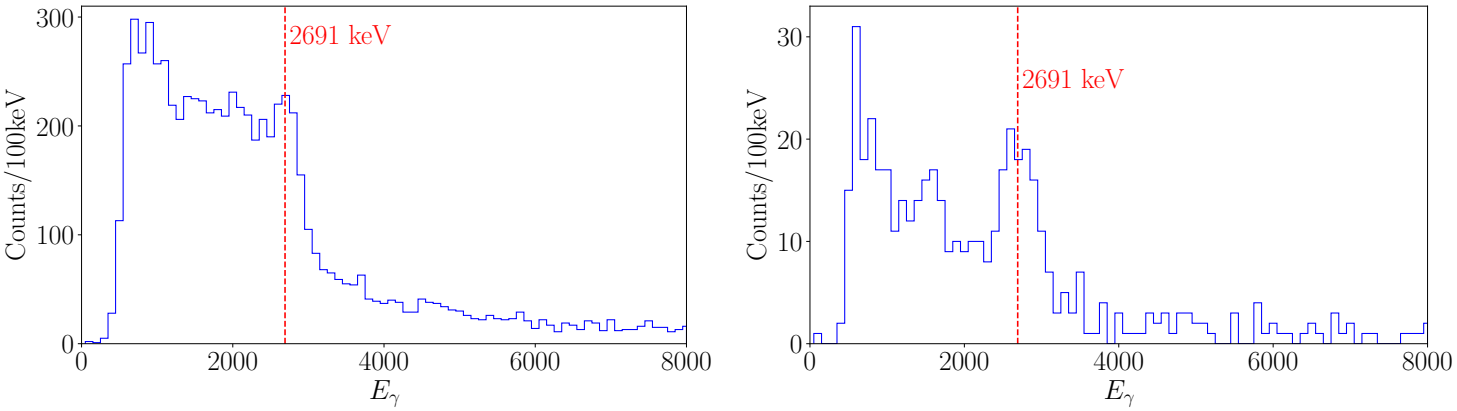

(a) (b)

Figure 9.29: (a) γ spectrum of ^{9}Li after the two-neutron decay of ^{11}Li. All the event multiplicities are taken into account. (b) γ spectrum of ^{9}Li after the two-neutron decay of ^{11}Li. Only event with their multiplicity equal to 1 are taken into account.

Figure 9.29a displays a ledge at the expected E_γ, that could be interpreted as a photopeak. As no addback procedure has been applied on these spectra, the signals in the DALI2 crystals with an incomplete energy deposit deteriorates the resolution and the separation of the peak. Not using any addback procedure here can be justified by the fact that the angular coverage of this reduced configuration of the DALI2 array is limited (the array partially covers angles ranging from 32° to 115°). As a consequence, if Compton scattering occurs in a DALI2 crystal, it is probable that the scattered γ ray leaves the detector, making the reconstruction via an addback procedure impossible.

However a simple way of improving the spectrum is to consider the events with a unitary multiplicity, as it is displayed in figure 9.29b. Indeed, γ rays going through Compton scattering in the DALI2 crystals exhibit usually high multiplicities, and considering events with low multiplicities only leaves mainly the γ rays that have deposited all their energy. Figure 9.29b displays a clear peak at the expected γ energy.

By constructing the three-body relative energy for events for which E_γ is around the photopeak of interest, one can see which resonant state of ^{11}Li is involved in the population of the excited state. This is displayed in figure 9.30.

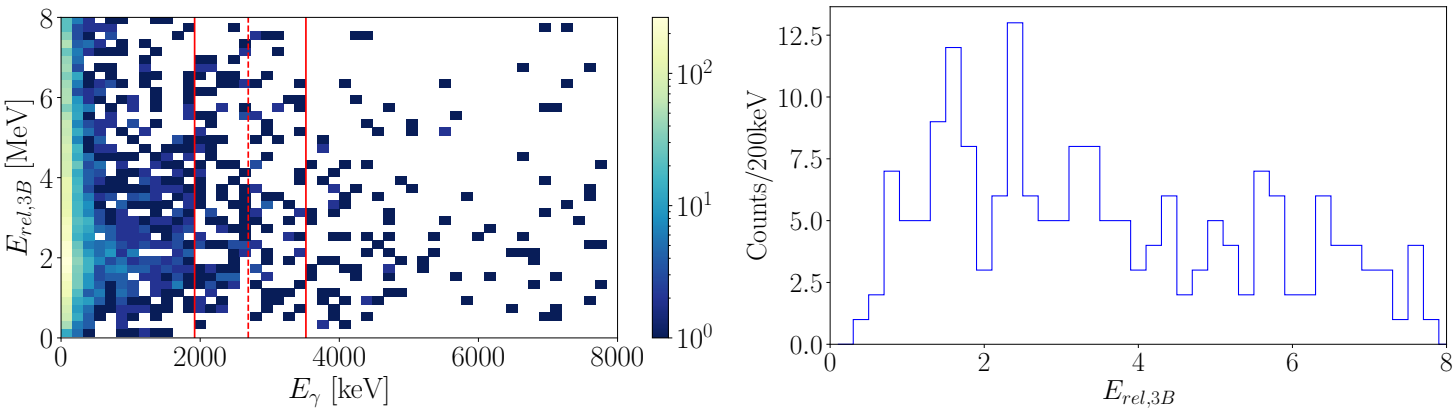

Figure 9.30: Coincidence between the three-body relative energy and the γ energy of ^{9}Li populated by the two-neutron decay of ^{11}Li. (a) $E_{rel,3B}$ as a function of E_γ. The dashed vertical red line indicates the energy of the excited state of ^{9}Li. The two solid red lines indicate the range for the projection on $E_{rel,3B}$, displayed in figure 9.30b. (b) $E_{rel,3B}$ for events with 1920 keV$<E_\gamma<$3520 keV.

The efficiency of the DALI2 array in this configuration at a γ energy of 2.7 MeV is 7.0(4)% [118]. One can compare the three-body relative energy spectrum coming from the ^{9}Li+n+n+γ coincidence, shown in figure 9.30b, to the one without γ coincidence, corrected by the efficiency of the DALI2 array. This can be seen in figure 9.31.

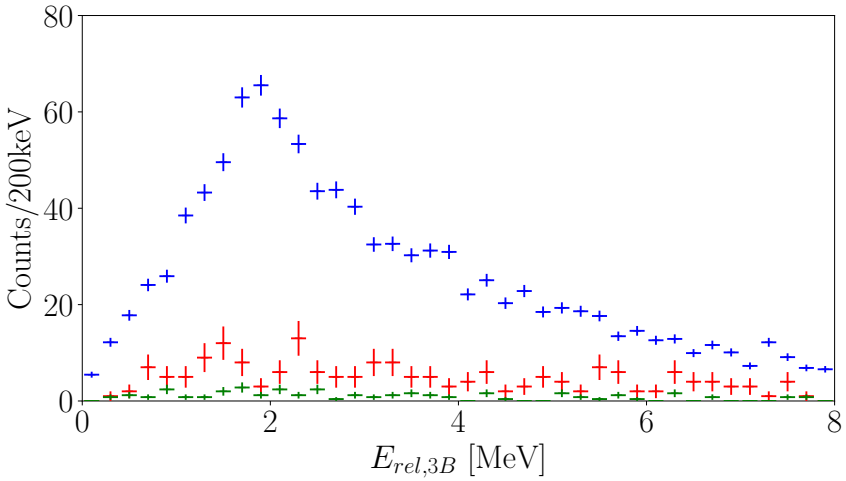

Figure 9.31: Comparison between the events correlated with the ^{9}Li core excitation and the total statistics of the two-neutron decay of ^{11}Li channel. The blue spectrum shows the whole statistics of the considered two-neutron decay channel, scaled with the efficiency of the DALI2 array. The red spectrum is the one presented in figure 9.30b. The green spectrum is the projection of the three-body relative energy for 4000 keV$<E_\gamma<$8000 keV, and shows the events correlated with the background of the γ energy spectrum.

The events correlated with the core excitation of ^{9}Li hints at two structures around 1.5 MeV and 2.3 MeV. These two structures are not visible in the spectrum yielded by a gate on the off-peak region between 4 and 8 MeV of the γ energy spectrum. Comparing the total statistics (the blue distribution in figure 9.31) with the statistics of the correlated

events (the red distribution in figure 9.31), one gets 17% of events in coincidence with a γ ray.

9.4 Comparison with theoretical calculations

The Lednicky-Lyuboshits formalism used here, and described in subsection 8.4.4, has the great advantage to offer a simple and analytical way to consider and quantify n-n correlations. However, this model is limited, especially when used to describe strongly correlated systems. Indeed, the quantification of the n-n correlations via the rms n-n distance r_{nn} in the case of the two-neutron decay of ^{11}Li is challenging, as this parameter is at its limit of validity in a range of values of three-body relative energy. As shown in section 9.2, it is difficult to fit the two-body relative energy, and the energy and angle in Jacobi coordinates, with a consistent interpretation in terms of resonant state and decay process.

This can also be due to the fact that the large structure around 2 MeV in the ^{11}Li three-body relative energy spectrum, in figure 9.14, has been considered as a single large resonant state, while, with a higher resolution, it could possibly appear as several overlapping resonances. Furthermore, the Lednicky-Lyuboshits model has the other limitation of washing out sharp structures in correlated quantities, such as $\cos(\theta_Y)$, in the case of a sequential decay. Indeed, the lifetime of a resonant state τ_{nn} is linked to its width (see equation (8.20)), which is constrained by the three-body relative energy spectrum, and can widen sharp structures in the response functions. These sharp structures are hints of strong correlations, and considering a smaller r_{nn} can help counter this effect and reproduce the data. However, it is sometimes not enough to satisfactorily reproduce the data, as the results for ^{11}Li and $1.92 < E_{rel,3B} < 2.72$ MeV show it (see the end of section 9.2). In other words, the Lednicky-Lyuboshits model does not entirely allow strong n-n correlations for sequential decays.

These considerations justify the use of more sophisticated three-body calculations. In the case of the present study, these calculations have been performed by J. Casal (Uni. de Sevilla, Spain). The considered model relies on a three-body (core+n+n) description of the isotopes of interest. The structure for the core+n two-body system is taken as an input and adjusted with a three-body force and a n-n interaction. The resonant states are described as combination of eigenstates and their time propagation is calculated. The result of this procedure is then matched with analytical asymptotic states. An article describing this method in more details is in preparation, as well as its application for the case of the unbound ^{16}Be.

This procedure yields a distribution for the f+n and n+n partial relative energies, that one can compare to a phase space distribution and to the experimental data. This is shown in figure 9.32 for the ground state of ^{13}Li. The calculated distributions shown here have been convoluted with the efficiency of the NEBULA array, using the SMSIMULATOR package, to reproduce the effect of the experimental apparatus. The correlated theoretical distributions reproduce the data satisfactorily, as opposed to the phase space distributions that do not reproduce the shifted structure in $E_{rel,2b,nn}/E_{rel,3B}$. These calculations also yield the width of the resonance for the ground state of ^{13}Li, which has been estimated to be 0.11 MeV, a consistent value with the one found experimentally of 0.12(4) MeV.

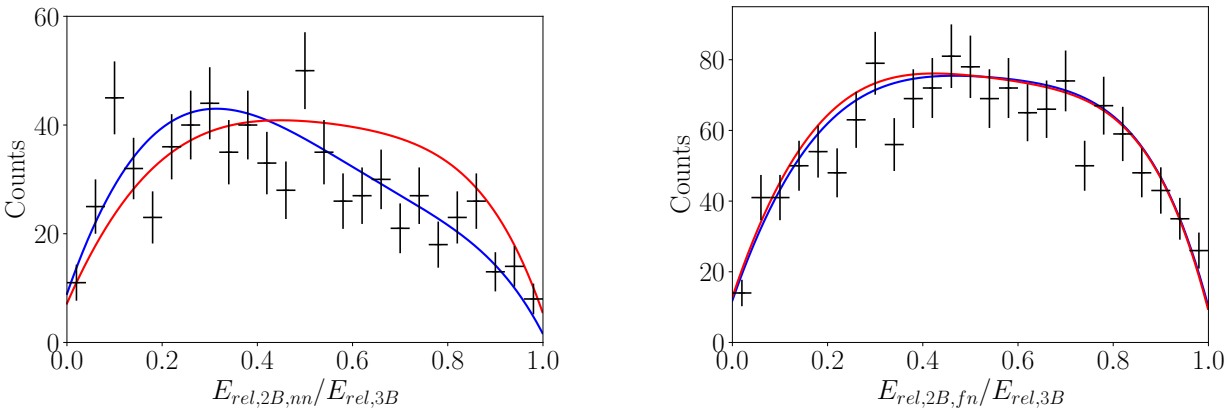

(a) (b)

Figure 9.32: Comparison between theoretical and experimental distributions for the partial relative energies of the ground state of ^{13}Li. The blue distribution is the theoretical one including n-n correlations, while the red distribution is the phase space distribution. The black crosses are experimental data. (a) The n+n partial relative energy, namely $E_{rel,2b,nn}/E_{rel,3B}$, for the ground state of ^{13}Li. (b) The n+n partial relative energy, namely $E_{rel,2b,fn}/E_{rel,3B}$, for the ground state of ^{13}Li.

As far as quantifying the n-n correlations is concerned, the calculations provide probability surfaces depending on the n-n distance, noted here r^{th}_{nn}, and the core-dineutron distance noted r^{th}_{c-nn}, for both the ground state of ^{11}Li and ^{13}Li. These are shown in figure 9.33. For the case of ^{11}Li, one can see a global maximum of probability for a small r^{th}_{nn} and a larger r^{th}_{c-nn}, in the so-called dineutron configuration [92]. The surface for ^{13}Li shows two local maxima, one for the dineutron configuration, and one for a small r^{th}_{c-nn} and a larger r^{th}_{nn}, in the so-called cigar-like configuration. These distributions have been projected on the x-axis, to determine the mean and rms value for r^{th}_{nn}. This is shown in figure 9.34.

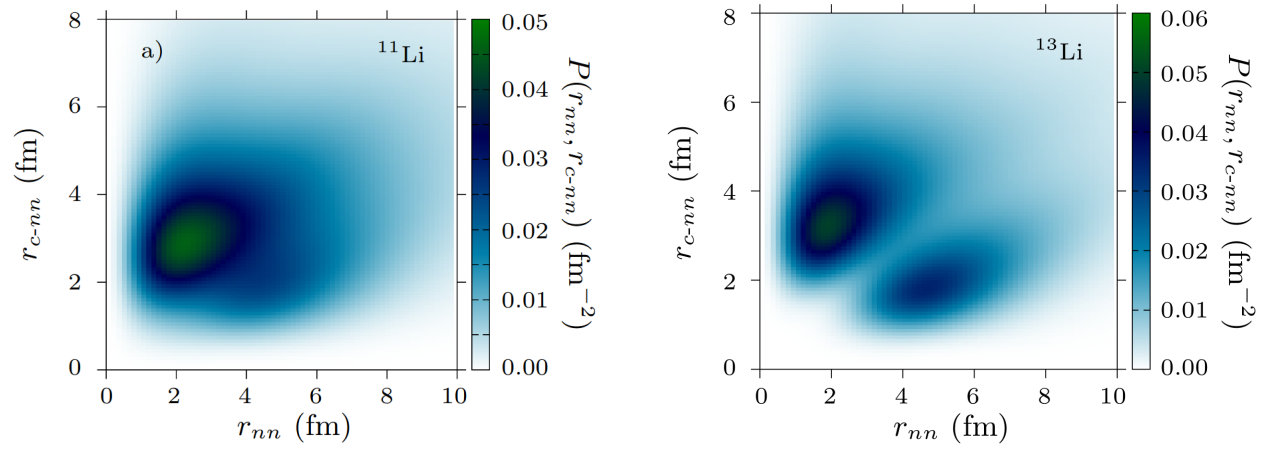

(a) (b)

Figure 9.33: (a) Probability distributions as a function of r^{th}_{nn}, simply r_{nn} noted on the x-axis, and r^{th}_{c-nn}, simply noted r_{c-nn} on the y-axis, for the ground state of ^{11}Li. (b) Probability distributions as a function of r^{th}_{nn}, simply r_{nn} noted on the x-axis, and r^{th}_{c-nn}, simply r_{c-nn} noted on the y-axis, for the ground state of ^{13}Li.

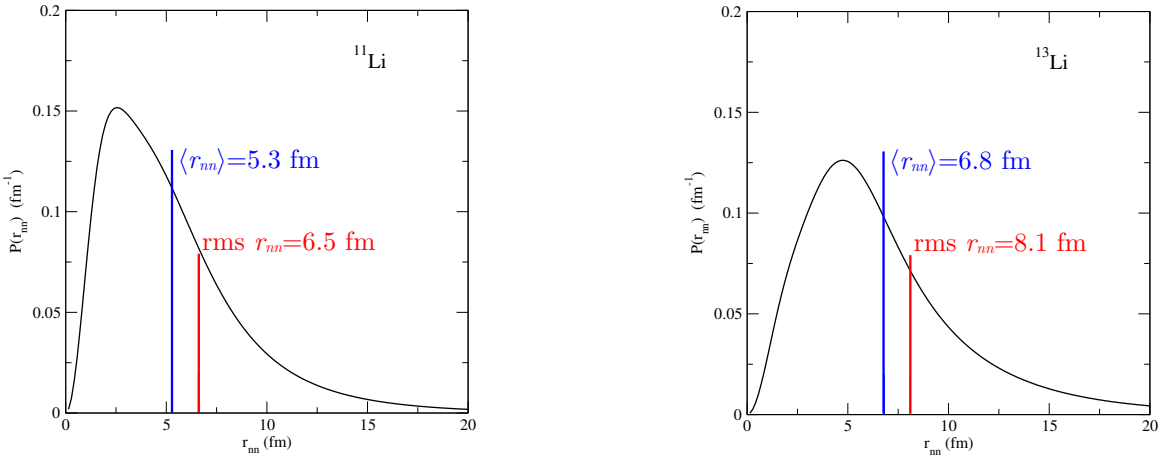

Figure 9.34: Probability distributions with respect to r_{nn}^{th}, calculated for the ground state of ^{11}Li and ^{13}Li. The mean value for r_{nn}^{th} is indicated in blue and noted $\langle r_{nn}\rangle$. The rms value is indicated in blue and noted rms r_{nn}. (a) Probability distributions as a function of r_{nn}^{th}, simply r_{nn} noted on the x-axis, for the ground state of ^{11}Li. (b) Probability distributions as a function of r_{nn}^{th}, simply r_{nn} noted on the x-axis, for the ground state of ^{13}Li.

It is important to note that the difference between the r_{nn} determined with the Lednicky-Lyuboshits formalism in the previous sections and the theoretical r_{nn}^{th} provided by the calculations of J. Casal does not only lie in the procedure for their determination, but also in their definition. Indeed, the n-n distance is in both cases a parameter that is highly dependent of the formalism used. This means that performing a quantitative comparison of these quantities between the two models is impossible. However, it is possible to compare their trends, and an increase from ^{11}Li to ^{13}Li is noticeable in both the values determined in sections 9.1 and 9.2, and the rms values shown in figure 9.34.

Chapter 10

Conclusion and perspectives

This study of the two-neutron decay of ^{11}Li and ^{13}Li provided several new results. Using the invariant mass method, two resonances observed previously in ^{13}Li have been confirmed. Its ground state and the resonance around 1.47 MeV have been observed in two different experiments performed at NSCL and GSI, respectively, and observed again in the present work, unifying these two previous measurements. Two new resonances have been observed as well. This study of the two-neutron decay kinematics of ^{13}Li reveals a mostly direct decay up to about $E_{rel,3B} = 2$ MeV, in agreement with results provided by Kohley *et al.* in [97]. However, the signature of a sequential decay mechanism has also been observed above $E_{rel,3B} = 2$ MeV, consistently with the study of Johansson *et al.* [117]. A value of the n-n distance has been determined by fitting the Jacobi coordinates: $r_{nn} = 12.7(27)$ fm. The study of ^{11}Li revealed a strong sequential character of its two-neutron decay, which is in contradiction with previous results obtained by Smith *et al.* [115]. This can be explained by the fact that the experiment analyzed in the present work benefits from a better resolution and acceptance at high relative energy. This way, intermediate states in ^{10}Li, populated in the two-neutron decay of ^{11}Li, are clearly resolved for the first time. It is rather challenging to constrain the contribution of the direct decay of the resonant states of ^{11}Li, and the contribution of the sequential decay through the resonant states of ^{10}Li. Nevertheless, it appears that the n-n correlations in ^{11}Li can be described with a r_{nn} distance of about 5 fm. One can note a slight discrepancy in the values of r_{nn} in different relative energy ranges is observed, and could be due to this parameter being at the limit of validity of the formalism used for the description of the correlations, as explained in section 9.2. It is visible that the extracted r_{nn} distances for ^{11}Li and ^{13}Li are rather different. One can compare those values to the one obtained for other nuclei in other studies following similar methods, as shown in figure 10.1.

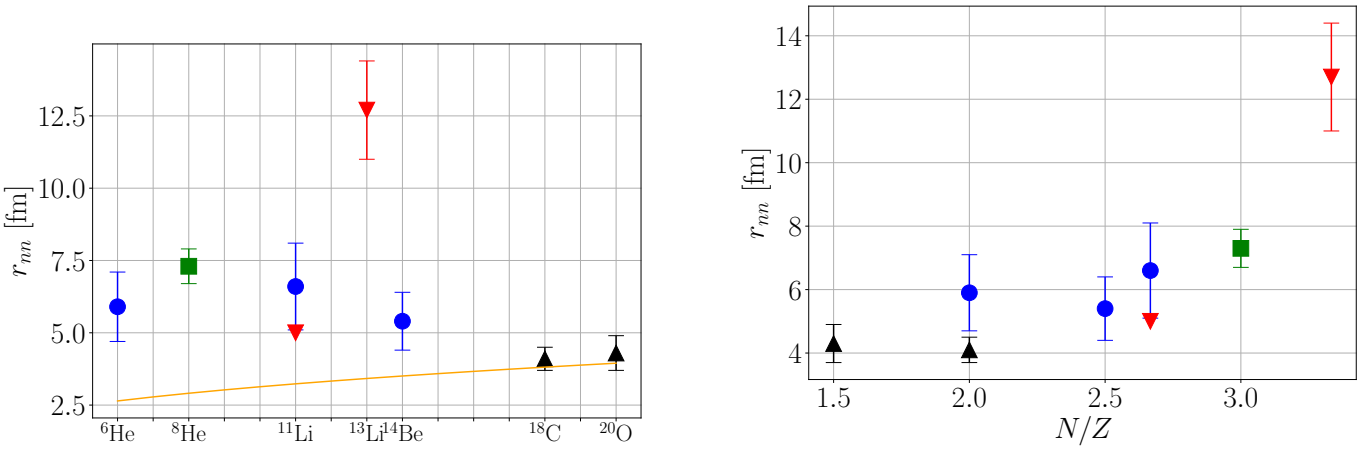

Figure 10.1: Comparison of the experimental values of r_{nn} as a function of the mass number A, and as a function of the proton-neutron assymetry N/Z. The markers are experimental values. ●: data from [114]. ▲: data from [135]. ■: data from [136]. ▼: data from the present study. The orange line is the computed values of r_{nn} for two independent neutrons within the liquid-drop model. (a) r_{nn} as a function of the mass number A. (b) r_{nn} as a function of the proton-neutron assymetry N/Z.

The results provided here regarding the r_{nn} distance for ^{11}Li is consistent with the one obtained previously, in an experiment where unbound states of ^{11}Li are populated by Coulomb breakup [114]. This value of 5 fm is also comparable with other halo nuclei, such as ^{6}He and ^{14}Be. Some n-n distances have also been extracted from the two-neutron decay of highly excited states in ^{18}C and ^{20}O [135]. For these two nuclei, the determined n-n distance is found to be compatible with the one expected between two independent neutrons computed with the liquid-drop model. The value for r_{nn} found for ^{13}Li does not seem to follow any of those trends. Although the sensitivity for r_{nn} in the present study could be overall improved, it is clear from figure 9.2 that the lower limit is rather well constrained. The present results call for theoretical calculations.

One can note that the first resonant state of ^{13}Li is rather narrow and lies very close to the four-neutron threshold ($S_{4n}(^{13}Li) \simeq -0.26MeV$). In the framework of the generalized Ikeda conjecture [138,139], in which clusters would appear at the corresponding thresholds, this state could have a four-neutron structure. Due to energy conservation, it decays via two-neutron decay, and not four-neutron decay. But, as a four-neutron cluster, it is expected to be more spatially extended than the other two-neutron resonances, which could explain a large value for r_{nn}.

We plan to extend the comparisons between the theoretical results of J. Casal and the experimental results presented in this work, presented in section 9.4. These calculations can also provide the energy and angle in the Jacobi coordinates. A comparison between the calculated and experimental distributions for these quantities would complete the discussion of the results. The calculations presented earlier have been performed for the ground state of the two isotopes of interest. The unbound states of ^{11}Li presented here are all excited states of this nucleus, and several excited states of ^{13}Li have also been proposed in this study. Comparing theoretical results for these states would also help in providing a more complete view of the two-neutron decay of ^{11}Li and ^{13}Li.

Theoretical calculations have been performed for the masses and structure of the Li isotopic chain, from ^{6}Li to ^{11}Li by X. Mao *et al.* in [140]. There, the Gamow Shell Model (GSM) is used with a ^{4}He core to build the Hamiltonian of the system. This model is based on the addition of a core-nucleon potential to a potential for the valence nucleons. The Hamiltonian is then diagonalized using the Density-Matrix Renormalization Group (DMRG) method [141, 142], which relies on the description of the Hamiltonian matrix in blocks and the use of the density matrix eigenstates. This method is especially suitable for systems of strongly correlated bodies with short-range interactions. Discussions are ongoing with K. Fossez to carry on these calculations for heavier Li isotopes, namely ^{12}Li and ^{13}Li. Discussions are also ongoing with E. Hiyama for the calculations of the excited states of ^{13}Li, represented as a ^{9}Li surrounded by four neutrons. This 5-body calculation would be performed using the Gaussian expansion method, which describes the wave function of the system as an expansion of Gaussian functions on the Jacobi coordinates of the system [143]. This method has been proven efficient for other neutron-rich unbound nuclei, such as ^{7}H [144]. The output of these calculations will provide an assignment for the angular momentum of the resonant states found in ^{13}Li.

Epilogue

In the present thesis, the results of two experiments have been reported. In part I, the relevance of the study of inelastic excitation reactions has been shown, and the determination of the inelastic excitation cross-sections for the first excited state for three $N = 52$ isotones, namely ^{98}Pd, ^{100}Cd and ^{102}Sn, has been reported. In part II, questions regarding n-n correlations in light neutron-rich nuclei have been exposed, and the quantification of these correlations in ^{11}Li and ^{13}Li has been shown. These two studies are relevant examples of modern, state-of-the-art, experimental studies on exotic nuclei.

One of the analysis presented here focused on systems close to the proton drip line, while the other one presented nuclei at the neutron drip line, and beyond. The great variety in terms of physical questions and issues, proper to each of these two specific regions of the nuclide chart, is especially striking when put next to each other. This also highlights the inherent challenge of nuclear physics, which is comprising under one vision extremely different phenomena and systems. Viewing the nuclide chart as the map of a partially known continent is a very relevant analogy. Indeed, the first nuclei that were studied were the stable ones, on which first grounds were established. The exploration of more and more unstable systems has been pushed carefully from that point on towards, and then beyond, the drip lines, by establishing bridges with the more familiar valley of stability. Following these considerations, the present work strengthens the idea that systematics available over a substantial number of systems are key to the understanding of nuclear structure. The data presented in this thesis propose, on the one hand, to look at structural variations when a pair of protons is added to the system, and on the other hand, to look at structural variations when a pair of neutrons is added to the system. Eventually, the results provided by the present work will hopefully pave the way to even deeper explorations of the nuclear landscape.

Appendices

Appendix A

Subtracting cross-sections

This sections presents the details for the comparison between the subtracted cross-section from C and CH_2, and the spectrum of inelastic excitation on H target. One can start by recalling equation (3.40),

$$\sigma^{2^+} = \frac{N_\gamma^{2^+} p_{2^+}}{N_m(BR, ZD) t_i}.$$

This equation is valid for all targets and, for a given transition, the cross-section on H target can be obtained in the following way,

$$\sigma_H^{2^+} = \frac{3\sigma_{CH_2} - \sigma_C}{2}. \tag{A.1}$$

As stated in section 3.2, this procedure is equivalent to directly subtracting the spectra on CH_2 and on C with the following expression,

$$E'_H = E_{CH_2} - R_s R_d E_C = E_{CH_2} - R E_C, \tag{A.2}$$

with E_i the energy on target i. R_s and R_s are normalization factors that account for the different statistics between the runs on CH_2 and on C, and for the different densities between both targets. They are defined as follows,

$$\begin{aligned} R_d &= \frac{t_{CH_2,C}}{t_C} = \frac{\frac{1}{3} t_{CH_2}}{t_C}, \\ R_s &= \frac{N_{m,CH_2}(BR, ZD)}{N_{m,C}(BR, ZD)}, \end{aligned} \tag{A.3}$$

$t_{CH_2,C}$ is the number of C atoms in the CH_2 target. One can define $t_{CH_2,H}$ analogously as the number of H atoms in the CH_2 target and that is equal to $\frac{2}{3} t_{CH_2}$. t_i and $N_m^i(BR, ZD)$ are the quantities defined in 3.2 for any target i. With this newly obtained spectra, one can compute the cross-section on H directly using equation (3.40):

$$\begin{aligned} (\sigma_H^{2^+})' &= \frac{N_\gamma^{2^+} p_H^{2^+}}{N_{m,CH_2}(BR, ZD) t_{CH_2,H}} \\ &= \frac{3 N_\gamma^{2^+} p_H^{2^+}}{2 N_{m,CH_2}(BR, ZD) t_{CH_2}}. \end{aligned} \tag{A.4}$$

Considering equation (A.2), one can write,

$$p_H^{2^+} = p_{CH_2}^{2^+} - R p_C^{2^+} . \tag{A.5}$$

This holds with the condition that $N_\gamma^{2^+}$ is the same for the simulation of inelastic excitation on CH_2, C and H. But $N_\gamma^{2^+}$ is an input parameter of the simulation, entirely set by the user, making this condition very easy to fulfill. Plugging equation (A.5) and the definition of R from equation (A.3) into equation (A.4), one can write:

$$\begin{aligned}
(\sigma_H^{2^+})' &= \frac{N_\gamma^{2^+}}{2} \left(\frac{3 p_{CH_2}^{2^+}}{N_{m,CH_2}(BR,ZD) t_{CH_2}} - \frac{3 R p_C^{2^+}}{N_{m,CH_2}(BR,ZD) t_{CH_2}} \right) \\
&= \frac{N_\gamma^{2^+}}{2} \left(\frac{3 p_{CH_2}^{2^+}}{N_{m,CH_2}(BR,ZD) t_{CH_2}} - \frac{3 \frac{\frac{1}{3} t_{CH_2}}{t_C} \frac{N_{m,CH_2}(BR,ZD)}{N_{m,C}(BR,ZD)} p_C^{2^+}}{N_{m,CH_2}(BR,ZD) t_{CH_2}} \right) \\
&= \frac{1}{2} \left(\frac{3 N_\gamma^{2^+} p_{CH_2}^{2^+}}{N_{m,CH_2}(BR,ZD) t_{CH_2}} - \frac{N_\gamma^{2^+} p_C^{2^+}}{N_{m,C}(BR,ZD) t_C} \right) \\
&= \frac{3\sigma_{CH_2} - \sigma_C}{2} \\
&= \sigma_H^{2^+} .
\end{aligned} \tag{A.6}$$

This demonstrates that subtracting the cross-sections on CH_2 and C target and subtracting the spectra on both targets are equivalent and that resulting cross-sections are the same.

Appendix B

Résumé en français

Les noyaux atomiques sont des systèmes multicorps de N neutrons et Z protons, formant ensemble A nucléons corrélés entre eux. La carte des noyaux compte presque de 300 nucléides stables, et plus de 3000 nucléides ont été découverts au total. Le défi de la physique nucléaire est en conséquence de trouver une description unifié, ainsi que des propriétés fondamentales, pour autant de systèmes différents. Depuis la découverte du noyau par E. Rutherford en 1911, de nombreuses méthodes et installations expérimentales de pointe ont vu le jour dans ce but. La présente étude propose la description, l'analyse et l'interprétation de deux expériences portant sur l'excitation inélastique de trois isotones $N = 52$, à savoir ^{98}Pd, ^{100}Cd et ^{102}Sn, et sur la décroissance deux-neutrons du ^{11}Li et du ^{13}Li. Ces deux expériences ont été réalisées à la Radioactive Isotope Beam Factory (RIBF) du RIKEN Nishina Center, Wakō, Japon.

B.1 Excitation inélastique de ^{102}Sn, ^{100}Cd et ^{98}Pd

B.1.1 Objectif de l'expérience

L'étain (Sn, $Z = 50$) bénéficie d'un grand intérêt pour les travaux de structure nucléaire. En effet, la chaîne isotopique des Sn est la plus longue entre deux noyaux doublement magiques, ^{100}Sn et ^{132}Sn, de toute la carte des noyaux, offrant donc la possibilité d'établir des études systématiques sur une large gamme de systèmes. Des données spectroscopiques sur ^{132}Sn existent et confirment la fermeture de couche pour cet isotope. Cependant, aucune donnée de ce type n'est disponible pour ^{100}Sn, et l'information est très incomplète pour ^{102}Sn. La probabilité de transition $B(E2)$ pour ^{104}Sn a été mesurée pour la première fois en 2013 par G. Guastalla *et al.* confirmant également la fermeture de couche attendue pour les isotopes riches en neutron de Sn [44]. Cependant, d'autres mesures ultérieures pour ce même isotope, avec une statistique plus élevée, réalisée par V.M. Bader *et al.* en 2013 [45] et P. Doornenbal *et al.* en 2014 [46] contredisent cette conclusion et fournissent des indices d'une fermeture de couche plus douce que prévue pour ces noyaux.

L'objectif de cette expérience est de mesurer la section efficace d'excitation inélastique du premier état excité 2^+ pour trois isotones avec $N = 52$, à savoir ^{98}Pd, ^{100}Cd et ^{102}Sn. Cette section efficace permet le calcul des éléments matriciels de transition pour les protons et les neutrons. Ces quantités, mesurées et déduites pour ^{102}Sn pour la première fois, permettront d'apporter des informations supplémentaires sur la fermeture de couche

à l'approche de ^{100}Sn, en prolongeant la systématique déjà existante en fonction de N. Ces sections efficaces permettront de plus d'établir une systématique en fonction de Z à l'approche de ^{100}Sn.

B.1.2 Dispositif expérimental : RIBF, DALI2 et le spectromètre ZeroDegree

L'expérience a été réalisée en 2019 à RIBF. Un faisceau primaire de ^{124}Xe a été fragmenté sur une cible de ^{9}Be. Le faisceau cocktail contenant les isotones d'intérêt ainsi produit réagit ensuite sur une cible de plastique (CH_2) ou de carbone (C). Les états excités des isotones cités précédemment sont peuplés au passage de la cible secondaire, et décroissent en émettant des rayons γ. Ces rayonnements sont détectés dans le spectromètre DALI2 [62]. Ce détecteur est composé de 226 scintillateurs NaI.

Les noyaux contenus dans le faisceau secondaire vont à une vitesse relativiste, approximativement 60% de la vitesse de la lumière. En décroissant, ils constituent des sources de rayonnement en mouvement. L'énergie mesurée est donc modifiée par l'effet Doppler et une correction doit être appliquée. Un rayon γ, dont l'énergie est de l'ordre de 1 Mev comme c'est le cas ici, interagissant avec un scintillateur peut potentiellement être soumis à la diffusion Compton. En conséquence, l'énergie du rayon γ n'est pas entièrement déposée dans le premier scintillateur touché. Le photon diffusé peut être absorbé dans ce même scintillateur ou quitté le cristal et déposé le reste de son énergie dans un scintillateur voisin. Une procédure appelé "addback" est appliquée pour identifier les groupes de cristaux voisins et additionner les signaux détectés dans ces scintillateurs pour un même événement.

B.1.3 Analyse des spectres d'énergie γ pour ^{98}Pd, ^{100}Cd et ^{102}Sn

Une fois les spectres γ corrigés, les sections efficaces sont déduites du nombre de rayons γ mesuré pour chaque transition. Pour compter ces photons, les fonctions de réponse du détecteur DALI2 sont simulées pour chaque transition γ, à l'aide d'un programme basé sur l'outil GEANT4 [66] appelé SHOGUN, développé par P. Doornenbal. Ces fonctions de réponse sont ensuite fittées sur les spectres γ reconstruits.

Pour ne pas surestimer la contribution de chaque transition γ, d'autres contributions sont ajoutées pour reproduire le fond du spectre. Une double exponentielle reproduit à la fois le rayonnement de basse énergie dû au bremsstrahlung, et à la fois le rayonnement de haute énergie dû aux états excités de haute énergie. Les noyaux de ^{12}C présents dans les deux cibles peuvent être excités au passage du faisceau. La cible peut donc être assimilée à une source de rayonnement à l'arrêt, et la correction Doppler appliquée à tous les événements étale le pic photoélectrique qui en résulte, contribuant au fond du spectre. Cette contribution est simulée et ajoutée au fit du spectre. Enfin, ^{100}Cd et ^{102}Sn possèdent chacun un état isomère. Ces états peuvent être peuplés à la cible primaire, lors de la production de ces isotones. La demi-vie relativement longue de ces états implique que leur décroissance se produit tout au long de la ligne faisceau selon une loi exponentielle. Aux abords du détecteur DALI2, des isomères décroissent, et le photon émis dépose de l'énergie dans les scintillateurs. Cependant, comme il est impossible de déduire le vertex d'émission pour de tels événements, la correction Doppler qui leur est appliquée est mauvaise, et contribue au fond du spectre. Après l'expérience, des implantations de

^{100}Cd et ^{102}Sn dans une cible épaisse de plastique ont été réalisées afin d'évaluer le rapport isomérique à la cible secondaire des ces deux isotones. Ces décroissances isomériques ont donc été simulées et leur amplitude contraintes par le résultat des implantations.

B.1.4 Résultats et perspectives

Les fits décrits précédemment donnent les intensités de chaque transitions pour chaque cible notées Γ_{CH_2} et Γ_C. Γ_C est retranchée de Γ_{CH_2} pour obtenir l'intensité sur cible hydrogène (H, ou proton) notée Γ_H. Les intensités des transitions qui peuplent l'état 2^+ sont retranchées de l'intensité de la transition $2^+ \rightarrow 0^+$ et donnent la section efficace expérimentale 2^+, notée σ^{2^+}. Les résultats pour les trois isotones sont données dans le tableau suivant :

	^{98}Pd	^{100}Cd	^{102}Sn
$\sigma_H^{2^+}$ (mbarn)	9.0(27)	7.7(17)	1.8(4)

Table B.1: Sections efficaces expérimentales $\sigma_H^{2^+}$ pour les trois isotones d'intérêt.

La tendance pour ces valeurs numériques est comme attendue, avec une diminution de la section efficace à l'approche de la fermeture de couche. Cependant, ces valeurs déterminées seulement à partir des données expérimentales ne tiennent pas compte de la population indirecte du premier état excité 2^+ par le continuum d'états à haute énergie, et constituent donc une limite supérieure pour la section efficace recherchée. Cette contribution est évaluée à l'aide d'un programme de calcul de réactions nommé TALYS, développé par A. Koning, S. Hilaire et S. Goriely [83]. Une première étape est de vérifier la stabilité des résultats données par TALYS pour une variété de modèles de réaction. Une fois cette vérification effectuée, la contribution du continuum sera estimée et retranchée des sections efficaces présentées dans le tableau B.1, fournissant une valeur centrale corrigée pour les sections efficaces.

La même expérience a également été réalisée sur cible d'or (Au) pour peupler les états excités par excitation coulombienne. Cette mesure, dont l'analyse et la discussion dépasse le champ de la présente étude, permettra la détermination de la probabilité de transition $B(E2)$ pour ^{102}Sn, et donc le calcul de l'élément matriciel de transition proton pour ce noyau. Associés aux valeurs fournies ci-dessus, des calculs permettront la détermination de l'élément matriciel de transition neutron, et permettront ainsi de conclure quant à la fermeture de couche à l'approche de ^{100}Sn.

B.2 Décroissance deux-neutrons de ^{11}Li et ^{13}Li

B.2.1 Objectif de l'expérience

Les noyaux légers riche en neutrons exhibent souvent des structures spécifiques comme les noyaux à halo ou les noyaux borroméens. Ces effets apparaissent même pour des systèmes avec un nombre réduit de nucléons, comme ^{6}He ou ^{11}Li. La problématique de l'émergence de ces structures est intimement liée à la limite d'existence des noyaux dans cette région. En effet, un calcul simple de l'énergie de liaison par la formule de Weizsäcker donne le ^{11}Li non-lié, alors que toutes les mesures confirment une structure borroméenne liée pour ce

noyau. Une explication possible pour l'existence de ces structures réside dans l'importance des corrélations neutron-neutron (n-n) pour ces noyaux. Il existe plusieurs manières de caractériser ces corrélations. L'une d'elle est la mesure de l'angle d'ouverture entre les deux neutrons émis par ^{11}Li, pour reprendre l'exemple de ce noyau, liée à la mesure de la probabilité de transition $B(E1)$. Un angle plus faible que 90° implique que les deux neutrons sont émis proches l'un de l'autre et indique la présence de corrélations. Une autre méthode, choisie dans le cadre de cette étude, est de considérer la distance neutron-neutron (n-n), notée r_{nn}, une quantité analogue à l'angle d'ouverture, déterminer via l'étude de la décroissance par émission de deux neutrons. De la même manière, une petite valeur pour r_{nn} indique la présence de corrélations. L'objectif de l'expérience présentée ici est de peupler les états excités du ^{11}Li et du ^{13}Li. Ces états excités sont non-liés dans le cas de ^{11}Li et ^{13}Li est également non-lié dans son état fondamental. Ces deux noyaux vont donc décroître via l'émission de deux neutrons (^{10}Li et ^{12}Li étant également non-liés). La mesure de l'énergie et des moments de chaque corps, le fragment de ^{9}Li ou ^{11}Li restant et les deux neutrons, permet la reconstruction de l'énergie relative du système ainsi que la reconstruction des coordonnées de Jacobi, et finalement la détermination de r_{nn} pour ces deux isotopes. Ces données permettront également de déterminer si l'émission des deux neutrons est directe (émission simultanée des deux neutrons) ou séquentielle (émission d'un neutron après l'autre).

B.2.2 Dispositif expérimental : SAMURAI, MINOS et NEBULA

Comme évoqué dans le paragraphe précédent, il est nécessaire pour reconstruire l'énergie relative et les coordonnées de Jacobi de détecter tous les produits de la désintégration, et c'est dans ce but que l'installation expérimentale décrite ci-dessous a été mise en place. Les réactions utilisées pour peupler les états de ^{11}Li et ^{13}Li sont respectivement ^{12}Be(p,2p)^{11}Li$\rightarrow$ ^{9}Li+2n et ^{14}Be(p,2p)^{13}Li$\rightarrow$ ^{11}Li+2n. Un faisceau primaire de ^{48}Ca a été accéléré et fragmenté sur une cible de ^{9}Be pour produire les faisceaux secondaires de ^{12}Be et ^{14}Be. Ces noyaux ont ensuite réagi sur le dispositif MINOS [123], composé d'une cellule épaisse d'hydrogène liquide couplé à une chambre à projection temporelle (TPC), permettant la reconstruction des trajectoires du proton de recul et du proton éjecté du noyau de Be incident. Ce dispositif permet donc d'avoir une bonne luminosité et une bonne résolution en énergie. Une fois les isotopes du Li d'intérêt produits et après leur décroissance, les neutrons et fragments traversent l'aimant SAMURAI [119, 120], qui dévie les fragments chargés, détecté ensuite dans des hodoscopes. La grande acceptance de l'aimant permet d'obtenir une statistique suffisante dans les spectres d'énergie relative. Les neutrons, non-chargés, traversent quant à eux l'aimant en ligne droite, et sont détectés dans le détecteur NEBULA [120], un ensemble de 120 scintillateurs en plastique. Certains événements présentant deux signaux dans le détecteur NEBULA peuvent en fait être dus à un seul neutron, qui déposent une partie de son énergie dans un scintillateur, puis le reste dans un autre scintillateur. Ces événements sont appelés "cross-talk", et une procédure de rejet de ces événements est appliquée aux données expérimentales.

B.2.3 Analyse des spectres de masse invariante, et des coordonnées de Jacobi de ^{11,13}Li

Les spectres d'énergie relative à trois corps (fragment+neutron+neutron) sont reconstruits et fittés à l'aide de fonctions de réponse simulées par le programme SMSIMULATOR,

basé sur l'outil GEANT4, développé par R. Tanaka et Y. Kondo [128]. La population des états résonants de ^{11}Li et ^{13}Li est simulée et leur décroissance est simulée selon deux modes possibles mentionnés précédemment : la décroissance directe ou séquentielle. Les corrélations n-n sont caractérisées selon le formalisme de R. Lednicky et V.L. Lyuboshits [113], et l'implémentation proposée par F.M. Marqués [114]. Une fois l'amplitude de chaque fonction de réponse déterminée, les coordonnées de Jacobi sont fittées avec la distance n-n r_{nn} laissée libre, et le mode de décroissance également laissé libre. Ces fits permettent de quantifier la contribution de décroissance directe ou séquentielle pour chaque état résonant. La décroissance séquentielle implique que des états résonants dans les systèmes intermédiaires ^{10}Li et ^{12}Li sont peuplés. En conséquence, les spectres d'énergie relatives à deux corps (fragment+neutron) sont également fittés, de manière cohérente avec les fits des coordonnées de Jacobi, permettant ainsi de contraindre la largeur et l'énergie de résonance des états de ^{10}Li et ^{12}Li.

B.2.4 Résultats et perspectives

Des indices de décroissance séquentielle de ^{13}Li à haute énergie relative ont été observées pour la permière fois. La valeur de 12.7 fm a été déterminée pour la distance n-n de ce noyau, correspondant à des corrélations modérées. Pour le ^{11}Li, la décroissance apparaît presque exclusivement séquentielle, allant à l'encontre des conclusions d'une précédente étude réalisée par J.K. Smith *et al.* [115]. Même si de légères incohérences subsistent dans les valeurs déterminées pour r_{nn} en fonction de l'énergie relative, de fortes corrélations n-n ont été mesurées pour ce noyau.

Des calculs théoriques vont être réalisés pour la masse et la structure de ^{11}Li et ^{13}Li. Les résultats fournis par ce calcul seront comparés aux résultats expérimentaux et permettront une meilleure contrainte du moment angulaire pour les états résonants. Ils pourront également servir être utilisés pour des calculs de réactions qui permettront un calcul théorique des spectres d'énergie relative et des coordonnées de Jacobi, dans le cas d'une décroissance directe ou séquentielle. Ces résultats théoriques pourront être à leur tour comparés aux spectres expérimentaux, et à la caractérisation des corrélations n-n déterminées à partir des données expérimentales.

Bibliography

[1] P. J. Karol, R. C. Barber, B. M. Sherrill, E. Vardaci, and T. Yamazaki, "Discovery of the element with atomic number Z = 118 completing the 7th row of the periodic table (IUPAC Technical Report)," *Pure and Applied Chemistry*, vol. 88, no. 1-2, pp. 155–160, 2016.

[2] M. Thoennessen, "2018 update of the discoveries of nuclides," *International Journal of Modern Physics E*, vol. 28, no. 01n02, p. 1930002, 2019.

[3] "NuDat3.0." https://www.nndc.bnl.gov/nudat3/. Accessed: 2022-06-17.

[4] N. Ishii, S. Aoki, and T. Hatsuda, "Nuclear force from lattice QCD," *Physical review letters*, vol. 99, no. 2, p. 022001, 2007.

[5] T. Hatsuda, "Lattice quantum chromodynamics and baryon-baryon interactions," *Frontiers of Physics*, vol. 13, no. 6, pp. 1–10, 2018.

[6] O. Sorlin and M.-G. Porquet, "Nuclear magic numbers: New features far from stability," *Progress in Particle and Nuclear Physics*, vol. 61, no. 2, pp. 602–673, 2008.

[7] R. Machleidt and D. R. Entem, "Chiral effective field theory and nuclear forces," *Physics Reports*, vol. 503, no. 1, pp. 1–75, 2011.

[8] P. Navrátil, J. Vary, and B. Barrett, "Large-basis ab initio no-core shell model and its application to ^{12}C," *Physical Review C*, vol. 62, no. 5, p. 054311, 2000.

[9] D. Dean and M. Hjorth-Jensen, "Coupled-cluster approach to nuclear physics," *Physical Review C*, vol. 69, no. 5, p. 054320, 2004.

[10] K. Tsukiyama, S. Bogner, and A. Schwenk, "In-medium similarity renormalization group for nuclei," *Physical Review Letters*, vol. 106, no. 22, p. 222502, 2011.

[11] H. Hergert, "A guided tour of ab initio nuclear many-body theory," *Frontiers in Physics*, vol. 8, p. 379, 2020.

[12] R. D. Woods and D. S. Saxon, "Diffuse surface optical model for nucleon-nuclei scattering," *Physical Review*, vol. 95, no. 2, p. 577, 1954.

[13] T. Skyrme, "The effective nuclear potential," *Nuclear Physics*, vol. 9, no. 4, pp. 615–634, 1958.

[14] A. B. Migdal *et al.*, "Theory of finite fermi systems and applications to atomic nuclei," 1967.

[15] D. Gogny, "Simple separable expansions for calculating matrix elements of two-body local interactions with harmonic oscillator functions," *Nuclear Physics A*, vol. 237, no. 3, pp. 399–418, 1975.

[16] D. Gogny and P.-L. Lions, "Hartree-fock theory in nuclear physics," *ESAIM: Mathematical Modelling and Numerical Analysis*, vol. 20, no. 4, pp. 571–637, 1986.

[17] G. Colò, "Nuclear density functional theory," *Advances in Physics: X*, vol. 5, no. 1, p. 1740061, 2020.

[18] F. Marino, C. Barbieri, A. Carbone, G. Colò, A. Lovato, F. Pederiva, X. Roca-Maza, and E. Vigezzi, "Nuclear energy density functionals grounded in ab initio calculations," *Physical Review C*, vol. 104, no. 2, p. 024315, 2021.

[19] T. Whitehead, Y. Lim, and J. Holt, "Proton elastic scattering on calcium isotopes from chiral nuclear optical potentials," *Physical Review C*, vol. 100, no. 1, p. 014601, 2019.

[20] T. Whitehead, Y. Lim, and J. Holt, "Neutron elastic scattering on calcium isotopes from chiral nuclear optical potentials," *Physical Review C*, vol. 101, no. 6, p. 064613, 2020.

[21] S. Michimasa, N. Imai, M. Dozono, J. Hwang, K. Yamada, S. Ota, K. Yoshida, Y. Yanagisawa, K. Kusaka, M. Ohtake, *et al.*, "New energy-degrading beamline for in-flight RI beams, OEDO," *Nuclear Instruments and Methods in Physics Research Section B: Beam Interactions with Materials and Atoms*, vol. 463, pp. 143–147, 2020.

[22] S. Gösta Nilsson, "Binding states of individual nucleons in strongly deformed nuclei," *Matematisk-fysiske Meddelelser*, vol. 29, no. 16, 1955.

[23] I. Ragnarsson and S. Gösta Nilsson, *Shapes and shells in nuclear structure*. Cambridge University Press, 2005.

[24] O. Haxel, J. H. D. Jensen, and H. E. Suess, "On the" magic numbers" in nuclear structure," *Physical Review*, vol. 75, no. 11, p. 1766, 1949.

[25] M. G. Mayer, "On closed shells in nuclei," *Physical Review*, vol. 74, no. 3, p. 235, 1948.

[26] N. Alamanos and A. Gillibert, "Selected topics in reaction studies with exotic nuclei," in *The Euroschool Lectures on Physics with Exotic Beams, Vol. I*, pp. 295–337, Springer, 2004.

[27] T. Otsuka, A. Gade, O. Sorlin, T. Suzuki, and Y. Utsuno, "Evolution of shell structure in exotic nuclei," *Reviews of Modern Physics*, vol. 92, no. 1, p. 015002, 2020.

[28] D. Sohler, Z. Dombradi, J. Timár, O. Sorlin, F. Azaiez, F. Amorini, M. Belleguic, C. Bourgeois, C. Donzaud, J. Duprat, *et al.*, "Shape evolution in heavy sulfur isotopes and erosion of the N=28 shell closure," *Physical Review C*, vol. 66, no. 5, p. 054302, 2002.

[29] R. Kanungo, C. Nociforo, A. Prochazka, T. Aumann, D. Boutin, D. Cortina-Gil, B. Davids, M. Diakaki, F. Farinon, H. Geissel, *et al.*, "One-Neutron Removal Mea-

surement Reveals ^{24}O as a New Doubly Magic Nucleus," *Physical review letters*, vol. 102, no. 15, p. 152501, 2009.

[30] C. Hoffman, T. Baumann, D. Bazin, J. Brown, G. Christian, D. Denby, P. DeYoung, J. Finck, N. Frank, J. Hinnefeld, *et al.*, "Evidence for a doubly magic ^{24}O," *Physics Letters B*, vol. 672, no. 1, pp. 17–21, 2009.

[31] K. Tshoo, Y. Satou, H. Bhang, S. Choi, T. Nakamura, Y. Kondo, S. Deguchi, Y. Kawada, N. Kobayashi, Y. Nakayama, *et al.*, "N=16 Spherical Shell Closure in ^{24}O," *Physical Review Letters*, vol. 109, no. 2, p. 022501, 2012.

[32] O. Tarasov, R. Allatt, J. Angélique, R. Anne, C. Borcea, Z. Dlouhy, C. Donzaud, S. Grévy, D. Guillemaud-Mueller, M. Lewitowicz, *et al.*, "Search for ^{28}O and study of neutron-rich nuclei near the N= 20 shell closure," *Physics Letters B*, vol. 409, no. 1-4, pp. 64–70, 1997.

[33] H. Crawford, R. Janssens, P. Mantica, J. Berryman, R. Broda, M. Carpenter, N. Cieplicka, B. Fornal, G. Grinyer, N. Hoteling, *et al.*, "β decay and isomeric properties of neutron-rich Ca and Sc isotopes," *Physical Review C*, vol. 82, no. 1, p. 014311, 2010.

[34] D. Steppenbeck, S. Takeuchi, N. Aoi, P. Doornenbal, M. Matsushita, H. Wang, H. Baba, N. Fukuda, S. Go, M. Honma, *et al.*, "Evidence for a new nuclear 'magic number' from the level structure of ^{54}Ca," *Nature*, vol. 502, no. 7470, pp. 207–210, 2013.

[35] O. Sorlin, S. Leenhardt, C. Donzaud, J. Duprat, F. Azaiez, F. Nowacki, H. Grawe, Z. Dombrádi, F. Amorini, A. Astier, *et al.*, "$^{68}_{28}$Ni$_{40}$: Magicity versus Superfluidity," *Physical Review Letters*, vol. 88, no. 9, p. 092501, 2002.

[36] R. Taniuchi, C. Santamaria, P. Doornenbal, A. Obertelli, K. Yoneda, G. Authelet, H. Baba, D. Calvet, F. Château, A. Corsi, *et al.*, "^{78}Ni revealed as a doubly magic stronghold against nuclear deformation," *Nature*, vol. 569, no. 7754, pp. 53–58, 2019.

[37] T. Otsuka, T. Suzuki, R. Fujimoto, H. Grawe, and Y. Akaishi, "Evolution of nuclear shells due to the tensor force," *Physical Review Letters*, vol. 95, no. 23, p. 232502, 2005.

[38] T. Otsuka, T. Suzuki, J. D. Holt, A. Schwenk, and Y. Akaishi, "Three-body forces and the limit of oxygen isotopes," *Physical Review Letters*, vol. 105, no. 3, p. 032501, 2010.

[39] P. Ring and P. Schuck, *The nuclear many-body problem*. Springer Science & Business Media, 2004.

[40] A. Bernstein, V. Brown, and V. Madsen, "Neutron and proton transition matrix elements and inelastic hadron scattering," *Physics Letters B*, vol. 103, no. 4-5, pp. 255–258, 1981.

[41] A. Bernstein, V. Brown, and V. Madsen, "Comments Nucl," *Part. Phys*, vol. 11, p. 203, 1983.

[42] K. Alder and A. Winther, "On the exact Evaluation of the Coulomb Excitation," *Dan. mat. fys. Medd.*, vol. 29, no. CERN-55-27, pp. 1–20, 1955.

[43] T. Björnstad, M. Borge, J. Blomqvist, R. Von Dincklage, G. Ewan, P. Hoff, B. Jonson, K. Kawade, A. Kerek, O. Klepper, *et al.*, "The doubly closed shell nucleus $^{132}_{50}Sn_{82}$," *Nuclear Physics A*, vol. 453, no. 3, pp. 463–485, 1986.

[44] G. Guastalla, D. DiJulio, M. Górska, J. Cederkäll, P. Boutachkov, P. Golubev, S. Pietri, H. Grawe, F. Nowacki, K. Sieja, *et al.*, "Coulomb Excitation of ^{104}Sn and the Strength of the ^{100}Sn Shell Closure," *Physical Review Letters*, vol. 110, no. 17, p. 172501, 2013.

[45] V. Bader, A. Gade, D. Weisshaar, B. Brown, T. Baugher, D. Bazin, J. Berryman, A. Ekström, M. Hjorth-Jensen, S. Stroberg, *et al.*, "Quadrupole collectivity in neutron-deficient Sn nuclei: ^{104}Sn and the role of proton excitations," *Physical Review C*, vol. 88, no. 5, p. 051301, 2013.

[46] P. Doornenbal, S. Takeuchi, N. Aoi, M. Matsushita, A. Obertelli, D. Steppenbeck, H. Wang, L. Audirac, H. Baba, P. Bednarczyk, *et al.*, "Intermediate-energy Coulomb excitation of ^{104}Sn: Moderate E2 strength decrease approaching ^{100}Sn," *Physical Review C*, vol. 90, no. 6, p. 061302, 2014.

[47] A. Corsi, S. Boissinot, A. Obertelli, P. Doornenbal, M. Dupuis, F. Lechaftois, M. Matsushita, S. Péru, S. Takeuchi, H. Wang, *et al.*, "Neutron-driven collectivity in light tin isotopes: Proton inelastic scattering from ^{104}Sn," *Physics Letters B*, vol. 743, pp. 451–455, 2015.

[48] R. Schneider, T. Faestermann, J. Friese, R. Gernhäuser, H. Geissel, H. Gilg, F. Heine, J. Homolka, P. Kienle, H.-J. Körner, *et al.*, "Production, identification, and halflife measurement of ^{100}Sn," *Nuclear Physics A*, vol. 588, no. 1, pp. c191–c196, 1995.

[49] M. Lipoglavšek, M. Górska, J. Nyberg, A. Atac, A. Axelsson, R. Bark, J. Blomqvist, J. Cederkäll, B. Cederwall, G. De Angelis, *et al.*, "In-beam study of ^{102}Sn," *Zeitschrift für Physik A Hadrons and Nuclei*, vol. 356, no. 1, pp. 239–240, 1996.

[50] M. Lipoglavšek, D. Seweryniak, C. Davids, C. Fahlander, M. Górska, R. Janssens, J. Nyberg, J. Uusitalo, W. Walters, I. Ahmad, *et al.*, "E2 polarization charge in ^{102}Sn," *Physics Letters B*, vol. 440, no. 3-4, pp. 246–250, 1998.

[51] A. Corsi, A. Obertelli, P. Doornenbal, F. Nowacki, H. Sagawa, Y. Tanimura, N. Aoi, H. Baba, P. Bednarczyk, S. Boissinot, *et al.*, "Spectroscopy of nuclei around ^{100}Sn populated via two-neutron knockout reactions," *Physical Review C*, vol. 97, no. 4, p. 044321, 2018.

[52] H. Grawe, K. Straub, T. Faestermann, M. Górska, C. Hinke, R. Krücken, F. Nowacki, M. Böhmer, P. Boutachkov, H. Geissel, *et al.*, "The 6^+ isomer in ^{102}Sn revisited: Neutron and proton effective charges close to the double shell closure," *Physics Letters B*, vol. 820, p. 136591, 2021.

[53] K. Sümmerer, R. Schneider, T. Faestermann, J. Friese, H. Geissel, R. Gernhäuser, H. Gilg, F. Heine, J. Homolka, P. Kienle, *et al.*, "Identification and decay spectroscopy of ^{100}Sn at the GSI projectile fragment separator FRS," *Nuclear Physics A*, vol. 616, no. 1-2, pp. 341–345, 1997.

[54] C. Hinke, M. Böhmer, P. Boutachkov, T. Faestermann, H. Geissel, J. Gerl, R. Gernhäuser, M. Górska, A. Gottardo, H. Grawe, *et al.*, "Superallowed Gamow–Teller

decay of the doubly magic nucleus ^{100}Sn," *Nature*, vol. 486, no. 7403, pp. 341–345, 2012.

[55] T. Togashi, Y. Tsunoda, T. Otsuka, N. Shimizu, and M. Honma, "Novel shape evolution in Sn isotopes from magic numbers 50 to 82," *Physical Review Letters*, vol. 121, no. 6, p. 062501, 2018.

[56] T. D. Morris, J. Simonis, S. Stroberg, C. Stumpf, G. Hagen, J. Holt, G. R. Jansen, T. Papenbrock, R. Roth, and A. Schwenk, "Structure of the Lightest Tin Isotopes," *Physical Review Letters*, vol. 120, no. 15, p. 152503, 2018.

[57] "Plan of the BigRIPS-ZeroDegree beam-line." https://www.nishina.riken.jp/ribf/SAMURAI/overview.html. Accessed: 2022-07-10.

[58] "Schematic view of the BigRIPS separator." https://www.nishina.riken.jp/ribf/BigRIPS/config.html. Accessed: 2022-07-10.

[59] G. F. Knoll, *Radiation detection and measurement*. John Wiley & Sons, 2010.

[60] H. Kumagai, T. Ohnishi, N. Fukuda, H. Takeda, D. Kameda, N. Inabe, K. Yoshida, and T. Kubo, "Development of parallel plate avalanche counter (PPAC) for BigRIPS fragment separator," *Nuclear Instruments and Methods in Physics Research Section B: Beam Interactions with Materials and Atoms*, vol. 317, pp. 717–727, 2013.

[61] K. Kimura, T. Izumikawa, R. Koyama, T. Ohnishi, T. Ohtsubo, A. Ozawa, W. Shinozaki, T. Suzuki, M. Takahashi, I. Tanihata, *et al.*, "High-rate particle identification of high-energy heavy ions using a tilted electrode gas ionization chamber," *Nuclear Instruments and Methods in Physics Research Section A: Accelerators, Spectrometers, Detectors and Associated Equipment*, vol. 538, no. 1-3, pp. 608–614, 2005.

[62] S. Takeuchi, T. Motobayashi, Y. Togano, M. Matsushita, N. Aoi, K. Demichi, H. Hasegawa, and H. Murakami, "DALI2: A NaI (Tl) detector array for measurements of γ rays from fast nuclei," *Nuclear Instruments and Methods in Physics Research Section A: Accelerators, Spectrometers, Detectors and Associated Equipment*, vol. 763, pp. 596–603, 2014.

[63] N. Fukuda, T. Kubo, T. Ohnishi, N. Inabe, H. Takeda, D. Kameda, and H. Suzuki, "Identification and separation of radioactive isotope beams by the BigRIPS separator at the RIKEN RI Beam Factory," *Nuclear Instruments and Methods in Physics Research Section B: Beam Interactions with Materials and Atoms*, vol. 317, pp. 323–332, 2013.

[64] O. Tarasov and D. Bazin, "LISE++: Exotic beam production with fragment separators and their design," *Nuclear Instruments and Methods in Physics Research Section B: Beam Interactions with Materials and Atoms*, vol. 376, pp. 185–187, 2016.

[65] K. S. Krane, D. Halliday, *et al.*, *Introductory nuclear physics*, vol. 465. Wiley New York, 1988.

[66] S. Agostinelli, J. Allison, K. a. Amako, J. Apostolakis, H. Araujo, P. Arce, M. Asai, D. Axen, S. Banerjee, G. . Barrand, *et al.*, "GEANT4—a simulation toolkit," *Nuclear instruments and methods in physics research section A: Accelerators, Spectrometers, Detectors and Associated Equipment*, vol. 506, no. 3, pp. 250–303, 2003.

[67] M. Cortés, P. Doornenbal, M. Dupuis, S. Lenzi, F. Nowacki, A. Obertelli, S. Péru, N. Pietralla, V. Werner, K. Wimmer, *et al.*, "Inelastic scattering of neutron-rich Ni and Zn isotopes off a proton target," *Physical Review C*, vol. 97, no. 4, p. 044315, 2018.

[68] F. James and M. Roos, "Minuit-a system for function minimization and analysis of the parameter errors and correlations," *Computer Physics Communications*, vol. 10, no. 6, pp. 343–367, 1975.

[69] J. Taylor, *Introduction to error analysis, the study of uncertainties in physical measurements*. 1997.

[70] S. M. Seltzer and M. J. Berger, "Bremsstrahlung spectra from electron interactions with screened atomic nuclei and orbital electrons," *Nuclear Instruments and Methods in Physics Research Section B: Beam Interactions with Materials and Atoms*, vol. 12, no. 1, pp. 95–134, 1985.

[71] M. Wang, W. Huang, F. Kondev, G. Audi, and S. Naimi, "The AME 2020 atomic mass evaluation (II). Tables, graphs and references," *Chinese Physics C*, vol. 45, no. 3, p. 030003, 2021.

[72] J. Kelley, J. Purcell, and C. Sheu, "Energy levels of light nuclei A=12," *Nuclear Physics A*, vol. 968, pp. 71–253, 2017.

[73] B. Singh and J. Chen, "Nuclear Data Sheets for A=100," *Nuclear Data Sheets*, vol. 172, pp. 1–542, 2021.

[74] M. Wang, G. Audi, A. H. Wapstra, F. G. Kondev, M. MacCormick, X. Xu, and B. Pfeiffer, "The AME2012 atomic mass evaluation (II). Tables, graphs and references," *Chin.Phys.C*, vol. 36, p. 1603, 2012.

[75] T. Kibedi, T. Burrows, M. B. Trzhaskovskaya, P. M. Davidson, and C. W. Nestor Jr, "Evaluation of theoretical conversion coefficients using BrIcc," *Nuclear Instruments and Methods in Physics Research Section A: Accelerators, Spectrometers, Detectors and Associated Equipment*, vol. 589, no. 2, pp. 202–229, 2008.

[76] Y. L. Tong, *The multivariate normal distribution*. Springer Science & Business Media, 2012.

[77] R. W. Schafer, "What is a Savitzky-Golay filter?[lecture notes]," *IEEE Signal processing magazine*, vol. 28, no. 4, pp. 111–117, 2011.

[78] D. De Frenne, "Nuclear data sheets for A= 102," *Nuclear Data Sheets*, vol. 110, no. 8, pp. 1745–1915, 2009.

[79] T. Bäck, C. Qi, B. Cederwall, R. Liotta, F. G. Moradi, A. Johnson, R. Wyss, and R. Wadsworth, "Transition probabilities near ^{100}Sn and the stability of the N, Z= 50 shell closure," *Physical Review C*, vol. 87, no. 3, p. 031306, 2013.

[80] S. Raman, C. Nestor Jr, and P. Tikkanen, "Transition probability from the ground to the first-excited 2^+ state of even–even nuclides," *Atomic Data and Nuclear Data Tables*, vol. 78, no. 1, pp. 1–128, 2001.

[81] T. Glasmacher, "Testing the structure of exotic nuclei via coulomb excitation of radioactive ion beams at intermediate energies," in *The Euroschool Lectures on Physics with Exotic Beams, Vol. III*, pp. 27–55, Springer, 2009.

[82] M. Wang, G. Audi, F. Kondev, W. Huang, S. Naimi, and X. Xu, "The AME2016 atomic mass evaluation," *Chin. Phys. C*, vol. 41, no. 030003, pp. 1674–1137, 2017.

[83] A. J. Koning, S. Hilaire, and M. C. Duijvestijn, "TALYS: Comprehensive nuclear reaction modeling," in *AIP Conference Proceedings*, vol. 769, pp. 1154–1159, American Institute of Physics, 2005.

[84] R. Barlow, "Asymmetric systematic errors," *arXiv preprint physics/0306138*, 2003.

[85] J.-P. Jeukenne, A. Lejeune, and C. Mahaux, "Optical-model potential in finite nuclei from Reid's hard core interaction," *Physical Review C*, vol. 16, no. 1, p. 80, 1977.

[86] E. Bauge, J. Delaroche, M. Girod, G. Haouat, J. Lachkar, Y. Patin, J. Sigaud, and J. Chardine, "Neutron scattering from the ^{155,156,157,158,160}gd isotopes: Measurements and analyses with a deformed, semimicroscopic optical model," *Physical Review C*, vol. 61, no. 3, p. 034306, 2000.

[87] A. Koning and M. Duijvestijn, "A global pre-equilibrium analysis from 7 to 200 Mev based on the optical model potential," *Nuclear Physics A*, vol. 744, pp. 15–76, 2004.

[88] M. Kerveno, M. Dupuis, A. Bacquias, F. Belloni, D. Bernard, C. Borcea, M. Boromiza, R. Capote, C. De Saint Jean, P. Dessagne, *et al.*, "Measurement of ^{238}U (n, n' γ) cross section data and their impact on reaction models," *Physical Review C*, vol. 104, no. 4, p. 044605, 2021.

[89] S. Chen. Private communications.

[90] F. M. Marqués, M. Labiche, N. Orr, J. Angélique, L. Axelsson, B. Benoit, U. Bergmann, M. Borge, W. Catford, S. Chappell, *et al.*, "Three-body correlations in Borromean halo nuclei," *Physical Review C*, vol. 64, no. 6, p. 061301, 2001.

[91] J. Rohlf, *Modern Physics from α to Z^0*. 1994.

[92] M. Zhukov, B. Danilin, D. Fedorov, J. Bang, I. Thompson, and J. Vaagen, "Bound state properties of Borromean halo nuclei: ^{6}He and ^{11}Li," *Physics Reports*, vol. 231, no. 4, pp. 151–199, 1993.

[93] J. Giovinazzo, B. Blank, M. Chartier, S. Czajkowski, A. Fleury, M. L. Jimenez, M. Pravikoff, J.-C. Thomas, F. de Oliveira Santos, M. Lewitowicz, *et al.*, "Two-Proton Radioactivity of ^{45}Fe," *Physical Review Letters*, vol. 89, no. 10, p. 102501, 2002.

[94] L. Grigorenko, T. Wiser, K. Miernik, R. Charity, M. Pfützner, A. Banu, C. Bingham, M. Ćwiok, I. Darby, W. Dominik, *et al.*, "Complete correlation studies of two-proton decays: ^{6}Be and ^{45}Fe," *Physics Letters B*, vol. 677, no. 1-2, pp. 30–35, 2009.

[95] A. Spyrou, Z. Kohley, T. Baumann, D. Bazin, B. Brown, G. Christian, P. A. DeYoung, J. Finck, N. Frank, E. Lunderberg, *et al.*, "First Observation of Ground State Dineutron Decay: ^{16}Be," *Physical Review Letters*, vol. 108, no. 10, p. 102501, 2012.

[96] F. Marqués, N. Orr, N. Achouri, F. Delaunay, and J. Gibelin, "Comment on "First Observation of Ground State Dineutron Decay: ^{16}Be"," *Physical Review Letters*, vol. 109, no. 23, p. 239201, 2012.

[97] Z. Kohley, E. Lunderberg, P. DeYoung, A. Volya, T. Baumann, D. Bazin, G. Christian, N. Cooper, N. Frank, A. Gade, *et al.*, "First observation of the ^{13}Li ground state," *Physical Review C*, vol. 87, no. 1, p. 011304, 2013.

[98] I. Tanihata, H. Hamagaki, O. Hashimoto, Y. Shida, N. Yoshikawa, K. Sugimoto, O. Yamakawa, T. Kobayashi, and N. Takahashi, "Measurements of interaction cross sections and nuclear radii in the light p-shell region," *Physical Review Letters*, vol. 55, no. 24, p. 2676, 1985.

[99] P. Hansen and B. Jonson, "The neutron halo of extremely neutron-rich nuclei," *EPL (Europhysics Letters)*, vol. 4, no. 4, p. 409, 1987.

[100] D. Millener, J. Olness, E. Warburton, and S. Hanna, "Strong E1 transitions in ^{9}Be, ^{11}Be, and ^{13}C," *Physical Review C*, vol. 28, no. 2, 1983.

[101] C. Brown, "3. On a Case of Interlacing Surfaces," *Proceedings of the Royal Society of Edinburgh*, vol. 13, pp. 382–386, 1886.

[102] R. J. Charity, J. M. Elson, J. Manfredi, R. Shane, L. G. Sobotka, B. A. Brown, Z. Chajecki, D. Coupland, H. Iwasaki, M. Kilburn, *et al.*, "Investigations of three-, four-, and five-particle decay channels of levels in light nuclei created using a ^{9}C beam," *Physical Review C*, vol. 84, no. 1, p. 014320, 2011.

[103] D. Tilley, J. Kelley, J. Godwin, D. Millener, J. Purcell, C. Sheu, and H. Weller, "Energy levels of light nuclei A= 8, 9, 10," *Nuclear Physics A*, vol. 745, no. 3-4, pp. 155–362, 2004.

[104] H. Simon, M. Meister, T. Aumann, M. Borge, L. Chulkov, U. D. Pramanik, T. W. Elze, H. Emling, C. Forssén, H. Geissel, *et al.*, "Systematic investigation of the dripline nuclei ^{11}Li and ^{14}Be and their unbound subsystems ^{10}Li and ^{13}Be," *Nuclear Physics A*, vol. 791, no. 3-4, pp. 267–302, 2007.

[105] Y. Aksyutina, H. T. Johansson, P. Adrich, F. Aksouh, T. Aumann, K. Boretzky, M. Borge, A. Chatillon, L. Chulkov, D. Cortina-Gil, *et al.*, "Lithium isotopes beyond the drip line," *Physics Letters B*, vol. 666, no. 5, pp. 430–434, 2008.

[106] Y. Kubota, *Neutron-neutron correlation in Borromean nucleus ^{11}Li via the (p,pn) reaction*. PhD thesis, University of Tokyo, 2015.

[107] M. Zinser, F. Humbert, T. Nilsson, W. Schwab, H. Simon, T. Aumann, M. Borge, L. Chulkov, J. Cub, T. W. Elze, *et al.*, "Invariant-mass spectroscopy of ^{10}Li and ^{11}Li," *Nuclear Physics A*, vol. 619, no. 1-2, pp. 151–176, 1997.

[108] A. Korsheninnikov, E. Kuzmin, E. Y. Nikolskii, O. Bochkarev, S. Fukuda, S. Goncharov, S. Ito, T. Kobayashi, S. Momota, B. Novatskii, *et al.*, "L= 1 excitation in the halo nucleus ^{11}Li," *Physical Review Letters*, vol. 78, no. 12, p. 2317, 1997.

[109] H. Sagawa and K. Hagino, "Theoretical models for exotic nuclei," *The European Physical Journal A*, vol. 51, no. 8, pp. 1–31, 2015.

[110] H. Esbensen and G. Bertsch, "Soft dipole excitations in ^{11}Li," *Nuclear Physics A*, vol. 542, no. 2, pp. 310–340, 1992.

[111] T. Nakamura, A. Vinodkumar, T. Sugimoto, N. Aoi, H. Baba, D. Bazin, N. Fukuda, T. Gomi, H. Hasegawa, N. Imai, *et al.*, "Observation of Strong Low-Lying $E1$ Strength in the Two-Neutron Halo Nucleus ^{11}Li," *Physical Review Letters*, vol. 96, no. 25, p. 252502, 2006.

[112] Y. Kubota, A. Corsi, G. Authelet, H. Baba, C. Caesar, D. Calvet, A. Delbart, M. Dozono, J. Feng, F. Flavigny, *et al.*, "Surface Localization of the Dineutron in ^{11}Li," *Physical Review Letters*, vol. 125, no. 25, p. 252501, 2020.

[113] R. Lednicky and V. Lyuboshits, "Effect of the final-state interaction on pairing correlations of particles with small relative momenta," *Sov. J. Nucl. Phys.(Engl. Transl.);(United States)*, vol. 35, no. 5, 1982.

[114] F. M. Marqués, M. Labiche, N. Orr, J. Angélique, L. Axelsson, B. Benoit, U. Bergmann, M. Borge, W. Catford, S. Chappell, *et al.*, "Two-neutron interferometry as a probe of the nuclear halo," *Physics Letters B*, vol. 476, no. 3-4, pp. 219–225, 2000.

[115] J. K. Smith, T. Baumann, D. Bazin, J. Brown, P. A. DeYoung, N. Frank, M. D. Jones, Z. Kohley, B. Luther, B. Marks, *et al.*, "Neutron correlations in the decay of the first excited state of ^{11}Li," *Nuclear Physics A*, vol. 955, pp. 27–40, 2016.

[116] C. Hall, E. M. Lunderberg, P. DeYoung, T. Baumann, D. Bazin, G. Blanchon, A. Bonaccorso, B. Brown, J. Brown, G. Christian, *et al.*, "First observation of excited states in ^{12}Li," *Physical Review C*, vol. 81, no. 2, p. 021302, 2010.

[117] H. T. Johansson, Y. Aksyutina, T. Aumann, K. Boretzky, M. Borge, A. Chatillon, L. Chulkov, D. Cortina-Gil, U. D. Pramanik, H. Emling, *et al.*, "Three-body correlations in the decay of ^{10}He and ^{13}Li," *Nuclear Physics A*, vol. 847, no. 1-2, pp. 66–88, 2010.

[118] A. Corsi, Y. Kubota, J. Casal, M. Gómez-Ramos, A. Moro, G. Authelet, H. Baba, C. Caesar, D. Calvet, A. Delbart, *et al.*, "Structure of 13Be probed via quasi-free scattering," *Physics Letters B*, vol. 797, p. 134843, 2019.

[119] T. Nakamura and Y. Kondo, "Large acceptance spectrometers for invariant mass spectroscopy of exotic nuclei and future developments," *Nuclear Instruments and Methods in Physics Research Section B: Beam Interactions with Materials and Atoms*, vol. 376, pp. 156–161, 2016.

[120] T. Kobayashi, N. Chiga, T. Isobe, Y. Kondo, T. Kubo, K. Kusaka, T. Motobayashi, T. Nakamura, J. Ohnishi, H. Okuno, *et al.*, "SAMURAI spectrometer for RI beam experiments," *Nuclear Instruments and Methods in Physics Research Section B: Beam Interactions with Materials and Atoms*, vol. 317, pp. 294–304, 2013.

[121] "SAMURAI Configuration." https://www.nishina.riken.jp/ribf/SAMURAI/config.html. Accessed: 2022-03-01.

[122] H. Sato, T. Kubo, Y. Yano, K. Kusaka, J.-i. Ohnishi, K. Yoneda, Y. Shimizu, T. Motobayashi, H. Otsu, T. Isobe, *et al.*, "Superconducting dipole magnet for

SAMURAI spectrometer," *IEEE transactions on applied superconductivity*, vol. 23, no. 3, pp. 4500308–4500308, 2012.

[123] A. Obertelli, A. Delbart, S. Anvar, L. Audirac, G. Authelet, H. Baba, B. Bruyneel, D. Calvet, F. Château, A. Corsi, *et al.*, "MINOS: A vertex tracker coupled to a thick liquid-hydrogen target for in-beam spectroscopy of exotic nuclei," *The European Physical Journal A*, vol. 50, no. 1, pp. 1–20, 2014.

[124] K. Yako, H. Sakai, M. Dozon, T. Fujii, S. Kawase, Y. Kikuchi, K. Kisamori, Y. Kubota, H. Matsubara, S. Michimasa, *et al.*, "Development of WINDS: wide-angle invserse-kinematics neutron detectors for SHARAQ," *RIKEN Accelerator Progress Report*, vol. 45, p. 137, 2012.

[125] V. Panin, J. Taylor, S. Paschalis, F. Wamers, Y. Aksyutina, H. Alvarez-Pol, T. Aumann, C. Bertulani, K. Boretzky, C. Caesar, *et al.*, "Exclusive measurements of quasi-free proton scattering reactions in inverse and complete kinematics," *Physics Letters B*, vol. 753, pp. 204–210, 2016.

[126] Z. Yang, Y. Kubota, A. Corsi, K. Yoshida, X.-X. Sun, J. Li, M. Kimura, N. Michel, K. Ogata, C. Yuan, *et al.*, "Quasifree Neutron Knockout Reaction Reveals a Small s-Orbital Component in the Borromean Nucleus ^{17}B," *Physical Review Letters*, vol. 126, no. 8, p. 082501, 2021.

[127] "R^{3}BRoot package." https://github.com/R3BRootGroup/R3BRoot. Accessed: 2022-11-18.

[128] "The SMSIMULATOR simulation package." http://be.nucl.ap.titech.ac.jp/~nebula/simulator.php. Accessed: 2022-07-22.

[129] G. F. Bertsch, K. Hencken, and H. Esbensen, "Nuclear breakup of Borromean nuclei," *Physical Review C*, vol. 57, no. 3, p. 1366, 1998.

[130] H. T. Johansson, Y. Aksyutina, T. Aumann, K. Boretzky, M. Borge, A. Chatillon, L. Chulkov, D. Cortina-Gil, U. D. Pramanik, H. Emling, *et al.*, "The unbound isotopes ^{9}, ^{10}He," *Nuclear Physics A*, vol. 842, no. 1-4, pp. 15–32, 2010.

[131] A. Lane and R. Thomas, "R-matrix theory of nuclear reactions," *Reviews of Modern Physics*, vol. 30, no. 2, p. 257, 1958.

[132] J. L. Powell, "Recurrence formulas for Coulomb wave functions," *Physical Review*, vol. 72, no. 7, p. 626, 1947.

[133] J. Kelley, E. Kwan, J. Purcell, C. Sheu, and H. Weller, "Energy levels of light nuclei A= 11," *Nuclear Physics A*, vol. 880, pp. 88–195, 2012.

[134] G. Kopylov, "Like particle correlations as a tool to study the multiple production mechanism," *Physics Letters B*, vol. 50, no. 4, pp. 472–474, 1974.

[135] A. Revel, F. Marqués, O. Sorlin, T. Aumann, C. Caesar, M. Holl, V. Panin, M. Vandebrouck, F. Wamers, H. Alvarez-Pol, *et al.*, "Strong Neutron Pairing in core+ 4 n Nuclei," *Physical Review Letters*, vol. 120, no. 15, p. 152504, 2018.

[136] B. Laurent, F. M. Marqués, C. Angulo, N. Ashwood, M. Borge, V. Bouchat, W. Catford, N. Clarke, N. Curtis, M. Freer, *et al.*, "Chronology of the three-body dissoci-

ation of ^{8}He," *Journal of Physics G: Nuclear and Particle Physics*, vol. 46, no. 3, p. 03LT02, 2019.

[137] J. Smith, T. Baumann, J. Brown, P. DeYoung, N. Frank, J. Hinnefeld, Z. Kohley, B. Luther, B. Marks, A. Spyrou, *et al.*, "Selective population of unbound states in ^{10}Li," *Nuclear Physics A*, vol. 940, pp. 235–241, 2015.

[138] H. Horiuchi and K. Ikeda, "A Molecule-like Structure in Atomic Nuclei of ^{16}O* and ^{20}Ne," *Progress of Theoretical Physics*, vol. 40, no. 2, pp. 277–287, 1968.

[139] W. Von Oertzen, "Covalently bound molecular structures in the α+^{16}O system," *The European Physical Journal A-Hadrons and Nuclei*, vol. 11, no. 4, pp. 403–411, 2001.

[140] X. Mao, J. Rotureau, W. Nazarewicz, N. Michel, R. I. Betan, Y. Jaganathen, *et al.*, "Gamow-shell-model description of Li isotopes and their mirror partners," *Physical Review C*, vol. 102, no. 2, p. 024309, 2020.

[141] S. R. White, "Density-matrix algorithms for quantum renormalization groups," *Physical Review B*, vol. 48, no. 14, p. 10345, 1993.

[142] J. Rotureau, N. Michel, W. Nazarewicz, M. Płoszajczak, and J. Dukelsky, "Density matrix renormalization group approach for many-body open quantum systems," *Physical Review Letters*, vol. 97, no. 11, p. 110603, 2006.

[143] M. Kamimura, "Nonadiabatic coupled-rearrangement-channel approach to muonic molecules," *Physical Review A*, vol. 38, no. 2, p. 621, 1988.

[144] E. Hiyama, R. Lazauskas, and J. Carbonell, "^{7}H ground state as a ^{3}H+ 4n resonance," *Physics Letters B*, vol. 833, p. 137367, 2022.

université PARIS-SACLAY

ÉCOLE DOCTORALE
Particules, hadrons, énergie et noyau : instrumentation, imagerie, cosmos et simulation (PHENIICS)

Titre : Spectroscopie des noyaux exotiques à travers la carte des nucléides : de ^{11,13}Li à ^{102}Sn

Mots clés: spectroscopie gamma, interaction nucléaire, noyaux exotiques, spectroscopie de masse invariante

Résumé : Cette thèse présente les résultats de deux expériences portant sur la structure des noyaux exotiques, réalisées à la Radioactive Isotope Beam Factory (RIBF), au sein du RIKEN Nishina Center, au Japon.

La première consiste en l'étude de l'excitation inélastique de trois isotones avec $N = 52$, à savoir ^{98}Pd, ^{100}Cd et ^{102}Sn. Ces trois noyaux sont excités sur une cible de 5 mm de CH_2 et une cible de ^{12}C de 3 mm. Les rayons γ produits lors de leur désexcitation sont détectés et la section efficace d'excitation inélastique du premier état excité 2^+ de chaque isotone en a été déduite. Après analyse, on observe la décroissance des sections efficaces d'excitation inélastique à l'approche de 102Sn, indiquant une possible fermeture de couche, attendue pour le noyau doublement magique 100Sn.

La deuxième expérience consiste en l'étude de la décroissance 2-neutrons de deux isotopes du Li : ^{11}Li et ^{13}Li. ^{11}Li et ^{13}Li sont produits via (p,2p) sur ^{12}Be et ^{14}Be respectivement. Après population d'états non liés du ^{11}Li et du ^{13}Li, ces isotopes décroissent par l'émission de deux neutrons, ensuite détectés dans le spectromètre SAMURAI. Ces mesures permettent la reconstruction de l'énergie relative et des coordonnées de Jacobi du système à trois corps, afin de déterminer la nature du processus de décroissance : décroissance directe avec émission simultanée des neutrons, ou décroissance séquentielle avec émission différée des neutrons. Cette analyse révèle le caractère principalement direct de la décroissance du ^{13}Li, ainsi qu'une première observation de décroissance séquentielle à haute énergie relative pour ^{13}Li. Cette expérience montre aussi le caractère principalement séquentielle de la décroissance du ^{11}Li.

Title: Spectroscopy of exotic nuclei across the nuclide chart: from ^{11,13}Li to ^{102}Sn

Keywords: gamma spectroscopy, nuclear interaction, exotic nuclei, invariant mass spectroscopy

Abstract: This thesis presents the results of two experiments on the structure of exotic nuclei, performed at the Radioactive Isotope Beam Factory (RIBF), at the RIKEN Nishina Center, Japan.

The first one consists in the study of the inelastic excitation of three isotones with $N = 52$, namely ^{98}Pd, ^{100}Cd and ^{102}Sn. These three nuclei are excited on a 5 mm CH_2 target and on a 3 mm ^{12}C target. The γ rays produced during the deexcitation are detected and the cross-section for the inelastic excitation for the first 2^+ excited state of each isotone is determined. After the analysis, the value of the cross-sections decreases when approaching ^{102}Sn, indicating a possible shell closure, expected near the doubly magic ^{100}Sn.

The second experiment consists in the study of the two-neutron decay of two Li isotopes: ^{11}Li and ^{13}Li. ^{11}Li and ^{13}Li are produced via a (p,2p) reaction on ^{12}Be and ^{14}Be respectively. After populating unbound states of ^{11}Li and ^{13}Li, they decay, emitting two neutrons then detected in the SAMURAI spectrometer. This measurement enables the reconstruction of the relative energy and the Jacobi coordinates for the three-body system, in order to determine the decay process: direct, with a simultaneous emission of the neutrons, or sequential, with a delayed emission of the two neutrons. This analysis reveals the mainly direct character of the decay of ^{13}Li, as well as a first observation of sequential behavior at high relative energy for this isotope. This also reveals the mainly sequential decay of ^{11}Li.